



**DEVELOPMENT AND CHARACTERIZATION OF A
CHROMOTOMOSYNTHETIC HYPERSPECTRAL IMAGING SYSTEM**

DISSERTATION

Randall L. Bostick, Civilian

AFIT-ENP-DS-13-M-02

**DEPARTMENT OF THE AIR FORCE
AIR UNIVERSITY**

AIR FORCE INSTITUTE OF TECHNOLOGY

Wright-Patterson Air Force Base, Ohio

DISTRIBUTION STATEMENT A. APPROVED FOR PUBLIC RELEASE;
DISTRIBUTION IS UNLIMITED.

The views expressed in this thesis are those of the author and do not reflect the official policy or position of the United States Air Force, Department of Defense, or the United States Government. This material is declared a work of the U.S. Government and is not subject to copyright protection in the United States.

AFIT-ENP-DS-13-M-02

**DEVELOPMENT AND CHARACTERIZATION OF A
CHROMOTOMOSYNTHETIC HYPERSPECTRAL IMAGING SYSTEM**

DISSERTATION

Presented to the Faculty

Graduate School of Engineering and Management

Air Force Institute of Technology

Air University

Air Education and Training Command

in Partial Fulfillment of the Requirements for the

Degree of Doctor of Philosophy

Randall L. Bostick, BS, MS

Civilian

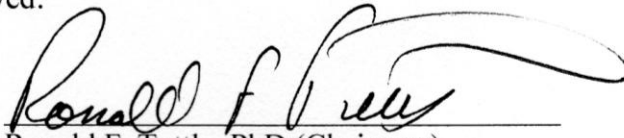
March 2013

**DISTRIBUTION STATEMENT A.
APPROVED FOR PUBLIC RELEASE; DISTRIBUTION IS UNLIMITED.**

DEVELOPMENT AND CHARACTERIZATION OF A
CHROMOTOMOSYNTHETIC HYPERSPECTRAL IMAGING SYSTEM

Randall L. Bostick, BS, MS
Civilian

Approved:



Ronald F. Tuttle, PhD (Chairman)

1/30/2013
Date



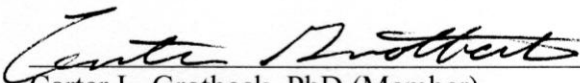
Glen P. Perram, PhD (Member)

4 Mar 2013
Date



Thomas N. Hangartner, PhD (Member)

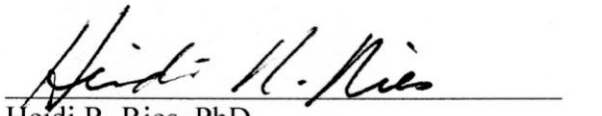
2/22/2013
Date



Carter L. Grotbeck, PhD (Member)

7 Feb. 2013
Date

Accepted:



Heidi R. Ries, PhD
Interim Dean, Graduate School of Engineering
and Management

8 Mar 2013
Date

Abstract

A methodology based upon mathematic reconstruction of a set of 2-D spectral projections to collect high-speed (>100 Hz) 3-D hyperspectral data cube has been proposed. Called to this point chromotomographic imaging, the term chromotomosynthetic imaging (CTI) is introduced here to better align with the conventional medical physics process of tomosynthesis. The CTI system can simultaneously provide usable 3-D spatial and spectral information, provide high-frame rate slitless 1-D spectra, and generate 2-D imagery equivalent to that collected with no prism in the optical system. With this prototype, data was collected 3-4 times faster than a Liquid Crystal Tunable Filter (LCTF) with a 100x increase in spectral bins due to the amount of data and high spectral throughput.

The designed laboratory CTI instrument operates over a spectral range of 400 – 900 nm with a field of view of 71.6 mrad. Resulting angular system resolution of 0.8 – 1.6 μ rad was found experimentally. Spectral resolution was measured to be 0.6 nm at the shortest wavelengths, degrading to over 10 nm at wavelengths approaching 800 nm and limited by chromatic aberration effect on the point spread function. A mathematical error function defining the degradation of performance in the 3-D reconstructed image cube was derived, capturing effects of systematic instrumental error caused by prism spectral dispersion, prism and mount misalignment, detector array position and tilt, and prism rotation angle. The wavelength region where prism dispersion is highest (<500 nm) is most sensitive to loss of spectral resolution in the presence of systematic error, while

wavelengths >600 nm suffer mostly from a shift of the spectral peaks. The quality of the spectral resolution in the reconstructed hyperspectral imagery was degraded by as much as a factor of two in the blue spectral region with less than 1° total angular error in mount alignment in the two axes of freedom. For larger errors than this, spectral peaks begin to split into bimodal distributions. Study of error improved calibration of the transformed wavelength axis needed for accurate reconstruction, improving both spectral and spatial resolution in the forward transform.

Instrument performance was assessed by exploitation of four diagnostic targets: (1) a random array of spectrally diverse point-like sources, (2) a regular 5×5 array of circular bandpass filters, (3) a propane flame, and (4) a large blackbody emitter. In the first two cases, a wideband image reconstructed from the CTI data matched the image collected by the system without the prism in place when using projections at 1° sampling over a range of $0^\circ - 180^\circ$. Acceptable results were obtained using 5° sampling, with over 100% degradation observed at 10° sampling in terms of noise and background bias. Target classification for point sources yielded the same 5-6 target classes for both the LCTF and CTI, although there was a 25% misclassification rate possibly due to the spectral similarity in the sources. For the mosaic, reported intensities for each element were within 10% of the baseline, with the extracted spectral and spatial information for the elements in the array matching that collected by the LCTF for the filters. In transitioning from the point targets to the spatially extended sources, reconstruction artifacts were observed causing significant spectral and spatial artifacts not present in the LCTF data.

Spectral intensity distributions were found to be a function of spatial location in the source images, deviating from the expected Gaussian shapes.

The CTI and LCTF produced hyperspectral imagery from an open propane flame clearly capturing the sharp C₂ Swan band emission lines in the 400 – 650 nm range. The spectral resolution of the CTI proved to be far better than the LCTF in the region as expected, resolving the CH and C₂ peak I emission lines in the flame core. However, the LCTF was superior in capturing spatial structure and intensity in the dimmer regions of the torch where artifacts left little contrast in the CTI image. The LCTF was able to detect spectral content at points 2-3 mm farther away from the core than the CTI. Many more projections are required when collecting on spatially continuous sources compared to diagnostic targets, likely approaching the $\pi \cdot N/2$ tomographic limit with N the number of pixels in the longest spatial dimension of the sampling array. Neither the CTI nor the LCTF had the spatial resolution necessary to calculate vibrational population distributions or temperatures in the flame.

Artifacts in the broadband reconstruction of the blackbody target were much more prevalent than in prior targets, causing shifting and broadening of the expected Planckian shape to the point where unrealistic blackbody temperatures of near 2000 K were calculated. Optimized data processing and a correction from model predictions allowed for compensation of artifacts to yield a more reasonable temperature changing spatially over the surface from 800 K to 1000 K. No molecular emissions were observed in the plume with the spreader in place, indicating low concentration of C₂ molecules.

To my mother, father, wife and children

Acknowledgments

My sincere appreciation to my wife for her patience as well as my children, all of whom were born and raised during the years spent on this pursuit. To my parents I am particularly grateful for the many years of support and encouragement which have led me to where I am today. I wish to express my deep appreciation to my advisor, Dr. Ron Tuttle, who provided the opportunity to continue my education and a good amount of “persuasion” to keep pushing towards the goal.

Likewise, I appreciate the patience and time of the committee members, Dr. Glen Perram, Dr. Thomas Hangartner, and Dr. Carter Grotbeck. Their support of the research and technical expertise was a great source of assurance and advice. I am most grateful to Dr. Perram who provided almost all of the focus and scientific counsel to ensure the relevance and ultimate success of this research.

I owe a debt of gratitude to many others at AFIT who have contributed to this success by either direct assistance or much needed encouragement: Dr. Kevin Gross, LtCol Michael Hawks, Dr. Bryan Steward, Greg Smith, Mike Ranft, Dr. Daniel LeMaster, Dr. Stephen Cain and Malcolm Gould. Finally, a very big “thank you” to everyone at NASIC for the support over the years, especially the group chiefs and flight directors who have allowed me the time to finish this work. There are many, but most notably Mr. Jim Engel, Ms. Sharon Staley, Ms. Korin Elder, Maj. Robin DelaVega, Maj. Carl Haney, and Mr. Curt Rowland.

Randall L. Bostick

Table of Contents

	Page
Abstract	iv
Acknowledgments	viii
Table of Contents	ix
List of Figures	xii
List of Tables	xxii
I. Introduction	1
Document Overview	12
II. Background	15
Basic Prism Spectroscopy	15
Basics of Medical Tomosynthesis	18
Reconstructive Tomography	22
CTI System Overview and Data Collection	26
Data Reconstruction	30
Target Phenomenology and Exploitation	34
III. Spatial and Spectral Performance of a Chromotomosynthetic Hyperspectral Imaging System	40
Preface	40
Introduction	41
Design Of The Chromotomosynthetic Imager	43
Data Reconstruction	48
Experiment	50
Results	53
Spatial Resolution	53
Spectral Resolution	57
Spectral Registration and Calibration	58
Conclusions	61

	Page
IV. Instrumental Error In Chromotomosynthetic Hyperspectral Imaging.....	63
Preface.....	63
Introduction.....	64
The CTI System.....	66
Image Reconstruction and Error Kernel.....	68
Sources of Error.....	79
Error in Prism Dispersion.....	80
Detector Array Distance and Tilt.....	81
Prism and Mount Misalignment and Field Angle.....	82
Error in Projection Angle θ	84
Modeling Effects of Systematic Error.....	84
Error in Prism Angular Deviation.....	85
Detector Array Distance and Tilt.....	86
Prism and Rotation Stage Misalignment.....	87
Error in Projection Angle θ	90
Experimental Validation.....	91
Conclusions.....	96
V. Classification of Visible Point Sources Using Hyperspectral Chromotomosynthetic Imagery.....	100
Preface.....	100
Introduction.....	101
Instrumentation.....	103
Data Collection and Processing.....	109
The 2-D Integrated Image.....	110
Target Spectra from 1-D Spectrograph Co-Addition.....	111
CTI 3-D HSI Data Cube Reconstruction.....	112
LCTF Data Processing.....	113
Data Analysis and Results.....	113
The 2-D Undispersed Image.....	113
The 3-D Hyperspectral Data and Target Characterization.....	117
Collection Requirements.....	122
Conclusions.....	124
VI. Hyperspectral Image Reconstruction of an Array of Extended Targets Using Chromotomosynthesis.....	127
Preface.....	127
Introduction.....	128
Instrument and Experiment.....	129

	Page
CTI Data Collection and Processing	129
LCTF Data Collection and Processing	132
Mosaic Target.....	133
Results	134
The 2-D Wideband Imagery	134
Hyperspectral Imagery	138
Artifacts in CTI Reconstruction	144
Conclusions	148
VII. Hyperspectral Analysis of a Propane Flame Using Chromotomosynthesis	151
Preface.....	151
Introduction	152
Instrumentation	153
Results	160
Panchromatic Images	160
Extracted Spectra.....	163
Hyperspectral Imagery	169
Conclusions	172
VIII. Conclusions	174
Data Collection and Reconstruction.....	175
Affect of Systematic Error	177
Utility Assessment of the CTI.....	179
Point Source Targets	180
Mosaic Array	182
Flame and Extended Blackbody Source.....	183
Summary	185
Recommendations and Future Work.....	186
Appendix A. Component Selection and Development	189
The Detector Array	191
Choosing Optical Elements.....	191
Appendix B. Calibration of the Chromotomosynthetic Imaging System	197
Bibliography	199
Vita.....	208

List of Figures

Figure	Page
1. CTI provides a methodology to provide high speed data at intermediate spectral and spatial resolutions compared to a dedicated hyperspectral imager such as an imaging FTIR and an imaging system that utilizes spectral filtering (multiple bandpass filter).....	7
2. The prism spectrograph. Collimated light entering the prism is dispersed according to wavelength and then focused onto a detector array.....	16
3. In the method of conventional tomography, the x-ray source and the film move at the same angular velocity but in opposite directions. The points in plane B that intersect the axis of rotation remain spatially registered on the film. The points in plane A and C are imaged onto different parts of the film thus blurred in the final image.	19
4. The geometry for circular tomography. The P_0 plane will remain in focus at the film for all points in the trajectory of the source and film. The position of P_0 is a function of the radius of the circular path of the source.....	20
5. The x-rays transiting through the object $f(x,y)$ at some angle θ with respect to the x-axis create a 1-D projection perpendicular to the direction of travel. These projections, $p(s,\theta)$, are used to reconstruct the density function $f(x,y)$	22
6. An illustration of the Radon Projection in circular tomosynthesis. Data projected through the 3-D volume is equivalent to a 2-D slice in the 3-D Fourier space. Many projections fill a volume in the Fourier Space which excludes a cone above and below the central plane. The size of this area is directly dependent on the projection angle, ϕ	26
7. Schematic design of the CTI instrument. L_1 and L_2 are essentially an afocal telescope to collimate incoming light. The rotating DVP disperses light as a function of wavelength, and L_3 acts as a focusing lens to produce an image on the detector array.....	27

Figure	Page
8. The DVP disperses the spectral components of an image as a function of wavelength, λ , and projection angle, θ as in (a) and (b). An image of a source with undispersed red (“R”), green (“G”), and blue (“B”) components is shown as it would be observed on the detector array in (c). Pictures (d), (e), and (f) show the dispersed image at $\theta = 0^\circ, 90^\circ$, and 180° . Note that the “G” component is at the undeviated wavelength and is not displaced at any θ	29
9. In (a), (b), and (c), each of the projection is shifted to reverse the spatial displacement imparted by the DVP corresponding to the wavelength at which the letter “B” is emitting. In (d) the shifted projections are added. The image of the letter “B” is spatially co-located while the other images are displaced. Panel (e) is the result as the number of projections goes to infinite.....	32
10. Because the radon projection through the undispersed image $f(x,y)$ is equivalent to that of the dispersed image, the 2-D undispersed image can be recovered from the set of $p(x,y,\theta)$ by performing a filtered back projection.	33
11. A schematic design of the CTI instrument is shown in (a). L_1 and L_2 are an afocal telescope to collimate incoming light. The rotating DVP disperses light as a function of wavelength, and L_3 acts as a focusing lens to produce an image on the detector array. Distances, D , are in mm. The material and geometry of the DVP are given in (b).....	44
12. The spectral displacement in terms of the angular spectral dispersion of the prism and the total displacement in pixels at the detector array for a 0° field angle.	46
13. The shift in displacement, Δr , at the array as a function of three input field angles θ_I to the prism; $\theta_I = 0.1^\circ$ (solid line), $\theta_I = 0.5^\circ$ (dashed line), and $\theta_I = 1.0^\circ$ (dotted line).....	47
14. An example of the peaks fit to the extracted Ne spectrum in the 3-D reconstructed imagery. The dotted line is the data; the solid line represents the fitted peaks.....	53
15. The spatial resolution results for the black body source (“o”), spectral sources (“□”) and the measured spatial resolution in the 3-D reconstructed data (“▲”). The dashed curve is the predicted resolution from the model of the system after adjusting for the detector coupling.....	54

Figure	Page
16. The expected PRF from the model of the system. The spatial resolution of the collection system is shown as the dotted line. The spatial resolution in the reconstructed 3-D hyperspectral data is shown as the dashed line.	56
17. The measured spectral resolution from the 3-D $r(x,y,\lambda)$ data (“o”), the predicted spectral resolution from the system (solid line), and the expected resolution given estimated error in reconstruction (“■”).	58
18. The predicted spectral displacement $r(\lambda)$ compared to that measured in the $p(x,y,\theta)$ sets: $\theta = 0^\circ$ (“♦”), $\theta = 90^\circ$ (“□”), $\theta = 180^\circ$ (“o”), and $\theta = 270^\circ$ (“x”). Residuals in terms of pixels and wavelength, λ , are shown below the plot with a noticeable correlation between the $p(x_i,y_i,0^\circ)$ and $p(x_i,y_i,90^\circ)$ data and the $p(x_i,y_i,180^\circ)$ and $p(x_i,y_i,270^\circ)$ data.	60
19. The residuals between the measured and modeled dispersion after a linear correction is applied based on measurements of the spectral dispersion in the data used in this experiment. The symbols are the same as those in Figure 18.	61
20. Schematic design of the CT instrument. L_1 and L_2 are essentially an afocal telescope to collimate incoming light. A field stop is located at the image plane between these two lenses. The rotating DVP disperses light as a function of wavelength, L_3 acts as a focusing lens to produce an image on the detector array.	67
21. The dispersion $\varphi(\lambda)$ of the DVP and resulting displacement at the detector array, $r(\lambda)$. The solid line is for a 0° field angle (angle of incidence) and the dashed line for a 0.2° field angle.	68
22. The system modeled spatial resolution (dotted line) and spectral resolution (solid line) with perfect reconstruction [57]. Spectral resolution, $\Delta\lambda$, is derived from the spatial resolution, $w(\lambda)$ using Equation (20).	68
23. Row (a) provides the undispersed image, $s(x,y,\lambda)$ for an on-axis, monochromatic ($\lambda = 540$ nm) point source. Row (b) illustrates the projections summed over all prism rotation angles, $\sum p(x,y,\theta)$, for the same point source with: (column 1) $r = -10.3$ pixels, $r_\varepsilon = 0$; (column 2) $r = -8$ pixels, $r_\varepsilon = -2.3$ pixels; and (column 3) $r = 6 \sin\theta + 12$ pixels, $r_\varepsilon = 6 \sin\theta - 1.7$ pixels. Row (c) is the spatial representation of the error function $h^\varepsilon(x,y,\lambda)$ with the same displacements. In row (d) the convolution of the error kernel with the undispersed image, yields the reconstructed image, $t(x,y,\lambda)$	70

24. The shifting of an on-axis, monochromatic point source from its undispersed location at the origin of the x-y plane. DVP dispersion displaces the source by $r(\lambda)$ at angle θ . In the direction perpendicular to dispersion, spatial resolution, $w(\lambda)$ is defined by the point spread function (PSF). In the dispersive direction, spectral resolution, $\Delta\lambda$, is defined by the line spread function (LSF). 71
25. A summary of the system errors considered for this study. The dispersion, detector distance and tilt, prism misalignment and mount misalignment are all described by the $r_e(\lambda, \theta)$ term input to the error kernel, H^e (Equation (31)). 80
26. The shift in spectral peak location as ε_φ increases from 0.01° (solid line) to 0.05° (dashed line) to 0.10° (dotted line). The effect is markedly increased at longer wavelengths. 86
27. Comparison of object and reconstructed hyperspectral images for detector tilt. The effects of error in terms of spatial shift Δs , spectral line shift $\Delta\ell$, loss of spatial resolution w and loss of spectral resolution $\Delta\lambda$ for four difference cases of detector distance error ε_d and detector tilt δ_x and δ_y . In each plot “◆” indicates $\varepsilon_d = 1$ mm, $\delta_x = 1^\circ$ and $\delta_y = 0^\circ$; “□” indicates $\varepsilon_d = 1$ mm, $\delta_x = 2^\circ$, and $\delta_y = 0^\circ$; “x” indicates $\varepsilon_d = 1$ mm, $\delta_x = 3^\circ$ and $\delta_y = 3^\circ$; and “o” indicates $\varepsilon_d = 2$ mm, $\delta_x = 3^\circ$, and $\delta_y = 3^\circ$ 87
28. The spectral peak shift $\Delta\lambda$ as a function of the prism misalignment α_x in the rotation stage mount. Plotted are $\alpha_x = -0.5^\circ$ (“◆”), $+0.5^\circ$ (“□”), -1.0° (“x”) and 1.0° (“o”). 88
29. Comparison of object and reconstructed hyperspectral images for mount misalignment. The effects of error in terms of spatial shift Δs , spectral line shift $\Delta\ell$, loss of spatial resolution w and loss of spectral resolution $\Delta\lambda$ for four different cases of mount misalignment components β_x and β_y : $\beta_x = 0.25^\circ$, $\beta_y = 0.00^\circ$ (“◆”); $\beta_x = 0.50^\circ$, $\beta_y = 0.00^\circ$ (“□”); $\beta_x = 0.25^\circ$, $\beta_y = 0.25^\circ$ (“▲”); $\beta_x = 0.50^\circ$, $\beta_y = 0.25^\circ$ (“o”); and $\beta_x = 0.50^\circ$, $\beta_y = 0.50^\circ$ (“x”). 89
30. Reconstructed hyperspectral images for an on-axis, monochromatic $\lambda = 400$ nm point source, at three nearby wavelengths: (a) 399 nm, (b) 400 nm and (c) 401 nm for $\beta_x = 0.50^\circ$, $\beta_y = 0.50^\circ$. The spectra for the (0,0) pixel at the center of the image provides the spectral lineshape functions for (d) progressively worse prism mount misalignment: $\beta_x = 0.00^\circ$, $\beta_y = 0.00^\circ$; $\beta_x = 0.25^\circ$, $\beta_y = 0.00^\circ$; $\beta_x = 0.50^\circ$, $\beta_y = 0.00^\circ$; and $\beta_x = 0.50^\circ$, $\beta_y = 0.50^\circ$. In part (e) the shift in peak wavelength is apparent for the $\beta_x = 0.50^\circ$, $\beta_y = 0.50^\circ$ case as prism misalignment, α_x , increases from 0.0° to 0.5° to 1.0° 90

Figure	Page
31. The loss of spatial and spectral resolution for given errors in θ , denoted by ε_θ : $\varepsilon_\theta = 0.10^\circ$ (“◆”), $\varepsilon_\theta = 0.25^\circ$ (“□”), and $\varepsilon_\theta = 0.50^\circ$ (“▲”).....	91
32. Measured and modeled $r_\delta(\lambda, \theta)$ for the 404.7 nm, 435.8 nm, 546.0 and 635.0 nm spectral lines for detector tilt $\delta_x=4^\circ$, $\delta_y=2^\circ$ and detector distance error $\varepsilon_d = -2$ mm as a function of θ . The measured data points are given by the “■”, with the solid line the model results with associated error estimate.....	94
33. Measured and modeled $r_\delta(\lambda, \theta)$ for the 404.7 nm, 435.8 nm, 546.0 nm, and 635.0 nm spectral lines for prism and mount misalignment of $\alpha_x=0.50^\circ$, $\alpha_y=0.50^\circ$, $\beta_x=0.75^\circ$, and $\beta_y=0.50^\circ$. The measured data points are given by the “■”, with the solid line the model results with associated error estimate.....	95
34. Description and components of the AFIT rotating prism CTI instrument.	104
35. The final model of $r(\lambda)$ plotted as a solid line for the CTI in this experiment after calibration with several sources: “o” – Hg lamp; “□” – laser; “Δ” – band pass filter.	106
36. The measured spectral transmission (solid line) and spectral resolution (dashed line) calculated for the DVP.....	107
37. The estimated spectral resolution (dotted line) and spectral transmission (dashed line) of the LCTF.....	108
38. A color image of the Christmas lights as they appear in the lab. The targets detected in the FOV of the instrument are shown on the right. Due to scaling, not all targets evident in the raw data may be observable in the picture. The scale on the detector array is 0.5 mm/pixel.....	109
39. Integrating projections along the dispersion axis at θ produces a 1-D projection $S(t, \theta)$ equivalent to taking the radon transform of the undispersed image at the undispersed location. Shown are line projections at $\theta=0^\circ$ and $\theta=45^\circ$	111
40. Panchromatic 2-D reconstructions for the set of projections $S(t, \theta)$ with different densities of projections: (b) P_{180} , c) P_{36} , and d) P_{18} . The undispersed image is also shown for comparison in (a).	115

Figure	Page
41. The measured target intensity in the reconstructed P_{180} (“♦”), P_{36} (“■”), and P_{18} (“▲”) images plotted against the intensities measured in the 2-D undispersed image. A linear fit indicates the degree to which the intensities are accurately recovered.	116
42. The extracted spectral intensity from (a) Target 1 and (b) Target 2 for the LCTF and the CTI. Dotted line is the spectrum from the CTI-1D method, the dashed line the CTI-3D method, and the solid line the LCTF.....	118
43. The five target classes calculated from the CTI-1D results are shown on the right and the CTI-3D hyperspectral cube classes on the left.	119
44. The target classes calculated from the LCTF data. The results are very similar to the CTI, with little residual energy in the blue (Classes I and Ia) at wavelengths greater than 600 nm.	120
45. Spectra for Target 15 which is associated with Class V from the LCTF and Class I in both CTI methods.	122
46. Basic description and components of the AFIT rotating prism CTI instrument. Drawing is not to scale.	130
47. The spectral resolution (dotted lines) and spectral transmission (solid lines) of the CTI (left) and LCTF (right). The LCTF only transmits linear polarized light.	130
48. The target mosaic with filter element position and center wavelength in nm is shown in (a). In (b), the image of the target taken with no filter or dispersive element; the negative of the image is presented for clarity. The measured intensities in detector counts of each image in the mosaic from (b) are plotted in (c). The 710 nm element is saturated.	134
49. The results for the 2-D wideband image of the mosaic. In (a)-(c), the image is reconstructed from the CTI data using 180, 36, and 18 projections. Artifacts in the scene become more apparent as fewer projections are used. The image from integrating LCTF frames is shown in (d). The undispersed image and a model derived image are provided in (e) and (f) for reference. The x-positions and y-positions are shown in mm and the normalized inverse of the intensity is used.	135
50. The percent difference images between I_{LCTF} and I_0 (top left), I_{180} and I_0 (top right), I_{36} and I_0 (bottom left) and I_{18} and I_0 (bottom right). The scaling is in units of percent difference.	138

Figure	Page
51. The residuals between the measured centers of the CTI and LCTF spectral peaks and the nominal centers of the band pass filters with the bias in the CTI data removed. “◆” = 360 projections, “■” = 72 projections, and “▲” = 36 projections.	140
52. Measured spectral resolution of the CTI and the LCTF. The spectral resolution of the CTI closely matches the predicted performance and is marginally better than the LCTF. “◆” = 360 projections, “■” = 72 projections, and “▲” = 36 projections.	141
53. The discrepancy metric, $\delta(q)$, for each of the filter elements as a function of the number of projections used in the reconstruction. “◆” = 360 projections, “■” = 72 projections, and “▲” = 36 projections.	142
54. The $\delta(q)$ plotted from the dimmest elements to the brightest. The worst fits are for intensities $<1 \times 10^4$ counts, as are the cases with noticeable differences in the number of projections used. “◆” = 360 projections, “■” = 72 projections, and “▲” = 36 projections.	143
55. The percent difference image between the LCTF and CTI at the 440 nm spectral bin. The leakage of the 430 nm filter into the bin is driving the discrepancy between the two data sets. The image scale is in mm in the object plane. The x- and y-axes are in pixel space, 13 $\mu\text{m}/\text{pixel}$	144
56. The spectral intensities are plotted for points in increasing distance from the center of the filter image as shown on the left. In both plots, the intensity decreases as r_n increases. The lineshape of the 600 nm filter in the CTI data becomes deformed as the spatial distance is increased. The LCTF lineshapes keep their Gaussian shape as the r increases, though intensity is decreasing.	145
57. Artifacts cause deformation of the 650 nm peak in the CTI data and secondary peaks when compared to the LCTF (solid line). The artifacts become worse as fewer projections are used. Reconstructions using 360 projections (“X”), 72 projections (“□”) and 36 projections (“Δ”) are plotted. The CTI lineshape is narrower despite the false secondary peak at 620 nm.	147

Figure	Page
58. The 620 nm bin images are shown for reconstruction with 360 (top left), 72 (top right), and 36 (bottom left) projections. The circle indicates the spatial location of the 650 nm filter. The artifact energy causes the false peak at 620 nm. The 620 nm bin from the LCTF is shown on the bottom right with no energy near the 650 nm filter. Scale for each image is mm in the object plane.....	148
59. Components of the AFIT rotating prism CTI instrument.....	154
60. The spectral response of the CTI system with: (a) the DVP in place and (b) replacing the DVP with the Liquid Crystal Tunable Filter (LCTF). The LCTF has much less transmission at shorter wavelengths.	156
61. The CTI projection system geometry as the DVP rotates from $\theta=0^\circ$ to $\theta=45^\circ$. The data sample in (a) represents $p(x,y,0^\circ)$ and (b) $p(x,y,45^\circ)$	157
62. Color image taken by a commercial digital camera of: (a) target flame alone and (b) with the spreader attached. An approximate image scale is shown.....	159
63. The 2-D reconstruction of the flame without spreader from: (a) the projection, (b) the integrated CTI hyperspectral data cube, and (c) the integrated LCTF hyperspectral data cube. In each figure, the x-y dimensions are in pixels at ≈ 0.75 mm/pixel. The (0,0) coordinate is approximately the optic axis for the collection, and numbers identifying points of further analysis.	161
64. The 2-D panchromatic images of the flame with spreader from (a) the integration of the CTI hyperspectral data cube and (b) the filtered backprojection. In each figure, the scale is in pixels with ≈ 0.75 mm/pixel. The (0,0) coordinate is approximately the optic axis for the collection.	162
65. The CTI (above) and LCTF (below) emission spectra at locations in the image as noted in Figure 63. In each case, the intensity decreases as the points, denoted in Figs. 63a and 63b become farther from the torch. The format of the plotted lines are varied for clarity.....	164
66. Near infrared spectra of the flame and spreader at several points in the image as denoted in Figure 64b. In the flame, points 4 (unmarked solid line), 5 (dashed line) and 6 (dotted line) show little if any spectral content as the open flame did. Points 1, 2, and 3 in the spreader indicate the emission is brighter in the center of the spreader.	166

Figure	Page
67. The BB intensity curves for an 800° C BB (solid line) and the reconstructed intensity using a model of the CTI with an 800° C BB in the shape of the spreader as input. Artifacts in the reconstruction cause the spectral intensity to be shifted to the right and misshapen.	167
68. Deriving a correction function from the CTI model using data such as that shown in Fig. 67, the intensity from the 3D CTI reconstruction can be corrected for the artifacts, plotted as a solid line. The best fit BB to this curve is at 750° C, plotted as a dashed line.	168
69. The temperature profile of the torch with the spreader in place. The brass spreader is at 1000° C or below, while the flame is near 1900° C in the hottest areas. The pixel scale is $\approx 1900^\circ\text{C}$	169
70. Spectral image of the CH emission peak for the CTI image (left) and the LCTF (right).	170
71. Spectral image of the C ₂ band I emission peak for the CTI (left) The LCTF could not separate the C ₂ band I peak from the CH peak at 432 nm.	170
72. Spectral image of the C ₂ band II emission peak for the CTI image (left) and the LCTF (right).	170
73. Spectral image of the C ₂ band III emission peak for the CTI image (left) and the LCTF (right).	171
74. Spectral image of the C ₂ band IV emission peak for the CTI image (left) and the LCTF (right).	171
75. Spectral image of the C ₂ band V emission peak for the CTI image (left) and the LCTF (right).	171
76. Schematic design of the CTI instrument. L_1 and L_2 are essentially an afocal telescope to collimate incoming light. The rotating DVP disperses light as a function of wavelength, and L_3 acts as a focusing lens to produce an image on the detector array.	189
77. The AFIT DVP. The full assembly is 21 mm in diameter, and 38.51 mm in length at the center. Definition of $\varphi_p(\lambda)$ is also shown in the diagram as well as the material (Schott Glass nomenclature).	190
78. The angular dispersion of the direct vision prim. The undeviated wavelength λ_c is at approximately 548 nm. Note the decrease in dispersion at longer wavelengths.	190

Figure	Page
79. The displacement $r(\lambda)$ at the detector in pixels for L_3 focal lengths of $f_3=50$ mm (dashed line), $f_3=100$ mm (solid line), and $f_3=150$ mm (dotted line).....	192
80. The plot of linear resolution $\Delta r/\Delta\lambda$ at the detector array for L_3 focal lengths of $f_3=50$ mm (dashed line), $f_3=100$ mm (solid line), and $f_3=150$ mm (dotted line).....	193
81. The change in the value of $r(\lambda)$ as a function of the field angle is given in the plot on the left for field angles of 0.1° (dashed line), 0.5° (solid line) and 1.0° (dotted line). The plot in the left shows the resulting error in wavelength that corresponds to the error in pixel displacement.....	194

List of Tables

Table	Page
1. A summary of the ground truth tests performed in recent years with targets and instrumentation.	35
2. Prominent pen lamp wavelengths.	51
3. The mean and standard deviation from the $r(\lambda, \theta)$ data for each measured wavelength in the presence of prism and mount misalignment and detector distance error and tilt.	96
4. Specifications of the AFIT CTI instrument.	105
5. The background mean and noise for the measured and reconstructed 2-D images. Also given are the results of a linear fit to the intensities plotted in Figure 41.	116
6. Targets assigned to member classes based on collection method. The CTI 1D and 2D methods match each other almost identically, with discrepancies between CTI and LCTF.	121
7. Collection and processing time necessary to acquire results for the study. The integration time for both the CTI and LCTF is 1 msec/frame.	123
8. Linear response for CTI and LCTF broadband imagery.	136
9. Comparison of broadband images using Colsher values, average percentage difference, and standard deviations.	137
10. The C ₂ Swan bands as measured by the CTI and LCTF.	165
11. Sources used and results of CTI system calibration.	198

DEVELOPMENT AND CHARACTERIZATION OF
A CHROMOTOMOSYNTHETIC HYPERSPECTRAL IMAGING SYSTEM

I. Introduction

There are many targets or events of interest with regard to military defense, civil unrest, technical intelligence and battlespace awareness which have been historically challenging to detect and classify due to short lifetimes and/or rapidly varying physical characteristics. Critical targets such as artillery shell blasts, bomb detonations, muzzle flashes, and improvised explosive devices all have lifetimes of ≈ 10 seconds or less with quickly changing features during this period due to the volatile thermal and chemical processes [1-9]. Even persistent emissions from targets such as a missile plume contain complex and very quickly fluctuating features, especially in the boundary layer [10, 11]. All of these events can be classified and further characterized based up physical properties of the event, most prominently the spatial and spectral energy distributions and their evolution over time. Analysis has been done using fast-framing imaging sensors operating at frame rates into the 100s of kHz to capture the spatial evolution in wideband panchromatic imagery or as very limited bandpass radiometer measurements [3, 5, 9, 12]. Further research has been focused on identifying changes in infrared spectra at speeds of 10's of Hz as a solution to the problem of classifying explosive targets [2, 13-15]. The encouraging results of this analysis and recent work by Gross and Steward [2, 7, 17, 18] indicate that an ability to acquire simultaneous spectral and spatial data at very high

speeds can make use of both spatial and spectral classification methodologies to improve the overall results.

The ability to record and exploit this spatial/spectral information is the focus of the field of hyperspectral imagery (HSI). Hyperspectral imagery is three dimensional data, two dimensions being spatial and the third the spectral content of a point in the spatial scene. Time becomes the fourth dimension of analysis when cubes of data are taken successively. The conventional approaches to collecting hyperspectral data are to use a spectrometer modified to collect imagery as in the case of imaging Fourier Transform Infrared (FTIR) systems, spatially scan the desired area of interest with a spectrometer, or use an imaging sensor and collect successive spectral bands [19-21]. These methods are temporally slow compared to the lifetimes of fast transient events. Also, they are optically inefficient in that data is being taken piece-by-piece with photons not collected simultaneously in all spatial or spectral regions, rejecting energy that could contribute to the final hyperspectral measurement. When speed is a primary requirement, these modes of collection tend to be optimized to provide exceptional spectral or spatial data, but not both. Further, to achieve high-speed performance these instruments are optimized to observe controlled and coordinated events in a specific known time and area with no or little use for battlespace monitoring. Imaging FTIR's have made advances in recent years, with a midwave instrument recently developed with a spectral range of 1800–6667 cm^{-1} (1.5–5.5 μm) and user-defined spectral resolution between 0.25–150 cm^{-1} . It has a 320x256 pixel Stirling-cooled InSb FPA that can be windowed to improve temporal resolution with a smaller field-of-view. The instrument has an IFOV of 0.35 mrad and uses a 16-tap read-out integrated circuit to achieve fast data rates, though still at <1 Hz

for usable spectral resolutions and fields of view [22-24]. Also, for events which change during the time it takes the FTIR to acquire a complete interferogram, it has been shown to suffer from artifacts which degrade spectral quality of the collection [25]. A hyperspectral method of collection is needed in which speed is the objective with compromised yet acceptable spectral and spatial performance over a large field of view.

A different approach to HSI collection called *chromotomographic* (or *chromotomosynthetic*) imaging (CTI) combines the tomosynthetic techniques found in medical imaging with dispersive element spectroscopy to capture data at the speeds necessary to exploit short lived targets. Medical tomography has customarily been defined as the technique of reconstructing a selected 2-D plane or 3-D volume internal to a patient from a series of 1-D or 2-D projections of x-rays passing through the patient. In a CTI system, the intensity of an object is dispersed (or projected) spectrally as a function of wavelength in a certain direction and projected onto a 2-D focal plane then spatially recorded. Multiple projections are acquired by changing the spectral projection angle. The resulting set of 2-D spectral projections is then reconstructed to build a 2-D undispersed panchromatic image of the object as well as the 3-D hyperspectral data cube. Suitable data post-processing is required to reconstruct spectral projections and can be optimized based on known target characteristics. As with x-ray tomosynthesis, the projection/dispersion angle of the system is not perpendicular to the rotation angle so that an exact reconstruction in the spectral dimension is not possible, with artifacts in the form of out of band energy decreasing the quality of the reconstructed data with fewer projections used [26-28].

The underlying principle of CTI lies in the field of medical physics and the mathematics of tomography first demonstrated by Ziedes des Plantes in 1932 [29]. The process of circular tomosynthetic projection and reconstruction of multiple planes into a 3-D data cube was presented by Grant [30] in 1972. The transition of the technology to hyperspectral imagery was first explored theoretically in the literature by Levin [31], with more application by Okamoto [32] who proposed a crossed phase grating to produce the spectral projections. The developments of a CTI hyperspectral instrument are nearly simultaneously documented by the Air Force Research Laboratory (AFRL) at Hanscom Air Force Base by Mooney [33, 34] and the Optical Sciences Center at the University of Arizona by Deriniak [35-37] beginning in the mid-1990's. The AFRL design, unlike Okamoto's, uses a direct vision prism as the spectral dispersive element which rotates to provide the different spectral projections. The most complete documentation of development and performance of a working CTI system is by the Arizona group and has been used mostly for biomedical imaging [38]. Subsequent work by Hagen and Dereniak sought to improve the instrument performance [39] and most importantly provide a definition of performance parameters in terms of a hyperspectral imaging instrument [40] with some parallels to the rotating prism instrument but with the basic differences in data collection. This implementation features a computer generated hologram diffraction grating as a dispersion element which has drawbacks with regard to the applications of interest in this work as opposed to the rotating prism design.

The hologram grating distributes spectral irradiance into multiple diffracted orders, with the 0th order at the center. These orders form a rectangular array of spectrally dispersed images onto a large-format focal plane array (FPA), with each image (or

element) in the array a 2-D projection of the image cube (not including the 0th order). The number of $N \times N$ elements in the array is dependent on the grating design. Very high temporal rates are possible because the entire set of projections is collected in one snapshot. However, in a remote sensing application there are also limitations. If the target energy is assumed equally spread into $N \times N$ orders on the array then each gets $1/N^2$ of the target signal reducing signal-to-noise ratio (SNR). Also, the spatial and spectral resolutions of this system are limited since all orders must share the area of the focal plane, constraining the number of pixels that can be used to collect a projection. The 0th order provides a non-dispersed image, but again at reduced irradiance and resolution and over an effective field of view that is only few percent of the detector array. With this particular grating design, the number of projections is fixed and cannot be changed based on desired performance. In the literature, $N = 3, 5,$ and 7 designs have been demonstrated [40]. The grating design has been most successfully used in biological applications where the required field of view is very narrow and active lighting can be used to ensure ample intensity from the target [38].

For the mission area of interest here, the AFRL design featuring the rotating direct vision prism is a better solution. Unlike the grating instrument, the entire detector array is used to collect a single spectral projection. This results in a reduction of collection speed inversely proportional to the number of projections used. However, using the entire array allows for a much wider field of view for event monitoring and increased sampling of the projection by the detector array greatly increases achievable spatial and spectral resolution with the increased field of view. Because target energy is dispersed into only one order, SNR can be maximized. Also, spectral projections are collected as

the prism rotates at discrete angles such that the number, location and density of projection angles are variable.

There are several design features of the rotating prism CTI which make it an attractive option for the acquisition of high speed HSI compared to conventional methods. The components and construction of CTI make it readily compatible with existing wide field of view imaging systems and is inexpensive to implement. In addition to the 3-D HSI data, the 2-D spectral projections allow for a complete 2-D reconstruction of the undispersed panchromatic image (similar to the 0th order of the grating design) thus preserving the functionality of a dedicated imaging system. Due to the 100% throughput of the CTI (not considering usual system response), each projection represents a 2-D spectrograph, which can be exploited to analyze high frequency changes in spectral content of unresolved targets as would be done with a traditional slitless spectrographic instrument. Finally, and most important is the ability of the CTI to collect data very quickly, with complete HSI data cubes collected at greater than 10Hz and possibly 100s of Hz, with associated 2-D spectrographs at nearly 1 kHz [31, 41, 42]. This makes the CTI very attractive to collecting relevant data on events occurring in a battlespace such as artillery fire, detonations and explosions and fast burning missiles at spatial and spectral resolutions adequate enough to allow for the characterization of events to meet mission requirements. Figure 1 shows notionally how the CTI may fill in the trade-space between spectral filtering and Fourier transform hyperspectral collection techniques.

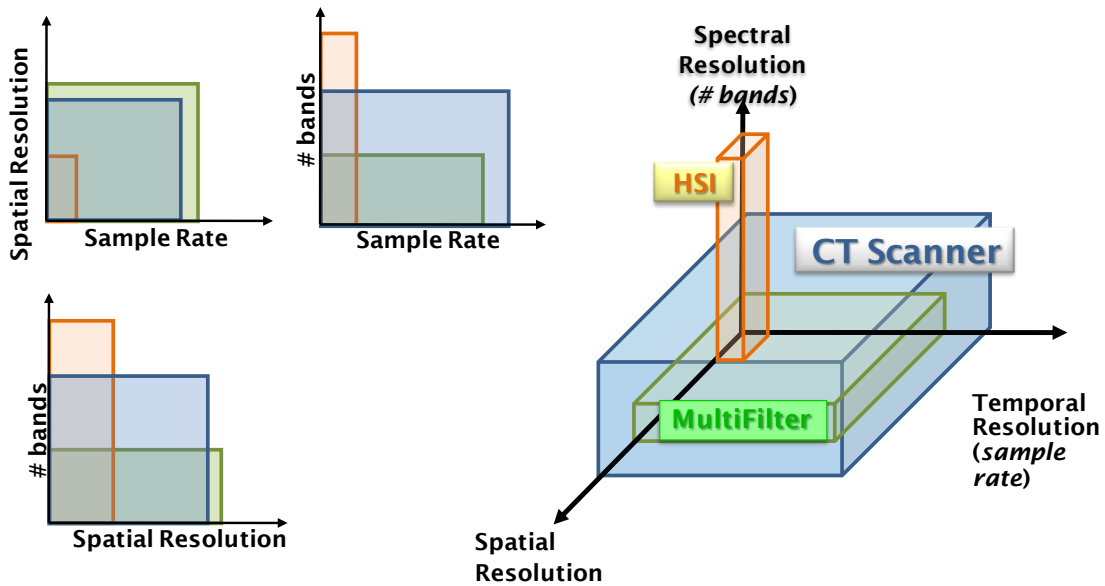


Figure 1. CTI provides a methodology to provide high speed data at intermediate spectral and spatial resolutions compared to a dedicated hyperspectral imager such as an imaging FTIR and an imaging system that utilizes spectral filtering (multiple bandpass filter).

The AFRL work contains a description and advantages of chromotomographic hyperspectral imaging system “CTHIS” designs with some performance parameters based on collection examples and a few diagnostic targets [33, 34]. The achievable spatial and spectral resolutions are reported for single collections in terms of what “should be” resolvable in the scenes examined, but general performance is unknown, the number of necessary projections needed is not addressed, and any dependencies on systematic errors are not discussed. More refined systems operating in the VNIR [43] and the MWIR [44] were subsequently described, but with less information on performance parameters than the earlier papers and more emphasis on collection examples. While some component details are described for the MWIR system, there is little information on the VNIR instrument which appears to be a more complex system. Unfortunately, while somewhat theoretically robust, the literature does not provide a

comprehensive description of the metrology or overall performance of a working rotating prism CTI to allow for a determination of the utility of this instrument to meeting mission area requirements.

Though a characterization of the instrument in terms of achievable spectral or spatial resolution is not documented, description of theoretical performance is found in the literature, including an assessment of noise performance and scan efficiency [42]. In most of the papers a mathematical discussion of the forward spectral and spatial transform of the CTI is found as well as the method of inverting the transform to recover the 3-D hyperspectral imagery from the 2-D projections. Later work by Mooney is focused on optimizing the reconstruction algorithms given the singularity in the inverse of the transform [45-47]. This work tends towards reconstruction techniques rather than system performance. Later work returns to the analysis of system performance, but only shows advantages of exploitation of the data as if it were a simple prism spectrograph collecting point source targets [48, 49]. A method using a mathematical backprojection algorithm has been presented, but not demonstrated on collected data [50].

The Air Force Institute of Technology (AFIT) began a more thorough analysis of the technology beginning in 2004. A model-based development of the optical system was described, but included no analysis of hyperspectral performance [51]. Subsequent work described the ability to process the data by direct inverse of the forward transform (as with AFRL) and assessments of algorithm performance based on synthetic data sets [52]. The performance of the CTI was again described theoretically in terms of the forward transform of the instrument by Gould [53, 54]. This work did include a more applicable data reconstruction technique based upon a maximum likelihood iterative method.

However, the target sets were synthetic and somewhat unrealistic, with the system performance in terms of a metrology not included. LeMaster's work [55] did advance the AFIT research to the development of an instrument and data collection, though it focused on validating the model of the forward transform and did not address reconstruction of hyperspectral imagery.

Following this, the AFIT Remote Sensing Group has examined the use of the CTI from an applied perspective for the purpose of component specification and data collection for a field-deployable and space-based system. The field-deployable, ground-based prototype built by O'Dell [41, 56] demonstrated AFIT's ability to collect remotely sensed data to monitor the potassium and sodium line emissions from transient combustion events.

Most recently, AFIT has conducted a component assessment for a space-based asset using the CTI laboratory design defined by the present work [57]. Components for the space system have been proposed in terms of a trade-space analysis of major instrument components to include: front-end optics, the rotating prism, focal plane array, on-orbit calibration, data production, storage and downlink [58]. Building on this initial study, the space based chromotomographic experiment (CTEx) is currently in development intended for operation on the International Space Station (ISS) as an engineering risk reduction enterprise for an operational system. A structural assembly was successfully fabricated, a successful design review for a Mersenne telescope design was conducted, and applicable methods and procedures were developed for the space-based on-orbit focus, alignment, and calibration schemes [59]. The most recent work encompassed both the engineering design process as well as a system-level characterization test series to

validate the enhancements to deviation angle, image quality, and alignment characterization methodologies. Finally, the third effort in this thesis related to the design, analysis, and characterization test campaign encompassing the space-based CTE_x instrument computer unit (ICU) [60]. This activity produced an experimentally validated thermal model supporting further trade-space refinement and operational planning aspects for this device. Results from the space studies support the transition of this next generation technology from the laboratory to a fully-realized, space-readied platform achieving intelligence preparation of the battlespace for the warfighter. However, this only addressed requirements and details necessary for transitioning the component level design into the given ISS host spacecraft. No work was done on the performance of the CTI as a hyperspectral imager.

At this time there is a lack of a complete study of the rotating prism system design details, achievable spectral and spatial resolutions, tolerances of the performance of the instrument with respect to systematic error, and a complete analysis of the performance against diagnostic targets. Because of this, it is difficult to assess whether the CTI can be used for spatial and spectral characterization of known target phenomenology. This lack of detail in design requirements, impact of error and how system properties are affected by the mathematical transforms have kept CTI systems from being considered outside of the specific AFRL team and more recently AFIT remote sensing group. A more general reconstruction method is also required as the direct inversion process is mathematically complex and inappropriate given incompleteness of the inverse. As a result, the objectives of this research are: (1) provide a documented system design that defines the spatial and spectral resolution achievable in 3-D hyperspectral space by the system,

limiting parameters and dependence on system components; (2) identify the chief contributors to systematic error in the instrument and define the degradation of spectral and spatial performance as function of the amount of error propagated through the forward transform and simplified data reconstruction; and (3) describe in terms of the instrument collection and data reconstruction the advantages and weaknesses of the instrument in being able to provide exploitable hyperspectral imagery against target sets with various spatial and spectral properties. As a result of this research, several key deficiencies in the existing literature will be addressed and documentation will be made available to allow informed decisions on use of the CTI technology to meet intelligence mission requirements.

To support all of these objectives, a CTI system was built to make diagnostic measurements of performance. In addition to the data collection system, a model of the CTI based on previous AFIT work will also be used, adjusted to incorporate the particular components of the instrument and observed system performance. The system will operate in the visible spectral range for practicality. The visible is chosen over the infrared as stray light (self emission) is more easily eliminated, optical components are cheaper and more readily available, overall construction is simpler (no cooling required) and optical aberrations are smaller due to shorter wavelength. Though combustion events contain most of their interesting features in the infrared, this research will provide the necessary details of analysis to allow results to be applied to other spectral ranges (e.g. infrared). A series of diagnostic tests over the range of the sensor will be used to define the basic sensor performance by measuring instrument parameters such as point spread function, prism spectral dispersion and prism rotation angle. These will be related to

measured performance in the reconstructed hyperspectral imagery where quality of data will be defined in terms of spectral resolution, spatial resolution, spectral line shift and spatial shifting of the source. A mathematical definition of the affect of systematic error will be developed to quantitatively assess the degradation of data quality for a given source of error. Finally, a series of targets will be used to determine how well the system performs in terms ability to characterize spatially and spectrally diverse scenes by comparing to predicted/theoretical performance, comparison to a conventional hyperspectral collection system, and the overall ability to characterize the target scene.

This research advances the understanding of the collection, processing and exploitation of hyperspectral imagery collection by a CTI system. This foundational research will define how system designers and those assessing remote sensing requirements determine utility of the technology. It is accepted that the CTI system will not provide the same high quality spectral data that the imaging FTIR delivers, nor will it achieve the spatial imaging capability of the variable filter design. The research and results of design, instrument performance, and limitations of the CTI presented here will allow potential users to assess whether CTI will meet needs based mission design constraints, required spatial and spectral performance, and the exploitation needed to reconstruct 3-D HSI from the 2-D spectral projections collected by the instrument.

Document Overview

Chapter II provides the background material necessary for understanding the overall research and use of the CTI. This includes a brief review of prism spectroscopy and hyperspectral imaging leading to the development of the theory of chromotomosynthesis

from medical tomography. The design of the AFIT instrument is presented with enough detail to define the overall performance trade-space given specific design parameters. The operation of the instrument is then described followed by a review of the standard data reconstruction algorithms that have been developed for circular tomosynthesis, the medical analogue to chromotomosynthesis. Finally, a summary of prior research in the field of chromotomography is provided.

Chapters III – VII of this document were written in the style of journal articles submitted or to be submitted for publication which results in some amount of information repetition. This somewhat redundant information in the discussions of motivation and background are presented in a context unique to the focus of each chapter and should serve to reinforce the use of the instrumentation for a particular experiment or application. The intent of these chapters is to supplement and expand the existing literature based on this research.

Chapters III and IV provide the basic metrology for the instrument by defining the theoretical spatial and spectral resolution of the system and assessing the impact of systematic error in the reconstruction of the hyperspectral data. Using system design parameters, the spatial and spectral response to a monochromatic point source is both modeled and measured and the model then updated based upon the empirical results. Following this, a mathematical development of the effects of error on the instrument performance is presented. Systematic error in prism dispersion, detector array placement and misalignment, and prism and mount misalignment are evaluated. Following the mostly theoretical assessment of CTI performance, Chapters V through VII discuss the application of the CTI in collecting data against representative targets of interest.

The target sets become more spatially and spectrally complex to incrementally show how the CTI performance is challenged to provide useful and exploitable hyperspectral imagery. In each case, the CTI does provide a unique capability compared to traditional collection methodologies, though spectral and spatial artifacts in the data begin to significantly degrade performance compared to the theoretical results.

An overall conclusion of the work and summary of results is presented in Chapter VIII along with recommendations for future study. Here, a utility assessment is made for the instrument given the stated mission areas and others for which the CTI may be well suited. Specialized reconstruction methods are recommended given the spatial and spectral properties of the target being exploited. Following the conclusions are appendices providing background information on CTI design and performance and calibration used in this research but whose length or direct relevance precluded inclusion in the main text.

II. Background

Chromotomosynthetic imaging is a mix of the basic principles of spectroscopy and the tomographic projection techniques with associated medical physics reconstruction algorithms. As such the performance of the instrument is not only dependent upon the design as it would be in spectroscopy, but also on the mathematics of the forward and reverse transforms. It is therefore instructive to present a brief description of prism spectroscopy as the definition of terms and spectral collection methodology are very similar. Following that is a discussion of the development of circular tomosynthesis, the medical physics analog to CTI.

The next section of the chapter combines the elements of the two concepts above to illustrate the data collection and reconstruction process that results in the hyperspectral imagery. Finally, with the operation of the CTI defined, a description of the spatial and spectral characteristics of the targets of interest is provided with notional requirements for target classification based on previous work. This gives a notional idea of minimum performance necessary in terms of temporal, spatial and spectral resolution.

Basic Prism Spectroscopy

Dispersive elements, such as diffraction gratings and prisms have been used in the field of spectrometry for hundreds of years. The CTI used in this research is based upon a design which features a prism as the dispersive element and therefore has much in common with the traditional prism spectrometer. Figure 2 shows how a simple prism spectrometer works given some source S which contains spectral red, green, and blue components I_R , I_G , and I_B . L_I is the collecting lens with focal length f_I , illuminated by the

source of light S . L_2 (focal length f_2) is the collimator and L_3 (focal length f_3) the focusing, or imaging lens. The aperture of the system, A_p , is generally a narrow slit which limits the field of view of the system. In this case, the spectral components I_R , I_G and I_B of the source are imaged at the detector array with the spatial sampling defined by the size of the slit.

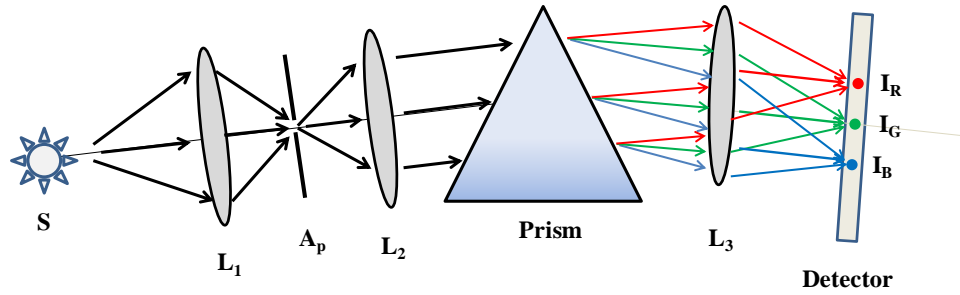


Figure 2. The prism spectrograph. Collimated light entering the prism is dispersed according to wavelength and then focused onto a detector array.

The prism disperses the light into various wavelengths based upon the refractive index of the prism material (glass usually) as a function of wavelength. For collimated light incident at the same input angle, the output angles for light will be a function of wavelength. If the difference between the input and output angle is $d\theta$ for a given difference in wavelength $d\lambda$, then the angular dispersion of the light, $\phi(\lambda)$, is defined as $d\theta/d\lambda$. The linear separation at the focal plane, dx , which fixes the actual scale of the final spectrum, is given by:

$$dx(\lambda) = f_3 \cdot \frac{d\theta}{d\lambda} \cdot \Delta\lambda \quad (1)$$

Even with infinitely small pixels and a slit which could be considered a true line source, diffraction due to the limiting aperture of the optics will broaden the image to

produce a line shape at the detector. The minimum resolvable distance is now defined by the width of the line on the focal plane and can be expressed using the Rayleigh Criterion [61] for any point as:

$$dx_{\min}(\lambda) = 1.22 \cdot \frac{f_3 \cdot \lambda}{D_A} \quad (2)$$

where D_A is the diameter of the effective aperture of the system.

In order to have enough energy throughput for detection on the image plane, and to image a spatially resolved target, D_A must have some finite diameter. The size of the slit image I_A on the focal plane can be expressed mathematically as:

$$I_A = D_A \cdot \frac{f_3}{f_2} \quad (3)$$

which simply states that the slit image is magnified in the ratio of the focal lengths of the focusing lens and collimator lens. This with Equation (1) provides a minimum separation between two spectral images such that they can be resolved. The resulting $\Delta\lambda$ that can be discriminated on the array of discrete pixels at the detector defines the spectral resolution of the system. Assuming the spatial sampling of the detector array with pixels of size d is sufficient, the minimum separation dx to discriminate two sources is:

$$\Delta\lambda \geq \left(\frac{1.22 \cdot \lambda}{D_A} + \frac{D_A}{f_2} \right) \cdot \left(\frac{d\theta}{d\lambda} \right)^{-1} \quad (4)$$

As expected, the higher the resolving power of the prism, the lower $\Delta\lambda$ and better the system resolution. Somewhat counter intuitive is the lack of dependence on the focal length of L_3 , as would be expected from Equation (1). This is because the size of I_A increases with f_3 , evident in Equation (3). The spectral resolution can be improved if a

longer f_3 is used and the ratio f_3/f_2 is kept constant. Also, if the size of the image of the source or aperture is dependent on system aberrations, defocus or other phenomena independent of f_3 , spectral resolution can be improved by increasing the distance between L_3 and the detector array.

The prism spectrometer does not provide an image of the source, only the spectral information of the source passed through the aperture, or slit. This defines the instantaneous field of view (IFOV) of the system. To extend this to a system which can provide hyperspectral imagery, the entire spatial extent of the object is sampled, recording the spectral information at each step. This is traditionally done by scanning the telescope over the desired spatial field of view. This type of system can provide very high spectral resolution but can be slow and requires very precise pointing knowledge.

Basics of Medical Tomosynthesis

Conventional focal plane tomography was first introduced in the form of X-ray transmission imaging in 1921 by Bocage [62, 63]. Later, des Plantes described the ability to represent the internal structures of a patient in an image plane by summation of a set of component radiographs, each imaging the object at a different projection angle [29]. The summation process is accomplished by continuously recording the x-rays transmitted through the body as the x-ray source and detector film are simultaneously translated at the same angular velocity in opposite directions. This way, the projection image for a particular plane in the 3-D patient volume coincides at every position. This plane is generally that which intersects the axis of rotation of the x-ray source. Figure 3 illustrates this process for three planes in the patient and a linear scan direction. Points in plane B

will always image at the same position on the film while those in planes A and C will move relative to the film. The tomographic reconstruction produces a sharp image of structures in the focus plane with the blurred images of objects lying outside superimposed.

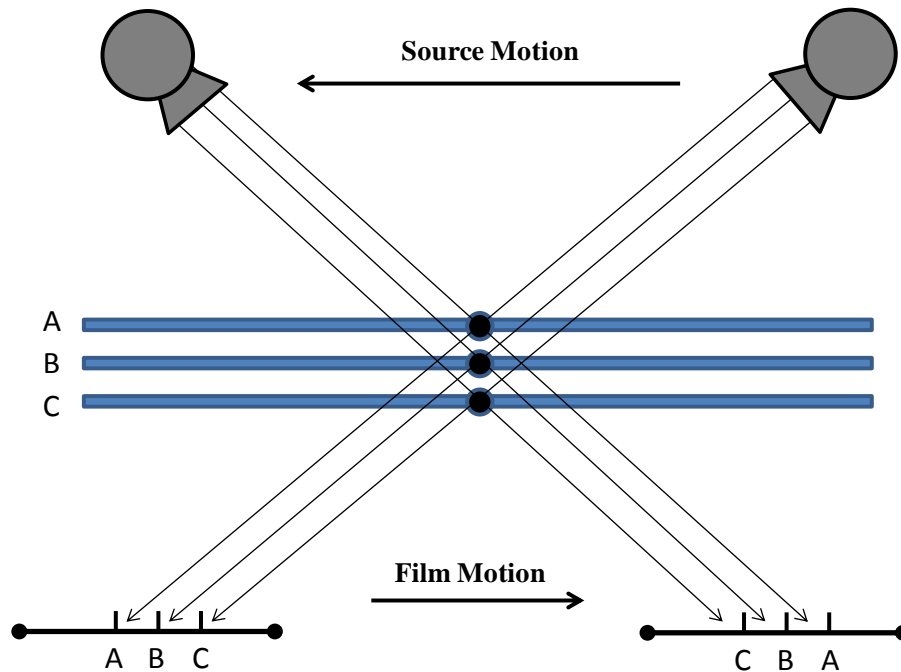


Figure 3. In the method of conventional tomography, the x-ray source and the film move at the same angular velocity but in opposite directions. The points in plane B that intersect the axis of rotation remain spatially registered on the film. The points in plane A and C are imaged onto different parts of the film thus blurred in the final image.

Figure 3 is a particular geometry that uses linear translation. Structures which appear bright and near the in-focus image plane can be especially problematic [30, 64], forming line artifacts in the radiograph. Also, frequency components which are perpendicular to the scan direction are not attenuated or blurred by the scanning motion. Thus, a circular scan geometry is preferred as the motion equally defocuses spatial content in all directions [30, 64]. Figure 4 shows a circular scan geometry in which the

plane in focus or tomographic plane, P_0 , is that which intersects the fulcrum at $z = 0$ at angle α , the projection angle. The source travels around the z -axis at radius R .

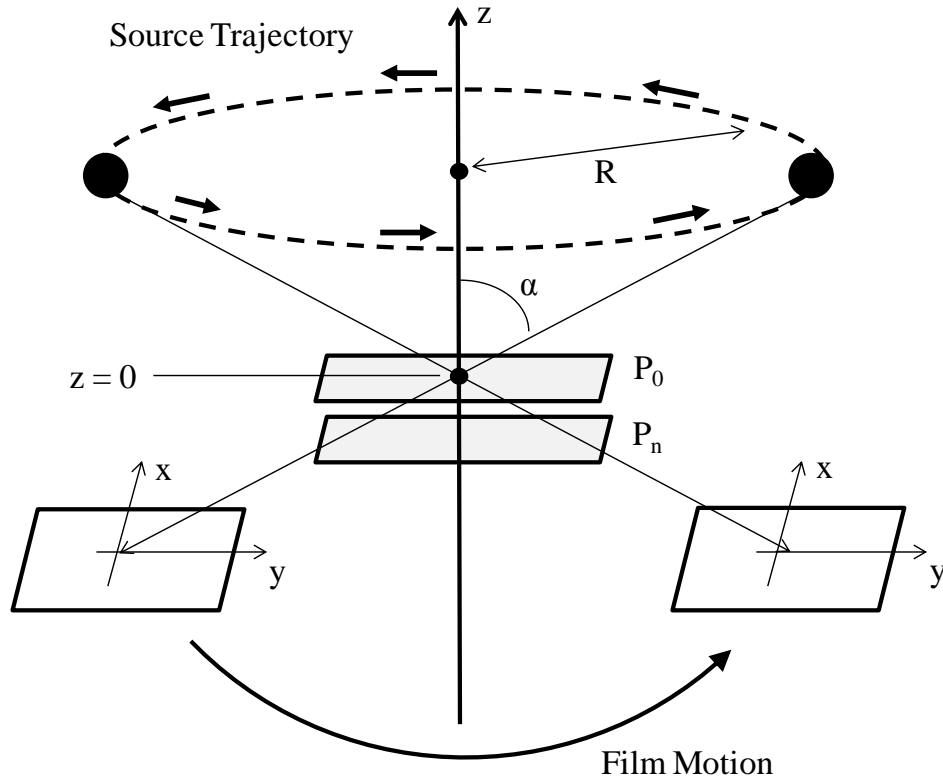


Figure 4. The geometry for circular tomography. The P_0 plane will remain in focus at the film for all points in the trajectory of the source and film. The position of P_0 is a function of the radius of the circular path of the source.

In conventional tomography, only one image plane could be acquired per x-ray scan, with additional planes necessitating additional scans increasing the radiation dose to the patient. The next advancement in tomography came when Grant proposed that it is not essential to integrate directly onto a single film, but that a tomographic image may be formed by collecting different views on N discrete films and then summing the resulting images [30]. The significance in obtaining discrete images is that any object plane can be

reconstructed from this set of projection data. The reasoning for this lies in the fact that any tomographic plane can be chosen by simply changing the scanning radius of the film (see Figure 4). This change shifts the system fulcrum along the z-axis to the desired plane. This does not explicitly change the data recorded on the film, but shifts the plane which is stationary and spatially added.

The advantage of collecting N separate radiographs becomes clear. To reconstruct the central tomographic plane, the radiographs are summed as they were collected by the system. To obtain a new plane, one simply displaces, or shifts, the radiographs by an amount corresponding to the radius necessary to virtually move the fulcrum to the desired plane and a new summation is performed. By varying the plane of reconstruction continuously, the entire patient volume can be determined.

The main disadvantage of conventional focus tomography is that while a plane of data can be exactly reconstructed, it is done so with unwanted artifacts and energy from planes that are not of interest and become more pronounced with fewer projections taken [26-28]. True reconstructive tomography is accomplished when both the source and detector are in the plane of interest, rotating about an axis perpendicular to the plane. The resulting projections can be used to reconstruct the spatial distribution of tissue densities in the scanned layer. This method of tomography was not generally pursued until the late 1960's as the process of reconstruction is mathematically intensive, requiring advanced (at the time) computer resources. The nomenclature Computed Tomography (CT) or as previously known, Computer Assisted Tomography (CAT) is now well established [66].

Reconstructive Tomography

The layer, or plane that is to be scanned can be represented using an (x,y) coordinate system. A density function $f(x,y)$ is used to describe the spatial distribution of signal in the plane. Ray paths through the plane are described in a rotated coordinate system (r,s) such that the r -axis is parallel to the direction of the x-ray projection and at some projection angle θ to the x -axis. Figure 5 illustrates the coordinate system.

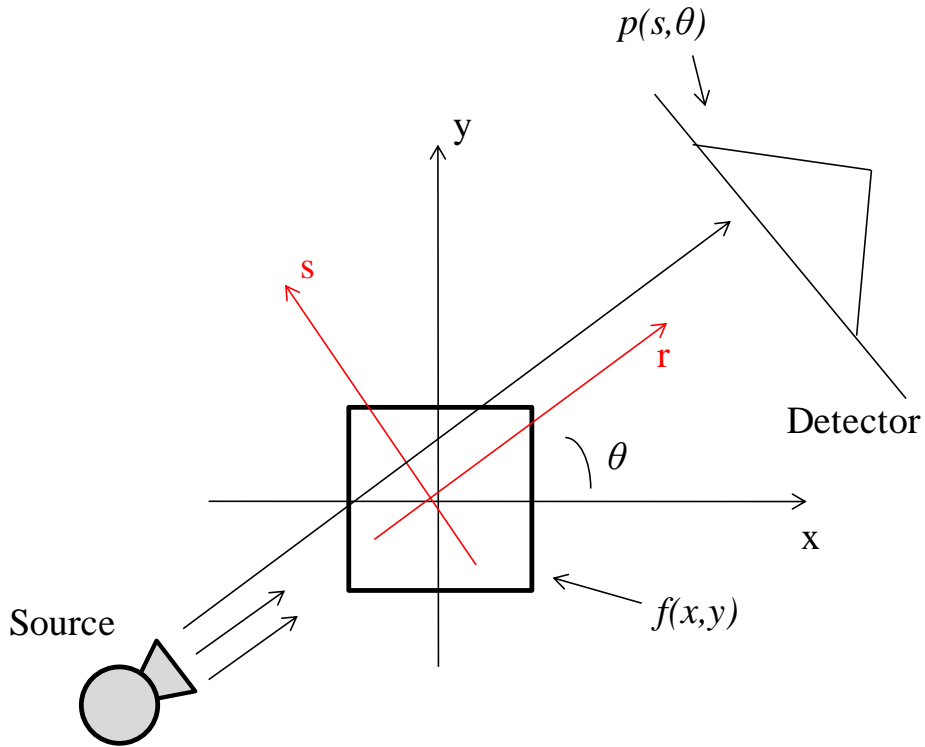


Figure 5. The x-rays transiting through the object $f(x,y)$ at some angle θ with respect to the x -axis create a 1-D projection perpendicular to the direction of travel. These projections, $p(s,\theta)$, are used to reconstruct the density function $f(x,y)$.

Each ray path through $f(x,y)$ can be expressed by the coordinates (s,θ) . The integral of $f(x,y)$ along a ray (r,θ) over the plane defines the projection $p(s,\theta)$:

$$p(s,\theta) = \int_s f(x,y) dr \quad (5)$$

The collection of these line projections at different projection angles can then be used to reconstruct the plane of information mathematically by using the Fourier Slice Theorem [64]. The theorem states mathematically that if the Fourier transform of $f(x,y)$ is defined as:

$$F(u,v) = \iint f(x,y)e^{-ik(u \cdot x + v \cdot y)} dx dy \quad (6)$$

and the Fourier transform of $p(s,\theta)$ is defined as:

$$P(w,\theta) = \int p(s,\theta)e^{-ikw} ds \quad (7)$$

then:

$$S(w,\theta) = F(w,\theta) = F(w\cos(\theta), w\sin(\theta)). \quad (8)$$

This implies that the Fourier transform of a parallel projection of an image $f(x,y)$ taken at an angle θ gives a slice of the two-dimensional transform, $F(u,v)$, at an angle of θ with the u -axis.

Equation (8) defines the method by which the 2-D image can exactly be reconstructed from the series of 1-D projections, and shows that a unique mathematical solution exists. Practically, this cannot be implemented because an infinite number of projections would be necessary to fill the Fourier space. Additional degradation of image reconstruction occurs since interpolation of the discrete projections is required as the Fourier coefficients obtained fall radially in the rectangular space such that higher frequency components become smoothed. Finally, noise and inaccuracy in the mapping of the projections cause significant artifacts in the reconstruction. For this reason, several mathematical approaches that have been used for image reconstruction that do not involve a direct inverse of the Radon transform illustrated in Figure 5. The methods fall into one of the following classifications:

Backprojection. The simplest concept to understand, it has been used since the earliest experiments and is subject to significant artifacts. This process is incorporated in the more exact methods as an initial or other constraining condition. It follows from the assumption that for any point s_l on the measured projection $p(s, \theta)$ the measured energy can be attributed to some point along a corresponding ray r_l . Thus, the values of s_l are attributed to all points along r_l effectively estimating the reverse of the projection process. This is repeated for all projection samples and produces a blurred version of the true object [64, 66, 67].

Iterative Reconstruction. Iterative methods are constraint based approaches that use continually updated estimations of the reconstruction to arrive at a solution. Iterative reconstruction is used in cases where analytic reconstruction fails due to complications or error in the projection data. The traditional method is the Algebraic Reconstruction Technique (ART) [66, 68], optimized with a Simultaneous ART (SART) algorithm [69,70]. With increased computing power available, similar but more statistical based maximum likelihood-expectation maximization (ML-EM) algorithms have been developed [64, 71, 72].

Analytic Reconstruction. Analytic methods are based on exact mathematical solutions to the imaging equations. Most, like those involving the Fourier Slice Theorem are not practically feasible due to the amount of data and calculation required and extreme sensitivity to noise or other errors. Consequently, an alternative approach to the solution of the Fourier Slice Theorem is used. The most common is the filtered backprojection (FBP) algorithm, used in most if not all commercial x-ray CT scanners [73]. The FBP provides a more accurate solution to the inverse projection than the

simple backprojection by applying the appropriate filter to each projection in frequency space prior to the backprojection process [64, 66, 67].

These and other algorithms falling into these classes are well documented in the literature. At this point, we emphasize that the key difference between planar or focus tomography and true reconstructive tomography is the fact that the projection angle in the prior is not perpendicular to the axis of rotation of the source-detector pair. Figure 6 illustrates the collection geometry for circular tomosynthesis and the mapping into the 3-D Fourier space as described by the Fourier Slice Theorem. The rotation of the projected plane as the data are collected does not sample the space leaving an empty cone above and below the central plane. Thus, the mathematical sampling of the object plane and volume is incomplete leaving an underdetermined projection space such that an inversion of the process (in terms of matrix algebra) is ill-conditioned. The complex analytic reconstruction methods are not appropriate as a unique mathematical solution is not possible.

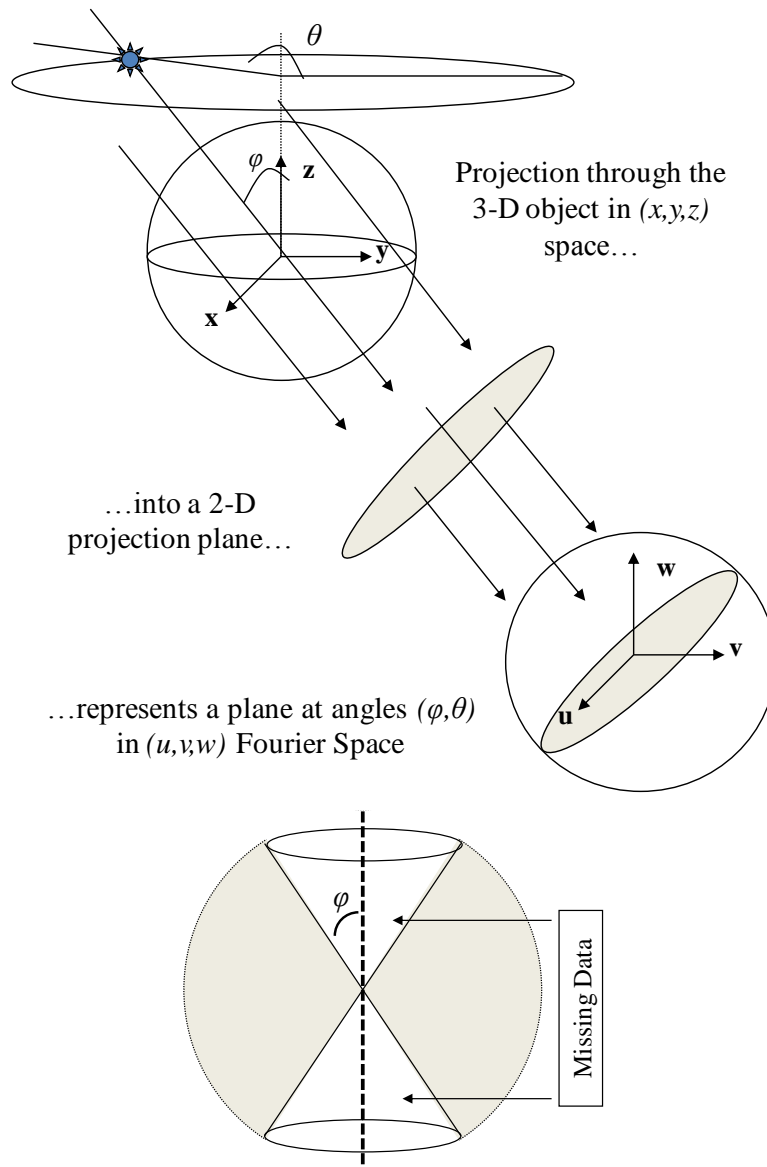


Figure 6. An illustration of the Radon Projection in circular tomography. Data projected through the 3-D volume is equivalent to a 2-D slice in the 3-D Fourier space. Many projections fill a volume in the Fourier Space which excludes a cone above and below the central plane. The size of this area is directly dependent on the projection angle, ϕ .

CTI System Overview and Data Collection

The CTI collects spectral projection data in mathematically the same way that spatial projection data is taken in circular tomography. The difference is in the 3-D volume that is reconstructed. In circular tomography, a 3-D spatial volume is reconstructed

from 2-D spatial projections of the volume. In CTI, a 3-D hyperspectral volume is reconstructed from 2-D spectral projections of a spatial scene. These spectral projections are created by spectrally dispersing the scene intensity as a function of wavelength as is done with a prism spectrometer.

A schematic of the CTI is shown in Figure 7. The two-glass DVP is centered on and rotates about the optical axis, similar to that used by Mooney [33,34,43].

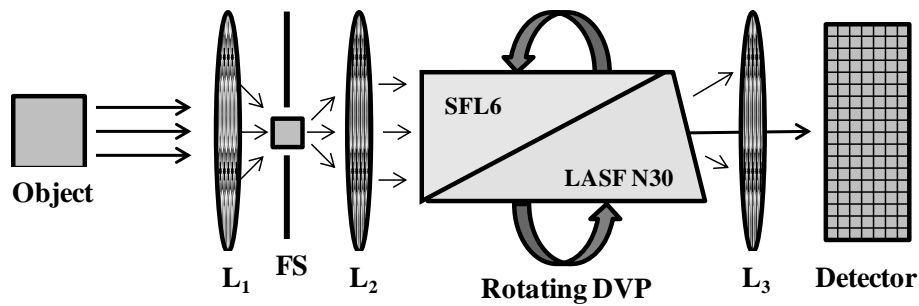


Figure 7. Schematic design of the CTI instrument. L_1 and L_2 are essentially an afocal telescope to collimate incoming light. The rotating DVP disperses light as a function of wavelength, and L_3 acts as a focusing lens to produce an image on the detector array.

The entry telescope formed by lens 1 and lens 2 (L_1 and L_2) is used to collimate the source rays input to the DVP, establishing a well defined incident angle with an aperture located at the image plane of L_1 . This defines the field of view and the field stop of the system. The dispersed light exiting the prism passes through a focusing lens (L_3) and is imaged onto a detector array in the focal plane of L_3 . As a result, a point is displaced some distance on the focal plane with respect to its location (x_0, y_0) had the prism not been present. This distance is a function of the rotation angle of the prism, θ , the angular dispersion of the prism as a function of wavelength, $\phi(\lambda)$, and the distance from the exit plane of the prism to the detector array (ostensibly f_3), given by the following:

$$\Delta x(\lambda, \theta) = r(\lambda) \cdot \cos(\theta) \quad (9a)$$

$$\Delta y(\lambda, \theta) = r(\lambda) \cdot \sin(\theta) \quad (9b)$$

$$r(\lambda) = f_3 \tan(\varphi(\lambda)) \quad (9c)$$

As the prism rotates, the image of the point source will proceed in a circle centered at the point (x_o, y_o) with a radius equal to $r(\lambda)$ given by Equation (9c). Because the detector array must collect energy not only from the field of view defined in the object space, but also the energy dispersed linearly by $(\Delta x, \Delta y)$, the field stop cannot be the detector array itself, but must be limited such that the field of view and its spectrally dispersed images are collected for all θ . As a constraint on the design of the instrument, the displacement of a point cannot be so great that for any point in the image space of the defined field of view, the desired spectrum of collection falls off of the detector array at any θ .

The CTI uses a direct vision prism so that at one wavelength there is no spatial displacement of the energy, similar to the focus or tomographic plane in tomography. The direct vision prism is used to disperse the spectral range of the CTI in both a positive and negative direction from the optic axis to make more efficient use of the detector array. Different discrete spectral projections of the scene are created by rotating the prism about the optical axis while sampling the detector array. An entire set of N projections is created as the prism rotation angle, θ , goes from 0° - 360° . Figure 8 illustrates this concept with a spatial source emitting at three distinct wavelengths, and three projections taken at 0° , 90° , and 180° shown in Figure 8d-f.

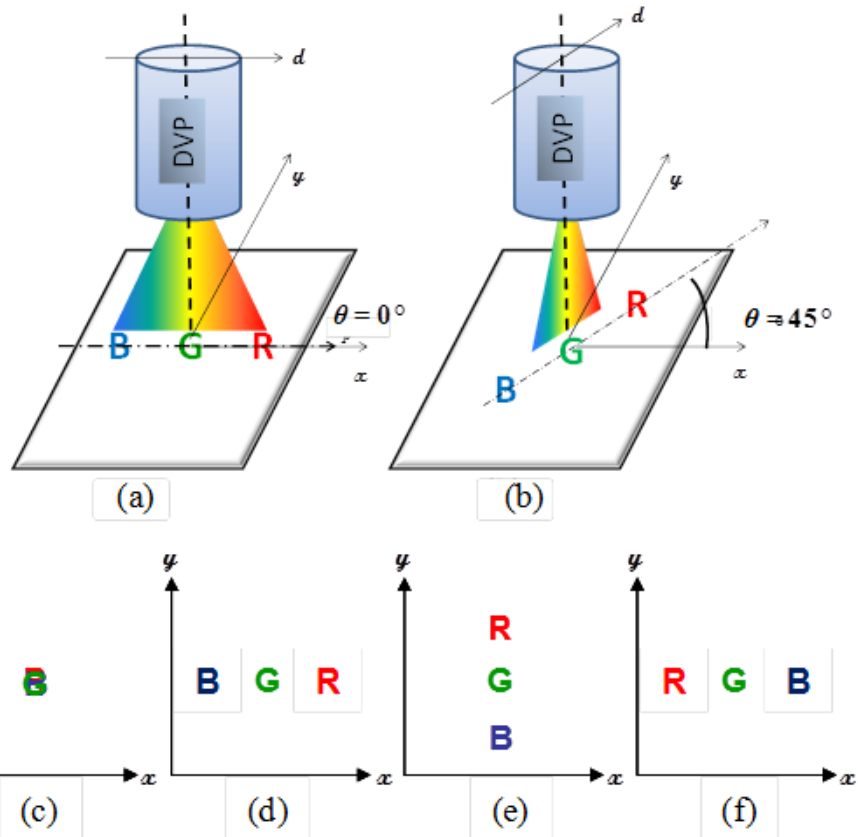


Figure 8. The DVP disperses the spectral components of an image as a function of wavelength, λ , and projection angle, θ as in (a) and (b). An image of a source with undispersed red (“R”), green (“G”), and blue (“B”) components is shown as it would be observed on the detector array in (c). Pictures (d), (e), and (f) show the dispersed image at $\theta = 0^\circ$, 90° , and 180° . Note that the “G” component is at the undeviated wavelength and is not displaced at any θ .

Unlike tomosynthesis where the projection angle is constant as the source and detector rotates, the prism dispersion is varying across the projection as a function of wavelength which complicates reconstruction. For example, the spectral dispersion of the prism used in the AFIT CTI ranges non-linearly from about -3° at 400 nm to 1° at 750 nm. This is compared to the constant $10^\circ - 30^\circ$ projection angle considered a minimum for the medical application [26, 28] (earlier studies showed that adequate results could be achieved with a 4.5° projection angle [74]). This reduces the achievable spectral resolution of the system and worsens the presence of spatial artifacts [27, 75].

Data Reconstruction

Most of the previous techniques in the field of chromotomography have used versions of the analytic reconstructive tomography methods described previously, though did not specifically make the connection to the medical physics application (Okamoto did propose an iterative ART-like method [32]). The AFRL work concentrated primarily on the analytic process of direct inversion of the forward transform [33, 34, 43], as did early work at AFIT [51, 52]. As documented, the incompleteness in the projection space makes these algorithms particularly difficult and ineffective. Also, the inverse transform is sparsely populated and thus no unique solution exists for the inverse, yielding a singularity. Most of this work consisted of estimating solutions based upon filling in the missing volume prior to inversion of the transform, or improving data in post processing [45-47]. These methods were found to be inefficient and are not implemented in medical tomography where the Fourier Space is completely populated [64, 67, 73], thus will not be used here.

The filtered backprojection algorithm has been proposed for both tomosynthesis [76, 77] and chromotomosynthesis [50], as well as number of iterative methods for tomosynthesis [75, 78, 79] and chromotomosynthesis [32, 54]. The algorithms which require filtering are very sensitive to the data being reconstructed, and often require an initial estimate to perform well. Similarly, the iterative algorithms converge faster with an estimate of the data space as an initial condition. Therefore, to generalize the algorithm for this research, a modified backprojection method without a filter will be used such that the 2-D backprojection essentially results in the shift-and-add (SAA) routine describe by Grant [30] and still used in medical tomosynthesis [75, 79]. The

results from this algorithm are straight forward, general, and also serve as initial conditions for other more advanced algorithms which can improve reconstruction in particular cases. Another advantage of the SAA algorithm is that reconstruction can be targeted to specific spatial and spectral areas in the data cube without needing to perform a full reconstruction of the entire space.

For any image in a spectral band of interest, the CTI will shift the image by some known amount and direction in a projection. By employing the appropriate reverse in the shift in each projection, the desired images will be stationary. In this way, any particular spectral bin can be reconstructed from the projections by shifting each projection by a determined distance and then adding the projections.

The SAA process is illustrated in Figure 9a-c where the data from Figures 7d-f have been shifted so that the spectral bin corresponding to the blue “B” image can be reconstructed. Here, the projection and shift are done perfectly with no consideration given for error. In Figure 9d, the result of adding the shifted projections is shown. Only the spatial component of the image corresponding to λ_B (the “B”) has been shifted to its correct position spatially on the focal plane while the other data is displaced as a function of the rotation angle. The result as $N \rightarrow \infty$ is that objects with energy at λ_B continue to be coincidentally added while all others are smoothed. The other wavelengths are reduced in intensity as they are “smeared” around the detector as shown in Figure 9e leaving artifacts in the spectral bin. This is analogous to projection radiography where in-plane objects remain in focus while out of plane objects are blurred as the source and detector move. Section IV provides a more detailed description of the SAA algorithm and addresses artifacts and the effects of error on data reconstruction.

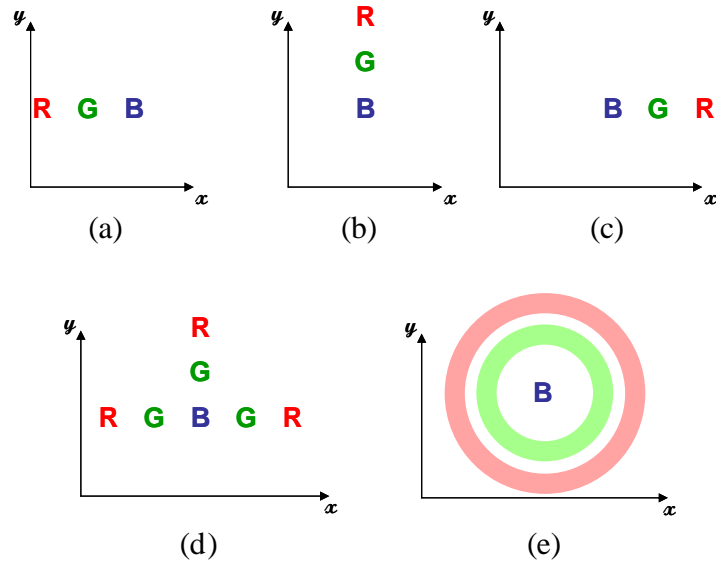


Figure 9. In (a), (b), and (c), each of the projection is shifted to reverse the spatial displacement imparted by the DVP corresponding to the wavelength at which the letter “B” is emitting. In (d) the shifted projections are added. The image of the letter “B” is spatially co-located while the other images are displaced. Panel (e) is the result as the number of projections goes to infinite.

In addition to the reconstruction of the 3-D hyperspectral cube, a 2-D wideband image of the object can be reconstructed from the 2-D spectrally projected data, equivalent to a spatial representation of the object integrated over the response of the detector. This requires a secondary integration of the 2-D projection data into a 1-D line projection at angle θ and parallel to the prism rotation angle. Because the line integration is in the direction of prism dispersion, the 1-D projection of a spectrally dispersed target is mathematically equivalent to that of the undispersed target as illustrated in Figure 10.

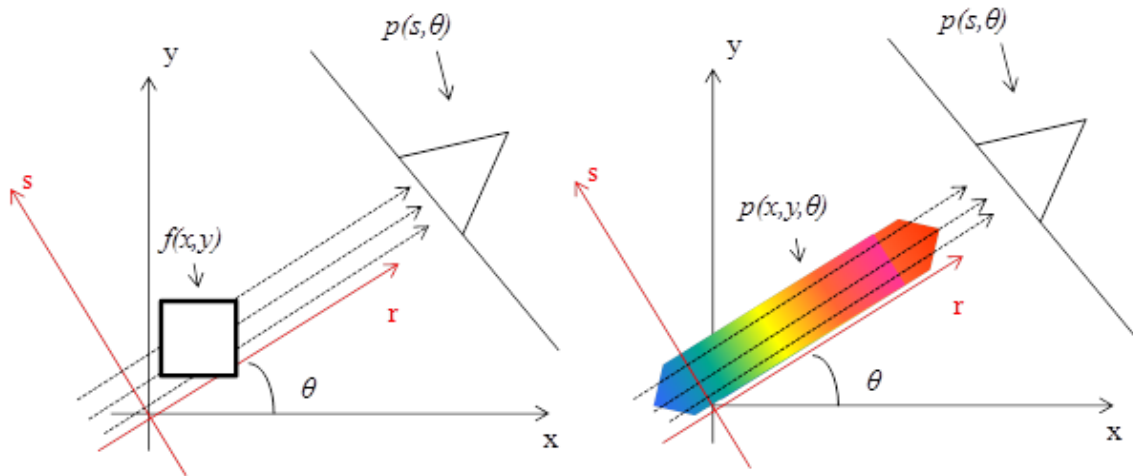


Figure 10. Because the radon projection through the undispersed image $f(x,y)$ is equivalent to that of the dispersed image, the 2-D undispersed image can be recovered from the set of $p(x,y,\theta)$ by performing a filtered backprojection.

The 2-D undispersed image can be reconstructed from the spectral projections using the more precise analytic methods as the rotation angle θ is perpendicular to the spectral projection plane. The undispersed image enables the CTI to function as an imaging camera as if no prism were in the optics chain and also provides a constraint to optimize the 3-D hyperspectral reconstruction as it is the summation of all spectral bins. The 2-D spatial representation of the scene also defines a constraining condition on the SAA algorithm, which allows performance to approach that of the iterative algorithms in certain cases without the additional calculations.

Improvement of the reconstruction can be made through more computationally intense algorithms. For a more complete description of tomosynthetic reconstruction, Dobbins and Godfrey's review of tomosynthesis methods [79] is recommended. Data reconstruction in medical tomosynthesis normally begins with a form of the SAA algorithm which may feature a filter, followed by any number of applications of the

Matrix Inversion Tomosynthesis (MITS) methods [80-83]. These inversion algorithms may still have limited use in CTI due to the small spectral projection angle.

Target Phenomenology and Exploitation

The phenomenology of short lived targets such as bomb detonations, improvised explosive devices, artillery fire and other events has been studied for some time. Recent research has been done to determine how time-resolved spectral intensity, band integrated radiometric intensity and spatially resolved imagery features can be used exclusively and together to characterize these events. The results indicate that successful classification in terms of type, size and yield of explosive events is possible based upon extracted features such as area, maximum radius, temperature, intensity profiles and molecular content from the measurements from these instruments. In Table 1, a summary of controlled ground truth tests is given with the instruments deployed and basic collection parameters. The work of Dills, Gross, and Steward [7, 16, 18, 84, 85] is recommended if a more complete listing and discussion of these tests and collection conditions are needed. One can see that in order to achieve results, data from several instruments were required at each test, with the FTIR requiring a complicated set-up and being optimized for either speed, field of view and/or spectral resolution depending on the test. Field of view for all instruments is limited so that signal to noise is maximized for these low throughput instruments. For the battlespace mission areas, the goal is to field a single instrument operating in a standard, compromised mode and collect over a large field of view to ensure detection.

Table 1. A summary of the ground truth tests performed in recent years with targets and instrumentation.

Field Test Name	Description	Events	Variables	Instruments
Radiant Brass III A, August 1999	Aircraft-delivered CMMS	33	12 (2 HEs, 3 weights, 4 approach vectors)	Bomem MR-154 FTS ($\Delta v = 7.71 \text{ cm}^{-1}$, $\Delta t = 0.049 \text{ s}$, range = 1.6-20 μm) 4-channel radiometer (InSb, 200 Hz, various filters)
Radiant Brass III B 26-29 Oct 1999	Statically-detonated CMMS	23	4 (3 HEs, 3 weights, 2 detonation methods)	Bomem MR-154 FTS ($\Delta v = 7.71 \text{ cm}^{-1}$, $\Delta t = 0.049 \text{ s}$, range = 1.6-20 μm) 4-channel radiometer (InSb, 200 Hz, various filters)
Brilliant Flash I 8-17 Jul 2002	ENEs (IEDs from readily available materials)	51	9 (3 HEs, 3 weights)	Bomem MR-154 FTS ($\Delta v = 1.83 \text{ cm}^{-1}$, $\Delta t = 0.123 \text{ s}$, range = 1.6-20 μm) Bomem MR-354 FTS (Δv , Δt unknown) 4-channel radiometer (InSb, 200 Hz, various filters) Indigo AlphaNIR FPA (320x256 InGaAs, 30 Hz, 0.9-1.7 μm) Canon XL-1 3-chip video (720x480 Si, 60 Hz interlaced)
Brilliant Flash II 2-13 Jun 2003	ENEs	44	9 (3 HEs, 3 weights)	Bomem MR-154 FTS ($\Delta v = 1.83 \text{ cm}^{-1}$, $\Delta t = 0.123 \text{ s}$, range = 1.6-20 μm) Bomem MR-354 FTS ($\Delta v = 1.83 \text{ cm}^{-1}$, $\Delta t = 0.029 \text{ s}$, range = 2-5 μm) 4-channel radiometer (InSb, 200 Hz, various filters) Indigo AlphaNIR FPA (320x256 InGaAs, 30 Hz, 0.9-1.7 μm)
Bronze Scorpio	Munitions-based IEDs	62	11 (3 HEs, 2 weights, 2 detonation methods)	Bomem MR-154 FTS ($\Delta v = 1.83 \text{ cm}^{-1}$, $\Delta t = 0.123 \text{ s}$, range = 1.6-20 μm) Bomem MR-254 FTS ($\Delta v = 1.83 \text{ cm}^{-1}$, $\Delta t = 0.029 \text{ s}$, range = .9-5.5 μm) Bomem MR-354 FTS ($\Delta v = 1.83 \text{ cm}^{-1}$, $\Delta t = 0.029 \text{ s}$, range = 2-5 μm) 4-channel radiometer (InSb, 200 Hz, various filters) Indigo AlphaNIR FPA (320x256 InGaAs, 30 Hz, 0.9-1.7 μm) Phantom high-speed 3-color camera (800x600 Si windowable, 4.8-150 kHz)
Iron Rose II	157 mm Howitzer	201	3 (full charge, Charge 1, Charge 2)	Phantom high-speed camera (1024x1024 monochrome v5.1, 4.8-150 kHz) Phantom high-speed 3-color camera (800x600 Si windowable, 4.8-150 kHz) Ocean Optics UV-NIR grating spectrometer ($\Delta\lambda = 0.75 \text{ nm}$, 10 Hz, range = 200 – 1100 nm) ABB-Bomem MR-254 (InGaAs: 1-1.7 μm and InSb: 1.3-5.6 μm) at 100 Hz ($\Delta v = 32 \text{ cm}^{-1}$), 82 Hz ($\Delta v = 16 \text{ cm}^{-1}$) and 35 Hz ($\Delta v = 4 \text{ cm}^{-1}$)

Initial research by Dills [16] on available data showed that the mid-infrared spectra from cased munitions can be reduced to a set of features that includes fireball temperature, area, and residuals to Planckian fits in selected spectral bands as a function of time. The residuals in the $1950 - 2250 \text{ cm}^{-1}$ band ($\Delta\lambda \approx 0.7 \mu\text{m}$) corresponding to hot CO_2 emissions provide the best discrimination between explosive type, size, and method of detonation (static or aircraft delivered). Discrimination based only on the peak residual provides accurate classification between static and dynamic detonation. The residual immediately after detonation was used to discriminate between large and small weights for static detonations. The ability to identify the non-Planckian behavior in the data offers a strong classification potential for conventional (TNT) and enhanced novel explosive (ENE) materials. From the imagery, the single best feature for classification between

uncased TNT and ENE materials is the time to peak of the fireball size, t_{mp} , in the near infrared.

Gross continued the empirical work of fireballs and extended it to a model of phenomenology from which a parameterized set of data was identified which may be used for classification [7, 17]. The derived parameter $\mathcal{R} = \text{H:C}$ (the ratio of Hydrogen to Carbon content) was used to distinguish TNT and ENE fireballs. A spectral emission at 6539 and 6592 cm^{-1} distinguishes what was termed as “boosted” ENE1 and ENE2 explosives from the “non-boosted” ENE0 explosive and TNT. The estimated temperature decay rate kT and mean fireball size r correlate with HE weight W in a power-law form: $kT \propto W^b$ with $-0.52 \leq b \leq -0.25$ and $r \propto W^b$ with $-0.33 \leq b \leq -0.21$. Uncased TNT and ENE charges between 10–1000 kg produce fireballs with a diameter between 450–2600 cm. Initial temperatures of TNT fireballs are between 1750–1950 K with a weight-dependent initial decay rate between $0.3\text{--}3 \text{ s}^{-1}$. In a separate analysis working from the model developed by Gross, Gordon [14] demonstrated that a four-times reduction in spectral resolving power (to 7.71 cm^{-1}) of an FTIR had a minimal impact in the precision of temperature and by-product concentrations derived from the model. This allows for improved temporal resolution and leads to improved understanding of the kinetic aspect of fireball phenomenology [14, 17]. This is a critical result for CTI, which is expected to provide high temporal resolution at the expense of spectral resolution.

Gordon’s work [86] focused on a different type of explosive event to improve the classification of aluminized conventional munitions based on a single explosive types such as RDX. In these experiments, high speed 4 kHz visible imagery with a field-of-view of about 70 m at 91 cm/pixel was collected for 13 field detonations of aluminized

novel munitions to study shock wave dynamics. The ABB-Bomem MR-254 FTS was also fielded and operated at 82 Hz using the InSb (1800–10,000 cm^{-1}) and InGaAs (5600–10,000 cm^{-1}) as in the other tests. The FTIR was configured with spectral resolution of 16 cm^{-1} , or $\Delta\lambda = 1.6 - 49$ nm for the InSb detector and $\Delta\lambda = 1.6 - 5$ nm for the InGaAs. Some interferograms were collected at 8 cm^{-1} resolution at a rate of 56 Hz. Both the 238 μs visible imagery and the 12 ms FTS spectra were used to examine shock wave dynamics and the time dependence of the fireball temperature, respectively. A drag model fit to data shows initial shock wave speeds of Mach 4.7–8.2 and maximum fireball radii ranging from 4.3–5.8 m with most of the radii reached by 50 ms upon detonation. Initial shock speeds are four times lower than theoretical maximum detonation speed of RDX and likely contributes to the low efficiencies. The temperatures decay from initial values of 1290–1850 K to less than 1000 K within 1 s after detonation.

Further studies of artillery fire by Steward [18] show similar results when analyzing the spatial and spectral phenomenology of artillery gun fire for the purpose of characterization. The temporal evolution of these events is much faster than the explosions studied by Dills, Gross and Gordon with event lifetimes of < 0.5 seconds. As with the explosions, both spatial evolution of the blast wave [9] and spectral signature analysis [15] from the muzzle flashes were shown to both be significant in discriminating gun type.

Infrared spectra of about 150 firings from a 152 mm Howitzer were acquired during the Iron Rose II tests (see Table 1). Munitions included unsuppressed and flash suppressed propellants. Secondary combustion occurred with unsuppressed propellants resulting in flash emissions lasting ≈ 100 ms and dominated by H_2O and CO_2 spectral

structure. Non-combusting plume emissions were one-tenth as intense and approached background levels within 20–40 ms. A peak temperature for the combusting plumes was found to be ≈ 1400 K, with emissive areas of greater than 32 m^2 , and a low soot emissivity of 0.04. The non-combusting plumes exhibited lower temperatures of 1000 K, areas of 5 m^2 , soot emissivity of greater than 0.38 and CO as the primary product. Temperature rate of change was used to characterize timescales and energy release for plume emissions. Heat of combustion was estimated to be 5 MJ/kg.

For Iron Rose II, imagery from the optical sensor provided the blast wave analysis. The blast waves from a 152 mm howitzer are nearly spherical and exhibit a near constant rate of propellant energy release. The blast wave and muzzle plume expansions have initial velocities of Mach 3-4 and are coincident until the shock-front detaches from the plume at about 0.5 - 0.9 ms. Beyond 5 ms the blast wave decays to near acoustic velocity and the plume has nearly stopped expanding. The efficiency of converting energy from the muzzle to the blast wave is 18-24% and does not change significantly with propellant configuration, although a trend proportional to mass was observed. Steward developed a method for estimating the plume temperature based on the blast wave imagery producing temperatures of ≈ 980 -1,210 K, increasing with reduced propellant weight and directly correlated with the probability of observing muzzle flash. The use of energy partitioning for temperature calculations still remains to be verified. The point blast model with extension to the far-field acoustic limit successfully reduces the trajectory data to a single parameter, the blast energy, with sufficient fidelity to partially distinguish between propellant masses of 4-9 kg.

From the above work, it is clear that a vast amount of information can be gleaned from the features in fireball and other explosions as well as with muzzle flashes. Generally, the analysis exploits spatial imagery data taken at a minimum of 1 kHz. Spectral features used for classification are found within a range of 1.667 - 5.000 μm , with much of the analysis in the MWIR. Data rates for the FTIR were generally <100 Hz, with spectral resolution sacrificed for speed. Most spectral features could be identified with 2 – 10 nm resolution across the MWIR. Broadband spectra are required to be measured such that temperatures of 500 – 2000 K can be calculated with differences of 100 K discernible. A suite of several different instruments per test was deployed to acquire this wide range of data, with some optimized on a per test basis. A single CTI instrument which can provide this level of data would for exploitation would be extremely advantageous from both the cost and risk perspectives.

III. Spatial and Spectral Performance of a Chromotomosynthetic Hyperspectral Imaging System

Preface

The spatial and spectral resolutions achievable by a prototype rotating prism chromotomosynthetic imaging (CTI) system (also referred to in the literature as chromotomography) operating in the visible spectrum are described. The instrument creates hyperspectral imagery by collecting a set of 2-D images with each spectrally projected at a different rotation angle of the prism. Mathematical reconstruction techniques that have been well tested in the field of medical physics are used to reconstruct the data to produce the 3-D hyperspectral image. The instrument operates with a 100 mm focusing lens in the spectral range of 400 – 900 nm with a field of view of 71.6 mrad and angular resolution of 0.8 – 1.6 μ rad. The spectral resolution is 0.6 nm at the shortest wavelengths, degrading to over 10 nm at the longest wavelengths. Measurements using a point-like target show that performance is limited by chromatic aberration. The system model is slightly inaccurate due to poor estimation of detector spatial resolution. This is corrected based on results, improving model performance. As with traditional dispersion technology, calibration of the transformed wavelength axis is required, although with this technology calibration improves both spectral and spatial resolution. While this prototype does not operate at high speeds, components exist which allow for CTI systems to generate hyperspectral imagery at rates greater than 100 Hz.

Introduction

Due to technological constraints, hyperspectral imagery (HSI) has traditionally been used to monitor static or, at most, events with slowly changing (> 1 minute) spatial and spectral features. However, there is considerable potential for exploiting features captured by HSI to characterize fast transient events, such as bomb detonations, muzzle flashes, and other battlefield combustion events [2, 3, 13-15]. Advances in technology have yielded several instrumental approaches for doing fast HSI, including two key technologies: imaging Fourier Transform Spectroscopy (imaging FTS) and CTI spectroscopy. Though significant advances have been made in FTS spectroradiometers [22, 23] CTI is investigated here due to anticipated advantages over FTS and other approaches, including: (1) simple design with less sensitivity to vibration, (2) easy integration with standard imaging sensors and technology, (3) high throughput similar to dispersive spectrometry constraints, (4) the flexibility to capture panchromatic imagery and perform high-speed non-imaging spectroscopy with the same dataset collected to produce the 3-D spatial / spectral image cubes, and (5) speed of data collection is limited only by the detector readout and not piston movement. In chromotomosynthesis, a dispersive instrument collects convolved spatial and spectral information that can be reconstructed using transforms similar to those employed in medical tomography. One method features the use of a computer generated hologram (CGH) disperser to simultaneously produce an array of diffraction orders onto a CCD detector array [35-37, 40]. A second form of chromotomosynthesis utilizes a rotating direct vision prism to collect spectral projections at different prism rotation angles [33, 34]. Due to the relatively low sensitivity, limited spectral range, and limited spectral resolution of the

CGH, we have chosen to pursue a rotating prism CTI design. The prism CTI offers potentially higher SNR as a single projection is taken for a given integration time and uses the entire spatial extent of the detector array to collect one projection, offering increased spatial resolution and spectral resolution. For applications such as classification of detonation events, higher spectral resolution is required as source spectra must be detangled from atmospheric transmission features to extract the key discriminators such as spectral fingerprints from hot combustion products and measure amounts of incomplete fuel consumption [6, 7].

The rotating direct vision prism (DVP) design was most notably developed by Mooney *et al* in connection with the Air Force Research Laboratory (AFRL) [33, 34]. A general description of the instrument with some component detail is provided for the infrared version of the instrument [44]. Prior to this, a VNIR instrument was also developed which is apparently more complex [43]. In neither case was the performance of the instrument in terms of spectral or spatial resolution provided, rather several examples of spectral measurements against static scenes are documented. Subsequent literature focuses on the system transform and mathematical reconstruction of the collected data sets [45-49, 52, 53]. The effects of instrumental design and performance parameters on temporal, spectral, and spatial resolution are not well documented. At the time of this writing, it is not clear that CTI can meet critical mission area requirements, nor is it known what effects such as jitter, field angle, and other instrument error has on the data collection or how these propagate through the data transform.

In this paper a prototype CTI instrument is presented. A short explanation of the data collection process and backprojection transform is then provided. Data is collected for an

unresolvable 200 μm pinhole to represent a point-like source which is illuminated by 4 spectrally emitting sources (Ar, He, Ne, and Xe pen lamps) as well as a 1200° C blackbody to measure the resolution of the system in the 2-D space as one would a traditional dispersion spectrometer. Resolution is then measured in the 3-D image cube to assess the effect of the transform. The results compare well to those predicted by a model of the system and transform mathematics with noticeable discrepancies attributable to error in knowledge of the forward transform of the system. The sources of error are identified and a methodology for system calibration is presented which is similar to that used in traditional prism spectroscopy. Our prototype is not a fieldable instrument, but one to be used specifically for assessment of metrology.

Design of the Chromotomosynthetic Imager

The basic CTI functionality is similar to that of the previous AFRL instrument [33, 34] and is shown schematically in Figure 11a. The system features a DVP as the dispersion element (Figure 11b) which is centered on and rotates about the optical axis. The entry telescope is formed by lens 1 and lens 2 (L_1 and L_2) and used to collimate the source rays input to the DVP and establish a well defined incident angle. The aperture located at the image plane of L_1 defines the field of view (the field stop of the system). The dispersed light exiting the prism passes through a focusing lens (L_3) and is imaged onto the detector array which is near the focal plane of L_3 . The telescope angular field of view α is 71.6 mrad for a spatial field of view, a , of 100 mm for an object 1400 mm in front of the instrument. The focal lengths of the first two lenses are $f_1 = 76.2$ mm and $f_2 = 250$ mm, establishing a ratio of $f_1/f_2 = 0.305$. The final focusing lens has a focal length of

$f_3 = 100$ mm. Though all lenses are achromatic doublets, the effective focus of the system has a noticeable wavelength dependence which is optimized at about 650 nm.

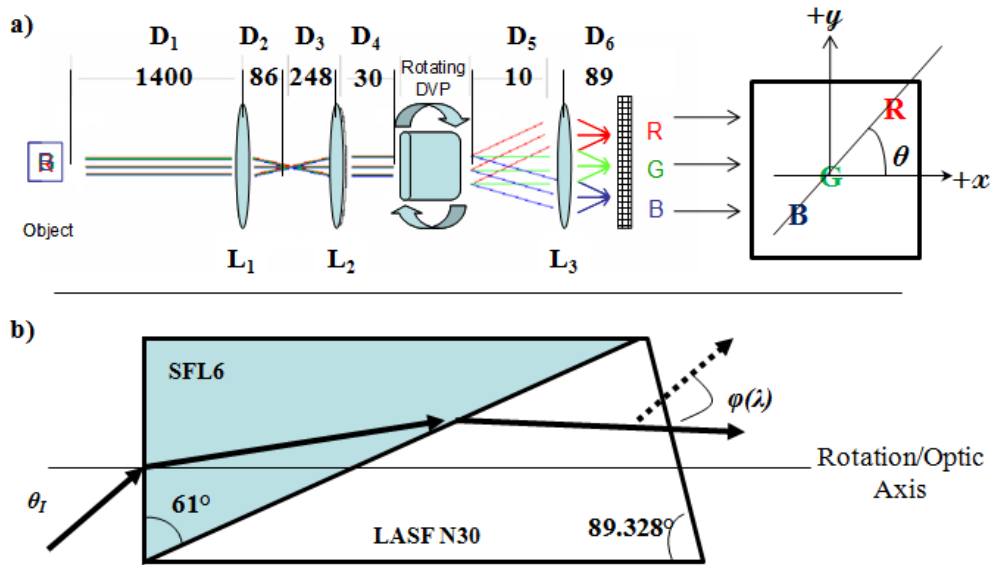


Figure 11. A schematic design of the CTI instrument is shown in (a). L_1 and L_2 are an afocal telescope to collimate incoming light. The rotating DVP disperses light as a function of wavelength, and L_3 acts as a focusing lens to produce an image on the detector array. Distances, D , are in mm. The material and geometry of the DVP are given in (b).

The detection array is a PI-MAX camera which features a proximity-focused microchannel plate (MCP) Gen-II image intensifier fiber-optically coupled to a 1024x1024 pixel CCD array. The CCD is red-blue (RB) enhanced and has a maximum quantum efficiency of about 20% at 450 nm with responsivity from 200 nm to near 900 nm. The detector is thermo-electrically cooled to -10° C and operated in shutter mode with variable exposure times. The camera is powered and controlled by an ST-133 controller connected to a computer for operation and display. The $13 \mu\text{m}$ pixel pitch provides a total detection area of about $1.33 \times 1.33 \text{ cm}^2$.

The DVP was purchased from Schott Glass and is fabricated from two glasses, with SFL6 the entrance and LaSF-N30 the exit material as illustrated in Figure 11 . The index of refraction for both SFL6 and LaSF-N30 at $\lambda = 619.29$ nm is $n = 1.8006$. The prism dispersion displaces the image some distance on the focal plane with respect to its location had the prism not been present. This distance, in terms of Δx and Δy displacement in focal plane space, is a function of the rotation angle of the prism, θ , the angular dispersion of the prism, $\varphi(\lambda)$, and the distance D_6 from the focus lens L_3 to the detector array and is given by:

$$\Delta x(\lambda, \theta) = r(\lambda) \cdot \cos(\theta) \quad (10)$$

$$\Delta y(\lambda, \theta) = r(\lambda) \cdot \sin(\theta) \quad (11)$$

where:

$$r(\lambda) = D_6 \tan(\varphi(\lambda)) \quad (12)$$

Because $r(\lambda)$ defines spectral performance of the system, the choice of f_3 and $\varphi(\lambda)$ are key system components. As noted, f_3 changes noticeably with λ despite use of achromatic doublets. Figure 12 shows a plot of $\varphi(\lambda)$ from a model of the DVP as well as the corresponding $r(\lambda)$. The undeviated wavelength, λ_c , is defined by $\varphi(\lambda_c) = 0^\circ$, which occurs at about 548 nm. The detector array must collect energy from a defined object space of compact support, $f(x,y)$. To ensure the space can be completely characterized in the case of limited spatial or spectral content, the field stop cannot be the detector array itself but must be limited such that $f(x,y)$ and its spectrally dispersed images are contained on the array for all θ . In terms of constraint on the design of the instrument, the displacement of a point cannot be so great that for any point in the image space of $f(x,y)$,

the desired spectrum of collection falls off of the detector array at any θ . With a desired coverage of 400 – 900 nm in spectral range, an $f_3 = 100$ mm lens was selected so that $r(\lambda)$ would be less than half the array length, with a margin of 200 pixels for the radius of the field of view. The prism linear dispersion is also shown in Figure 12, with pixel displacement, $r(\lambda)$, plotted on the second axis.

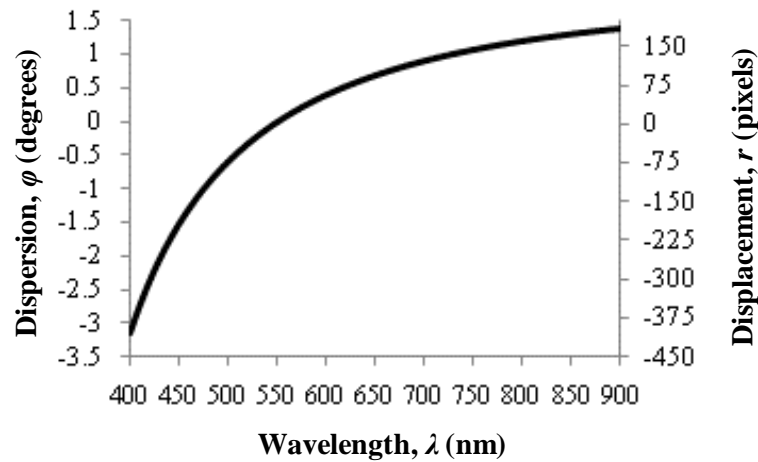


Figure 12. The spectral displacement in terms of the angular spectral dispersion of the prism and the total displacement in pixels at the detector array for a 0° field angle.

Figure 13 shows the shift in pixel displacement, $\Delta r(\lambda)$, from that in Figure 12 as a function of field angle, θ_l . Notice that for $\theta_l = 1^\circ$, the value for $r(\lambda = 400 \text{ nm})$ is nearly 10 pixels different than for the center of the field of view (FOV) where the $\theta_l = 0^\circ$. From Figure 12, this would produce a registration error of approximately 2 nm, for the chosen $f_3 = 100$ mm lens. Though a smaller shift is incurred at higher λ , the lower prism dispersion results in an 8 nm error at $\lambda = 750$ nm. Unlike traditional spectroscopy, spatial blurring in the transformed 3-D data would occur as a result of the systematic error in the

knowledge of $r(\lambda)$. The relationship between the field angle θ_I , the field of view diameter at the object plane, α , and the focal lengths f_1 and f_2 is:

$$\tan(\theta_I) = \frac{\alpha/2 \cdot f_1}{(D_1 - f_1) \cdot f_2} \quad (13)$$

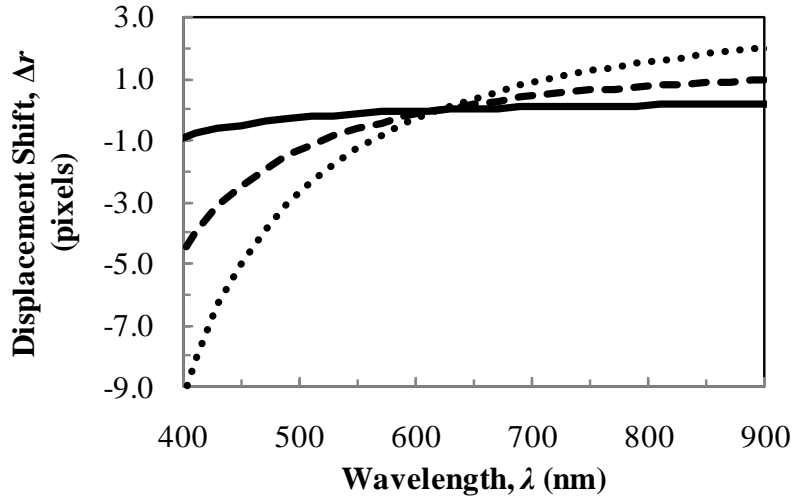


Figure 13. The shift in displacement, Δr , at the array as a function of three input field angles θ_I to the prism; $\theta_I = 0.1^\circ$ (solid line), $\theta_I = 0.5^\circ$ (dashed line), and $\theta_I = 1.0^\circ$ (dotted line).

To achieve a spectral resolution of 1 nm or less at $\lambda = 400$ nm with the design, θ_I must be less than 0.65° . For a reasonably distant object, this requires the ratio of f_1 and f_2 be ≤ 0.32 . Using readily available lenses and maintaining a somewhat optically fast system, the combination of $f_1 = 75$ mm and $f_2 = 250$ mm was chosen. The lenses are separated by 334 mm to render the combination afocal and ensure that exit rays are parallel. All lenses are Thorlabs positive visible achromats with a diameter of 50.8mm. The resulting optical chain gives a reasonable field of view of about 100 mm in the object plane while maintaining favorable imaging parameters.

Data Reconstruction

Several analytic and iterative data reconstruction methods are available, which are well documented and use the same mathematical processes to reconstruct imagery in medical computed tomography [64, 66]. In tomosynthesis (unlike tomography), the rotation axis is not perpendicular to the dispersion axis and a number of discrete 2-D exposures are collected. This incomplete set of data can be transformed to yield images similar to conventional tomography. However, the acute dispersion angle allows for a series of slices at different depths and with different thicknesses to be reconstructed from a single acquisition, saving time and minimizing patient exposure to radiation. The CTI spectral collection system has the same mathematical collection geometry and is thus most similar to circular tomosynthesis [30]. Because the projection angle in CTI is small ($<10^\circ$) the direct inversion of the system transformation is nearly singular and, as Mooney points out [33, 34], complicated mathematical methods are required to estimate a direct solution. More suitable algorithms have been developed for clinical use in circular tomosynthesis [79, 80]. An algorithm based on backprojection of the data was used in this study and described below. It is a simple algorithm and is generally the starting point for any of the other higher level algorithms which optimize performance based on specific application or known systematic errors in circular tomosynthesis.

A projection $p(x,y,\theta)$ is defined as the 2-D sample of the detector array at any prism rotation angle θ . Generally, the projections are filtered in frequency space to compensate for the blurring effects of the backprojection process, referred to as Filtered Backprojection (FBP) [64, 66]. Because the test objects here are simple and all bins are sampled with the same spatial resolution, an unfiltered backprojection technique is used.

With this method the image at any wavelength bin λ can be reconstructed from a set of projections taken over $0^\circ < \theta < 360^\circ$ with resolution dependent on the spatial resolution of the system and density of samples. For any $p(x,y,\theta)$, the spatial data in the 2-D is described in terms of the object as:

$$P(x, y, \theta) = I_0(x + \Delta x(\lambda, \theta), y + \Delta y(\lambda, \theta)) \quad (14)$$

where $I_0(x,y)$ is the image as it would appear without any prism dispersion. With the linear shifts $\Delta x(\lambda, \theta)$ and $\Delta y(\lambda, \theta)$ established from Equations (10-12), an estimate of $I_0(x,y)$ at any λ denoted by $I_p(x,y,\lambda,\theta)$ can be calculated from $p(x,y,\theta)$ by reversing the shift so that the energy is placed back at its original position in image space. Because $\Delta x(\lambda, \theta)$ and $\Delta y(\lambda, \theta)$ are rarely integers, the value assigned to a particular point in $I_p(x,y,\lambda,\theta)$ will be the value of a pixel multiplied by the fraction of the area of overlap upon shifting (x, y) by some real-valued $\Delta x(\lambda, \theta)$ and $\Delta y(\lambda, \theta)$. If $a(x - \Delta x(\lambda, \theta), y - \Delta y(\lambda, \theta), x', y')$ represents this fractional overlap then:

$$I_p(x, y, \lambda, \theta) = \sum_{x', y'} P(x - \Delta x(\lambda, \theta), y - \Delta y(\lambda, \theta)) \times a(x - \Delta x(\lambda, \theta), y - \Delta y(\lambda, \theta), x', y'). \quad (15)$$

A complete reconstructed image cube $R(x,y,\lambda)$ all projections is estimated from the weighted summation over all θ and λ as:

$$R(x, y, \lambda) = \frac{1}{N} \sum_{\theta, \lambda} I_p(x, y, \lambda, \theta) \quad (16)$$

In any particular spectral bin λ_n the spatial data at that wavelength is co-added such that the spatial information is reinforced. Spatial information from other spectral bins are also included, but for $\lambda \neq \lambda_n$ the information is not coherently added and appears blurred in $R(x,y,\lambda_n)$. For complex spectral and special data, additional image process would be

needed to discern or remove these artifacts [76, 77, 79]. From Equation (15) it is obvious that systematic error in knowledge of $\Delta x(\lambda, \theta)$ and $\Delta y(\lambda, \theta)$ results in variations between I_p and I_0 . Depending on the type of error, this results in either a loss of spatial resolution at a particular wavelength, a shift in the peak spectral location, or both in the final $R(x, y, \lambda)$. An additional loss of resolution occurs as the backprojection process essentially is resampling the data, which mathematically represents a second convolution with the detector array. Some of these differences can be rectified and the original resolution restored by using more advanced drizzle techniques to recombine the shifted datasets [87], or, as is commonly done in medical CT, filtering the data prior to backprojection. Reconstruction algorithms utilize $\Delta x(\lambda, \theta)$ and $\Delta y(\lambda, \theta)$ as input, and thus the accuracy of the data reconstruction is dependent on knowledge of system performance.

Experiment

To measure the spatial point response function (PRF) and spectral line shape function (LSF) of the CTI, a 200 μm diameter pinhole is illuminated as the object for the CTI system. The image size predicted by geometric optics is a circle of diameter 4.6 μm , about 1/3 of a pixel. The pinhole was illuminated separately by argon, mercury, neon, and xenon pen lamps and a 1200 $^\circ\text{C}$ blackbody. The spectral peak locations for lines used in this analysis are given in Table 2, taken from a combination of the lamp documentation [88] and the NIST database [89]. To acquire data at shorter wavelengths, a second collection of the blackbody was made with a 500 nm short pass filter in place. This allowed the integration time to be increased to detect energy at the shorter

wavelengths while avoiding extreme saturation and artifacts from scattered light from the longer wavelengths.

Table 2. Prominent pen lamp wavelengths.

Ar	Ne	Hg	Xe
404.44	585.25	404.65	450.1
415.86	588.19	435.83	452.1
416.42	594.48	546.08	453.25
418.19	609.62	576.96	462.4
419.81	615.34	579.07	467.1
425.94	621.73		469.8
426.63	626.65		473.4
430.01	633.44		480.7
433.41	640.16		482.97
434.51	650.65		491.95
451.07	660.1		502.83
452.23	667.8		
	671.7		
	692.25		
	702.83		
	724.52		
	748.89		

For the spectral sources a single measurement was made by the CTI without the prism in place to determine a reference point for the undeviated image location, or $r(\lambda=\lambda_c)$. Four measurements of $p(x,y,\theta)$ with the prism in place at $\theta = 0^\circ, 90^\circ, 180^\circ$ and 270° were made for the spectral and blackbody sources. The $p(x,y,\theta)$ data of the spectral sources were transformed into the reconstructed 3-D space, $R(x,y,\lambda)$. The bin size for the reconstructions was 0.1 nm over 400 – 500 nm for each source and 0.5 nm from 500 – 800 nm due to lower spectral resolution of the instrument at the longer wavelengths.

The spectral intensity of each of the Ar, Hg, Ne, and Xe sources is extracted from each of the four $p(x,y,\theta)$ by integrating the center 4 rows or columns (as appropriate) around the center line of the spectra. This resulted in an intensity plot vs. pixel location for the 2-D instrument collection space which was converted to intensity vs. wavelength using the predicted performance and measured $r(\lambda)$ using the undeviated images. The average of the $p(x,y,\theta)$ were taken to provide a single spectrum for each element in the 2-D collection space. The spectra for the $R(x,y,\lambda)$ were extracted by integrating the 2x2 pixel area at the center of the image location at every reconstructed plane. The widths of peaks in the direction perpendicular to the dispersive axis of the DVP were used to obtain spatial resolution. In the 3-D reconstructed data, spatial resolution was measured in both the x - and y -axis in the plane of peak spectral intensity.

Peak center locations and PRF/LSF functional fits were estimated by fitting the collected data to a Gaussian line shape. With a few exceptions, the Gaussian shape was the best functional fit to the data with an r -squared fit coefficient of >0.99 for all peaks used in the assessment. The FWHM of the Gaussian shapes were then calculated to find the spatial/spectral resolution. Contributions from instrument bias, background, or continuum energy in the spectra were removed prior to fitting. An example of the fit to the Ne spectrum is shown in Figure 14 plotted with peaks extracted from the data.

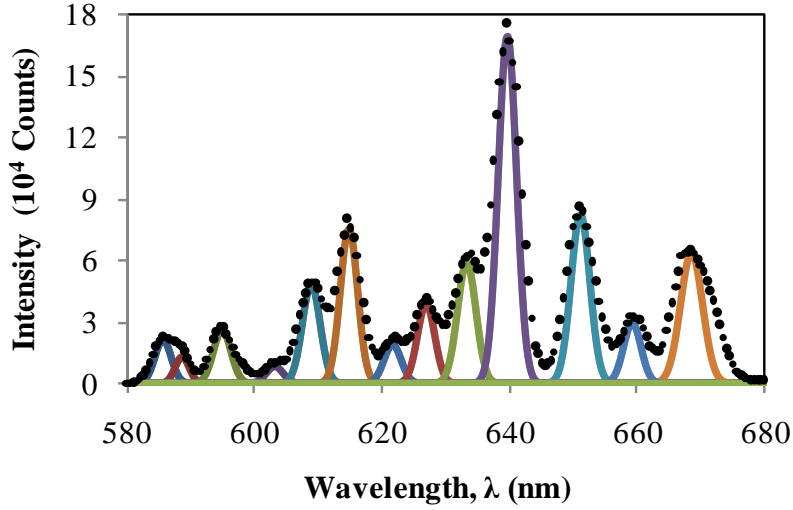


Figure 14. An example of the peaks fit to the extracted Ne spectrum in the 3-D reconstructed imagery. The dotted line is the data; the solid line represents the fitted peaks.

Results

Spatial Resolution

The wavelength dependence of the observed spatial resolution of the collection system in the $p(x,y,\theta)$ for both the pen lamps and the blackbody are illustrated in Figure 15. The spatial resolution varies from 2 – 4 pixels or 26 – 52 μm . This corresponds to an object resolution of 0.8 – 1.6 μrad or 1.2 – 2.4 mm for an object at 1400 mm from the instrument. The best spatial resolution of 2.05 pixels is observed at $\lambda = 650$ nm, the wavelength at which system focus is optimized. The average of the PSF in the x- and y-directions of the $R(x,y,\lambda)$ reconstructed data are also plotted in Figure 15. The resolution is constant across the spectral range at about 3.4 pixels. This indicates that there is residual error in the estimation of $\varphi(\lambda)$ which dominates the performance in the $R(x,y,\lambda)$.

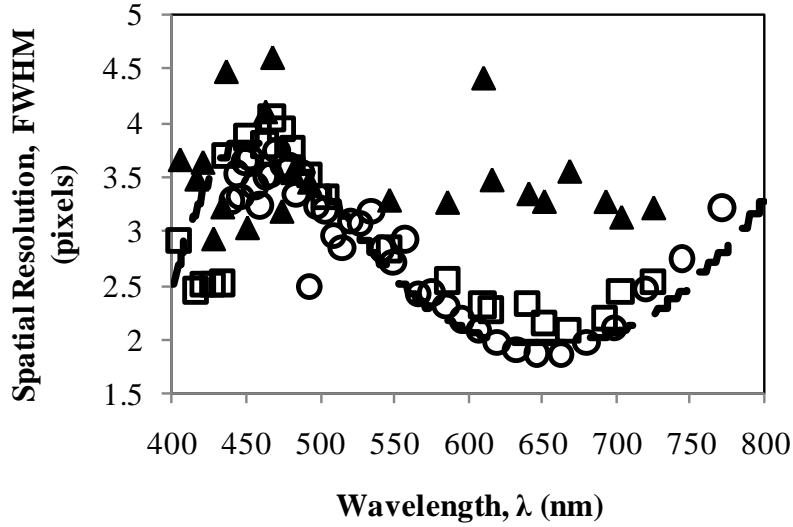


Figure 15. The spatial resolution results for the blackbody source (“o”), spectral sources (“□”) and the measured spatial resolution in the 3-D reconstructed data (“▲”). The dashed curve is the predicted resolution from the model of the system after adjusting for the detector coupling.

The overall shape of the curve of the PRF as a function of λ indicates that the performance of the system is limited by chromatic aberration, as the effective focal length, f_s , of the system depends on λ . A model of the image system is developed to support this conclusion. Four components were assumed main contributors to the overall PRF of the system: diffraction, detector sampling, effect of the intensifier, and chromatic aberration. The (assumed circular) prism is the limiting aperture of the system and the diffraction term is described by an Airy disk with radius:

$$d(\lambda) = 1.22 \cdot \frac{f_s \cdot \lambda}{A_p} \quad (17)$$

where A_p is the aperture size of the prism (21 mm) and f_s is assumed equivalent to f_3 assuming that the front telescope is afocal¹. The radius of the diffraction circle is $d \approx 4.7$ μm at $\lambda = 800$ nm, just over $2/3$ of a pixel in total diameter for the spectral range of interest.

Sampling due to physical spatial detector size was modeled as a constant, 1 pixel wide $rect(x)$ function. The PI-MAX camera has an intensified array and the pixel pitch will not alone define the spatial sampling resolution of the system. Incident photons excite the photocathode, which causes a release of electrons that are attracted to the voltage biased microchannel plate that acts as the photomultiplier. The exited high energy electrons strike a fluorescent screen to create the photons that are incident on the CCD. The fiberoptic coupling between the photocathode and CCD array introduces a FWHM blur with diameter of about 45 μm (or nearly 3.5 pixels) according to instrument documentation [90]. The coupling contribution to the PSF is modeled as a Gaussian function to produce the required FWHM.

It was necessary to also consider chromatic aberration as the λ dependent effects were easily observed in initial data sets. The distances between lenses were fixed to provide best focus at $\lambda = 650$ nm. In particular, $D_6 = 89$ mm which can be most easily adjusted if improved resolution is desired at different λ . At this wavelength f_1 and f_2 form an afocal telescope so that $f_s = f_3$. The effective focal length each lens was then modeled to determine image quality over the full range of λ . The blur size of the image of a point source was then modeled using geometric optics over the spectral range and

¹ This is not explicitly true given the achromaticity of the system.

was found to be approximated as a uniform disk, such that it is represented by a $circ(r)$ function. The size of r was estimated as half the distance between marginal rays at the fixed distance D_6 from back face of L_3 .

Complete spatial resolution in the $p(x,y,\theta)$ data was approximated by convolving the four effects described. The spatial resolution in any 3-D $R(x,y,\lambda)$ bin (assuming perfect reconstruction) was found by incorporating the additional pixel sampling factor as a result of the backprojection algorithm. The estimation of the FWHM of the PSF in the $p(x,y,\theta)$ and $R(x,y,\lambda)$ space are shown in Figure 16. There is small difference between the two, with the minimum spatial resolution dependent on the intensifier fiber coupling and added modulation due to chromatic aberration.

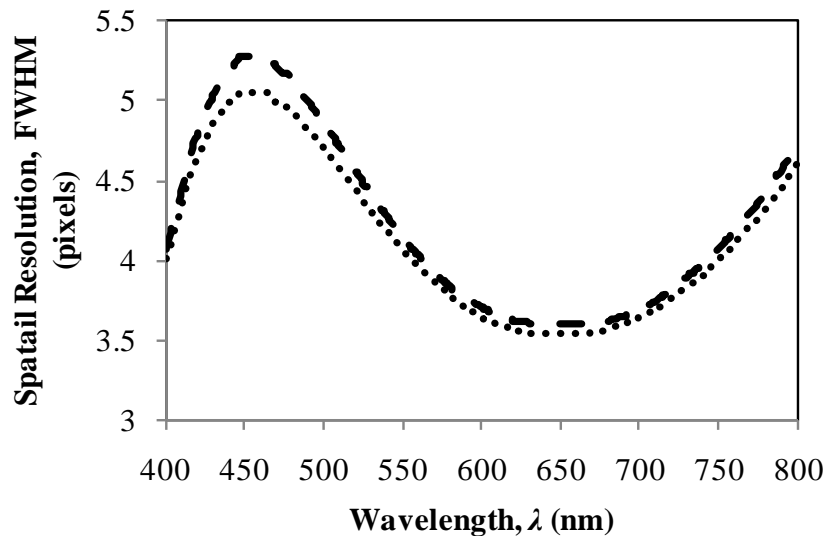


Figure 16. The expected PRF from the model of the system. The spatial resolution of the collection system is shown as the dotted line. The spatial resolution in the reconstructed 3-D hyperspectral data is shown as the dashed line.

Comparing the model results with the data in Figure 15, the measured shape and amplitude of the system resolution agrees well with the model, but the minimum of the

curve at 650 nm is much lower at a FWHM of 2 pixels compared to the predicted 3.5 pixels. This indicates that the estimated intensifier coupling term is too high. Adjusting this term to have a FWHM of 1.9 pixels (24 μm) produces a predicted spatial resolution that is much closer to the data as indicated in Figure 15 by the dashed line representing the adjusted model curve.

Spectral Resolution

The measurements of the LSF for the spectral sources indicate that the system is capable of providing a spectral resolution $\Delta\lambda$ of about 0.75 nm at 400 nm, rising fairly linearly to nearly 9 nm at 750 nm. The results are shown in Figure 17 with the line indicating the theoretical best spectral resolution derived from the model-based spatial resolution. This dependence can be shown to have the same relationship that exists in prism spectroscopy where:

$$\Delta\lambda_m = \frac{w}{f_3(\lambda) \cdot \frac{d\phi(\lambda)}{d(\lambda)}} \quad (18)$$

with $\Delta\lambda_m$ the minimum spectral resolution and w the spatial resolution. At $\lambda < 550\text{nm}$, the measured width of the LSF is near the theoretical limit and considerably higher at the longer wavelengths.

The deviation from the model at wavelengths greater than 550 nm is where the spatial resolution was found to be worse in the reconstructed data compared to the systematic and modeled spatial resolution. Thus, as in traditional 2-D spectroscopy, the

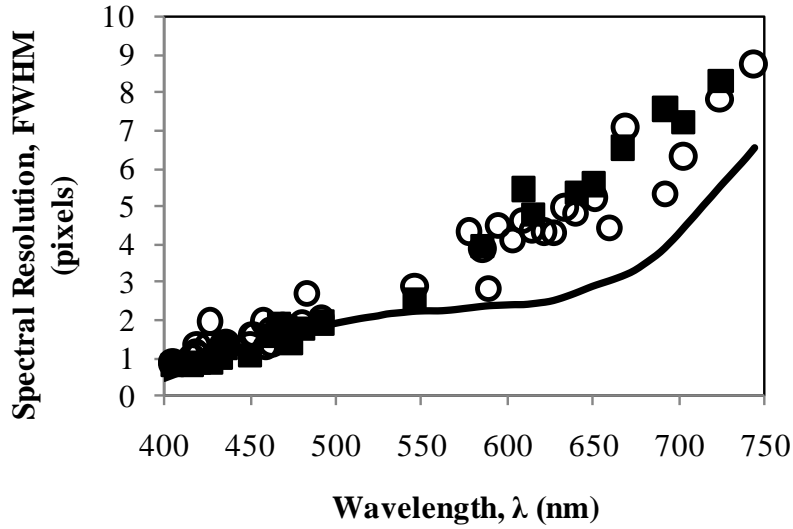


Figure 17. The measured spectral resolution from the 3-D $r(x,y,\lambda)$ data (“o”), the predicted spectral resolution from the system (solid line), and the expected resolution given estimated error in reconstruction (“■”).

spectral resolution in the $R(x_i, y_i, \lambda)$ space is dependent on the spatial resolution *in this same space*, not the projection space. By using the measured spatial resolution in the 3-D data set as the basis for the predicted spectral resolution instead of the modeled spatial resolution, values much closer to those measured are found as shown in Figure 17.

Spectral Registration and Calibration

The system spatial performance is well known and modeled but some error exists in the predicted spectral dispersion of the system as the measured performance in the reconstructed hyperspectral data is not as good as predicted. The error caused by differences between the model and reality can be quantified by examining the location $r(\lambda)$ of the spectral point source images on the array for each θ and compared to the model. Figure 18 plots the expected $r(\lambda)$ due to dispersion from the model, with measured peak center locations of the spectral source images at $\theta = 0^\circ, 90^\circ, 180^\circ$, and

270° overlaid. The displacement error increases linearly with wavelength with some random error. By incorporating a single linear correction, Figure 19 shows that the residuals are now scattered mostly about $\Delta r = 0$, with a slight bias of about 0.2 pixels.

It is clear from Figure 18 and Figure 19 that the error is more apparent for results at $\lambda > 550$ nm, where poorer agreement between the measurements and the model were observed. The sensitivity to decreased $d\lambda/dr$ causes higher inaccuracy per λ at these wavelengths, as a larger change in λ is produced for an equivalent change in r . Most outliers contributing to the randomness in Δr is likely caused by noise in the data, effects of under sampling the PSF, the presence of the continuum, overlapping peaks, or difference in emission spectra between the pen lamps used and/or documented emission lines. The remaining bias is evident in the correlation between the 0° and 90° and the 180° and 270° projections. Applying distinct linear corrections to each of the projections would further improve the performance, with a complete calibration that describes spectral displacement in terms of $r(\lambda, \theta)$ necessary. The single linear correction improves spatial results by 25% and spectral by 10%.

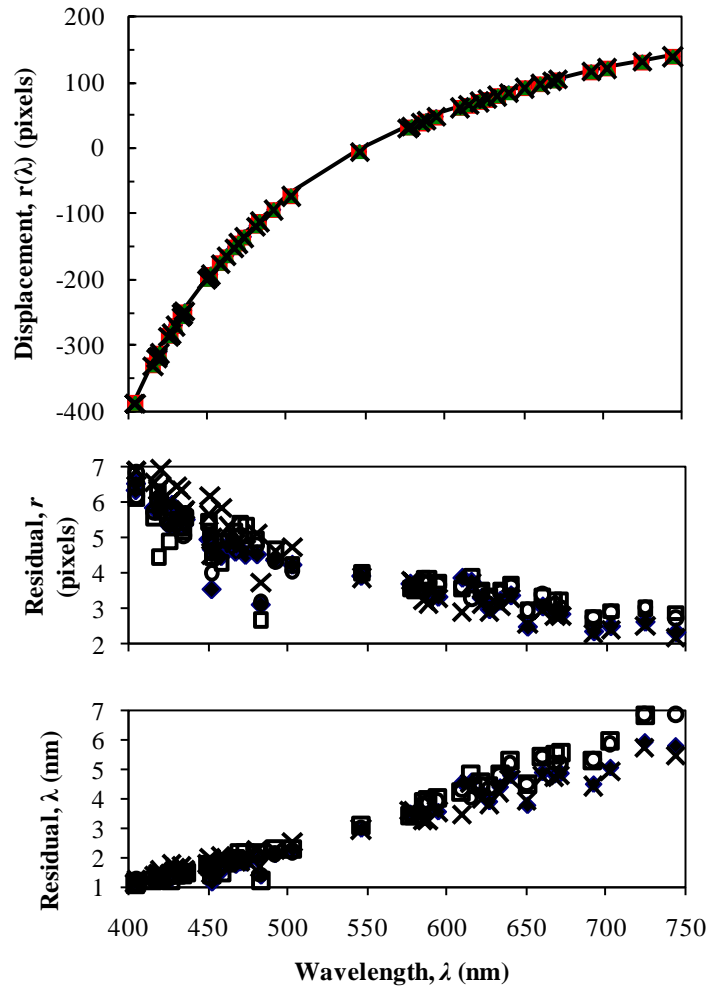


Figure 18. The predicted spectral displacement $r(\lambda)$ compared to that measured in the $p(x,y,\theta)$ sets: $\theta = 0^\circ$ (“♦”), $\theta = 90^\circ$ (“□”), $\theta = 180^\circ$ (“o”), and $\theta = 270^\circ$ (“x”). Residuals in terms of pixels and wavelength, λ , are shown below the plot with a noticeable correlation between the $p(x,y,0^\circ)$ and $p(x,y,90^\circ)$ data and the $p(x,y,180^\circ)$ and $p(x,y,270^\circ)$ data.

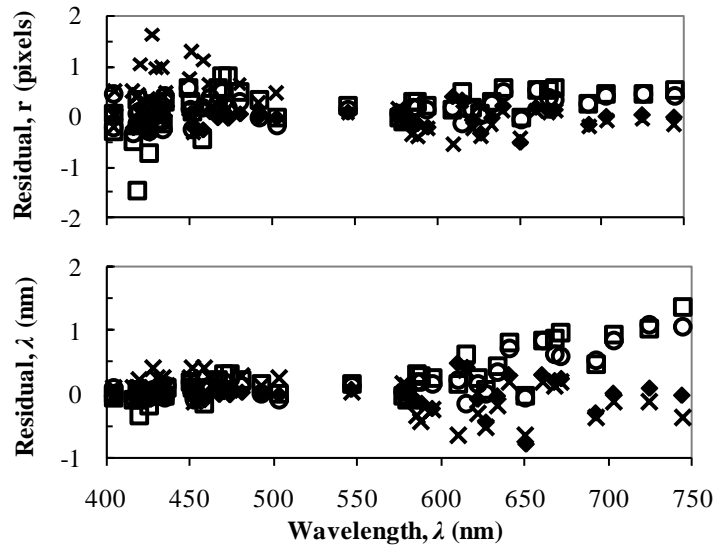


Figure 19. The residuals between the measured and modeled dispersion after a linear correction is applied based on measurements of the spectral dispersion in the data used in this experiment. The symbols are the same as those in Figure 18.

Conclusions

A prototype CTI instrument has been designed, built and characterized which broadly covers visible wavelengths from 400 – 900 nm with spectral resolution of 0.6 – 10 nm depending on wavelength. The compact, $f = 100$ mm, instrument provides hyperspectral images with per pixel field of view of 0.6 mrad and a full field of view of 71.6 mrad. A simple backprojection algorithm for image reconstruction does not significantly degrade the native spatial and spectral resolution when the system linear dispersion and other instrument properties are adequately characterized. Indeed, system performance is primarily limited by chromatic aberrations for the transmissive optics. The distance between the back lens and the detector array can be adjusted to minimize blur at a desired wavelength.

Unlike the usual dispersive spectrometers, CTI cannot dramatically improve spectral resolution by simply increasing the focal length, except near the undispersed wavelength. This is because the image of the field of view must be rotated for all wavelengths. However, resolving the visible spectrum into several hundred bins can be achieved with the $f = 100$ mm system. Calibration of the wavelength axis is required for absolute wavelength determinations and also improves the resulting spectral resolution. Calibration may be necessary for all rotation angles as r is a function of θ as well as λ in the presence of systematic error.

Further development of the CTI instrument is required for objects with more diverse spatial frequencies. In particular, the sensitivity of reconstructed images to systematic errors for scenes with increased spatial and spectral mixing must be developed. Extension to a fast framing, field deployable system is in progress [41]. Many factors affect the achievable spatial and spectral resolution attainable from an operational CTI system. More specifically, the contrast values that define the ability to detect and resolve spatial features at a given wavelength require further study.

IV. Instrumental Error In Chromotomosynthetic Hyperspectral Imaging

Preface

Chromotomosynthetic imaging (CTI, also referred to a “chromotomography”) is a method of convolving spatial and spectral information which can be reconstructed into a hyperspectral image cube using the same transforms employed in medical tomosynthesis. A direct vision prism instrument operating in the visible (400 – 725 nm) with 0.6 mrad IFOV and 0.6 – 10 nm spectral resolution has been constructed and characterized. Reconstruction of hyperspectral data cubes require an estimation of the instrument component properties which define the forward transform. We analyze the systematic instrumental error in collected projection data resulting from prism spectral dispersion, prism alignment, detector array position and prism rotation angle. The shifting and broadening of both the spectral lineshape function and the spatial point spread function in the reconstructed hyperspectral imagery is compared with experimental results for monochromatic point sources. The shorter wavelength ($\lambda < 500\text{nm}$) region where the prism has the highest spectral dispersion suffers mostly from degradation of spectral resolution in the presence of systematic error, while longer wavelengths ($\lambda > 600\text{nm}$) suffer mostly from a shift of the spectral peaks. The quality of the reconstructed hyperspectral imagery is most sensitive to the misalignment of the prism rotation mount. With less than 1° total angular error in the two axes of freedom, spectral resolution was degraded by as much as a factor of two in the blue spectral region. For larger errors than this, spectral peaks begin to split into bimodal distributions, and spatial point response

functions are reconstructed in rings whose radius is proportional to wavelength and spatial resolution.

Introduction

There is considerable potential for exploiting both spectral and spatial information to characterize fast transient events, such as bomb detonations, muzzle flashes, and other battlefield combustion targets of interest. However, the lifetime of these events is on the order of 5 seconds or less, with spatial and spectral properties changing at rates of >10 Hz [1-9] making it difficult for traditional hyperspectral imaging (HSI) to exploit the information. A CTI system, using a rotating prism design, has the potential to produce hyperspectral images at rates approaching 100 Hz. A single design is able to produce panchromatic imagery, high speed non-imaging spectra and hyperspectral image cubes with low sensitivity to platform vibration. The drawbacks of the CTI approach include limited spectral resolution and reconstruction induced imagery artifacts for complex scenes.

In 1995, Mooney et al developed a mid infrared CT imager using a two component, direct vision prism [33]. Subsequent CTI systems operated in the VNIR/IR and explored stationary scenes, or slow moving motor vehicles [34, 43, 44]. More recently, a non-rotating double Amici prism with coded aperture and bandpass filter system has developed flames imagery at 30 Hz [91]. A space based chromotomographic experiment (CTEx) is currently in development [58, 59] intended for operation on the International Space Station (ISS) as a risk reduction enterprise. A visible CTI system with 8" aperture capable of framing hyperspectral data cubes at 100 Hz would be launched to image forest

fires and analyze the spectra of industrial flares. A field deployable, ground based prototype has demonstrated the ability to monitor the potassium and sodium line emission from transient combustion events [41, 56]. An evaluation of various orbital mechanics [58], assessment of onboard metrology and calibration [59], an analysis of system weight and mechanical stability [60] have been accomplished.

The present work is focused on the impact of various instrumental errors on spatial and spectral resolution. A backprojection algorithm with optional filtering for point source image reconstruction does not significantly degrade the native spatial and spectral resolution in a reconstructed plane of interest when the system linear dispersion and other instrument properties are adequately characterized [26, 57, 78]. However, two factors must be considered which can diminish the observed performance in a reconstructed spectral bin. Systematic error due to poor knowledge of the instrument's forward projection caused by inexact characterization of system performance will reduce the spatial and spectral resolution in a bin of reconstruction. Also, even with a perfect reconstruction in the spectral bin of interest, blurred artifacts from out-of-bin spectral emissions will appear in the reconstructed bin diminishing contrast and imposing unwanted structure. These effects are illustrated in the present work by considering the mathematics of the projection and subsequent backprojection. The model for systematic errors is validated with experimental observations.

Iterative methods such as the Simultaneous Algebraic Reconstruction Technique (SART) [65] and Maximum Likelihood Estimation Methods [69] have been evaluated for the medical application as well as by AFIT for chromotomography [52-54]. Analytic 3-D Fourier reconstruction and direct inverse methods are also used in medical imaging.

These methods are very computationally expensive and in CTI the incomplete sampling of the Fourier Space results in the “missing cone” of information producing artifacts identical to those observed by backprojection [45-47, 77]. For digitally sampled systems, the missing cone represents a region of highly attenuated signal [40]. More recent work in filtered backprojection techniques has been used in medical tomosynthesis with improved results [27, 75, 76], as well as the newer matrix inversion tomosynthesis (MITS) [80]. The backprojection algorithm is used in this study due to its simplicity, generality and the fact that it is the basis for more exact methods of iterative or analytic reconstruction [66, 71, 75]. The more advanced techniques can substantially enhance performance given the characteristics of the data that are to be exploited [76-79].

The CTI System

The basic design of our visible (400 – 725 nm) CTI system is shown schematically in Figure 20 and has been described in detail previously [57]. The system features a two-element direct vision prism (DVP) with an undispersed wavelength of $\lambda_c \approx 548$ nm, which is centered on and rotates about the optical axis. The prism is mounted in a Newport PM360A-0065 high-precision rotation stage that can spin at a uniform rate of 200°/s. Lenses L_1 , L_2 and L_3 are achromatic doublets with respective focal lengths $f_1 = 76.2$ mm, $f_2 = 25.0$ mm and $f_3 = 100$ mm. The detector is a Princeton Instruments PI-MAX intensified 1024 x 1024 array with a pixel pitch of 13 μm and is run using an ST-133 controller. Images are taken at discrete prism rotation angles, θ , with each image being a different projection of the spectral image. A set of projections from 0 – 360° is used to reconstruct one hyperspectral image cube.

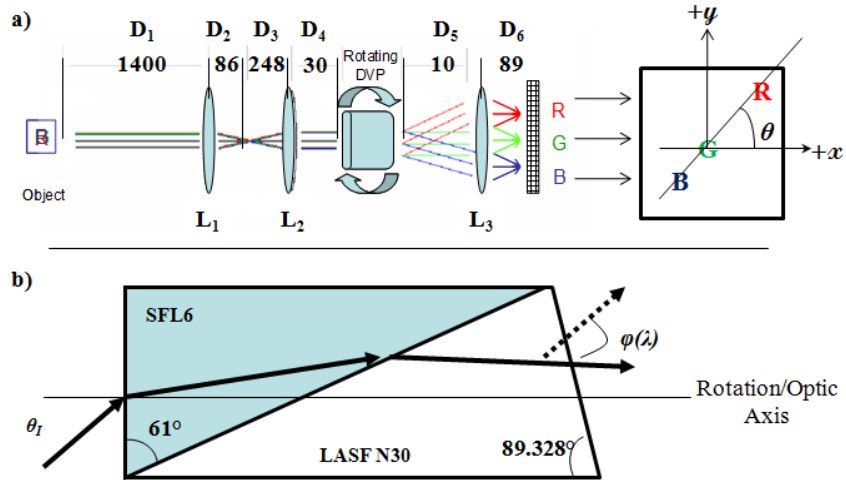


Figure 20. Schematic design of the CT instrument. L_1 and L_2 are essentially an afocal telescope to collimate incoming light. A field stop is located at the image plane between these two lenses. The rotating DVP disperses light as a function of wavelength, L_3 acts as a focusing lens to produce an image on the detector array.

Figure 20 illustrates the prism angular deviation, $\varphi(\lambda)$, and the linear displacement at the detector array, $r(\lambda)$, for the spectral region with greatest dispersion, 400 – 750 nm. For $D_6 = 89$ mm, the linear dispersion ranges from 0.2-2.5 nm/pixel. The individual pixel field of view is 0.6 mrad, providing a full field of view of 71.6 mrad. The choice of $f_3 = 100$ mm yields a maximum linear displacement in the blue of about 400 pixels such that an undispersed image of 200 pixels in extent is not projected off of the detector array. The dispersion does depend on incident angle and the weak dependence to field angle, θ_i , for off axis objects is illustrated in Fig. 2 for the case $\theta_i = 0.2^\circ$. The spectral resolution is 0.6 nm at 400 nm, increasing to 6.5 nm at 750 nm as shown in Figure 22. Despite the use of achromatic doublets, the effective focal length of the system has noticeable wavelength dependence. For this experiment, the system is optimized to have best focus at 650 nm (see Figure 22).

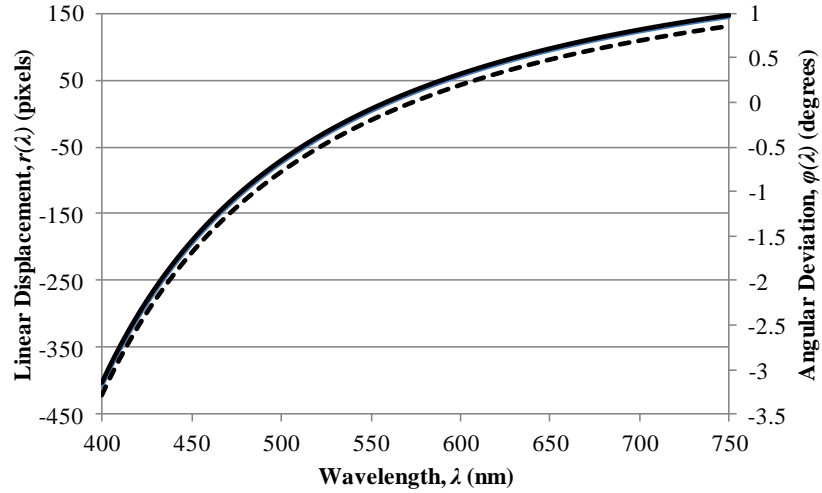


Figure 21. The dispersion $\varphi(\lambda)$ of the DVP and resulting displacement at the detector array, $r(\lambda)$. The solid line is for a 0° field angle (angle of incidence) and the dashed line for a 0.2° field angle.

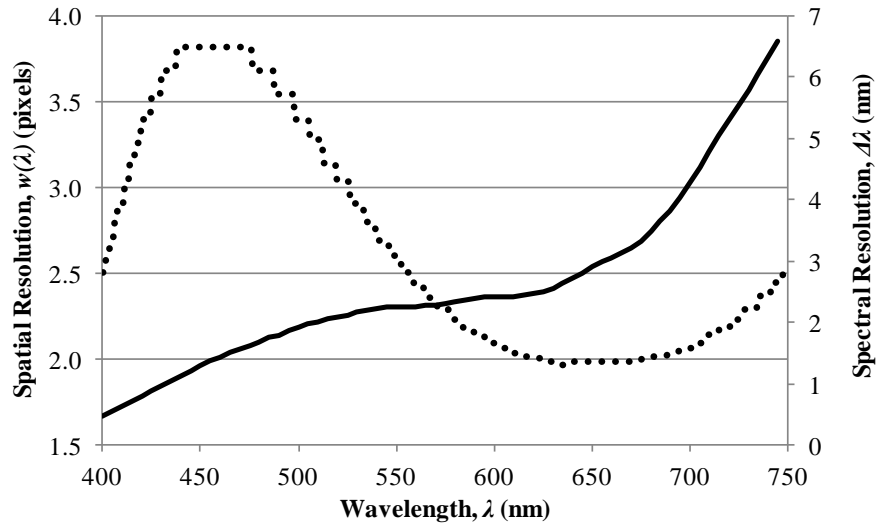


Figure 22. The system modeled spatial resolution (dotted line) and spectral resolution (solid line) with perfect reconstruction [57]. Spectral resolution, $\Delta\lambda$, is derived from the spatial resolution, $w(\lambda)$ using Equation (20).

Image Reconstruction And Error Kernel

Let $s(x,y,\lambda)$ represent the undispersed (without the prism) image at the detector plane. For a broadband source, the observed image would include contributions from all

wavelengths, $\int s(x,y,\lambda)d\lambda$. To develop the effects of systematic errors on reconstruction of the hyperspectral data cube for the CTI system, we begin by considering the imaging of a monochromatic, point source located on the optic axis which defines the origin of the (x,y) coordinate system on the detector array. The picture in row (a) of Figure 23 illustrates the expected image for our CTI system for a point source at $\lambda = 540$ nm located on axis at $(0,0)$. For this source the system point spread function can be approximated as a Gaussian with FWHM of 2.7 pixels or $35 \mu\text{m}$ [57]. The spatial resolution is degraded from the diffraction limited value of 0.2 pixels ($2.8 \mu\text{m}$) obtained at $\lambda = 540$ nm, due to chromatic aberration in the focal length of lens L_3 [57].

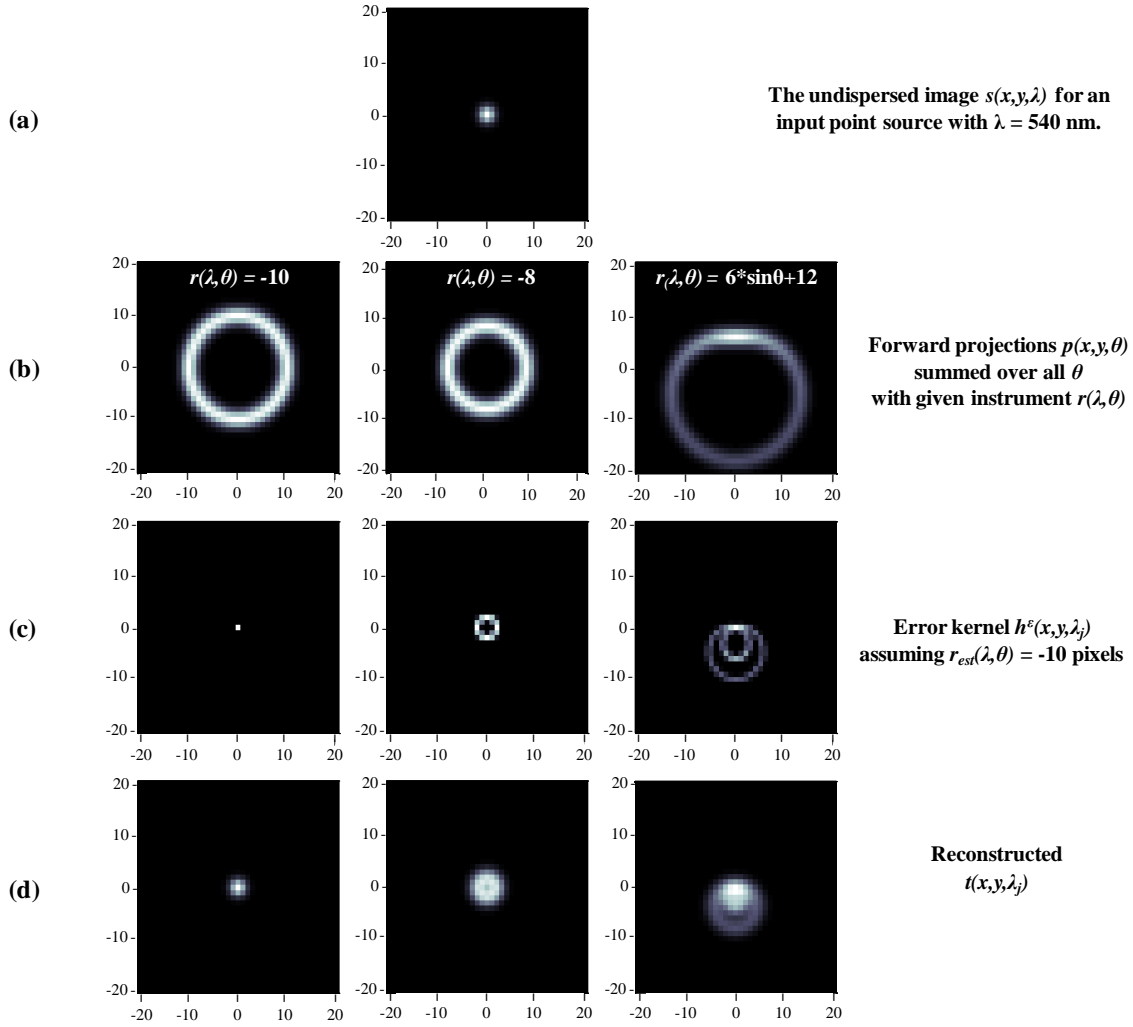


Figure 23. Row (a) provides the undispersed image, $s(x,y,\lambda)$ for an on-axis, monochromatic ($\lambda= 540$ nm) point source. Row (b) illustrates the projections summed over all prism rotation angles, $\sum p(x,y,\theta)$, for the same point source with: (column 1) $r = -10.3$ pixels, $r_\epsilon=0$; (column 2) $r = -8$ pixels, $r_\epsilon=-2.3$ pixels; and (column 3) $r = 6 \sin\theta + 12$ pixels, $r_\epsilon = 6 \sin\theta - 1.7$ pixels. Row (c) is the spatial representation of the error function $h^\epsilon(x,y,\lambda)$ with the same displacements. In row (d) the convolution of the error kernel with the undispersed image, yields the reconstructed image, $t(x,y,\lambda)$.

With the DVP in the system, the image of the monochromatic point source is displaced from the optical axis (0,0) by some $(\Delta x, \Delta y)$ in Cartesian coordinates or (r, θ) in polar coordinates, as shown in Figure 24. The image exhibits the point spread function described above which defines the spatial resolution Δw . The size of the imaged spot in

the direction perpendicular to the dispersion axis represents the spectral resolution, $\Delta\lambda$. The rotation angle, θ , is defined relative to the imager x-axis. Actually achieved displacements, $r(\lambda, \theta)$, and corresponding Cartesian shifts Δx and Δy , may depend on prism angle due systematic error such as prism or prism mount misalignment.

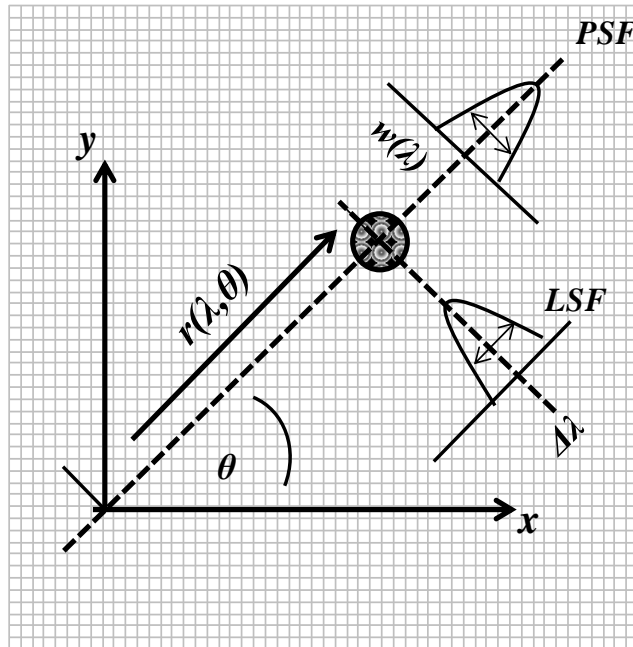


Figure 24. The shifting of an on-axis, monochromatic point source from its undispersed location at the origin of the x-y plane. DVP dispersion displaces the source by $r(\lambda)$ at angle θ . In the direction perpendicular to dispersion, spatial resolution, $w(\lambda)$ is defined by the point spread function (PSF). In the dispersive direction, spectral resolution, $\Delta\lambda$, is defined by the line spread function (LSF).

The spectrally dispersed image at prism angle θ is called a *projection*, $p(x,y,\theta)$, and is defined by applying the appropriate, spectrally dependent, displacement to $s(x,y,\lambda)$ as:

$$p(x,y,\theta) = \int s(x - \Delta x(\lambda,\theta), y - \Delta y(\lambda,\theta), \lambda) d\lambda. \quad (19)$$

The prism displaces all wavelengths in the space domain to create a projection. This is equivalent to a linear phase shift in the frequency domain (Fourier transform shift theorem):

$$\begin{aligned}\mathfrak{F}\{p(x, y, \theta)\} &= \mathfrak{F}\left\{s(x - \Delta x, y - \Delta y, \lambda)d\lambda\right\} \\ &= \int \mathfrak{F}\{s(x, y, \lambda)\}e^{-ik_x\Delta x}e^{-ik_y\Delta y}d\lambda\end{aligned}\quad (20)$$

where \mathfrak{F} is the 2-D Fourier transform:

$$\mathfrak{F}\{s(x, y)\} = \iint s(x, y)e^{-i(k_x x + k_y y)}dxdy \equiv S(k_x, k_y) \quad (21)$$

and k_x and k_y are the spatial frequencies. The detector sampling is equivalent in the x and y directions so that $k_x = k_y = k$.

For the monochromatic source at $\lambda = 540$ nm, the modeled system displacement from Figure 21 is about -10 pixels ($\varphi(\lambda) = -0.11^\circ$). An example image for these projections summed over a full prism rotation, $\sum_{\theta} p(x, y, \theta)$, is provided in Figure 23b.

For no systematic error, the displacement is independent of rotation angle and the sum of all projections produces a ring of radius 10 pixels with thickness of the image PSF and centered at the spatial location of the source.

The second and third images in Figure 23b illustrate the expected summed projections for two cases where systematic error has caused $r(\lambda, \theta)$ to be different than expected: 1) $r(\lambda, \theta) = 8$ pixels, possibly due to incorrect prism dispersion characterization and 2) $r(\lambda, \theta) = 6 \sin\theta + 12$, possibly due to both prism and prism mount misalignment as developed below. For the second angle dependent systematic error, the projection is composed of two elements: 1) a dimmer ring of radius 12 pixels, and 2) a brighter spot nearer the optical axis with characteristic lobes aligned with the x -axis. The total

intensity is the same for all three cases, with the signal spread across more pixels for the larger displacements.

We employ a simple, modified backprojection algorithm to reconstruct the hyperspectral data cube, $t(x,y,\lambda)$, from the observed projections, $p(x,y,\theta)$. This requires an estimate of the shift elements from the system model or other possible calibration for any wavelength. In the present work, we use the shift derived from the system model of ideal dispersion given in Figure 21. This estimated displacement, $r_{est}(\lambda)$, is a function of both the expected angular deviation of the prism, $\varphi(\lambda)$, and the expected distance from the focusing lens to the detector array, D_6 (which is approximately equal to f_3):

$$r_{est}(\lambda) = D_6 \tan(\varphi(\lambda)) \quad (22)$$

The corresponding Cartesian coordinates for the displacement are:

$$\Delta x_{est}(\lambda, \theta) = r_{est}(\lambda) \cos(\theta) \quad (23)$$

$$\Delta y_{est}(\lambda, \theta) = r_{est}(\lambda) \sin(\theta) \quad (24)$$

In this ideal case the displacement, r_{est} , is independent of angle θ .

The backprojection algorithm uses these estimates of system performance to reverse the shift for a particular spectral bin and return the image to its estimated spatial location for all θ in $p(x,y,\theta)$. While the forward projection of $s(x,y,\lambda)$ is performed continuously and simultaneously over λ , the reconstruction of $t(x,y,\lambda)$ is performed discretely and for one spectral bin at a time. The reconstructed image for a particular wavelength, λ_k , is defined as the average of the m number of projections with the inverse estimated shift applied to $p(x,y,\theta)$:

$$t(x, y, \lambda_k) = \frac{1}{m} \sum_{\theta} p(x + \Delta x_{est}(\lambda_k, \theta), y + \Delta y_{est}(\lambda_k, \theta), \theta). \quad (25)$$

The Fourier transform of Equation (25) can be expressed in terms of the undispersed image, $s(x, y, \lambda)$ using the Fourier shift theorem and the definition of the projection from Equation (19):

$$\begin{aligned} \mathfrak{F}\{t(x, y, \lambda)\} &= \frac{1}{m} \sum_{\theta} \mathfrak{F}\{p(x + \Delta x_{est}(\lambda_k, \theta), y + \Delta y_{est}(\lambda_k, \theta), \theta)\} \\ &= \frac{1}{m} \sum_{\theta} \mathfrak{F}\{p(x, y, \theta)\} e^{ik_x \Delta x_{est}(\lambda_k, \theta)} e^{ik_y \Delta y_{est}(\lambda_k, \theta)} \\ &= \frac{1}{m} \sum_{\theta} \int \mathfrak{F}\{s(x, y, \lambda)\} e^{-ik_x \Delta x(\lambda, \theta)} e^{-ik_y \Delta y(\lambda, \theta)} e^{ik_x \Delta x_{est}(\lambda_k, \theta)} e^{ik_y \Delta y_{est}(\lambda_k, \theta)} d\lambda \end{aligned} \quad (26)$$

Defining $T(k_x, k_y, \lambda_k) \equiv \mathfrak{F}\{t(x, y, \lambda_k)\}$ and $S(k_x, k_y, \lambda_k) \equiv \mathfrak{F}\{s(x, y, \lambda_k)\}$, then:

$$T(k_x, k_y, \lambda_k) = \frac{1}{m} \sum_{\theta} \int S(k_x, k_y, \lambda) e^{ik_x (\Delta x_{est}(\lambda_k, \theta) - \Delta x(\lambda, \theta))} e^{ik_y (\Delta y_{est}(\lambda_k, \theta) - \Delta y(\lambda, \theta))} d\lambda \quad (27)$$

For a monochromatic extended source emitting only at $\lambda = \lambda_k$ and assuming no error in the estimated displacement terms such that the exponents are zero, the reconstruction is exact as the Equation (27) reduces to $T(k_x, k_y, \lambda_k) = S(k_x, k_y, \lambda_k)$. In practice, r_{est} and corresponding Cartesian shifts Δx_{est} and Δy_{est} are not exactly accurate due to systematic error and/or inadequate system characterization and may depend on prism angle due to systematic error such as prism or prism mount misalignment. The errors in the radial and Cartesian displacements are defined simply as:

$$\begin{aligned} r_{\varepsilon}(\lambda, \theta) &= r(\lambda, \theta) - r_{est}(\lambda) \\ \varepsilon_x(\lambda, \theta) &= \Delta x(\lambda, \theta) - \Delta x_{est}(\lambda, \theta) \\ \varepsilon_y(\lambda, \theta) &= \Delta y(\lambda, \theta) - \Delta y_{est}(\lambda, \theta) \end{aligned} \quad (28)$$

with functional forms for these error terms for various types of systematic errors developed further below as the primary topic of this paper.

Realistic (or at least interesting) sources are not monochromatic and thus do not emit at some single discrete wavelength λ_k . Therefore, the exponential functions in Equation (27) will not go to zero for all λ and there will be an inclusion of artifact energy for any $\lambda \neq \lambda_k$. Similar to the error residuals, we will define the artifact residual terms as:

$$\begin{aligned} r_\alpha(\lambda, \lambda_k, \theta) &= r(\lambda, \theta) - r_{est}(\lambda_k, \theta) \\ \alpha_x(\lambda, \lambda_k, \theta) &= \Delta x(\lambda, \theta) - \Delta x_{est}(\lambda_k, \theta) \\ \alpha_y(\lambda, \lambda_k, \theta) &= \Delta y(\lambda, \theta) - \Delta y_{est}(\lambda_k, \theta). \end{aligned} \quad (29)$$

To further demonstrate the difference between systematic error and artifacts, the integral of Equation (27) can be split into two parts corresponding to: 1) the contribution by only the wavelength of the bin being reconstructed, λ_k , and 2) the residual energy from other spectral components in the source, $\lambda \neq \lambda_k$:

$$T(k_x, k_y, \lambda_k) = \frac{1}{m} \sum_{\theta} [S(k_x, k_y, \lambda_k) H^\varepsilon(k_x, k_y, \lambda_k, \theta) + \int S(k_x, k_y, \lambda_k) H^\varepsilon(k_x, k_y, \lambda, \theta) d\lambda] \quad (30)$$

where the *error kernel* is defined as:

$$H^\varepsilon(k_x = k, k_y = k, \lambda, \theta) = e^{-ik\varepsilon_x(\lambda, \theta)} e^{-ik\varepsilon_y(\lambda, \theta)} \quad (31)$$

or in polar notation:

$$H^\varepsilon(k_x = k, k_y = k, \lambda, \theta) = e^{-ikr_\varepsilon(\lambda, \theta)\cos(\theta)} e^{-ikr_\varepsilon(\lambda, \theta)\sin(\theta)} \quad (32)$$

and the *artifact kernel* is defined as:

$$H^\alpha(k_x = k, k_y = k, \lambda, \theta) = e^{-ik\alpha_x(\lambda, \theta)} e^{-ik\alpha_y(\lambda, \theta)}. \quad (33)$$

Again, with no systematic error, $H^\varepsilon = 1$, and the first term of Equation (30) leads an exact reconstruction for λ_k as all images $s(x, y, \lambda_k)$ are coincidentally added (or *co-added*)

and reinforced. All other wavelengths as described by H^α are shifted by differing amounts over all θ and thus do not coincidentally accumulate. By averaging over many projections, m , the image is reconstructed for the correct wavelength bin, λ_k and spatially blurred for all other $\lambda_{j \neq k}$.

The in-band errors are associated with the diagonal elements of the error kernel, H^ϵ , and are the focus of this study. The out of band artifacts represented by the cross terms of the artifact kernel, H^α for $j \neq k$ are not addressed and assumed to be zero for the analysis to isolate the determination of effect of systematic error on instrument performance. There are several image processing methods that can minimize the effects associated with artifacts, including principal component analyses and higher order reconstruction techniques [26, 45-47, 65, 69, 76-79]. For a source with a few point sources, the artifacts are a set of rings centered at the source locations and with radius dependent on the degree of wavelength error. One might readily remove the error by locating the wavelength bin where the circle radius is minimized. Indeed, this is an example of how some *a priori* knowledge of the source can be used to filter out or remove artifacts. However, for a source with a complex distribution of spatial and spectral features, such image correction may be problematic.

The reconstruction process is illustrated in Figure 23 in the spatial domain where a bin in the reconstructed hyperspectral data cube, $t(x,y,\lambda_k)$ can be described by the convolution of the undispersed image, $s(x,y,\lambda_k)$, and the inverse Fourier transformed error kernel, h^ϵ . The convolution theorem provides:

$$\begin{aligned} \mathfrak{T} \left\{ \iint s(\xi, \eta, \lambda_k) h^\varepsilon(x - \xi, y - \eta, \lambda_k, \theta) d\xi d\eta \right\} &= s(x, y, \lambda_k) \otimes h^\varepsilon(x, y, \lambda_k, \theta) \\ &= S(k_x, k_y, \lambda_k) H^\varepsilon(k_x, k_y, \lambda_k, \theta) \end{aligned} \quad (34)$$

where h^ε is the inverse Fourier transform of H^ε :

$$\begin{aligned} h^\varepsilon(x, y, \lambda_k, \theta) &= \mathfrak{T}^{-1} \left\{ H^\varepsilon(k_x = k, k_y = k, \lambda_k, \theta) \right\} \\ &= \mathfrak{T}^{-1} \left\{ e^{-ik\varepsilon_x(\lambda_k, \theta)} e^{-ik\varepsilon_y(\lambda_k, \theta)} \right\} = \delta(x - \varepsilon_x) \delta(y - \varepsilon_y) \end{aligned} \quad (35)$$

where for the artifact kernel we can write:

$$h^\alpha(x, y, \lambda, \theta) = \delta(x - \alpha_x) \delta(y - \alpha_y) \quad (36)$$

and:

$$S(k_x, k_y, \lambda) H(k_x, k_y, \lambda, \theta) = s(x, y, \lambda) \otimes h^\alpha(x, y, \lambda, \theta) \quad (37)$$

such that:

$$t(x, y, \lambda_k) = \frac{1}{m} \sum_{\theta} \left(s(x, y, \lambda_k) \otimes h^\varepsilon(x, y, \lambda_k, \theta) + \int s(x, y, \lambda) \otimes h^\alpha(x, y, \lambda_k, \theta) d\lambda \right). \quad (38)$$

Returning to the example of monochromatic point source in Figure 23, the error kernel, $h^\varepsilon(x, y, \lambda_k)$, summed over all projections, m , are shown in row (c) of the figure. In the first column, with an exact description of the displacement, $H^\varepsilon(k_x=k, k_y=k, \lambda_k, \theta)=1$ and there is no error in reconstruction. The corresponding $h^\varepsilon(x, y, \lambda_k)$ is a 2-D spatial delta function centered at the origin and the convolution of Equation (37) yields a spectral bin, $t(x, y, \lambda_k)$ which is identical to the undispersed image, $s(x, y, \lambda_k)$. This reconstruction is illustrated in the row (d) of Figure 23.

In the second column of row (b) in Figure 23, the estimated displacement is such that $r_{est}(\lambda_k, \theta)$ is a constant -8 pixels, and the spatial representation of the error kernel in row (c) when summed over all prism rotations forms a ring of radius $r_\varepsilon = -2$ pixels. The

convolution of this error kernel with the undispersed image, $s(x, y, \lambda)$ as specified in Equation (37), reconstructs a larger on-axis spot with a slightly lower intensity in the center such that the image becomes non-Gaussian. The best fit FWHM to the image of nearly 7 pixels results in a reduced spatial resolution of over 50%. It should be noted that the ring of radius -8 pixels would be perfectly reconstructed in the bin $\lambda \approx 542.25$ nm where $r(\lambda, \theta) = -8$ such that this error could alternatively be interpreted as a spectral shift. Finally, in the third column, the asymmetric displacement error leads to an image with decidedly non-Gaussian structure that has a larger spread (loss of resolution) and a centroid shifted downward by about 4 pixels (spatial displacement).

The effects of systematic error described in the spatial domain propagate to a loss of spectral resolution. For perfect reconstruction, the best achievable spectral resolution, $\Delta\lambda$, is related to the spatial resolution, $w(\lambda)$ by:

$$\Delta\lambda = \frac{w(\lambda)}{f_3(\lambda) \cdot \frac{d\phi}{d\lambda}} \quad (39)$$

where $f_3(\lambda)$ is the focal length of the final lens, L_3 . Due to chromatic error the quantities f_3 , w , and $\Delta\lambda$ are a function of wavelength. Calculated best values for the spatial and spectral resolution based on the current instrument design [57] are shown in Figure 22.

Several sources of systematic error will be considered in this analysis. A model will be used to simulate the forward projections with a particular systematic error included. The reconstruction of the hyperspectral data cube is without the systematic error. The effect of each type of error in the final hyperspectral data cube will be measured in terms of the spatial and spectral shift from the source locations, and degradation of spatial and

spectral resolution. The model results will then be compared with experimental results from the CTI system.

Sources of Error

Many of the instrumental errors prevalent in CTI are similar to those found in traditional prism spectroscopy. However, the outcomes are different due to the rotation of the prism and mathematical reconstruction of the imagery. The instrumental errors addressed in this study are those caused by: 1) error in estimation of the prism dispersion, 2) inaccurate distance from the focusing lens to the detection array and tilt of the detection array with respect to the optical axis, 3) prism misalignment in the mount, mount misalignment and non-zero incident angle to the prism due to field angle, and 4) and prism rotation angle. Figure 25 summarizes these error types, providing an image associated with the effect and an equation for the displacement error or error kernel. The functional form of the errors will be expressed in terms of r_ε as spatially shown in Figure 23 and mathematically derived from Equation (31) as $H^\varepsilon = e^{-ikr_\varepsilon}$ or $h^\varepsilon = \delta(r_\varepsilon(\lambda, \theta))$.

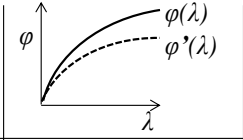
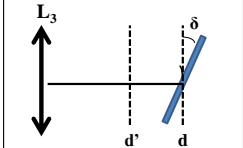
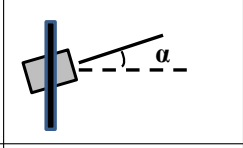
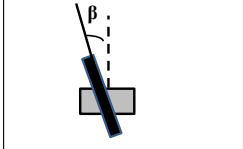
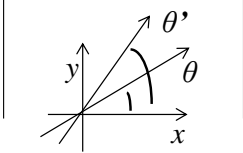
(a)	Prism Angular Dispersion		$r_\varepsilon(\lambda, \theta) = D_6 \cdot (\varphi'(\lambda) - \varphi(\lambda))$
(b)	Detector Distance and Tilt		$r_\varepsilon(\lambda, \theta) = \frac{(D_6 + \varepsilon_d) \cdot \sin(\varphi(\lambda))}{\cos(\varphi(\lambda) + \delta_x \cdot \cos(\theta) + \delta_y \cdot \sin(\theta))}$
(c)	Prism Misalignment		$r_\varepsilon(\lambda, \theta) = D_6 \cdot (\varphi'(\lambda : \theta_I = \alpha_x) - \varphi(\lambda : \theta_I = 0^\circ))$
(d)	Mount Misalignment		$r_\varepsilon(\lambda, \theta) = D_6 \cdot (\varphi'(\lambda : \theta_I = \beta x \cdot \cos(\theta) + \beta y \cdot \sin(\theta)) - \varphi(\lambda : \theta_I = 0^\circ))$
(e)	Prism Rotation Angle		$H^\varepsilon(\lambda_j, \theta') = e^{-2\pi i \cdot f_{xy} \cdot (\varepsilon_x(\lambda_j, \theta'))} e^{-2\pi i \cdot f_{xy} \cdot (\varepsilon_y(\lambda_j, \theta'))}$

Figure 25. A summary of the system errors considered for this study. The dispersion, detector distance and tilt, prism misalignment and mount misalignment are all described by the $r_\varepsilon(\lambda, \theta)$ term input to the error kernel, H^ε (Equation (31)).

Error in Prism Dispersion

The estimation of prism dispersion, $\varphi_{est}(\lambda)$, is initially based on modeled performance given design specifications. Instrument calibration can be performed to refine $\varphi_{est}(\lambda)$. However there may be situations where this is not possible (e.g. a space borne application), or the measurement itself is flawed. The error in dispersion is denoted by $\varepsilon_\varphi(\lambda) = \varphi_{est}(\lambda) - \varphi(\lambda)$ and shown in Figure 25a. Assuming that $\varepsilon_\varphi(\lambda)$ is small the error in displacement is:

$$r_\varepsilon(\lambda) = D_6 \cdot \varepsilon_\varphi(\lambda) \quad (40)$$

and can be substituted into Equation (32) to obtain the error kernel. Spatially, this results in convolving the source emitting with a ring of radius $r_\varepsilon(\lambda_k)$ in the k^{th} reconstructed bin degrading spatial resolution in that bin.

Error in prism dispersion and indeed any systematic error that is independent of prism rotation angle such that $r_\varepsilon = r_\varepsilon(\lambda) = r_\varepsilon(\lambda, \theta)$, including an axial displacement in the detector plane, reconstructs the correct image in some spectral bin. Specifically, it is the spectral bin λ_j at which $r_{est}(\lambda_k) = D_6 \cdot \tan(\varphi(\lambda_j))$. This is most readily seen mathematically in Equation (40). The reconstruction assumes the correct functional form and there exists a wavelength where the radial shift correctly matches the true system response. Thus these errors result in either a spectral shift with no loss of spatial resolution or a reconstruction of the image in the incorrect wavelength bin, the dispersion error is equivalent to an artifact, H^α .

Detector Array Distance and Tilt

The linear displacement $r(\lambda)$ at the detector is defined by the orientation of the detector array with respect to the optical axis and distance D_6 . As shown in Figure 25, the detector array is assumed to be perpendicular to the optical axis at an estimated distance D_{est} from L_3 . Any error in the approximation of D_{est} is given by ε_d , the residual between D_{est} and D_6 and will lead to a defocused image. For points away from the optical axis, D_6 is also a function of any tilt, δ , of the detector array. Tilt will produce a set of projections that trace out an ellipse at the detector array for a particular point source instead of the expected circle. Keystone distortion may also be observed in the image with detector tilt; this however is not an error as a result of the reconstruction process and therefore is not included in the analysis.

The displacement at a point on the tilted detector array in terms of ε_d and the tilt angle components δ_x and δ_y is given by:

$$r_\delta(\lambda, \theta) = \frac{(D_6 + \varepsilon_d) \cdot \sin(\varphi(\lambda))}{\cos(\varphi(\lambda) + \delta_x \cdot \cos(\theta) + \delta_y \cdot \sin(\theta))} \quad (41)$$

and the error term $r_\varepsilon(\lambda, \theta)$ in Equation (32) is the difference between $r_\delta(\lambda, \theta)$ and $r(\lambda)$.

Prism and Mount Misalignment and Field Angle

In standard CTI design the front face of the prism is perpendicular to the optic axis so that parallel rays are incident at 0° for a target in the center of the field of view. If the prism and/or the rotation stage are out of alignment, the rays will instead be incident at some angle θ_I that varies as a function of θ . This situation is shown in Figure 25 for incident rays parallel to the optical axis \boldsymbol{o} from the left and perpendicular the prism's dispersive axis \boldsymbol{d} . The magnitude of the misalignment is given by angle α with x- and y-components α_x and α_y .

Assume the prism is misaligned in the mount by some angle α , with x-component α_x and y-component α_y (the y-axis is parallel to \boldsymbol{d} at $\theta = 0^\circ$ in our convention). When $\theta = 0^\circ$, misalignment causes the rays to be incident at $\theta_I = \alpha_x$. At $\theta = 180^\circ$, θ_I has changed from α_x to $-\alpha_x$ with respect to the optic axis, but the direction of \boldsymbol{d} has also switched such that again $\theta_I = \alpha_x$. In fact, as the prism rotates the normal to its face rotates about the optical axis at angle α_x and thus $\theta_I = \alpha_x$ for all θ . It is assumed that there is no random error, or that the prism is not loose and changing orientation as it rotates in the mount. The prism may also have a tilt component α_y perpendicular to the x-axis, but this angle will be perpendicular to the dispersive axis at all θ and thus have no effect on the dispersion angle.

Even with the prism in perfect alignment the rotation stage may be oriented at some angle β to the optic axis, with x- and y-components β_x and β_y such that when $\theta = 0^\circ$ then $\theta_I = \beta_x$. At $\theta = 180^\circ$, the prism is still oriented to the optic axis by the same angle β_x while the dispersion axis has reversed so that now $\theta_I = -\beta_x$. The normal to the prism face is fixed with only the prism's dispersive axis and rotating with θ . Therefore β_y will contribute to θ_I , with $\theta_I = \beta_y$ at $\theta = 90^\circ$ and $\theta_I = -\beta_y$ at $\theta=270^\circ$ and the expression for θ_I in the presence of mount misalignment becomes $\beta_x \cdot \cos(\theta) + \beta_y \cdot \sin(\theta)$. Adding this to the prism misalignment contribution yields:

$$\theta_I = \alpha_x + \beta_x \cdot \cos(\theta) + \beta_y \cdot \sin(\theta). \quad (42)$$

The consequence of rays entering the prism at varying incident angles is that rays exit at varying angles and thus is observed as a direct impact on the estimate $\varphi_{est}(\lambda)$ where it is assumed rays are incident at $\theta_I = 0^\circ$. Therefore the error is very similar to that of $\varepsilon_\varphi(\lambda)$ although now a function of θ in the presence of β :

$$\varepsilon_\varphi(\lambda, \theta) = \varphi_{est}(\lambda : \theta_I = 0) - \varphi(\lambda : \theta_I = \alpha_x + \beta_x \cdot \cos(\theta) + \beta_y \cdot \sin(\theta)). \quad (43)$$

Note that this is derived for an on-axis point and that in general the error do to mount misalignment is equivalent to having incident rays at some of-axis field angle with components corresponding to β_x and β_y . Because field angle θ_F is not strictly an error in the system and can identified and removed in post processing it is not described as such. To include it, it would be treated in the same manner as the rotation stage angle β . The expression for $\varepsilon_\varphi(\lambda, \theta)$ can be inserted into Equation (29) to provide the $r_\varepsilon(\lambda, \theta)$ for Equation (32).

Error in Projection Angle θ

To this point, the examined systematic errors are those which lead to inaccuracy in estimating $r(\lambda)$ at the detector array. The displacement is not only described by the magnitude but also by the azimuth direction defined by θ . If the projection angle is assumed to be some $\theta_{est} \neq \theta$, the accuracy of the estimation of the shift components Δx_{est} and Δy_{est} calculated from Eqs. 5a and 5b is reduced. If the residuals as a consequence of $\theta_{est} \neq \theta$ are $\varepsilon_x(\lambda_k, \theta) = r(\lambda_k) \cdot (\cos(\theta) - \cos(\theta_{est}))$ and $\varepsilon_y(\lambda_k, \theta) = r(\lambda_k) \cdot (\sin(\theta) - \sin(\theta_{est}))$ then the error term for the k^{th} bin is derived from Equations (23), (24) and (31):

$$H^\varepsilon(k, k, \lambda_k, \theta) = e^{-ik \cdot \varepsilon_x(\lambda_k, \theta)} e^{-i \cdot k \cdot \varepsilon_y(\lambda_k, \theta)} \quad (44)$$

The mathematical expressions for these systematic errors are summarized in Figure 25e can be used to model the spatial and spectral characteristics of the reconstructed hyperspectral image cube assuming the described reconstruction technique is used. Though derived separately, the effects are cumulative. The expressions can be used to assess cumulative effects and to also determine the chief contributor.

Modeling Effects of Systematic Error

To assess the change in the spatial and spectral resolution, w and $\Delta\lambda$, and the spectral shift, Δl , and spatial shift, Δs , the current CTI system is modeled to predict the projected images, $p(x, y, \theta)$, using a point, monochromatic source with Gaussian point spread function, PSF. The various systematic errors of Figure 25 are incorporated in the model and the forward projections created using a chosen error. The reconstruction of the datacube $t(x, y, \lambda)$ is performed using the shift-and-add algorithm *without* accounting for the systematic error. The empirical spatial and spectral locations were measured by

calculating the PRF/LSF fits to a Gaussian line shape function in each case. With a few exceptions, the Gaussian shape was the best functional fit to the data with an r-squared fit coefficient of >0.99 for all peaks used in the assessment, except in the situation where error significantly affected the line shapes (see next section). The full width at half maximum (FWHM) of the Gaussian shapes were reported as the spatial and spectral resolution. Contributions from instrument bias, background, or continuum energy in the spectra were removed prior to fitting.

Error in Prism Angular Deviation

As previously discussed, error in $\varphi(\lambda)$ can be interpreted in two different ways: 1) loss of spatial resolution in the k^{th} spectral bin due to incorrect reconstruction or 2) the shift of the spectral peak due to accurate reconstruction in some other bin. The first case is described by the error kernel. The second case results from the fact that there is some λ_j such that $\varphi(\lambda_j) - \varphi_{est}(\lambda_k)$ is minimized and therefore the residual error $\varepsilon_\lambda(\lambda_j)$ is near zero. The spectral line center is shifted to λ_k while spectral resolution, spatial resolution and spatial location are unchanged at this wavelength. This is the likely conclusion as a result of error in estimating $\varphi(\lambda)$ except in the rare case that one is using the instrument to reconstruct a single bin to analyze spectral line emissions. Figure 26 shows the shift $\Delta l = (\lambda_j - \lambda_k)$ at each wavelength given increasing values of $\varepsilon_\varphi(\lambda)$. The greater shift at longer wavelengths is a result of the decreased dispersion, or larger $d\lambda/dr$.

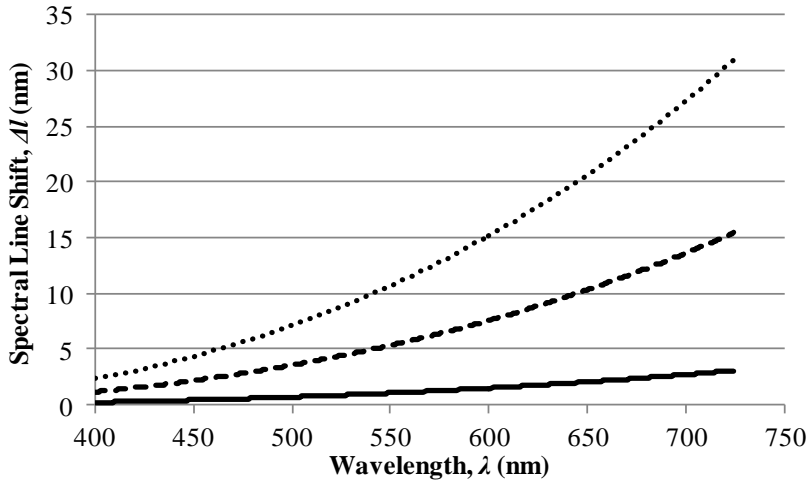


Figure 26. The shift in spectral peak location as ε_ϕ increases from 0.01° (solid line) to 0.05° (dashed line) to 0.10° (dotted line). The effect is markedly increased at longer wavelengths.

Detector Array Distance and Tilt

The results for given errors in distance and tilt of the detector array are plotted in Figure 27 for values of $\varepsilon_d = 1 - 2$ mm, $\delta_x = 1 - 3$ degrees, and $\delta_y = 0$ and 3 degrees. A spatial shift is most apparent for $\lambda < 450$ nm and particularly sensitive to tilt, δ . Spectral shifts are observed in the blue and red with no shift at $\lambda = \lambda_c$. The shift is proportional to spectral resolution of the instrument with magnitude driven by the size of ε_d . We have chosen here to measure the spatial resolution in the bin of best reconstruction. Thus, the error is realized in spectral shift, not in degradation of spatial or spectral resolution as to not report the same effect twice. The change in spatial resolution is therefore largely unaffected with differences, a consequence of the mostly random error in the fitting of the peaks. Random error is a result of the sparse number of points in the data being fitted, essentially a quantization error in fitting undersampled data (see Fig. 23a). Some trend in the spectral resolution is apparent with considerable random error, however small compared to the ideal resolution of the system.

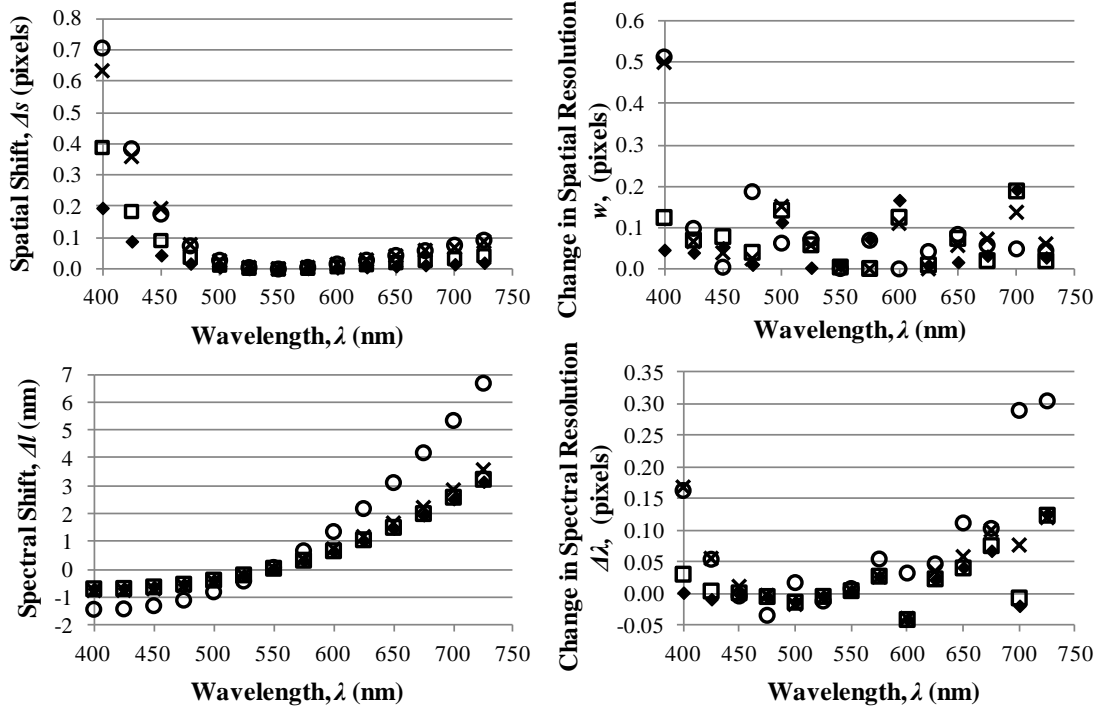


Figure 27. Comparison of object and reconstructed hyperspectral images for detector tilt. The effects of error in terms of spatial shift Δs , spectral line shift Δl , loss of spatial resolution w and loss of spectral resolution $\Delta \lambda$ for four difference cases of detector distance error ϵ_d and detector tilt δ_x and δ_y : $\epsilon_d = 1$ mm, $\delta_x = 1^\circ$, and $\delta_y = 0^\circ$ (“◆”); $\epsilon_d = 1$ mm, $\delta_x = 2^\circ$, and $\delta_y = 0^\circ$ (“□”); $\epsilon_d = 1$ mm, $\delta_x = 3^\circ$, and $\delta_y = 3^\circ$ (“×”); $\epsilon_d = 2$ mm, $\delta_x = 3^\circ$, and $\delta_y = 3^\circ$ (“○”).

Prism and Rotation Stage Misalignment

Figure 28 shows the dependence on error in reconstruction on α , with both positive and negative x-components considered. The only change from expected performance is in a shift in peak wavelength as illustrated in Figure 28, with all other data the result of noise in the measurements. This is expected, as the angle α_x has no dependence on θ . There is constant error in $r_\epsilon(\lambda)$ which is observed as a shift in peak wavelength with no other degradation of the data in the same way that the error $\epsilon_\phi(\lambda)$ affects the results.

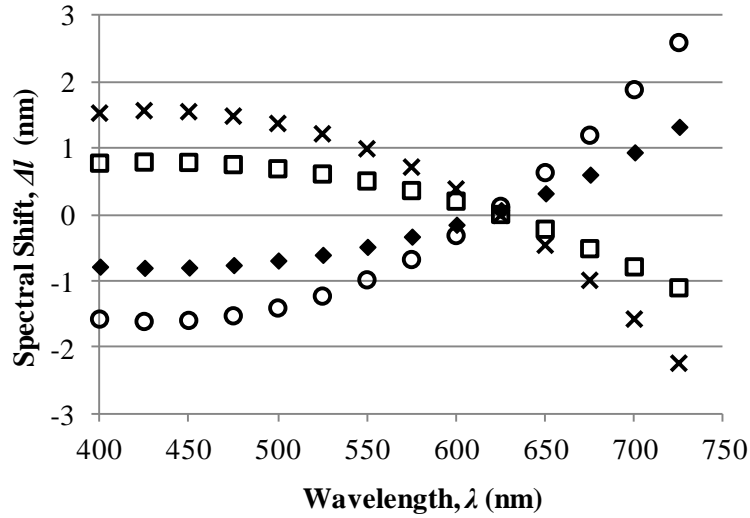


Figure 28. The spectral peak shift Δl as a function of the prism misalignment α_x in the rotation stage mount. Plotted are $\alpha_x = -0.5^\circ$ (“ \blacklozenge ”), $+0.5^\circ$ (“ \square ”), -1.0° (“ \times ”) and 1.0° (“ \circ ”).

The error due to mount misalignment is more interesting as the magnitude of misalignment β is now a dependent on θ . Unlike previous results, Figure 29 exhibits little shifting of peaks and noticeable loss of spectral and spatial resolution especially at shorter wavelengths. Measurements at off-axis field points would be necessary to assess the effects of misalignment and field angle, θ_F .

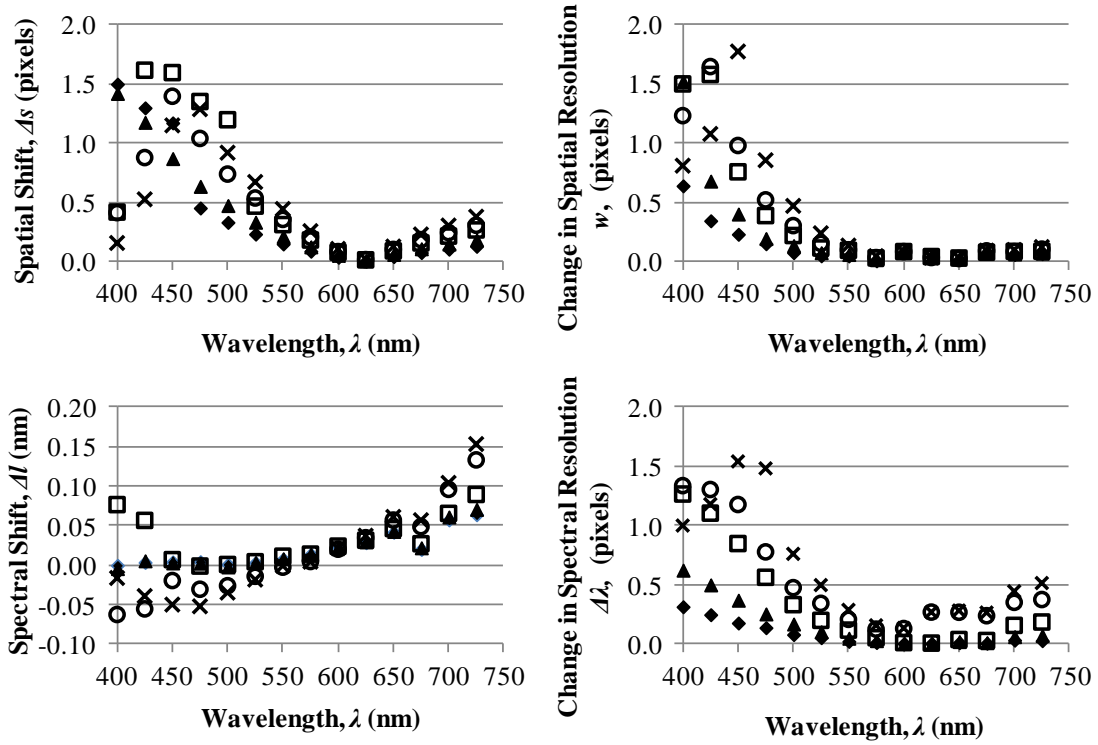


Figure 29. Comparison of object and reconstructed hyperspectral images for mount misalignment. The effects of error in terms of spatial shift Δs , spectral line shift Δl , loss of spatial resolution w and loss of spectral resolution $\Delta \lambda$ for four different cases of mount misalignment components β_x and β_y : $\beta_x = 0.25^\circ$, $\beta_y = 0.00^\circ$ (“◆”); $\beta_x = 0.50^\circ$, $\beta_y = 0.00^\circ$ (“□”); $\beta_x = 0.25^\circ$, $\beta_y = 0.25^\circ$ (“▲”); $\beta_x = 0.50^\circ$, $\beta_y = 0.25^\circ$ (“○”); $\beta_x = 0.50^\circ$, $\beta_y = 0.50^\circ$ (“x”).

The apparent improvement in results for the largest values of β arises from the inability to accurately fit a function to the degeneration of the peaks for errors this large. Figure 30 shows both the degraded spatial image as well as the spectral line-shape function of the instrument at $\lambda = 400$ nm. The images in Figure 30a-c demonstrate the reconstructed images of an on-axis, monochromatic ($\lambda = 400$ nm) point source in three adjacent wavelength bins. The “donut” shape arises as the radius of the ring in the error function becomes larger than the image PSF which is just starting to occur for the example in the center column of Figure 23. The images in the adjacent, $\lambda = 399$ and 401 nm, bins are out of band artifacts. The asymmetric rings exhibited in these artifacts arise

from the prism mount misalignment. For the combination of β_x and β_y prism mount misalignment illustrated in Figure 30d, the spectral lineshapes become wider and, for the two worse cases, begin splitting. Figure 30e illustrates the shifting of the peak for a constant β and changing prism misalignment, α . That is, the correct image is reconstructed at the wrong wavelength.

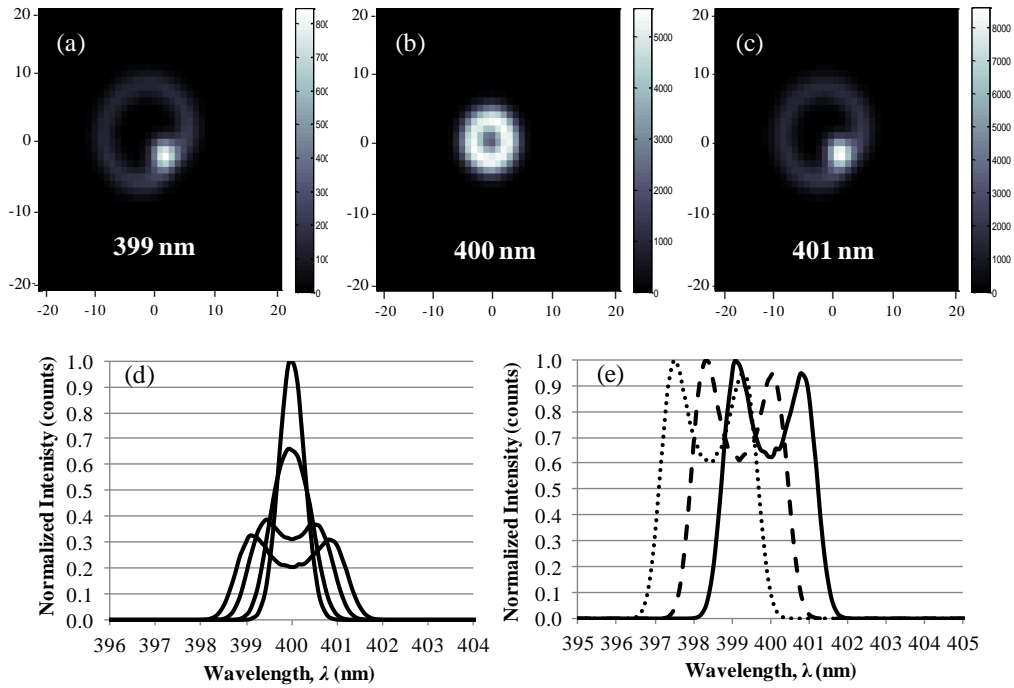


Figure 30. Reconstructed hyperspectral images for an on-axis, monochromatic $\lambda = 400$ nm point source, at three nearby wavelengths: (a) 399 nm, (b) 400 nm and (c) 401 nm for $\beta_x = 0.50^\circ$, $\beta_y = 0.50^\circ$. The spectra for the (0,0) pixel at the center of the image provides the spectral lineshape functions for (d) progressively worse prism mount misalignment: $\beta_x = 0.00^\circ$, $\beta_y = 0.00^\circ$; $\beta_x = 0.25^\circ$, $\beta_y = 0.00^\circ$; $\beta_x = 0.50^\circ$, $\beta_y = 0.00^\circ$; and $\beta_x = 0.50^\circ$, $\beta_y = 0.50^\circ$. In part (e) the shift in peak wavelength is apparent for the $\beta_x = 0.50^\circ$, $\beta_y = 0.50^\circ$ case as prism misalignment, α_x , increases from 0.0° to 0.5° to 1.0° .

Error in Projection Angle θ

In the reconstruction of the data, error in estimation of θ is observed as a multiplication in Fourier space of the Fourier transform original PSF by error kernel

given by Equation (32) in each spectral bin. Unlike the case of error in $\varphi_p(\lambda)$, there is no wavelength at which the error in reconstruction is minimized therefore there is no shift of spectral or spatial location. There is a loss of spatial and spectral resolution, which is shown for given values of ε_θ in Figure 31. Note the minimum at the undeiated wavelength due to the fact that $r(\lambda_c) = 0$ pixels.

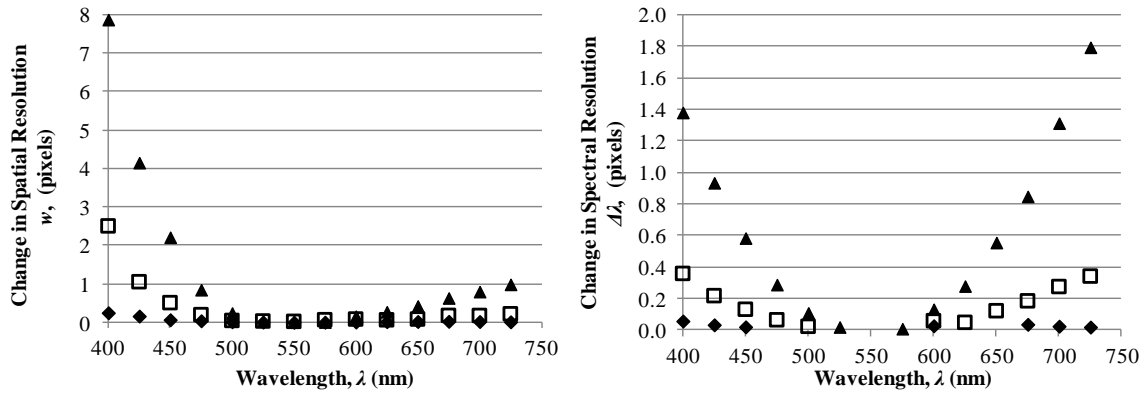


Figure 31. The loss of spatial and spectral resolution for given errors in θ , denoted by ε_θ : $\varepsilon_\theta = 0.10^\circ$ (“♦”), $\varepsilon_\theta = 0.25^\circ$ (“□”), and $\varepsilon_\theta = 0.50^\circ$ (“▲”).

Experimental Validation

Experimental observations from the AFIT CTI instrument were examined to determine how well the model is able to capture the impact of the systematic error with controlled instrumental inaccuracies purposefully introduced. This is not a thorough validation of the model, as it is impossible to isolate the effect of a single source of error. Furthermore, detector tilt and prism alignment were measured indirectly. Representative systematic error is introduced with sufficient magnitude such that it is the overwhelming error. Because error in $\varphi(\lambda)$ and θ cannot be introduced to the system and are essentially inaccuracy in reconstruction, they will not be considered. Error in distance to the focal

plane, focal plane tilt, and prism misalignment can be incorporated experimentally. Uncertainty in the magnitude of the intentional systematic error is included in the model.

A 300 μm pinhole at the object plane illuminated by a combination of an Hg pen lamp and red laser pointer was used to simulate a point source with isolated spectral lines at 404.7 nm, 435.8 nm, 546.0 nm, and 635 nm. For each instance of induced systematic error in the instrument, projections were collected at $\theta = 0^\circ$ - 345° in 15° increments for a total of 23 projections. At each projection, the displacement of the image is calculated to produce a measurement of $r(\lambda, \theta)$ by finding the center of the Gaussian and subtracting the location of the undeviated point source. A direct comparison to the model derived $r(\lambda, \theta)$ is made in each case to assess how well the model matches the performance. Several measurements of the induced systematic errors were made to estimate the uncertainty in the measurements. The model derived $r(\lambda, \theta)$ included error bars which encompass possible values given the uncertainty of the measurements. These comparisons are made to verify that the model predictions were correct, although limitations of the system and ability to measure $r(\lambda, \theta)$ to the necessary fidelity made a direct comparison somewhat difficult. These results can also be examined in terms of how they match the expected impact on system performance. The mean, μ , of $r(\lambda, \theta)$ represents spectral location and the standard deviation, σ , of $r(\lambda, \theta)$ the spatial and spectral resolution. Loss of symmetry may also be an indicator of loss of spatial resolution depending on the spatial distribution.

To measure the affect that of detector tilt, the PIMAX camera was rotated 4° in the +x-direction ($\delta_x = +4^\circ$) and tilted upward ($\delta_y = +2^\circ$). The camera was moved toward L_3 by 2 mm ($\varepsilon_d = -2$ mm). It is estimated that the tilt angle of the camera can be measured to $\pm 0.25^\circ$, and that the error in ε_δ (from both components) is within ± 0.5 mm. These

measurement error estimations will be used in the model to determine a maximum and minimum range of model results. Because the camera was rotated about its mount point, which is displaced from detector by 70 mm, the rotation angle also moves the array toward L_3 , providing some very small amount of variable ε_d across the array. Swiveling the camera also rotates the array away from the image plane, so there is a limit on the δ that can be imparted before the image of the spectrum is displaced off of the array.

Equations (28) and (41) were used to calculate $r(\lambda, \theta)$ for each of the 5 wavelengths as a function of rotation angle. The results are plotted in Figure 32. The corresponding $r(\lambda, \theta)$ was then measured. The 404.7 nm source image was projected off of the array at $\theta = 140^\circ - 200^\circ$ thus the gap in data. Because of the change in D_δ , the spectral images are slightly out of focus. For the situation with detector tilt and distance error, no real significant change in spatial resolution or location with some decreased spectral resolution at shorter λ is expected (see Figure 27). This is reflected in the $r(\lambda, \theta)$ model and data as σ is largest for $\lambda = 404.7$ nm, decreases at $\lambda = 435.8$ nm and is mostly consistent for the three longer wavelengths.

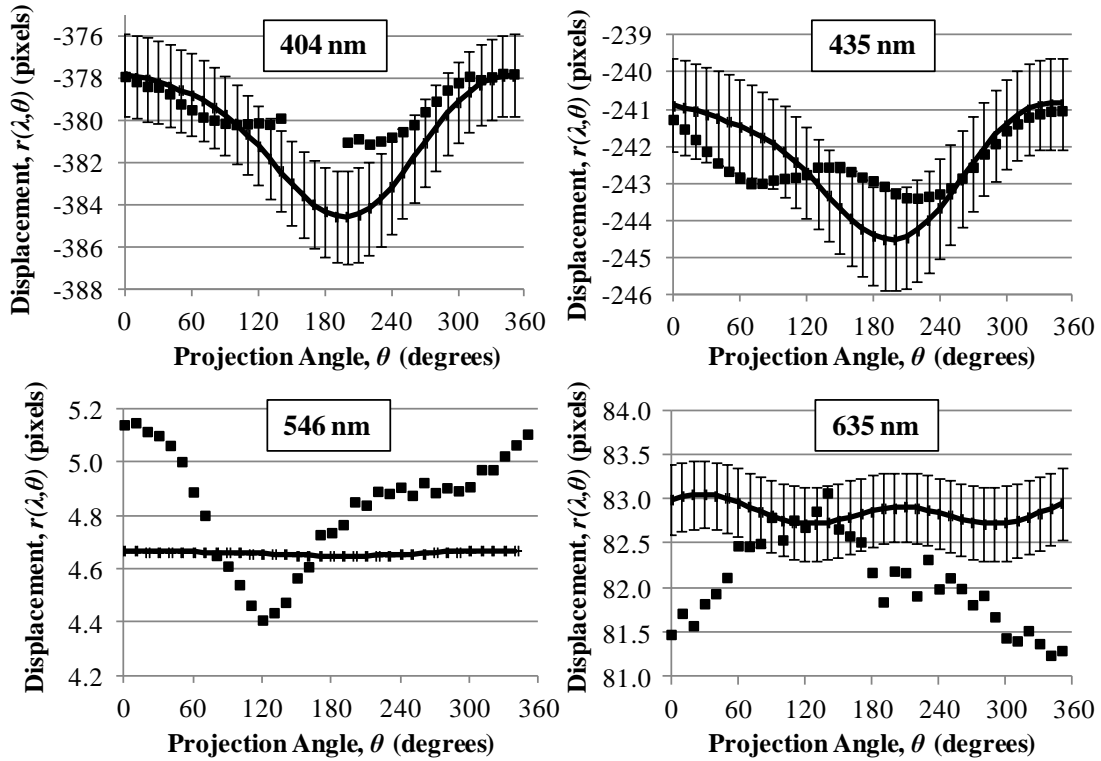


Figure 32. Measured and modeled $r_{\delta}(\lambda, \theta)$ for the 404.7 nm, 435.8 nm, 546.0 nm, and 635.0 nm spectral lines for detector tilt $\delta_x=4^\circ$, $\delta_y=2^\circ$ and detector distance error $\varepsilon_d = -2$ mm as a function of θ . The measured data points are given by the “■”, with the solid line the model results with associated error estimate.

To examine the effect systematic error caused by a misaligned mount and prism, the prism was angled in the mount in two directions to create the angles α_x and α_y between the prism face and the normal to the optical axis as shown in Figure 25. The mount itself was tilted in two directions to create the misalignment angles β_x and β_y . The magnitudes of these angles were measured by a laser reflected off of the face of the prism to a point nearly 100 cm from the prism. Misalignment in the instrument was used that gave values $\alpha_x = 0.50^\circ$, $\alpha_y = 0.50^\circ$, $\beta_x = 0.75^\circ$, and $\beta_y = 0.50^\circ$ with the instrument design again limiting the amount of error that could be imparted. The estimation in error for angles α and β is $\pm 0.2^\circ$. The predicted $\varphi(\lambda, \theta)$ resulting from the calculated θ_l using the expression from

Equation (43) was used to find the displacement $r(\lambda, \theta)$ for each of the 5 wavelengths.

The predicted values are plotted with the measurements in Figure 33.

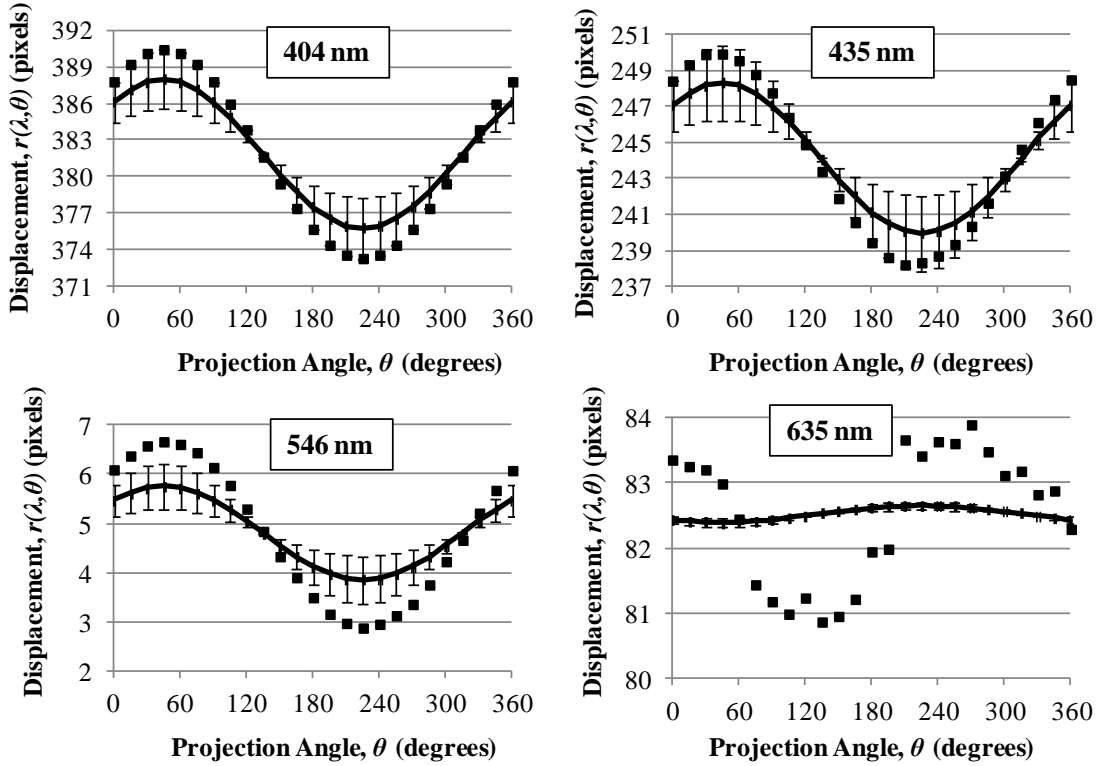


Figure 33. Measured and modeled $r_{\delta}(\lambda, \theta)$ for the 404.7 nm, 435.8 nm, 546.0 nm, and 635.0 nm spectral lines for prism and mount misalignment of $\alpha_x=0.50^\circ$, $\alpha_y=0.50^\circ$, $\beta_x=0.75^\circ$, and $\beta_y=0.50^\circ$. The measured data points are given by the “■”, with the solid line the model results with associated error estimate.

A summary of the modeled and observed μ and σ for the displacements in the cases of prism misalignment and detector tilt and displacement is provided in Table 3. For prism and mount misalignment, the mean of $r(\lambda, \theta)$ are in agreement at all λ except at 546 nm so that the small peak shift predicted by the model is also observed in the data. The exception at $\lambda=546$ nm may be indicative of inaccuracy in $\varphi(\lambda)$ near the undeviated wavelength. Spatial location again is not expected to change here, with the data in top

left of Figure 29 signifying the inability to measure the centroid location in the degenerative spatial function. The standard deviation for each $r(\lambda, \theta)$ displacement decrease as λ increases analogous to the greater loss of spatial and spectral resolution at the shorter λ . The standard deviation reaches a lower limit of near 1 pixel, while the model standard deviation for the 635 nm point rises slightly perhaps capturing the effect of mount misalignment (bottom right plot in Figure 29). For the $r(\lambda, \theta)$ with appreciable (>1 pixel) change, the model and data are showing nearly identical trends. The consistency of the model and the data here suggest that the tilt and distance error measurements were influenced by some additional misalignment of the prism and mount.

Table 3. The mean and standard deviation from the $r(\lambda, \theta)$ data for each measured wavelength in the presence of prism and mount misalignment and detector distance error and tilt.

λ	$r(\lambda, \theta)$ Calculations for Prism and Mount Misalignment (pixels)				$r(\lambda, \theta)$ Calculations for Detector Distance and Tilt (pixels)			
	Modeled		Measured		Modeled		Measured	
	μ	σ	μ	σ	μ	σ	μ	σ
404.7	-379.48	5.62	-381.98	6.18	-380.74	2.40	-379.40	1.12
435.8	-245.41	3.87	-244.22	4.24	-242.42	1.30	-242.44	0.74
546	2.50	0.90	4.82	1.36	4.66	0.01	4.84	0.21
577.5	31.91	0.42	31.97	1.00	21.98	0.04	21.98	0.21
635	81.20	0.12	82.52	1.02	82.85	0.11	82.09	0.50

Conclusions

Chromotomosynthetic imaging spectrally disperses each point in an extended object, convolving spatial and spectral information. By rotating the prism about the optical axis, a series of projected images are recorded. Reconstruction of hyperspectral data cubes requires an estimation of the instrument component properties which define the forward transform. We have analyzed the forward projections with various systematic errors

included, and then reconstructed the hyperspectral data cube as if the error did not exist. It is necessary to consider degradation of performance in the reconstructed image cube, not in the measured 2-D (projection) space. Four types of systematic error were examined in this study; those due to tilt in the detector array (δ), distance between the detector array and the lens L_3 (ε_d), error in knowledge of the angular prism dispersion (ε_ϕ), and error in estimation of the prism rotation angle θ (ε_θ).

Errors may be classified in two categories: (1) systematic errors associated with incomplete estimates of the displacement, $r_\varepsilon \neq 0$, and (2) artifacts for the reconstructed wavelength bin arising from other spectral components in the source, $\lambda \neq \lambda_k$. Errors in estimating the displacement that introduce no angular dependence, such as inaccurate characterization of prism dispersion or simple axial shifts of the image, simply shift the correctly reconstructed image to a different wavelength bin. However, artifacts are introduced in the expected wavelength bin. In contrast, errors in estimating the displacement that are not independent of prism rotation degrade both the spatial and spectral resolution of the reconstructed hyperspectral image.

An error kernel function was developed for each source of error to model the effects so that design tolerances can be diagnosed. The results are specific to the AFIT CTI design and are quantified relative to the modeled performance with perfect reconstruction referred to as the “expected performance”. It is intended that the relative magnitude of each error and result on the reconstructed data will apply to any set of data given the general nature of the equations describing the reconstruction and error kernel that is convolved with each spectral bin.

The prism and mount misalignments are essentially errors in the assumption that the input rays are perpendicular to the prism face and therefore result in a poor estimation of $\varphi(\lambda)$. Poor estimation of $\varphi(\lambda)$ and prism misalignment leads to significant spectral line shifting, while mount misalignment results in highly distorted and asymmetric spatial patterns of point images. Detector array tilt degrades both spatial and spectral location of sources. This is expected given the dependence of $r(\lambda, \theta)$ on D_6 , with additional distortion due to prism rotation and reconstruction. Variation of the incident angle θ_I as the prism rotates leads to degradation of both spectral and spatial resolution. Overall, the system is most sensitive to mount misalignment with misalignment on the order of 0.25° in both x and y directions causing considerable performance loss in all four areas, though much less spectral shift.

The AFIT CTI is most sensitive to spectral resolution loss and spectral line shifts at wavelengths less than 500 nm where expected spectral resolution is best, with $\Delta\lambda < 2$ nm. An array distance error of 1 mm caused a greater than 1 nm shift in this region. Prism misalignment parallel to the dispersion axis of 0.5° produces a similar shift. Shifts in the wavelength of the reconstructed spectrum on the order of the spectral resolution were observed across the entire spectral range. These shifts were caused by both array distance error of 2 mm and constant prism dispersion error of 0.05° . No substantial spectral resolution loss occurred at wavelengths longer than 500 nm, with nearly a factor of two degradation in spectral resolution for mount misalignment of 0.25° and prism rotation angle error of 0.25° at the shorter wavelengths. Line shape distortion occurs with mount misalignment and may lead to further error in spectral performance.

Spatial performance is also a function of wavelength, with the expected system performing best at wavelengths greater than 550 nm and less than 425 nm. Significant loss in spatial resolution due to prism mount misalignment, uncertainty in the prism rotation angle and detector array tilt in terms of magnitude are present, but in the shorter wavelength region where the relative effect is less, though for wavelengths shorter than 425 nm the error will be substantial. Errors of 0.50° in rotation angle and mount misalignment of 0.50° can produce a factor of 2 degradation in spatial resolution in this region. Shifts in the centroid of the 2-D point spread function are caused primarily by detector array tilt and prism mount misalignment but are only significant for $\lambda < 450$ nm. Distortion of the PSF is also observed in the case of array tilt and more so with mount misalignment. Spatial resolution and location measurements may not be exact and could imply worse performance than captured with these metrics alone.

V. Classification of Visible Point Sources Using Hyperspectral Chromotomosynthetic Imagery

Preface

A hyperspectral chromotomosynthetic imaging (CTI) system (also referred to as chromotomography) is used to detect and classify a collection of 21 scattered, spectrally diverse point-like sources. The instrument operates in the visible to near IR (400 – 800 nm) and has the potential to collect spectral imagery at greater than 10 Hz. A 2-D wideband spatial image of the target scene is used to detect and spatially characterize the targets leading to optimization of the 3-D spatial/spectral reconstruction of the hyperspectral image cube. The instrument is assessed by directly comparing results to spatial data collected by a wideband imager and hyperspectral data collected using a liquid crystal tunable filter (LCTF). Target classification using k-means clustering of observed spectra yielded 5-6 target classes for each methodology, indicating information obtained using CTI was similar to that collected by the LCTF. The wideband spatial content of the scene reconstructed from the CTI data is of same or better quality in terms of background noise and target intensities as a single frame collected by the undispersed imaging system with projections taken at every 1°. Performance is dependent on the number of projection used, with projections at 5° producing adequate results in terms of target characterization. The CTI has 2-4 times the spectral resolution of the LCTF. The data collected by the CTI system can simultaneously provide spatial information of equal quality as a bandpass imaging system, high-frame rate slitless 1-D spectra, and 3-D hyperspectral imagery which can be exploited to produce the same results as a traditional multi-band spectral imaging system.

Introduction

Hyperspectral imagery (HSI) of spatially unresolved targets is often exploited to determine accurate location and spectral data needed for classification. Static sources in the scene may be unresolved, yet can be classified by overall size from larger (cities) to smaller (flare stacks, single building infrastructure, etc.) and assigned a location. For example, visible imagery can be used to identify light from major cities and combustion sources. Further spectral classification may determine predominant types of man-made lights (e.g. incandescent or fluorescent) or distinguish other emitters such natural gas flares, burning oil, or other effluents [92-94]. This paper will explore the use of a recently developed hyperspectral CTI device [57] to detect and characterize unresolved point sources spatially and spectrally and estimate temporal performance compared to a traditional HSI method.

The underlying principle for CTI technology lies in the field of medical physics and the mathematics of tomography first demonstrated by Ziedes des Plantes in 1932 [32]. The circular tomosynthetic projection and reconstruction of multiple planes into a 3-D data cube was presented by Grant [30] in 1972. The transition of the technology to hyperspectral imagery was first explored in the literature by Levin [31] and by Okamoto [32]. The development and demonstration of working remote sensing systems has since been demonstrated using both a computer generated hologram disperser [35-37] and a rotating direct vision prism (DVP) [33, 34] to collect projections of spectral imagery as a function of prism rotation angle. The Air Force Institute of Technology (AFIT) has built a CTI system based on the latter design due to higher throughput of the system and better achievable spatial and spectral resolution [57] on the detector array. The technology has

been referred to as chromatography in the previous literature; we have decided to use the term chromotomosynthesis as the projection geometry and reconstruction mathematics more closely resemble those used in medical tomosynthesis [30, 26, 27, 74, 79] than those used in traditional tomography. A field-deployable system [41, 56] has also been tested and further work is being pursued for a space-based CTI instrument [58-60].

Each projection (frame) of data taken by the CTI represents a 2-D spectrograph, which can be exploited to analyze high frequency changes in spectral content. The advantage of taking the spectrographs at many projection angles greatly reduces the likelihood of spectral interference in a set of dense point sources. Perhaps the most important attribute of CTI is the ability to collect complete HSI data cubes at rates easily exceeding 10 Hz, limited only by the detector array read rates. Due to symmetry, panchromatic imagery can be reconstructed using projections from $\frac{1}{2}$ of the full prism rotation, and two dimensional spectrographs at the read rate of the array. This makes the CTI very attractive to characterizing events occurring in a battlespace such as artillery fire, detonations, explosions and fast burning missiles [2, 3, 10, 11, 13-15].

An exact 3-D reconstruction described by the Radon transform cannot be achieved in CTI (or tomosynthesis) as the direction of the spectral dispersion is not perpendicular to the rotation axis of the prism. Data quality is further degraded by the small projection angle associated with the DVP. Thus, while an exact spatial representation of a particular 2-D spectral bin can be reconstructed, residual artifacts from adjacent spectral bins reduce the quality of imagery compared to conventional medical CT images [26-28]. This exact reconstruction is subject to systematic errors associated with the instrument [95]. For these reasons, spectral resolution is inferior to that of more conventional

techniques such as imaging Fourier transform spectrometers and traditional scanning systems. However, the CTI systems offer several advantages, including: (1) a simple, inexpensive design, (2) flexible adaptation form many targets and missions, (3) simultaneous HSI and panchromatic imaging, (4) operation as a slitless spectrograph, and (5) high speed operation.

For this experiment, a representative set of unresolved targets with differing spectral features are randomly arranged in the field of view. The quality of the CTI reconstructed 2-D wideband (undispersed) data is described in terms of the characteristics of the targets detected and residual scene variance compared to a image of the scene collected without the prism in place. The 3-D hyperspectral image cube is reconstructed and extracted spectral information is used to classify the targets using the k-means classification methods. Target spectra are also found and classified using an optimized technique based on spatial knowledge of the targets from the 2-D reconstruction. The CTI performance is compared to data collected by imaging the sources with the LCTF. Optimization of the reconstruction algorithms to reduce the total processing time is addressed with acquisition times estimated for the various techniques and algorithms.

Instrumentation

A basic schematic of the AFIT CTI system is displayed in Figure 34. The lenses L_1 and L_2 serve as the forward telescope which collimates light as it enters the rotating DVP. The two-component prism transitions from negative to positive dispersion in the green at $\lambda_c \approx 538$ nm [57, 95]. The spectrally dispersed light exits the DVP and is focused by L_3 onto a PI-MAX Gen II intensified RB fast-gate 1024x1024 array with responsivity

primarily in the 400 - 800 nm region. The specifications associated with the design are given in Table 4. The instrument's instantaneous field of view is 0.4 μ rad with 71.6 mrad across the field stop (FS). The undispersed image of the field stop fills only the center of the detector array, so that all dispersed wavelengths are observed. The instrument's spectral resolution is wavelength dependent, from 0.4 – 10 nm [57], and bins can be reconstructed at any wavelength in the spectral range.

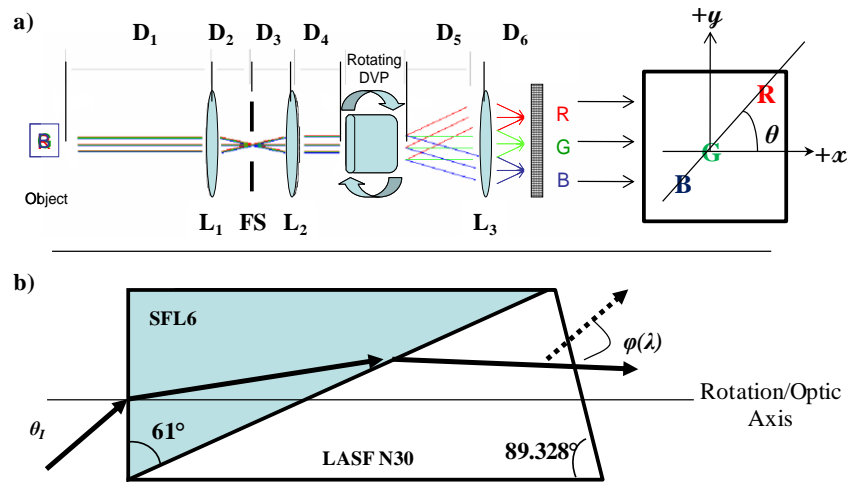


Figure 34. Description and components of the AFIT rotating prism CTI instrument.

Table 4. Specifications of the AFIT CTI instrument.

<u>Focal Lengths (mm)</u>		<u>Distances (mm)</u>	
f_1	76.2	D_1	1397
f_2	250	D_2	80.6
f_3	100	D_3	≈ 248
		D_4	30*
		D_5	10*
		D_6	≈ 89

* - variable, though the DVP is the aperture stop of the system

As the DVP rotates about the optical axis, spectrally dispersed images of the object are collected by the detector at discrete rotation angles of $\theta = 0^\circ - 360^\circ$ by framing the detector at some rate as opposed to continuously integrating energy over the period of prism rotation. The latter case is simple tomography, which would result in recording an image of the λ_c spectral component object. In tomosynthesis, by observing N discrete frames all object planes can be reconstructed [6], or in the case of CTI all spectral bins. Each frame of data is referred to as a *projection*, $p(x,y,\theta)$. The displacement r at the detection array is given as a function of λ by:

$$r(\lambda) = D_5 \cdot \tan(\varphi(\lambda)) \quad (45)$$

where $\varphi(\lambda)$ is the spectral dispersion of the DVP and has been previously characterized [57]. Due to systematic error, $r(\lambda)$ may also be a function of θ . The system is most sensitive to error in estimation of $\varphi(\lambda)$ from misalignment of both the prism in the mount and of the mount itself [95]. To properly assign spectral values and adjust for any systematic error, the instrument was calibrated using a Hg pen lamp, several laser

sources, and a set of known bandpass filters [see Appendix B]. The observed and modeled displacements are illustrated in Figure 35.

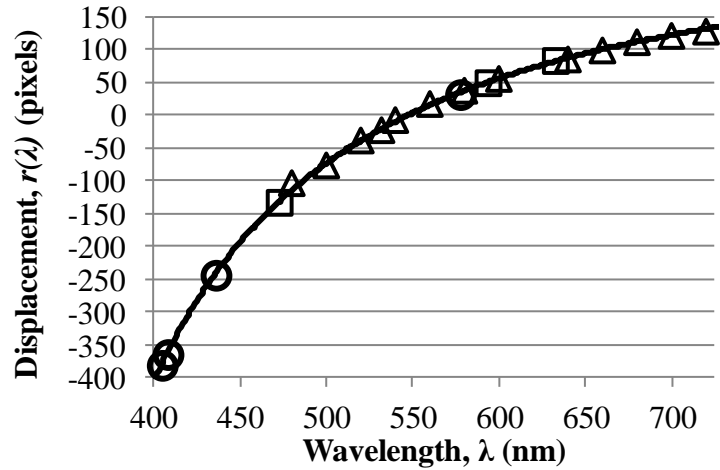


Figure 35. The final model of $r(\lambda)$ plotted as a solid line for the CTI in this experiment after calibration with several sources: “o” – Hg lamp; “□” – laser; “Δ” – bandpass filter.

Using $r(\lambda)$, the spectral resolution of the system can be calculated [57]. The spectral transmission of the DVP is calculated by estimating the reflection at the interfaces of the prism using the Fresnel equations and the transmission properties of the glasses. Both the system spectral resolution and transmission are plotted in Figure 36.

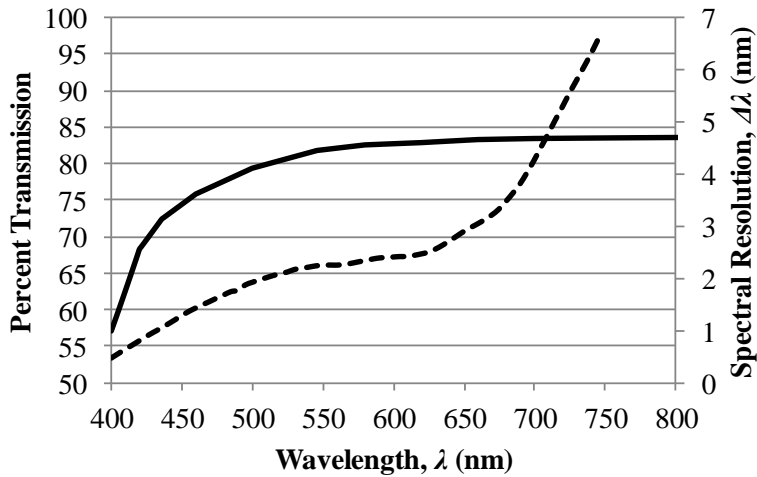


Figure 36. The measured spectral transmission (solid line) and spectral resolution (dashed line) calculated for the DVP.

Hyperspectral imagery was also collected at discrete band passes through the desired range of wavelengths by removing the DVP from the CTI instrument and replacing it with the LCTF manufactured by Cambridge Research Instrumentation [96]. All properties of the collection system and target were identical except for the method of spectral collection (dispersion vs. filtering). The LCTF is cycled through bands collecting one image at a time for a specific center wavelength. The spectral resolution and transmission for the LCTF are shown across the spectral range of 400-720 nm in Figure 37. Note that light exiting the LCTF is polarized resulting in an additional 50% loss in transmission for the randomly polarized sources.

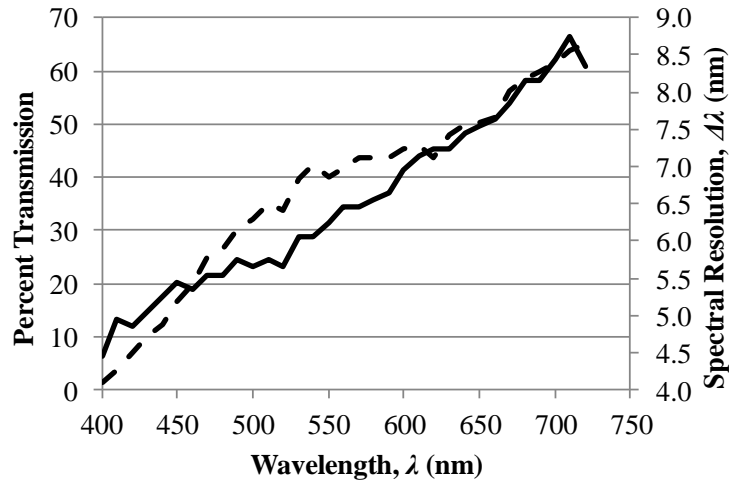


Figure 37. The estimated spectral resolution (dotted line) and spectral transmission (dashed line) of the LCTF.

The point source targets for this experiment were a collection of incandescent Christmas tree lights arranged randomly in the field of view of the instrument as shown in Figure 38. The digital camera picture is shown for reference on the left in Figure 38. This image has higher spatial resolution and a larger field of view than the CTI. Four classes of lights are apparent when viewing the color image: blue, orange, green, and pink/red. To characterize the sources as observed by the CTI and LCTF, an image was formed using the instrument with no dispersive element or filter in place. The image on the right in Figure 38 shows the image with the detected number of lights (the negative image is presented for better contrast). The integration time of the array was 50 μ s, with slight saturation allowed for brighter targets to ensure detection of the dimmest sources. Twenty-one point sources are readily identified in the field of view of the instrument.

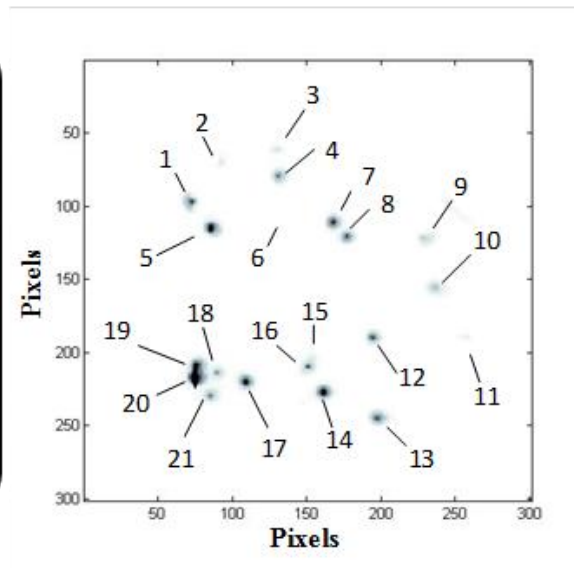


Figure 38. An image of the Christmas lights as they appear in the lab. The targets detected in the FOV of the instrument are shown on the right. Due to scaling, not all targets evident in the raw data may be observable in the picture. The scale on the detector array is 0.5 mm/pixel.

A few of the targets (6, 11, and 15) are not visible in the image due to the limited dynamic range of intensities in the picture, while 19 and 20 saturate the collection array and appear as a single extended source. Reflections from a cord connecting the lights are barely discernible to the right of Target 9.

Data Collection and Processing

With the CTI, a set of 360 projections, $p(x,y,\theta)$, were collected as the prism rotated over $1^\circ - 360^\circ$ in 1° increments. Because of the delay in readout of the detector array, the prism was stopped incrementally to collect each $p(x,y,\theta)$. To not saturate the brightest intensities of the targets occurring at $\lambda \approx 700$ nm, a 1 ms detector integration time was used with no intensification of the array. A delay time of 0.5 s was used between 1° rotations reducing the effective frame rate for the experiment.

A longer 8 ms detector integration time was used with the LCTF as its spectral range does not include the brightest target intensities at longer wavelengths and the spectral transmission is about 50% that of the CTI. Spectral images were taken at every 2 nm over the range of the device, with 50 ms needed to change the filter from one band to the next. Frames were collected at a rate of 0.5 Hz.

The 2-D Integrated Image

The set of projections $p(x,y,\theta)$ were used to reconstruct the 2-D wideband image with the same methods used in projection tomography. The integration each of the 2-D $p(x,y,\theta)$ projection into a 1-D line projection $S(t,\theta)$ is illustrated in Figure 39. Each resulting $S(t,\theta)$ is a 1-D projection of the 2-D energy in the image and is equivalent to the radon projection of the undispersed image because direction of projection is equivalent to the direction of energy dispersion. The image was reconstructed from each $S(t,\theta)$ using a filtered backprojection [66]. Due to symmetry, only the projections from 0° - 180° are required. Optimal number of projections needed is dependent on the spatial content in the scene and spatial resolution of the collection system. The MATLAB filtered inverse radon transform [67] was used to perform the 2-D reconstruction with a Shepp-Logan filter to reduce noise and artifacts.

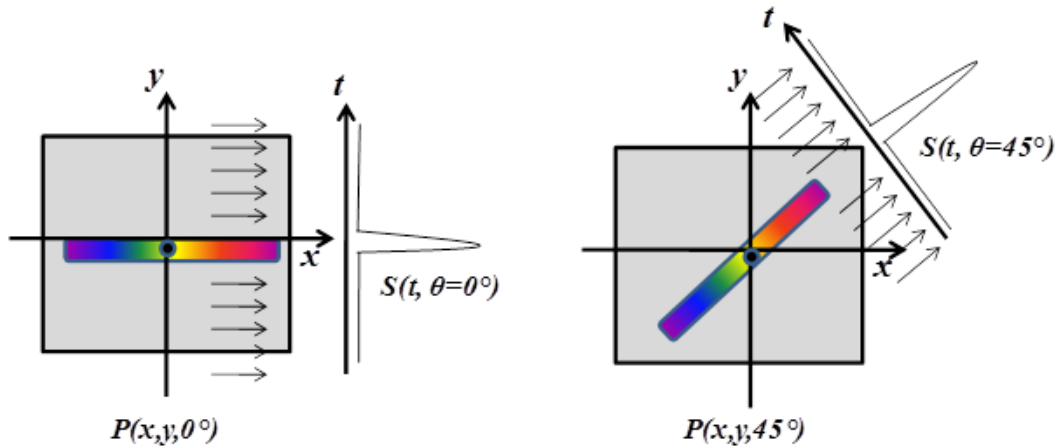


Figure 39. Integrating projections along the dispersion axis at θ produces a 1-D projection $S(t, \theta)$ equivalent to taking the radon transform of the undispersed image at the undispersed location. Shown are line projections at $\theta=0^\circ$ and $\theta=45^\circ$.

Target Spectra from 1-D Spectrograph Co-Addition

For targets which are point sources, or at least small symmetric objects with no intrinsic spatial information, their spatial properties are rotationally invariant. Therefore, each target spectrum in the $p(x,y,\theta)$ is essentially a rotated 1-D spectrograph of a particular target. Rotating by $-\theta$ about its undispersed spatial location (x_c, y_c) will align the spectra so that the data can be statistically combined to produce a final estimated spectrum for each point source.

Because there are 21 total sources in the target scene, it is nearly certain that any one projection will contain overlapping or entangled spectra. Thus, an uncontaminated spectrum cannot be obtained by simple averaging the entire set of aligned data. Since any one point from one spectral source can overlap another only one time in each projection, there are a maximum of 20 chances for a point in a spectrum be entangled with another. Each of the 360 projections is co-aligned and the minimum 25 values for each point selected and averaged to create a 1-D target spectrum. For these types of

targets, this represents an alternative method to finding spectral and spatial information. More advanced methods could be used to statistically combine the spectra, including methods that use the many spatial samples to achieve higher spectral resolution [87].

CTI 3-D HSI Data Cube Reconstruction

General reconstruction of CTI projection data requires a full spectral/spatial reconstruction of the 3-D hyperspectral data cube and assumes no prior knowledge of the target locations or spatial properties. There are several techniques available [30, 52, 54, 65, 76-79], here a previously described shift-and-add (SAA) technique [57, 96] is used to reconstruct the 2-D $p(x,y,\theta)$ into the 3-D hyperspectral image cube. In this process, each projection is spatially translated (the shift) to properly compensate for the spectral displacement imparted at particular wavelength λ_i by the prism at each prism rotation angle θ . This ensures that there is complete coincidence in the spatial pattern of the images with respect to λ_i , while spatial components associated with any $\lambda_{j \neq i}$, are not spatially correlated and thus blurred upon addition. The greater the number of projections used, the more reinforcement of the desired image and blurring of the undesired image. The process is repeated for bins at discrete λ_i to build the data cube. Given a specific application and target set, more complex or optimized reconstruction algorithms may be used to improve the quality of data or increase the efficiency over the simple SAA technique. This 3-D method requires more computational time than the 1-D spectrograph method above.

Some knowledge of the target does decrease the amount of 3-D data processing. If a target location is known, only a spatial subset of the $p(x,y,\theta)$ need to be processed. One may choose to reconstruct only a specific wavelength bin or set of wavelength bins as

desired. With some knowledge of target or scene complexity, a reduced number of projections may be used in the reconstruction, such as using θ samples in 5° or 10° increments.

LCTF Data Processing

The processing of the data collected with the LCTF and formation of the HSI data cube is straightforward and less time consuming than the CTI. Each frame of data represents a spatial collection centered at a particular λ_i . Thus, each frame is a plane in the HSI data cube, with the spectral resolution described by the spectral response of the LCTF at each wavelength. A two-dimensional median filter was used to eliminate the low-frequency spatial background in each frame while preserving the spatial characteristics of each point source, similar to the processing applied to the CTI projection data to remove artifacts.

Data Analysis and Results

The 2-D Undispersed Image

The quality of the 2-D undispersed panchromatic data sets from the tomographic reconstruction of the $p(x,y,\theta)$ were measured by comparing the recovered target intensities and the amount of background mean and noise residual in the scene to the wideband image of the target set taken by the instrument with no prism in place. An assessment is also made of the dependence of the tomographic reconstruction quality on the number of projections used. The data is reconstructed using 3 sets of projection data; a set of 180 $p(x,y,\theta)$ taken from 0° - 180° denoted by P_{180} , a subset of 36 projections taken at equal 5° increments (P_{36}) and a subset of 18 projections taken at equal 10° increments

(P_{18}). The target signal is calculated by integrating a 3x3 pixel area around the centroid location of each target in each image. A larger 10x10 pixel mask is created around the target centroid to leave background pixels which contain no target intensity. The background pixels are used to calculate the background mean and noise, given by the standard deviation of the data.

The reconstructed 2-D wideband images from the CTI P_{180} , P_{36} , and P_{18} projections are presented in Figure 40, with the undispersed image also shown. The spoke artifacts, characteristic of the filtered backprojection, are present in P_{36} and P_{18} indicating degraded performance. The spokes occur at discrete projection angles and are less evident using more projections as they are effectively smoothed throughout the image. Despite the presence of the artifacts, all targets detected in the undispersed image were recovered in the 2-D tomographic reconstructions.

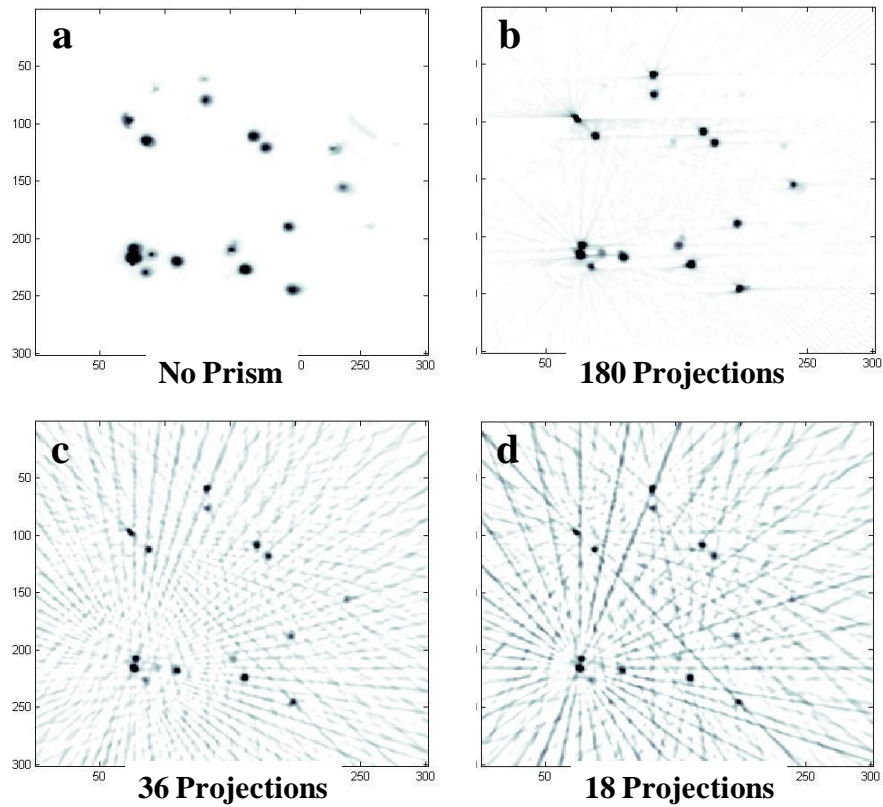


Figure 40. Panchromatic 2-D reconstructions for the set of projections $S(t, \theta)$ with different densities of projections: (b) P_{180} , c) P_{36} , and d) P_{18} . The undispersed image is also shown for comparison in (a).

The target intensities extracted from the reconstructed images are compared to those in the undispersed image in Figure 41. The intensities are normalized to the brightest, non-saturated source (Target 17), and data from the saturated targets are not included. A linear correlation is evident for each set of projections. The slope of the P_{180} is 0.964 ± 0.150 , closest to the expected value of 1. The slopes of the P_{36} and P_{18} data are 0.915 ± 0.148 and 0.874 ± 0.286 , respectively. The slope, y-intercept and correlation coefficient, r^2 , for the fits are summarized in Table 5.

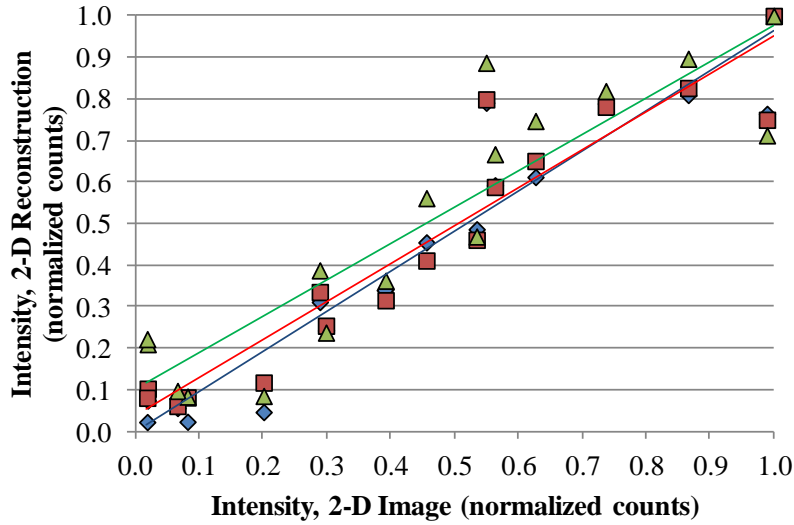


Figure 41. The measured target intensity in the reconstructed P_{180} (“♦”), P_{36} (“■”), and P_{18} (“▲”) images plotted against the intensities measured in the 2-D undispersed image. A linear fit indicates the degree to which the intensities are accurately recovered.

Table 5. The background mean and noise for the measured and reconstructed 2-D images. Also given are the results of a linear fit to the intensities plotted in Figure 41.

	Background Mean (Normalized Counts)	Noise Background (Normalized Counts)	Slope	y-intercept (Normalized Counts)	r^2 Fit
2-D Image	1.16×10^{-3}	5.70×10^{-3}	—	—	—
180 Projections	1.15×10^{-2}	3.67×10^{-3}	0.964 +/- 0.150	0.002 +/- 0.08	0.913
36 Projections	7.02×10^{-2}	1.74×10^{-2}	0.915 +/- 0.148	0.034 +/- 0.09	0.905
18 Projections	1.28×10^{-1}	4.87×10^{-2}	0.874 +/- 0.286	0.102 +/- 0.11	0.818

The normalized mean and noise calculated for the background, non-target pixels are given in Table 5. The mean of the background steadily rises as the number of projections is reduced as does the noise content due to the increase of scene variation as a result of artifacts in the background relative to the true image. The noise rises at a rate greater than the square root of the background implying the artifacts are structured and non-statistical in nature. Similarly, the background increases as the number of projections decreases due to the increased presence of the artifacts. Even with 180 projections, the

background mean is an order of magnitude higher than in the undispersed image. However, the variation in the P_{180} scene is comparable to that in the undispersed image. The dimmest three targets, numbers 2, 10, and 17, have a signal-to-noise ratio (SNR) of less than 2 in the P_{18} image making it unlikely they would be detected whereas the same targets have $SNR > 4$ in the P_{36} image.

The 3-D Hyperspectral Data and Target Characterization

Three separate sets of target spectra were extracted from the LCTF, the 3-D hyperspectral data cube reconstruction and using the 1-D spectral co-addition method. The co-addition method was suitable as the 2-D reconstruction revealed that the targets were point sources as well as their undeviated location. The 1-D spectral reconstruction (CTI-1D) and the CTI hyperspectral 3-D cube (CTI-3D) were created from projections at 5° resolution. Spectral bins for the 3-D dataset were reconstructed at 1 nm resolution over $\lambda = 400 - 800$ nm using a 501x501 pixel area. The three sets of target spectra were analyzed to evaluate the ability to classify the targets based on the 21 extracted spectral intensities for each target. All 21 spectra were corrected for the LCTF and the DVP transmission accordingly for comparison and classification purposes. No correction was made for the PiMax detector response since it is common to both methods of collection. The intensities were corrected for difference in detector integration times, though unnecessary as the spectra are normalized in the classification process accounting for absolute intensity differences. Example spectra prior to normalization for Targets 1 and 2 are shown in Figure 42. Although spectra from the CTI are recorded out to nearly 1000 nm, only the data in the 400 nm - 700 nm range of the LCTF will be used for comparison and classification purposes. The absolute spectral intensities for all methods agree for

Target 1, with some discrepancy apparent in the lower intensity Target 2. Note the low energies for shorter wavelengths.

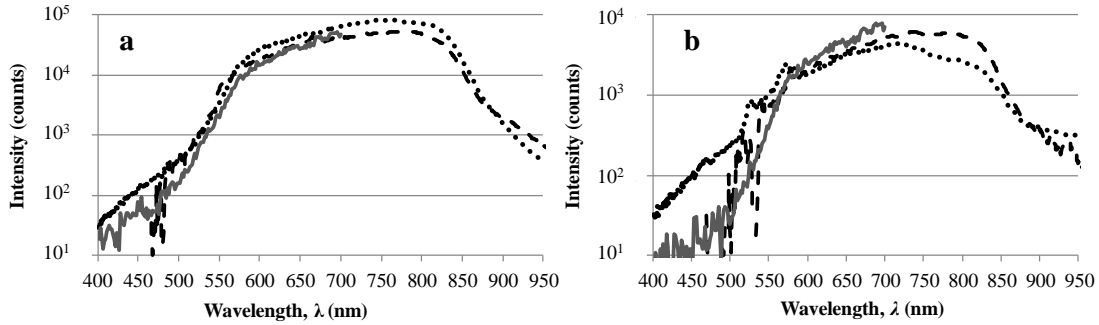


Figure 42. The extracted spectral intensity from (a) Target 1 and (b) Target 2 for the LCTF and the CTI. Dotted line is the spectrum from the CTI-1D method, the dashed line the CTI-3D method, and the solid line the LCTF.

The k-means clustering algorithm [97, 98] is used to classify the normalized target intensities. The spectra are partitioned into groups which minimize the sum of the squared errors of the members of the group from a specified centroid. The 21 target spectra are partitioned into an appropriate number of classes determined by increasing the number of classes from 1 until the within-cluster sums of point-to-centroid distances for one class is very small or zero, indicating that one target is the single member of a spectral class. This assumption that no one target is a class by itself follows from examination of the individual spectra as well as some knowledge of the lights (there are primarily four colors or classes). The accuracy of the characterization is relative in this experiment with the goal being to show that the CTI can match the results of a traditional method of hyperspectral collection and determining if the optimized CTI-1D co-addition data reconstruction matches the quality of the full 3-D hyperspectral cube reconstruction.

The CTI-1D spectral co-addition and CTI-3D reconstruction are compared in Figure 43. In both cases, the optimal number of member classes is found to be 5, one more than estimated from visual analysis. The spectral characteristics of the observed classes are nearly identical for both the 2-D and 3-D reconstructed sets. Classes III and IV appear very similar while Classes I, II and V are more distinct. As in Figure 42, it is evident that the system has poor sensitivity at the shorter wavelengths where the blue lights would be brightest. The visible colors of the lights are assigned to the classes as: Class I, blue; Class II, green; Class III, yellow/orange; Class IV, orange; and Class V, red.

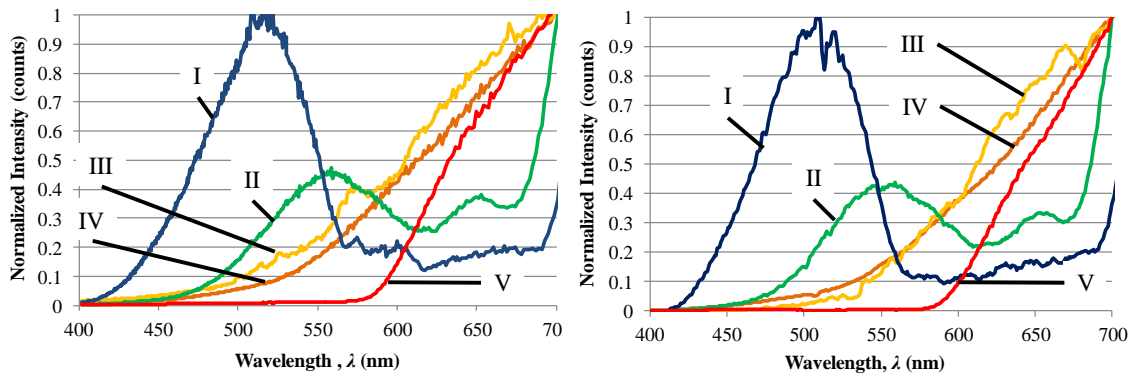


Figure 43. The five target classes calculated from the CTI-1D results are shown on the right and the CTI-3D hyperspectral cube classes on the left.

The k-means classification of the LCTF spectra yielded six classes of targets, plotted in Figure 44. Two of the spectra which peak near 500 nm are nearly identical, thus named Class I and Ia. The LCTF does show a larger discrepancy between Classes III and IV making it more apparent that these could be two spectrally different targets appearing orange.

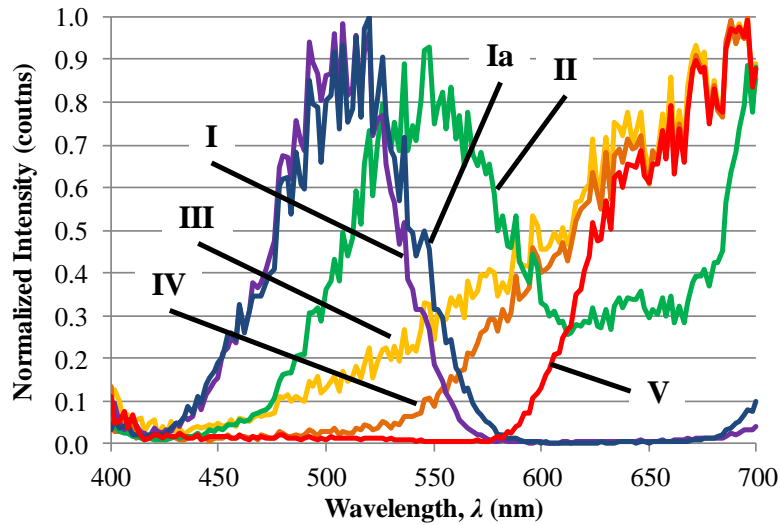


Figure 44. The target classes calculated from the LCTF data. The results are very similar to the CTI, with little residual energy in the blue (Classes I and Ia) at wavelengths greater than 600 nm.

Aside from the additional class of target, the LCTF spectral classes are generally in good agreement with those found using the CTI data. A noticeable difference is the lack of intensity for wavelengths greater than 600 nm for the Class I (blue) targets. Table 6 lists the member classes, and which targets were assigned to these classes based on the collection method. There is only one discrepancy in target assignment between the two CTI spectral reconstruction methods; Target 1 is in Class IV for CTI-1D and in the similar Class III for CTI-3D. Comparing the LCTF and CTI results spectra, there are several minor differences in the assigned target classes with four noted consistencies: 1) Targets 1, 2, 3, 5, 10, 19 and 20 were assigned to either Class III or Class IV; 2) Targets assigned to Class II are identical; 3) Targets 4, 12, 16, and 18 are all included in Class I (or Ia); and 4) Targets 7, 11, and 14 are included in Class V for all cases.

Table 6. Targets assigned to member classes based on collection method. The CTI 1D and 3D methods match each other almost identically, with discrepancies between CTI and LCTF.

Member Class	Target Collection Method		
	LCTF	CTI-1D	CTI-3D
I	16,18	4,6,12,15,16,18	4,6,12,15,16,18
Ia	4,12		
II	8,13,17,21	8,13,17,21	8,13,17,21
III	1,2,3	2,9,10	1,2,9,10
IV	5,6,10,19,20	1,3,5,19,20	3,5,19,20
V	7,9,11,14,15	7,11,14	7,11,14

The remaining outliers are Targets 6, 9, and 15. Targets 6 and 9 are the dimmest sources in the scene and therefore may be affected by noise in the measurement. Target 15 is a true anomaly as it is placed in either blue Class I (CTI) or red Class V (LCTF), very dissimilar classes. Figure 45 compares the three spectral intensity plots for Target 15. The CTI-3D data at first seems a better match to the Class V and LCTF data, however examination of the shorter wavelengths in the log plot shows that there is good agreement for $\lambda < 500$ nm. There is a slight peak in data near 500 nm for the LCTF but not enough to associate with Class I. The peak is magnified in the CTI due to the drop in intensity at the shorter wavelengths which is likely driving the Class I association.

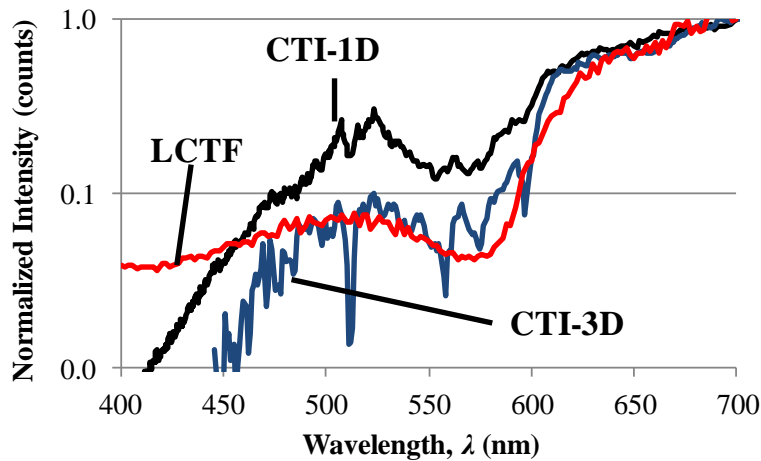


Figure 45. Spectra for Target 15 which is associated with Class V from the LCTF and Class I in both CTI methods.

Collection Requirements

The time to acquire and process the data is very different for the four methods: 1) 2-D wideband imagery, 2) a single CTI projection which is a 1-D spectrograph, 3) the co-added 1-D spectral intensity, and 4) the 3-D hyperspectral data cube. Table 7 compares the collection and processing times of the data for each instrumental method and different processing approaches. A key assumption for both the LCTF and CTI collection times is that data can be collected as fast as the hardware will allow, not given the rate limiting specification. For the CTI this means collecting while continuously rotating the prism, not stopping at each $p(x,y,\theta)$. All of the processing was accomplished using MATLAB code and could certainly be optimized to increase efficiency. It is the relative performance that reflects the acquisition and processing requirements.

Table 7. Collection and processing time necessary to acquire results for the study. The integration time for both the CTI and LCTF is 1 msec/frame.

Product	Broadband Imager		LCTF		CTI	
	Collection Time	Processing Time	Collection Time	Processing Time	Collection Time	Processing Time
2-D Wideband Image	50 μ sec	1 msec	7.55 sec	1-2 sec	1 sec	14 sec
Single 1-D Spectrograph	N/A	N/A	7.55	1-2 sec	6 msec	< 1 sec
1-D Co-Add Spectral	N/A	N/A	N/A	N/A	1 sec	210 sec
3-D Hyperspectral Image Cube	N/A	N/A	7.55 sec	<1 sec	2 sec	~ 1 hr

The CTI is the only instrument which can provide all four data products. The method of collection for the Varispec LCTF does not require co-addition of different projections to eliminate effects of spectral entanglement; however co-addition will reduce noise in the data. To produce any of the products, the LCTF requires a full cycle through the band passes. The entire set of data taken with the LCTF was collected in 7.55 s, which provided a set of 151 spectral bins over the range of 400 nm – 720 nm. In comparison the full CTI collection took 2 s to collect data used to generate full HSI datacube of 600 spectral bins over the range of 400 nm – 1000 nm. The LCTF technology would have taken over 30 s to acquire the same data even if it were capable of doing so.

In addition to faster collection time, an advantage of the CTI is the flexibility in the data processing. The 2-D wideband tomographic reconstruction and 1-D spectral co-addition can be done in less than 3 min using projections over $\theta = 0 - 180^\circ$ which are collected at 1 Hz. In addition, the best resolution for CTI is inherent in the collection and specified in the reconstruction whereas in LCTF the higher spectral resolution requires more collection time. While the targets were temporally constant spatially and spectrally, it is still important to note that the major benefit of using CTI is in the time per collection.

Using the optimized method, the collection time was reduced to 1s and the processing time to nearly 3.5 min.

In this experiment, the ultimate limitation of the LCTF is the speed at which the bandpass can be changed and the fixed rotation speed of the prism (0.5 rotation/sec). If the prism could be rotated faster such that the detector integration time of 1 ms integration time, were the limit, an equivalent set of CTI data to that used in this experiment could be taken in about 1 s without incurring a degradation of the spatial resolution of more than 1 pixel in the outer edges of the FOV. Thus, 1 Hz hyperspectral imagery, 2 Hz wideband imagery, 2 Hz co-added spectral data, and 360 Hz slitless spectrographs would be achievable due to the increase in throughput of the CTI over the LCTF. The processing algorithms must be optimized as data analysis takes much longer with CTI compared to the LCTF. Still, it is time of collection that is critical in exploiting high frequency spatial/spectral variations in targets of interest.

Conclusions

The current CTI system was used to collect data on a collection of randomly spaced point-like targets with varying spectral properties which were used to reconstruct wideband 2-D imagery and 3-D hyperspectral data. In both instances, results of analysis of the spatial and spectral properties of the CTI were very comparable to those obtained from traditional collection methods.

The 2-D wideband image reconstructed from the filtered backprojection of the CTI projections at 1° increments was comparable to the undispersed image taken without the prism in the system in terms of background variance and target intensity. The variation

from artifacts in the reconstructed scene increases and degrades quality as the number of projections is reduced. An acceptable representation of the scene is reconstructed with 5° projections. An image can be reconstructed with projections over half a full prism rotation, such that imagery is provided at twice the rate of prism rotation. This demonstrates the CTI's ability to produce imagery from the spectrally dispersed data.

An optimized algorithm was used to retrieve the 1-D spectral information from the point source targets using the 2-D image as *a priori* knowledge the spatial characteristics. Combining the spectral data from each projection via co-addition at different angles allows for full recovery of spectral information even at points in the spectra where there is target overlap. The algorithm provides a 30x decrease processing time over the full 3-D HSI reconstruction.

The HSI data from the full 3-D reconstruction and optimized 1-D methods were used to classify the targets using a k-means classification algorithm. The CTI-3D and CTI-1D methods produced nearly identical results with one target placed in a different but very similar class. The results of the CTI classification were compared to the results of HSI data collected by a LCTF technique. Overall target classes from of the CTI matched those calculated from the LCTF data. Though there were several discrepancies, analysis of the data showed that there was still consistency in the results, with the target intensity and similarity of spectral classes contributing to cross-classification. The CTI spectra for the blue targets did indicate a considerable amount of intensity at longer wavelengths in both the 1-D and 3-D cases.

The key advantage of the CTI is the ability to collect more data at a higher rate than the LCTF which is crucial in exploiting fast transient events. In this experiment, with a

continuous framing camera it would have taken 2 s to collect the CTI data used to reconstruct the 400 spectral bins, with the time to collect limited by the system. The LCTF would have taken 40 s to acquire an equivalent number of bins, with the collection time directly proportional to the number of bins desired.

VI. Hyperspectral Image Reconstruction of an Array of Extended Targets Using Chromotomosynthesis

Preface

The ability of a chromotomosynthetic imaging (CTI) (also referred to as chromotomography) system to accurately represent spatial and spectral characteristics of a spectrally diverse mosaic of extended sources was evaluated in this study. Accuracy is determined by comparing results to those of a liquid crystal tunable filter (LCTF). The reconstructed CTI 2-D image was equivalent to a wideband, undispersed image for images reconstructed using 1° projection separation. The Colsher discrepancy metric degrades from 0.44 for the 1° sampling to 0.72 for a 10° sampling, with 5° sampling still equivalent to the image obtained by integrating the spectral frames of the LCTF. Hyperspectral data cubes are reconstructed with image quality dependent primarily on source intensity, not wavelength. Through nearly the entire range, narrower spectral lineshapes are attained from CTI data with little degradation in results from the 1° , 5° , and 10° sampled projections. The measured spectral locations were in agreement between the CTI and LCTF for most elements in the mosaic. Spectral and spatial artifacts are observed in the CTI hyperspectral imagery particularly for dim objects adjacent to bright and spectrally similar sources. As a scene becomes more continuous with spatially and spectrally similar sources, more complex processing will be necessary to avoid degraded performance.

Introduction

The underlying principle for CTI technology lies in the field of medical physics. The circular tomosynthetic projection technique was presented by Grant [30] in 1972 as an alternative form of tomographic reconstruction of multiple spatial planes into a 3-D data cube. This process has since been implemented in the field of hyperspectral imagery to produce 3-D data cubes with multiple spectral planes [31, 32]. The basic Air Force Institute of Technology (AFIT) design is similar to a rotating prism application described by Mooney, et al [33, 34]. Unlike medical computed tomography (CT), the direction of the projection angles are not perpendicular to the rotation axis of the prism. Therefore an exact reconstruction of the 3-D data set described by the Radon transform cannot be achieved. Quality is further reduced by the limited projection angle. The maximum dispersion in the CTI instrument used here is about 3° , whereas circular tomosynthesis generally uses a minimum angle of $\sim 20^\circ$ [28]. This does not diminish in-plane spatial resolution of the instrument but degrades resolution in the spectral dimension [26-28]. This also reduces the overall contrast and quality of imagery compared to medical CT images due to the presence of out of plane artifacts in each reconstruction plane [26-28, 57, 79, 96].

The CTI system in this study uses a rotating direct vision prism (DVP) to collect 2-D projections of spectral imagery as a function of prism rotation angle, θ [57]. These projections can be mathematically reconstructed to produce both a wideband, undispersed 2-D image of the target and a 3-D hyperspectral image cube. The 2-D image can be produced from a set of projections taken over a 180° rotation, whereas data from a full prism rotation is optimal in reconstructing the 3-D HSI cube. While the 2-D wideband

image can be exactly reconstructed as in medical computed tomography (CT), artifacts and the limited dispersion of the DVP reduce the quality of spectral imagery compared to that of more conventional techniques such as imaging Fourier transform spectrometers and spatial or spectral scanning systems. However, CTI is inexpensive and compatible with existing remote sensing systems, has a framing rate as high as 100 Hz limited only by the camera readout [91], and is versatile in collecting 3-D HSI data, panchromatic imagery and high speed, non-imaged spectra.

This paper investigates the ability of the CTI to collect against a static, visible target with sharp boundaries between regions of narrow spectral bandwidth. A previous study was limited to classification of spectrally diverse point sources within a scene [99]. Extending CTI for studies of land use, geological surveys, vegetation index, and polluted areas depends on the imaging extended sources as addressed in the present study. We compare the quality of panchromatic and hyperspectral imagery obtained from the CTI instrument and a liquid crystal tunable filter LCTF. The influence of the number of spectral projections on image quality and spectral resolution is developed. The variation of spectral lineshape within an extended object, relative radiometric performance, and temporal resolution is characterized.

Instrument and Experiment

CTI Data Collection and Processing

The CTI instrument has been described previously in detail [57, 95]. Briefly, the direct vision prism is rotated about the optical axis as shown in Figure 46. The lenses L_1 and L_2 act as the forward telescope and collimate the incident light. The prism has an

undeviated wavelength of $\lambda_c=548$ nm and the exiting dispersed light is focused by L_3 onto a intensified PI-MAX camera with spectral response primarily from 400 – 800 nm. The 13 μm pitch pixels provide an instantaneous field of view of 0.4 mrad with a 71.6 mrad field stop. With a back lens focal length of 100 mm, the spectral resolution degrades from about 0.7 nm in the blue to 6 nm in the red, as shown in Figure 47. The instrument's throughput increases to more than 80% in the red. Spatial resolution is primarily limited by chromatic aberration [57].

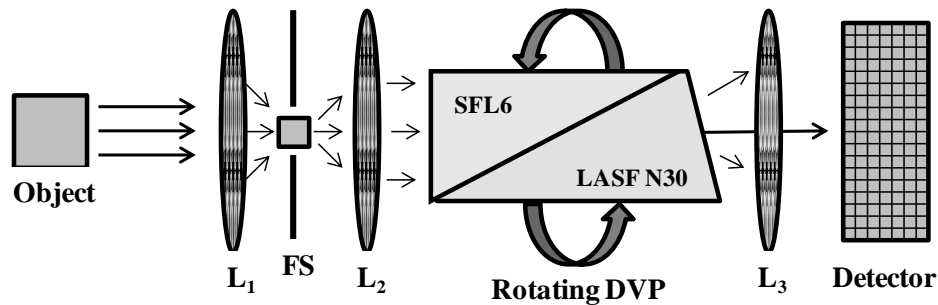


Figure 46. Basic description and components of the AFIT rotating prism CTI instrument. Drawing is not to scale.

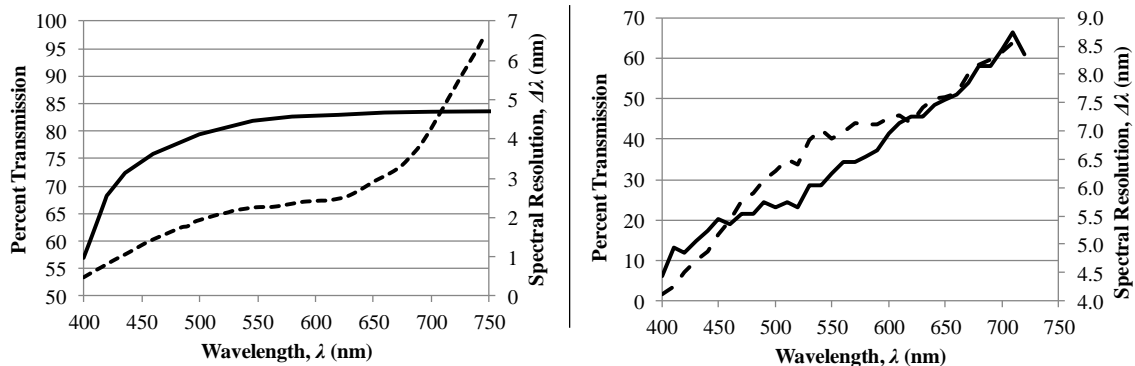


Figure 47. The spectral resolution (dotted lines) and spectral transmission (solid lines) of the CTI (left) and LCTF (right). The LCTF only transmits linear polarized light.

As the DVP rotates about the optical axis, spectrally dispersed images of the object are collected by the detector at discrete rotation angles of $\theta = 0^\circ - 360^\circ$ by framing the detector at some rate as opposed to continuously integrating energy over the period of prism rotation. The latter case is simple tomography, which would only serve to make an image of the object component emitting at λ_c . By taking N discrete projections all object planes can be reconstructed or in the case of CTI all spectral bins can be reconstructed. Each frame of data is referred to as a *projection*, $p(x,y,\theta)$.

A complete set of projections are used to reconstruct the 2-D wideband image using the properties of the radon transform as in medical tomography [64, 66]. The radon projection is accomplished by first projecting each of the 2-D $p(x,y,\theta)$ into a 1-D line projection $s(t,\theta)$. This is done by integrating each $p(x,y,\theta)$ on parallel lines across the plane at angle θ . Because the energy at each point in the hyperspectral data is projected by the CTI along the same angle θ as the radon projection, this is equivalent to the radon projection of the integrated hyperspectral data or the wideband image. Thus the undispersed image can be reconstructed from each $s(t,\theta)$ using a filtered backprojection [64, 66]. Due to symmetry, only the projections from 0° - 180° need to be used with the optimal number of projections needed dependent on the scene thus two images are possible per one prism rotation. The MATLAB filtered backprojection algorithm “iradon” [67], was used to perform the 2-D reconstruction with a Shepp-Logan filter to reduce noise and artifacts [64, 66].

A modified backprojection algorithm similar to a shift-and-add (SAA) technique is used to reconstruct the 2-D $p(x,y,\theta)$ into the 3-D hyperspectral image cube [95]. In this process, each projection is spatially translated (the shift) to properly compensate for the

spectral displacement imparted at particular wavelength, λ_i , by the prism at each prism rotation angle, θ . This ensures that there is complete coincidence in the spatial pattern of the images emitting at λ_i , while any other spectral components at $\lambda_{j \neq i}$, are changing spatial location at every θ . Upon addition over all θ there is more reinforcement of the desired spatial structure and loss of spatial content or smearing of the $\lambda_{j \neq i}$ images, the latter causing spatial artifacts in the spectral bin. Desired spectral bins at a chosen resolution are reconstruction to build the HSI data cube.

An additional spatial filtering was done to limit the amount of artifacts in each spectral bin. A threshold is applied to the $p(x,y,\theta)$ data to set any pixels which are below a certain intensity to 0. The threshold is based on both noise and bias measurements in the $p(x,y,\theta)$ and target intensities from the 2-D image reconstructed in the previous step. Any remaining energy is assumed to be associated with the targets. A second filter is used which assumes that any real energy in a spectral bin will have contributions from all projections used in the reconstruction. Any energy that does not have contribution from all or some chosen number of projections is considered an artifact and set to 0. The threshold and required number of projections are adjustable parameters.

Given a specific application and target set, more complex or optimized reconstruction algorithms may be used to improve the quality of data or increase the efficiency over the simple SAA technique [76-79]. Unlike the 2-D reconstruction, a projection at θ is unequal to that at $\theta+180^\circ$ so that the full set over $0^\circ - 360^\circ$ are used.

LCTF Data Collection and Processing

The DVP was replaced by a Cambridge Research Varispec LCTF [96] in the instrument to collect spectral data for comparison. Data were collected at 2 nm

increments over the 400 – 720 nm range of the filter, with spectral resolution and transmission of the filter provided in Figure 47. Note that light exiting the LCTF is polarized, reducing the transmission compared to the CTI. The 161 samples were collected in about 8 seconds, with time to change the LCTF transmission band about 50 ms. Each image frame is a plane in the hyperspectral data cube. For both the CTI and LCTF, a background was estimated and subtracted from each frame removing bias from scattered light and dim reflections. A threshold of two times the standard deviation in the background noise was applied to all image frames. The detector array exposure was 25 ms for the CTI and 183 ms for the LCTF.

Mosaic Target

A target was designed for this experiment consisting of a 5x5 mosaic of narrow bandpass filters in an opaque frame. Inter 1/2" optical filters were inserted into a 6"x6" aluminum panel with a 5x5 array of 1/2" holes in it separated by 1/8" in the arrangement shown in Figure 48a. The Inter filter peak centers are +/-2 nm of the specified values and have a full-width of about 4 nm at the 50% transmission values. The mosaic is back-lit by a GE 10 W compact fluorescent light bulb, which provided more intensity in the blue wavelengths as compared to an incandescent bulb. A prediction of the spectral intensity of the target is not easily obtained as the bulb does not uniformly illuminate all filters.

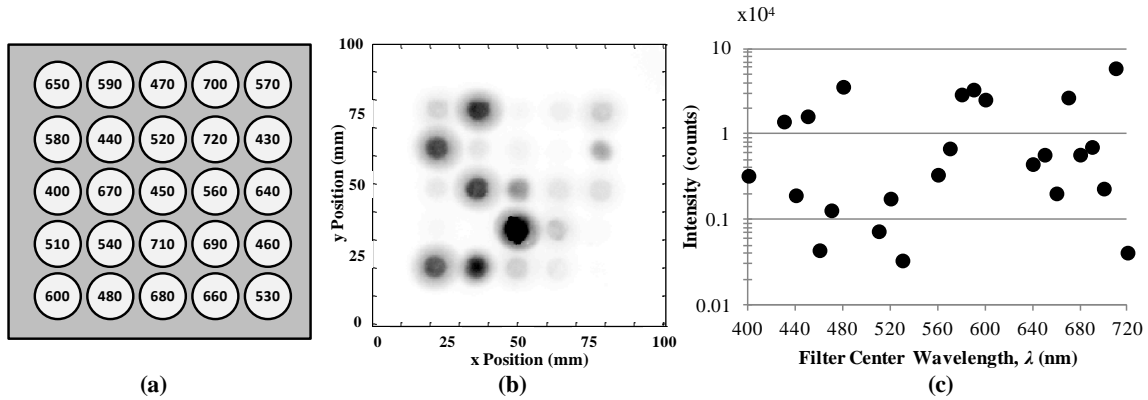


Figure 48. The target mosaic with filter element position and center wavelength in nm is shown in (a). In (b), the image of the target taken with no filter or dispersive element; the negative of the image is presented for clarity. The measured intensities in detector counts of each image in the mosaic from (b) are plotted in (c). The 710 nm element is saturated.

Results

The 2-D Wideband Imagery

The undispersed image, I_0 , provides the baseline spatial and intensity representation of the target accounting for common properties of the CTI and LCTF systems such as detector responsivity, optical transmission, and non-uniform illumination of the mosaic by the light. Shown in Figure 48b is a wideband, undispersed image of the mosaic backlit by the fluorescent bulb captured with the prism removed from the collection system. The relative intensities of the various target regions are provided in Figure 48c. The 710 nm source saturates the 16-bit detector with more than 65,000 counts. The 530 and 540 nm filters are barely observable.

Three 2-D images were reconstructed from the CTI projections using 18, 36, and 180 equally spaced projections over $\theta = 0^\circ - 180^\circ$ and are denoted respectively by I_{18} , I_{36} , and I_{180} . These images are compared to I_0 and to the 2-D image I_{LCTF} created from the LCTF spectral data by adding all of the frames (spectral bins). Each frame is corrected for the

response of the LCTF prior to the summation. Each of the 2-D images is shown in Figure 49, including an optical model of the target, I_m . The intensities in each case have been normalized to the maximum value in the target. The relative brightness of each filter in the mosaic is consistent across all images the increase in artifacts is evident as fewer number of projections are used in I_0 , I_{18} , I_{36} , and I_{180} .

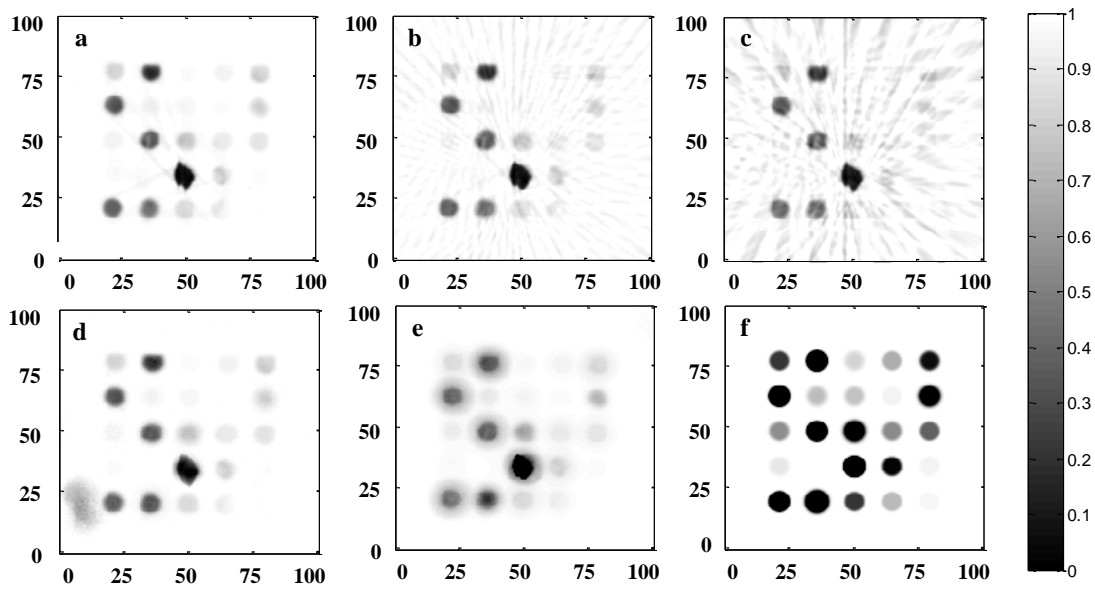


Figure 49. The results for the 2-D wideband image of the mosaic. In (a)-(c), the image is reconstructed from the CTI data using 180, 36, and 18 projections. Artifacts in the scene become more apparent as fewer projections are used. The image from integrating LCTF frames is shown in (d). The undispersed image and a model derived image are provided in (e) and (f) for reference. The x-positions and y-positions are shown in mm and the normalized inverse of the intensity is used.

To examine the accuracy of the CTI reconstruction technique, the relative intensities from each filter were compared with the undispersed intensities, I_0 . The average intensity of the filters in each image was measured by averaging the pixel intensities in a 4x4 area at the center of each filter image. The intensities are then normalized to the intensity of

the 670 nm filter to ensure operation in the linear portion of the ICCD detector's response. A linear fit to each set of data produces a slope of near one and near zero y-intercept, as given in Table 8. All of the results scale linearly with source intensity with minimal off-set. The CTI technique produces more scatter and a fit slope uncertainty of less than 13%. The fit correlation coefficient increases with the number of observed projections (angles). The LCTF instrument is somewhat less noisy with slope uncertainty of about 8%.

Table 8. Linear response for CTI and LCTF broadband imagery.

Images	Slope	Intercept (Normalized Counts)	r^2
I_{180} vs. I_0	1.007 +/- 0.111	-0.023 +/- 0.055	0.941
I_{36} vs. I_0	0.980 +/- 0.127	-0.017 +/- 0.059	0.929
I_{18} vs. I_0	0.984 +/- 0.127	-0.020 +/- 0.062	0.921
I_{LCTF} vs. I_0	1.023 +/- 0.077	-0.029 +/- 0.038	0.970

The relative quality of the spatial imagery is compared using the Colsher discrepancy metric [100], $\delta(q)$. This measures how well an estimated image $D(x,y)$ compares to a reference image $T(x,y)$. The metric is defined as

$$\delta(q) = \sqrt{\frac{\sum_x \sum_y (D(x,y) - T(x,y))^2}{\sum_x \sum_y (T(x,y) - \bar{T})^2}} \quad (46)$$

with \bar{T} the mean value of all elements in $T(x,y)$. This relative measure of similarity has been used in other previous imaging studies [69] with normal values in the range of 0.3 – 0.9 and a $\delta(q) < 1$ considered acceptable for image reproduction.

The Colsher discrepancy metric, $\delta(q)$, was calculated using Equation (46) for each of the $D(x,y)$ and $T(x,y)$ pairs in Table 9. Using I_0 as the standard image, both I_{180} and I_{36} are a better match than I_{LCTF} . I_{180} is a better match to I_0 than is I_{LCTF} . As the number of projections is reduced to 18, $\delta(q)$ is much higher indicating degraded performance. The loss of quality with 18 projections is also evident by comparing both I_{36} and I_{18} to I_{180} .

Table 9. Comparison of broadband images using Colsher values, average percentage difference, and standard deviations.

$D(x,y)$	$T(x,y)$	$\delta(q)$	P_d	$STDev$
I_{LCTF}	I_0	0.591	0.729	0.399
I_{180}	I_0	0.438	0.676	0.713
I_{36}	I_0	0.497	0.806	0.401
I_{18}	I_0	0.722	1.324	1.004
I_{36}	I_{180}	0.342	0.767	0.266
I_{18}	I_{180}	0.800	1.670	0.857
I_{180}	I_{LCTF}	0.523	0.656	0.215

To illustrate the differences between images in more absolute terms and provide some reference for the $\delta(q)$ metric, percent difference images P_d are created and shown in Figure 50. The P_d of $I_{180}-I_0$ and $I_{LCTF}-I_0$ appear very similar, with a light blur noticeable in the edges of the $I_{LCTF}-I_0$ image causing the higher $\delta(q)$ value between the two. The characteristic artifacts of the backprojection algorithm become more evident in the two images at the bottom of Figure 50 as the number of projections is reduced. The average P_d for each of the images compared are shown in Table 9 and reflect the changes in the relative metric $\delta(q)$. The standard deviation, σ , is also calculated for each of the P_d images. All of the statistics demonstrate that the CTI reconstruction with either 180 or 36

projections is an acceptable representation of the undispersed image and as good as or better than the image produced by integrating the spectral bins from the LCTF.

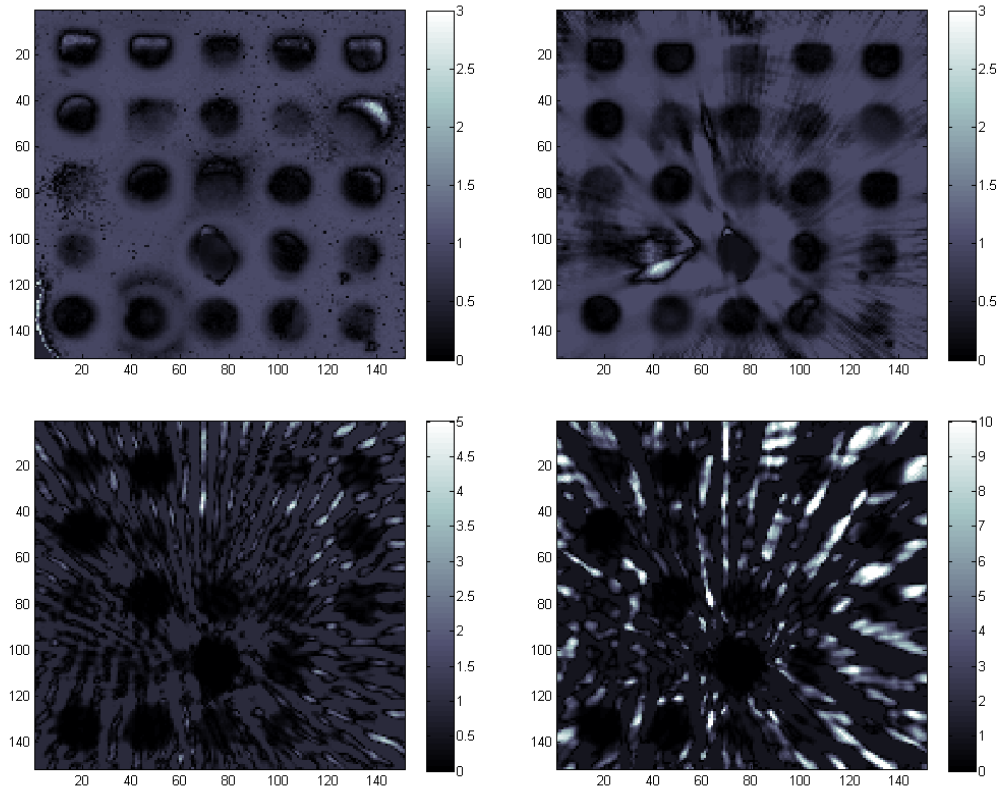


Figure 50. The percent difference images between I_{LCTF} and I_0 (top left), I_{180} and I_0 (top right), I_{36} and I_0 (bottom left), and I_{18} and I_0 (bottom right). The scaling is in units of percent difference.

Hyperspectral Imagery

A hyperspectral image cube was created from the data collected using the LCTF images, denoted by H_{LCTF} . The CTI data were reconstructed using three densities of projections at 1° , 5° and 10° angular separation to yield three HSI cubes: H_{360} , H_{72} , and H_{36} . In each case the CTI data is reconstructed from $\lambda=400 - 500$ nm at a bin resolution of 0.25 nm and 0.5 nm for $\lambda=500 - 720$ nm using the process described in the prior

section. Spectral intensities were extracted from each data cube by taking the average of the four center pixels that correspond to the spatial center of the image of each of the 25 filter elements in every spectral bin. The resulting sets of data were fit to a Gaussian function to estimate the peak intensity value, the center wavelength, and the full-width at half maximum (FWHM) of each line shape. Because of the differences in collection methodologies, normalized intensities were used in comparisons to minimize error from the lack of absolute radiometric calibration.

The spectral registration accuracy of the LCTF data and CTI reconstructions was evaluated by comparing the center of the lineshape functions to the filter manufacturer's reported center wavelength. Measurement error is estimated from the system specifications for the LCTF, and from the prism dispersion calibration for the CTI. This residual, $\Delta\lambda$, between the centers of the measured line shapes and the center wavelength of the bandpass filters are plotted in Figure 51. A ± 2 nm region of filter center wavelength uncertainty based on manufacturer reported tolerance is indicated. The spectral centers for the H_{360} , H_{72} , and H_{36} sets are nearly identical at all λ . The poor registration of the 720 nm filter can be attributed to saturation for the target. Seventeen of the remaining 24 CTI center wavelengths are within the ± 2 nm region of the correct filter center wavelength with measurement error included. Of the seven which are not, only the 520 nm and 660 nm filters are inconsistent with LCTF peak locations. Filters at 460 nm and 540 nm were too dim to provide accurate measurements.

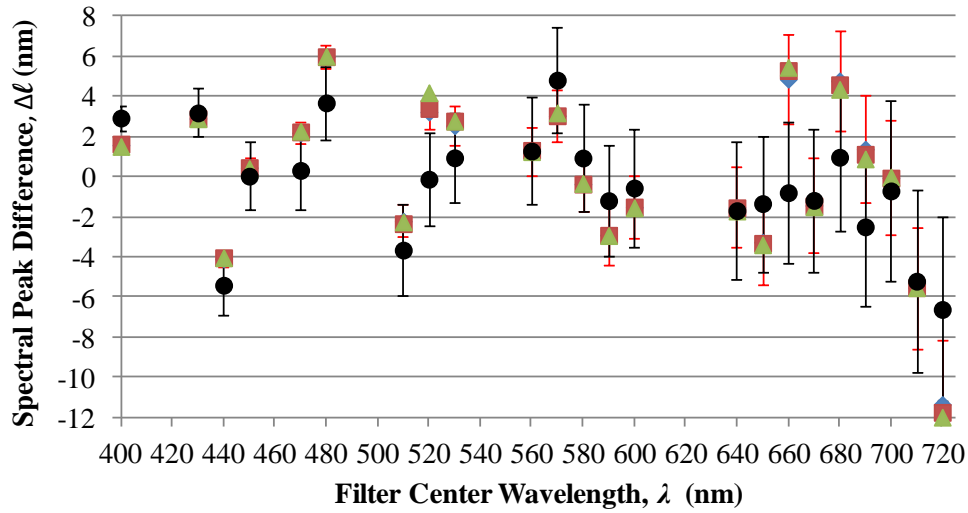


Figure 51. The residuals between the measured centers of the CTI and LCTF spectral peaks and the nominal centers of the bandpass filters with the bias in the CTI data removed. “◆” = 360 projections, “■” = 72 projections, and “▲” = 36 projections.

Spectral line width for each filter element, $\Delta\lambda$, is defined here as the FWHM of the Gaussian function fit to each spectral peak. This is not the instrument resolution, as there is no correction for bandpass filter spectral width and the width of the peak is a function of the spatial size of the image for the CTI. The $\Delta\lambda$ calculated for each element in H_{36} , H_{72} , and H_{360} were nearly identical as seen in Figure 52, with the 660 nm and 720 nm elements having slightly narrower widths in H_{360} . At all $\lambda < 670$ nm, the CTI showed smaller $\Delta\lambda$ than the LCTF and is a good fit to the expected CTI spectral resolution taking into account the spatial extent of the target elements, manufacturers specifications for spectral width of the filters, spatial resolution of the system optics, and prism dispersion using documented methods [57]. For both the CTI and LCTF, the 460 nm and 540 nm elements were too dim to get an accurate measurement of the Gaussian function. The 710 nm element was saturated in the LCTF data and an accurate width could not be measured.

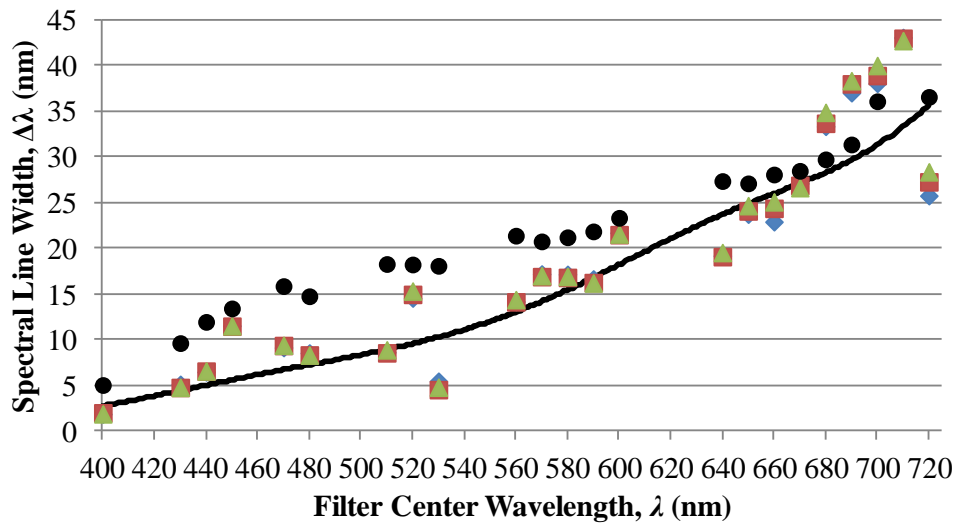


Figure 52. Measured spectral resolution of the CTI and the LCTF. The spectral resolution of the CTI closely matches the predicted performance and is marginally better than the LCTF. “♦” = 360 projections, “■” = 72 projections, and “▲” = 36 projections.

To determine how well the CTI captures the spatial information in the reconstructed HSI cubes, the Colsher metric $\delta(q)$ is used to calculate the discrepancy between the H_{360} , H_{72} , and H_{36} data and the reference H_{LCTF} for the plane of peak emission for each given filter in the target set. This is not the plane corresponding to the filter center so that error in spectral registration is not a factor. The results are plotted in Figure 53.

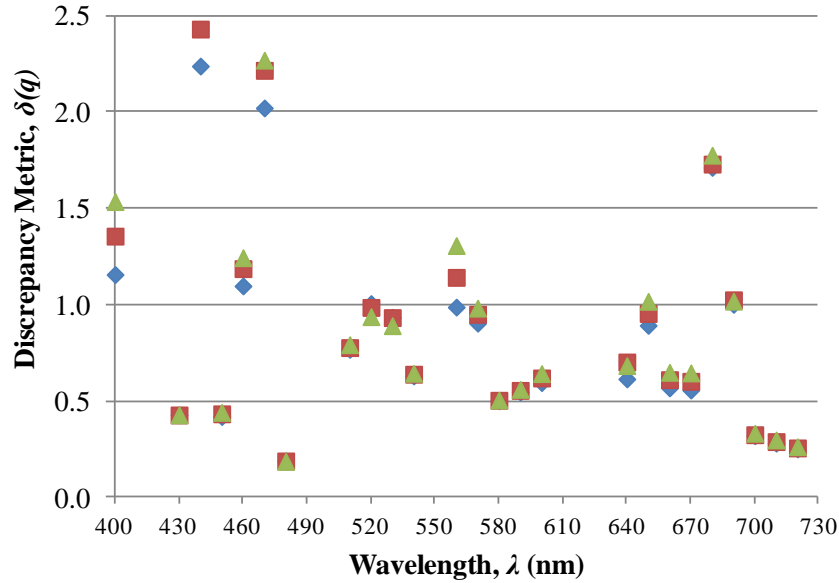


Figure 53. The discrepancy metric, $\delta(q)$, for each of the filter elements as a function of the number of projections used in the reconstruction. “ \blacklozenge ” = 360 projections, “ \blacksquare ” = 72 projections, and “ \blacktriangle ” = 36 projections.

For most of the filters the $\delta(q)$ is nearly identical between the H_{360} , H_{72} , and H_{36} data. The 400 nm and 560 nm filters are the only instances with a noticeable reduction in $\delta(q)$ with increase in projections used, primarily due to spatial artifacts in the data (see artifact discussion below). In the 520 nm and 530 nm filters there appears to be a slightly lower $\delta(q)$ when using fewer projections. In six of the filters the $\delta(q)$ is above 1, most notably the 440 nm, 460 nm and 680 nm filters. Because these are among the dimmest objects in the mosaic, it is likely that $\delta(q)$ is being driven higher by energy from out of bin filters or noise/bias. Plotting the $\delta(q)$ vs. object intensity in Figure 54, it is evident that these worse cases are in the dimmest region, as are the filters where the H_{360} , H_{72} , and H_{36} showed distinctive $\delta(q)$ and the instances where the reconstruction of the data using fewer projects appeared to show better results.

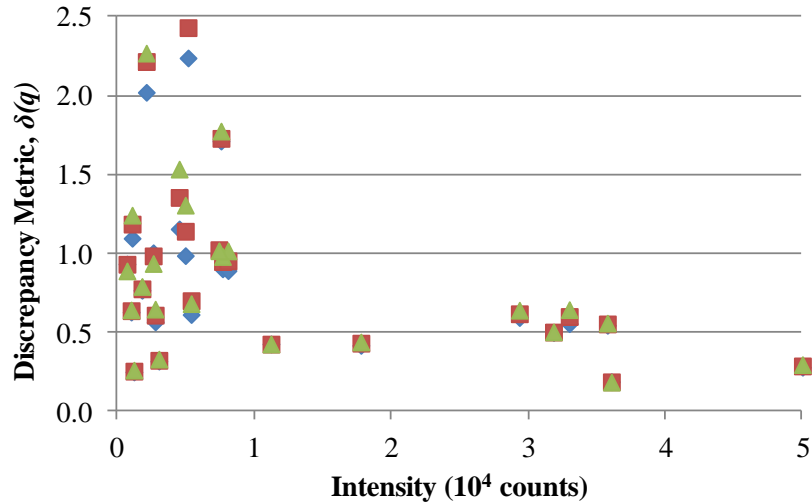


Figure 54. The $\delta(q)$ plotted from the dimmest elements to the brightest. The worst fits are for intensities $<1 \times 10^4$ counts, as are the cases with noticeable differences in the number of projections used. “◆” = 360 projections, “■” = 72 projections, and “▲” = 36 projections.

There are several dim targets with $\delta(q) < 1$ suggesting that target intensity alone does not lead to worse results. Referring to Figure 48c, the 440 nm, 470 nm, 680 nm and 690 nm all have a bright spectral (not necessarily spatial) neighbor; 450 nm for 440 nm, 480 nm for 470 nm, and 670 nm for both the 680 nm and 690 nm elements. In these cases, the higher $\delta(q)$ in the spectral bin is dependent upon the difference in intensity observed for the spectrally *adjacent* filters. As an example, Figure 55 shows the percent difference between the CTI and LCTF for spectral bin at 440 nm. The majority of variation in the scene is due to the bright 430 nm filter which is over 30% brighter in the LCTF than in the CTI.

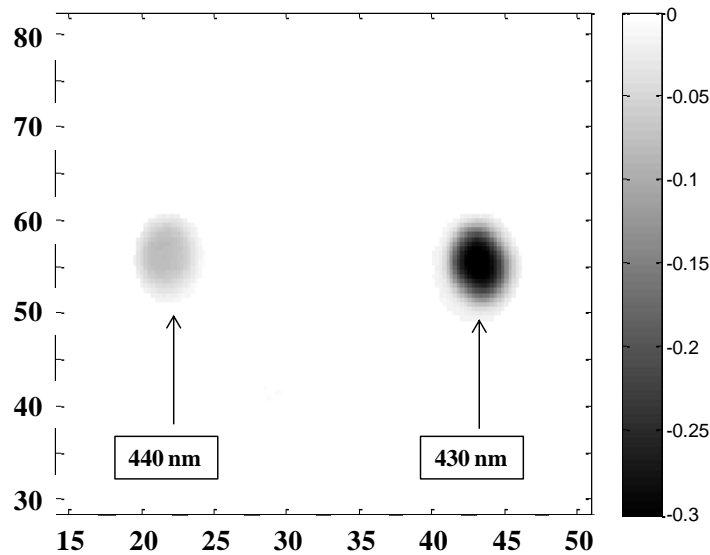


Figure 55. The percent difference image between the LCTF and CTI at the 440 nm spectral bin. The leakage of the 430 nm filter into the bin is driving the discrepancy between the two data sets. The image scale is in mm in the object plane. The x- and y-axes are in pixel space, 13 $\mu\text{m}/\text{pixel}$.

Artifacts in CTI Reconstruction

The effects of artifacts were apparent in the 2-D reconstruction as image quality degraded when the number of projections used was decreased. The HSI results demonstrate that the spectral location, image bandwidth and spatial bin reconstruction are mostly independent of number of projections used. This is not consistently the case and spatial artifacts in the data which are not accurately captured by the metrics or measurement process are observable in the data.

Spectral widths $\Delta\lambda$ in Figure 52 were measured for spectral intensities at the center of the filter element images. In Figure 56, the spectral line shape is shown as a function of the radial distances r_0 (center) to r_6 (12 pixels) from the center of the 600 nm filter. The LCTF lines shapes maintain their intensity and shape to 8 pixels from the center and then proceed to become less intense for distances of 10 and 12 pixels. The CTI, however,

begins to lower in intensity at 4 pixels from the center, and also changes shape at 10 pixels. This is due to the non-uniform intensity profile of the filter image. Because the filter image is brighter in the middle and falls off at the edges, the spectral intensity at the edges becomes larger in adjacent spectral bins when the brighter center energy is displaced from its undispersed location at the center into toward the image edge [57].

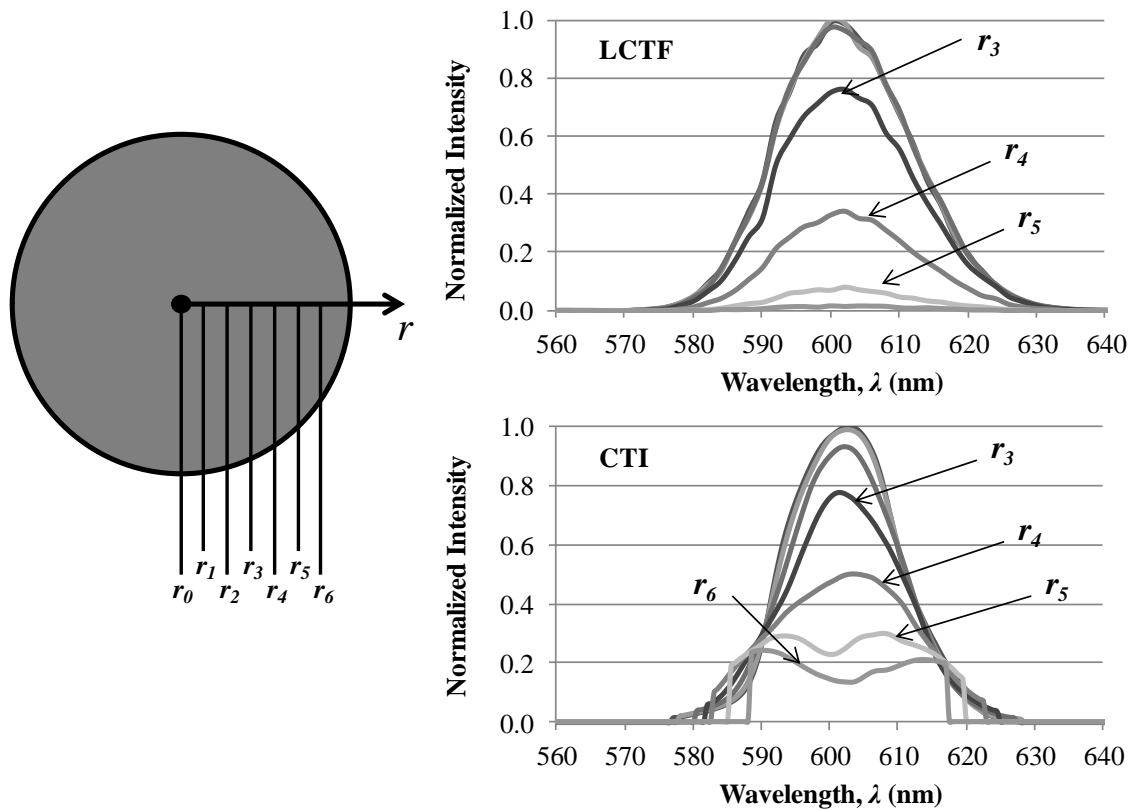


Figure 56. The spectral intensities are plotted for points in increasing distance from the center of the filter image as shown on the left. In both plots, the intensity decreases as r_n increases. The lineshape of the 600 nm filter in the CTI data becomes deformed as the spatial distance is increased. The LCTF lineshapes keep their Gaussian shape as the r increases, though intensity is decreasing.

Out of plane artifacts in the spectral bins are defined as energy that appears in the bin where none is expected in either the spatial or spectral location. These were not observed in previous studies which examined point sources [99] and the processing method chosen

in this study eliminates many of these artifacts, however some are still evident. Figure 57 shows the spectral intensity plot for the 650 nm filter. The LCTF spectral intensity is shown as the solid line, with the H_{360} , H_{72} and H_{36} plotted as points. A major portion of the peak centered at 650 nm is Gaussian with acceptable spectral width and centering. However, the intensity rises and peaks near 620 nm before cutting off in the CTI spectra, more prominent with fewer projections. Figure 58 shows the spectral bins at $\lambda = 620$ for the four collections with the spatial location of the 680 nm filter indicated by a circle. The intensity appearing from artifacts in the area of the 680 nm filter falsely increase the measured intensity of the filter element. Another prominent spectral artifact exists near 560 nm which becomes greatly reduced with number of projections used. The impact is not only spectrally significant, but also spatially as evident in the $\delta(q)$ in Figure 53 where there is a clear dependence on number of projections used for the 560 nm filter. This is less of a factor in the 660 nm bin where the $\delta(q)$ degrade from 0.695 to 0.835 to 0.958 for H_{360} , H_{72} and H_{36} , respectively.

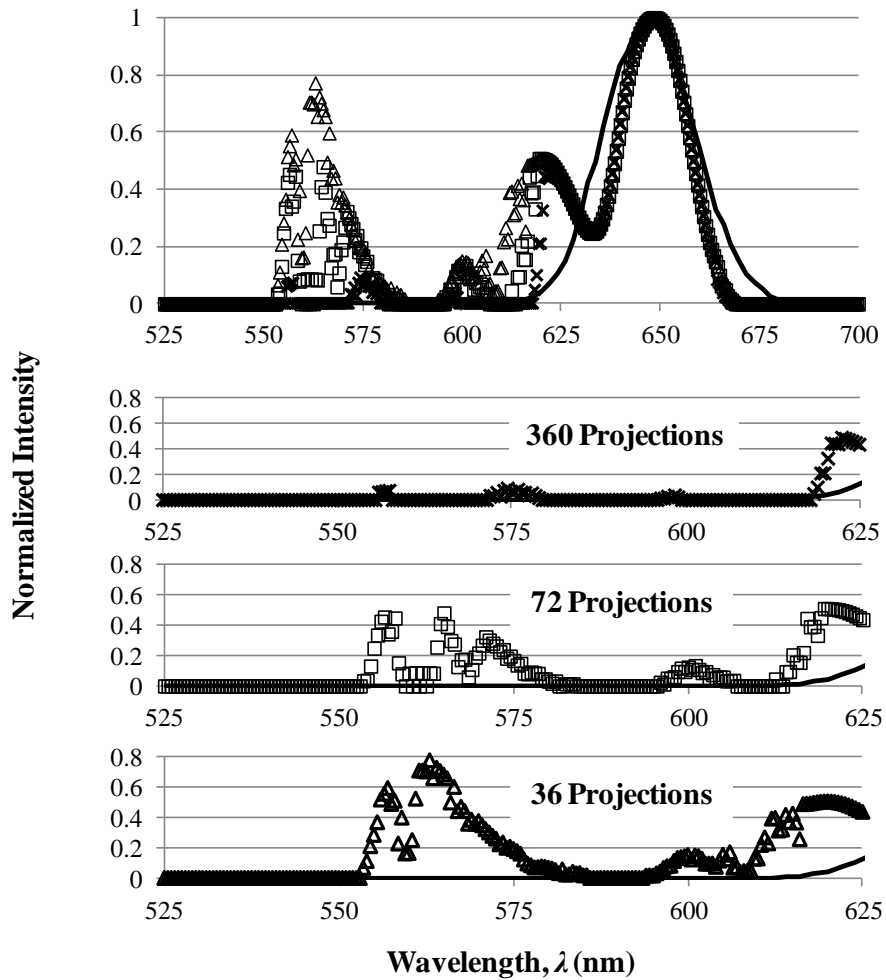


Figure 57. Artifacts cause deformation of the 650 nm peak in the CTI data and secondary peaks when compared to the LCTF (solid line). The artifacts become worse as fewer projections are used. Reconstructions using 360 projections (“X”), 72 projections (“□”) and 36 projections (“Δ”) are plotted. The CTI lineshape is narrower despite the false secondary peak at 620 nm.

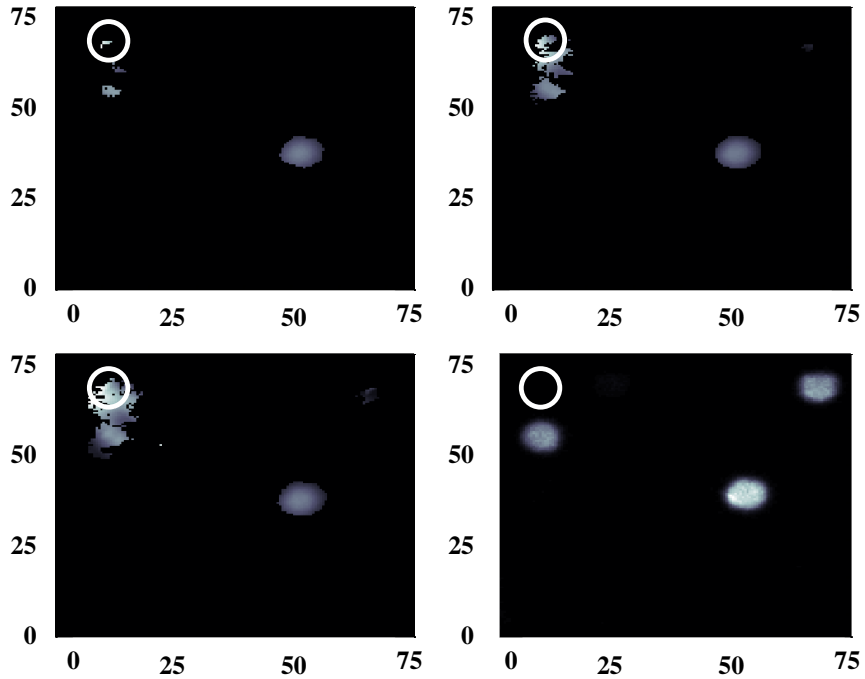


Figure 58. The 620 nm bin images are shown for reconstruction with 360 (top left), 72 (top right), and 36 (bottom left) projections. The circle indicates the spatial location of the 650 nm filter. The artifact energy causes the false peak at 620 nm. The 620 nm bin from the LCTF is shown on the bottom right with no energy near the 650 nm filter. Scale for each image is mm in the object plane.

Conclusions

The CTI has the ability to provide acceptable wideband and hyperspectral imagery at high data rates which could exceed 100 Hz. The design can be integrated into any simple telescope system. The amount of data collected allows for flexibility in analysis and reconstruction methods which leads to optimal use for specific target sets without change to collection hardware or configurations. The projection data from the CTI can be used to create a 2-D image that is comparable to imagery taken by the system with no prism in place, a unique capability for a dispersive element system. When using projections at 1° sampling, the Colsher metric is 0.438 with an average percent difference of 0.676, when compared to the undispersed image taken with the prism removed from the system.

Projections at a 5° sampling were comparable to the 1° reconstructions and have a better Colsher metric and percent difference than the summed LCTF spectral bins. The 10° reconstruction provided an acceptable image, but with noticeable degradation. The usual artifacts are present as a result of the filtered backprojection and could be removed with further processing. The intensities for all CTI and LCTF images varied linearly with intensity in the undispersed images with the CTI 1° reconstruction having the best fit.

The spectral peak centers measured in the CTI hyperspectral data matched those found for the LCTF for 22 of the 24 unsaturated filter elements when estimated error is considered. This was true for elements where both measured band centers were out of the manufacturers specifications for the filters. The measured spectral bandwidths of the filters were in good agreement with that predicted from the model, and expectedly better than the LCTF for wavelengths less than 680 nm. Neither spectral peak location nor bandwidth was affected by the number of projections used. The spatial representation in the HSI matched the LCTF fairly well as demonstrated by the Colsher metric. In 3 of 5 cases (400 nm, 440 nm, and 470 nm) where the $\delta(q)$ was considered large (>1), it is due spatial artifacts from the presence of dim filters near those which were bright and spectrally adjacent (the 580 nm and 590 nm filters). The same effect from these filters is apparent in the 560 nm bin. Aside from these cases, $\delta(q)$ was largely unaffected by number of projections. Artifacts near the two brighter 580 nm and 590 filters not only reduced spatial quality but also affect spectral performance. Energy from these filters appeared in the location of the 650 nm filter in bins from 550 nm – 575 nm and from 615 nm to 630 nm causing false spectral peaks. These were greatly reduced with the number of projections used, though not completely eliminated. Similar spatial artifacts and

spectral distortion are observed near the 680 nm and 690 filters but are much less noticeable as these filters are less intense.

These results indicate that for this target set the CTI can provide hyperspectral data reasonably equivalent to that of a conventional filter system. The performance of the CTI is degraded due to artifacts which become much more prevalent as a scene evolves from isolated point sources to more continuous spatial energy. Furthermore, artifacts are most apparent for cases where energy is spectrally similar and spatially near, indicating that the more homogenous and continuous the scene is the more difficult it will be for the CTI to discriminate spectrally without more complex processing and human analysis.

VII. Hyperspectral Analysis of a Propane Flame Using Chromotomosynthesis

Preface

The spectral and spatial performance of a chromotomosynthetic imager (CTI) when observing the extended flame from a propane torch is compared to sequential band imaging using a Liquid Crystal Tunable Filter (LCTF). Visible spectra of the optically thin flame in the range of 400 – 800 nm clearly indentifies the C₂ Swan ($A^3\Pi_g \rightarrow X^3\Pi_u$) bands, a CH band in the blue, and blackbody emission from a flame spreader. The spectral resolution of the CTI of 1 – 7 nm provided significantly improved spectra compared with the LCTF imager. The CTI 2-D reconstruction is comparable to a wideband image and a spectrally integrated image from the LCTF data. However, artifacts from the small, bright portion of the flame negatively affect the CTI 3-D spatial structure and intensity in the dimmer regions of the torch. Spectral artifacts in the reconstruction were more prevalent in the case with a large metal spreader on the torch. Extraction of temperature from blackbody emission requires the 2-D wideband imagery and estimation of source properties using a iterative system model. Neither the CTI nor LCTF instruments provide adequate radiometric data to extract vibrational population distributions from the C₂ Swan bands. While the CTI instrument offers significant advantages for analyzing the spectra of extended, transient combustion events, the radiometric integrity through the transform and highly resolved spatial and spectral are compromised by artifacts using simple reconstruction methods.

Introduction

Hyperspectral data collected on combustion or other exhaust sources such as gas and oil flares, rocket plumes, and smokestack plumes provide information which can determine temperature and fuel type or at least confirm/deny the presence of certain chemical or molecular constituents [23, 24]. The spatial distribution of the spectral properties of the plume provides further insight into the extinction rate of the constituents in the plume, temperature profiles, and information on chemical processes. Capturing the variations of these spectral and spatial features temporally allows a remote sensing analyst to further characterize the source. Attaining a complete set of this information with acceptable quality can be challenging as most remote sensing instruments are designed to optimize the collection in one or possibly two of the spectral, spatial, or temporal domains. Hyperspectral CTI data has the potential to provide satisfactory spectral information with good spatial resolution at high temporal resolution (>100 Hz) [41, 56]. Specific features of CTI which make it a viable alternative to traditional approaches include: (1) the components and construction of CTI make it inexpensive and compatible with existing remote sensing systems designed for imaging, (2) in addition to the 3-D HSI data, the projections over a range of $0^\circ - 180^\circ$ allow for a complete 2-D reconstruction of the wideband (panchromatic) image, and (3) each CTI projection (frame) represents a 2-D spectrograph of all targets in the field of view simultaneously. These features combined with very fast data collection make the CTI attractive to characterizing events occurring in a battlespace such as artillery fire, detonations and explosions, and fast burning missiles having spectral and spatial phenomenology occurring on the order of 10 Hz [1-11].

The CTI concept using a two component, direct vision prism was introduced in 1995 by Mooney et al [33, 34]. CTI systems operating in the visible-near IR (VNIR) and mid-IR have explored stationary scenes, or slow moving motor vehicles [43-44] with analysis of some combustion events but only as point sources [42, 49]. A non-rotating double Amici prism with coded aperture and bandpass filter system has developed for flame imagery at 30 Hz [91]. A field deployable, ground based prototype CTI system has demonstrated the ability to monitor the potassium and sodium line emission from transient combustion events [41, 56]. A space based chromotomographic experiment (CTEx) is currently in development [58-60].

We recently developed a CTI system that uses a rotating direct vision prism (DVP) to collect 2-D projections of spectral imagery as a function of prism rotation angle, θ [57]. These projections can be mathematically reconstructed to produce both a wideband, undispersed 2-D image of the target and a 3-D hyperspectral image cube [99]. For this experiment, a propane torch was used to represent a combustion plume and examine the CTI instrument's ability to characterize the spectral and spatial properties. The quality of the CTI imagery is compared to those obtained from a liquid crystal tunable filter (LCTF). Both molecular emission from the optically thin plume and broader spectral features from a hot flame spreader are examined to evaluate spectral artifacts.

Instrumentation

A basic schematic of the AFIT CTI system is displayed in Figure 59 and has been described previously [57, 95]. The detector is a PI-MAX Gen II intensified RB fast-gate 1024x1024 array with responsivity primarily in the 400 – 850 nm region. There is

chromatic aberration observed with this system which limits overall spatial and spectral resolution. The spectral resolution ranges from 1 - 10 nm with the DVP dispersion poorest at the longest wavelengths [57]. The distance between L_3 and the detector is used as an adjustable focus and is currently chosen so that best focus is achieved at 635 nm to optimize the spectral resolution in the red. The full field of view is 71.6 mrad and provides an angular resolution of 0.8–1.6 μ rad.

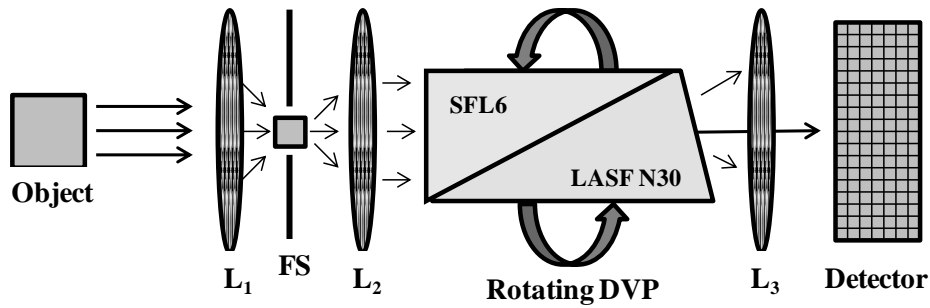


Figure 59. Components of the AFIT rotating prism CTI instrument.

The spectral response of the system with the prism in place is provided in the top plot in Figure 60. The system response, $R_{CTI}(\lambda)$, was estimated by both calculation and measurement. The initial estimation was made by combining the manufacturer's documented response function for the PI-MAX detector array, the calculated spectral transmission of the DVP using glass properties and the Fresnel Equations, and from the achromatic lens specifications. The $R_{CTI}(\lambda)$ was also estimated by measuring the spectral intensity from two data sets from a blackbody source emitting at 1000° C and then at 1200° C. The calculated spectral response from the measurements is:

$$R_m(\lambda) = \frac{I_m(\lambda, T = 1200^\circ\text{C}) - I_m(\lambda, T = 1000^\circ\text{C})}{I_{BB}(\lambda, T = 1200^\circ\text{C}) - I_{BB}(\lambda, T = 1000^\circ\text{C})} \quad (47)$$

where $I_m(\lambda, T)$ is the measured intensity from the blackbody source and $I_{BB}(\lambda, T)$ is the calculated Planckian spectral intensity. These temperatures did not provide adequate intensity at wavelengths less than 500 nm and there is little variation in the blackbody intensities at these temperatures. Therefore the component estimate was relied upon for $\lambda < 500$ nm. There was overall agreement at longer wavelengths, and minor adjustments were made to the spectral curve calculated from the component data to provide the final curve for $R_{CTI}(\lambda)$ at the top of Figure 60.

As the DVP rotates about the optical axis, spectrally dispersed images of the object are collected by the detector at discrete rotation angles of $\theta = 0^\circ - 360^\circ$ by framing the detector at some rate as opposed to continuously integrating energy over the period of prism rotation. The latter case is simple tomography, which would result in recording an image of the λ_c spectral component object.

In medical tomosynthesis, by taking N discrete frames, all object planes can be reconstructed, or in the case of CTI all spectral bins. Each frame of data is referred to as a *projection*, $p(x, y, \theta)$. Figure 61 illustrates the projection process and collection geometry with an example object that has some spatial/spectral components given by the co-located letters “R” (spectrally red), “G” (spectrally green), and “B” (spectrally blue). The spatial x - y coordinate system is referenced to the detector array with the origin coincident with optic axis at the center pixel of the array. We define $\theta = 0^\circ$ at the position where the prism’s dispersive axis is parallel to the x -axis and λ increasing in the $+x$ direction. In Figure 61 “G” is emitting at exactly at the undispersed wavelength, λ_c so the image is stationary, whereas the images of “B” and “R” are dispersed some distance r_B and r_R . Summing all projections would exactly reconstruct the “G” spectral bin.

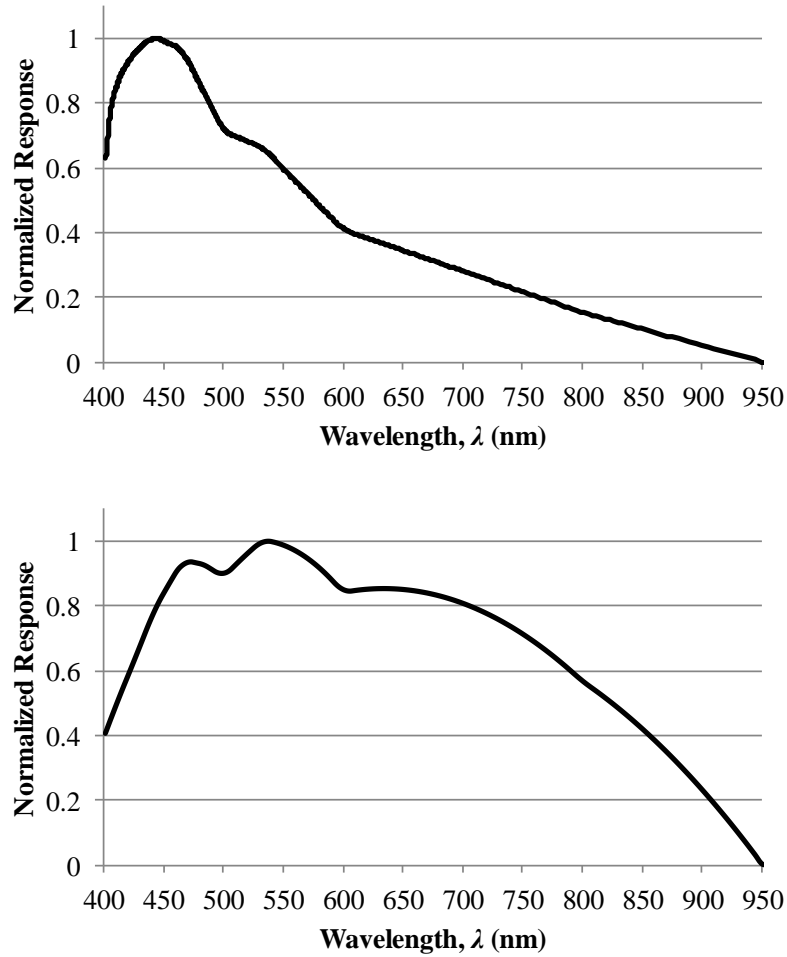


Figure 60. The spectral response of the CTI system with: (a) the DVP in place and (b) replacing the DVP with the LCTF. The LCTF has much less transmission at shorter wavelengths.

Energy from the neighboring “R” and “B” though blurred will also be contained in the bin making absolute intensity measurements difficult without more advanced artifact removal processing. The larger the neighboring energies are either spectrally, spatially, or in intensity, the greater the impact of artifacts in a particular bin.

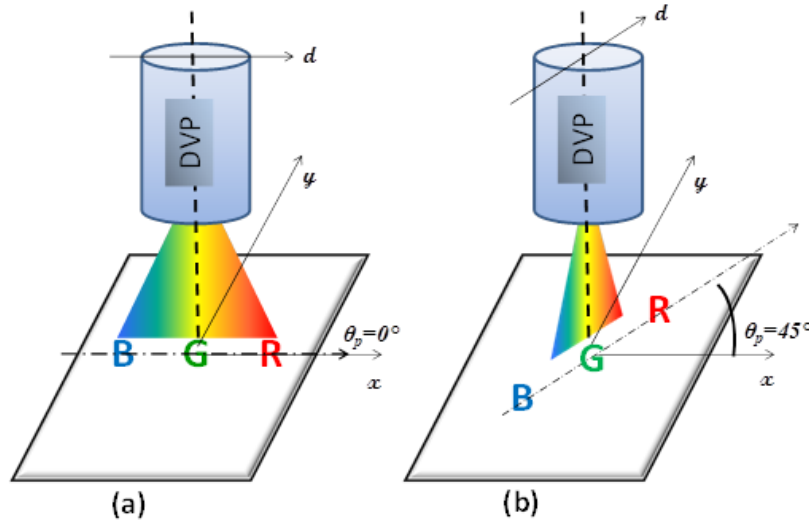


Figure 61. The CTI projection system geometry as the DVP rotates from $\theta=0^\circ$ to $\theta=45^\circ$. The data sample in (a) represents $p(x,y,0^\circ)$ and (b) $p(x,y,45^\circ)$.

Data was collected using the CTI with a θ resolution of 5° for a total of 72 sampled projections per rotation. The instrument's field of view is such that the entire emitting area is imaged with each pixel in the detector corresponding to about 0.5 mm in the object plane. A 300 ms detector integration time was used with a gain setting of 0 and no intensification of the array to prevent saturation in any one projection. The data was reconstructed at a spectral sampling of 0.5 nm from 400 – 550 nm, and 1 nm from 550 – 1000 nm. A modified backprojection algorithm was used to do the reconstruction with the estimated system $r(\varphi,\lambda)$ based on system calibration done prior to the experiment. In addition to reconstruction of the 3-D hyperspectral data cube, a 2-D wideband intensity map was also created by performing a filtered backprojection (FBP) of the $p(x,y,\theta)$ using a Shepp-Logan filter [66,67]. Any contribution of the atmosphere in terms of emission or attenuation is negligible, as is self emission from the instrument.

Hyperspectral imagery was also accomplished by removing the DVP from the CTI instrument and replacing it with the Varispec LCTF manufactured by Cambridge Research Instrumentation [96]. In doing this, all properties of the collection system and target were identical except for the method of spectral collection (dispersion vs. filter). The LCTF is cycled through bands collecting one image at a time for a specific center wavelength. Unlike the CTI, each frame of data collected by the LCTF only contains a narrow sample of the spectral energy, greatly reducing throughput. The range of the LCTF responsivity is limited to 400 – 725 nm, less than that of the detection array. The filter spectral bandwidth increases almost linearly from 4.5 nm at 400 nm to 8.5 nm at 725 nm. The spectral response of the LCTF system is shown at the bottom of Figure 60. This response function, $R_{LCTF}(\lambda)$, was estimated by dividing the spectral response of the prism from $R_{CTI}(\lambda)$ and multiplying by the manufacturer's documented spectral response for the system [96], as all other system components are the same. LCTF spectral images were taken every 5 nm over the range of the device, with 50 ms needed to change the filter settings. The PiMax camera settings are the same as those used in the CTI.

A standard propane torch consisting of a variable flow nozzle on a 14.1 oz fuel cylinder was used as the target to investigate the ability of the CTI to provide exploitable hyperspectral imagery on a combustion source. The flame was imaged in a dark laboratory setting to reduce the effects of stray light and scattering. Two target configurations were used: (1) a torch flame in the instrument field of view and (2) with a brass spreader attached to the torch nozzle to provide a Planckian emitter in addition to the torch flame. Figure 62 is an image from a commercial digital camera of both

configurations. The inclusion of the spreader changes the shape and intensity of the plume, and the spreader becomes hot enough to glow orange in color.

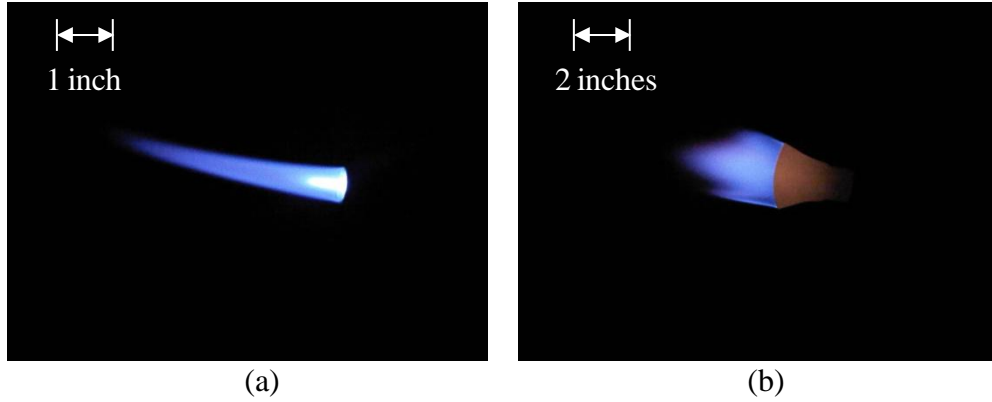


Figure 62. An image taken by a commercial digital camera of: (a) target flame alone and (b) with the spreader attached. An approximate image scale is shown.

It is assumed that the source radiance can be represented as:

$$L_{obs}(\lambda) = L_{BB}(\lambda, T) + L_M(\lambda, T) + B(\lambda) + C_a(\lambda) \quad (48)$$

where $L_{BB}(\lambda, T)$ and $L_M(\lambda, T)$ are the Planckian function and molecular emission, respectively, $B(\lambda)$ is background contribution due to detector bias or scattered light, and $C_a(\lambda)$ represents the artifact energy projected into a spectral bin from neighboring bins. The background term was initially estimated by finding pixels that did not contain target energy in each projection and creating a flat field estimate. Any remaining background and C_a were estimated from the reconstructed spectral data.

Results

Panchromatic Images

Panchromatic images were derived using three different methods: (1) taking the FBP of the $p(x,y,\theta)$, (2) summing all the spectral bins from the reconstruction of the CTI spectral data cube and (3) summing all the spectral bins from the LCTF images. The results for each approach are shown in Figure 63 for the torch with no spreader. The characteristic artifacts caused by the very bright core of the plume in contrast to the dimmer regions farther from the torch nozzle is apparent in filtered backprojection of Figure 63a. These are similar to artifacts observed in medical CT when high density, high contrast material (e.g. metal implants) are present in a patient [101, 102]. Taking projection data at higher angular resolution to smooth the artifacts can mitigate the spatial structure but is not desirable as it results in longer collection times (or increased patient dosage in the case of medical CT). The integrated 3-D reconstruction of the hyperspectral data cube in Figure 63b-c provides a better spatial representation of the plume structure when compared with the digital image in Figure 62a. However, due to the artifacts in the CTI reconstruction, the contrast between the bright core and the dimmer part of the flame is decreased, and the spatial structure of the core does not appear to be as well defined as compared to the integrated LCTF image.

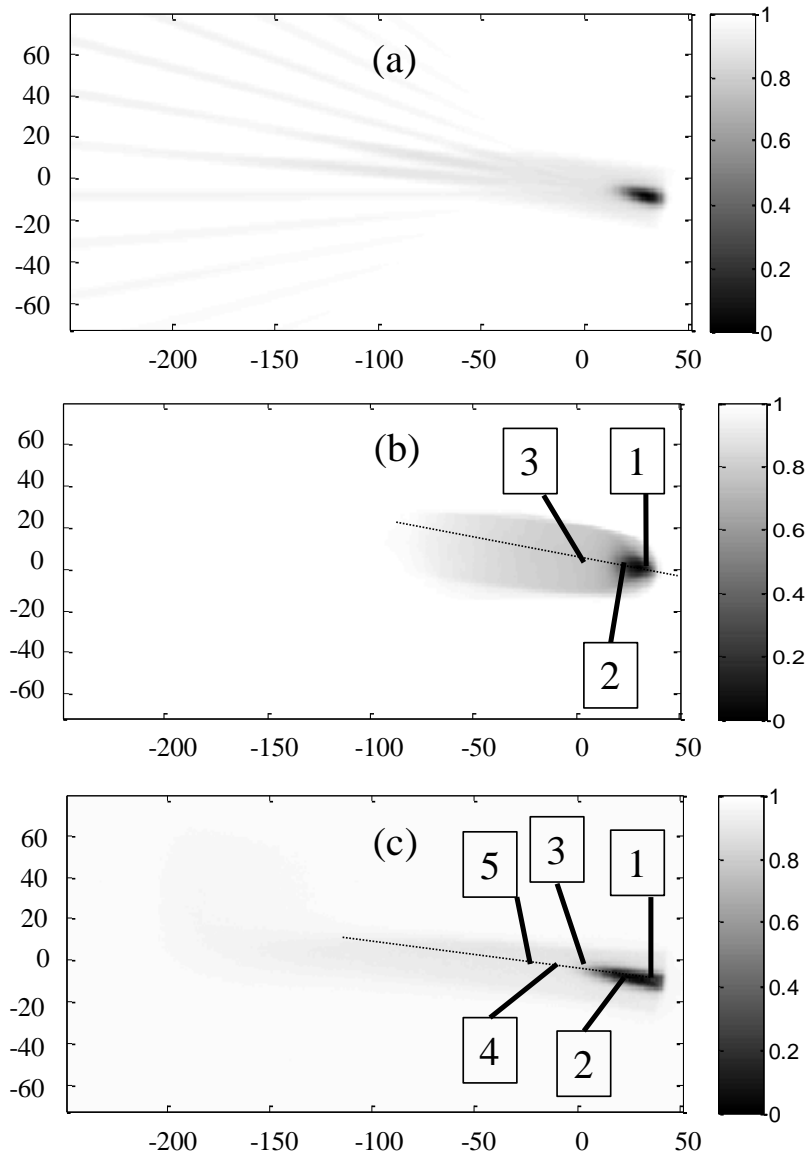


Figure 63. The 2-D reconstruction of the flame without spreader from: (a) the projection, (b) the integrated CTI hyperspectral data cube, and (c) the integrated LCTF hyperspectral data cube. In each figure, the x-y dimensions are in pixels at ≈ 0.75 mm/pixel. The (0,0) coordinate is approximately the optic axis for the collection, and numbers identifying points of further analysis.

The CTI panchromatic images of the torch with the spreader using both the FBP and the reconstructed CTI hyperspectral cube integrated over all wavelengths are shown in Figure 64. In both of the images, the bright shape of the spreader is clearly visible and distinct from the flame. The image produced by the FBP is noticeably clearer and much

more consistent with the image shown in Figure 62b. This is opposite of the results from the flame alone where the integrated CTI data provided the better imagery which featured higher spatial frequency components and a wider dynamic range of intensities. Note the differences in the plume as the spreader affects it. The spreader conceals the core, and the observed portion is fairly uniform and much broader and thinner.

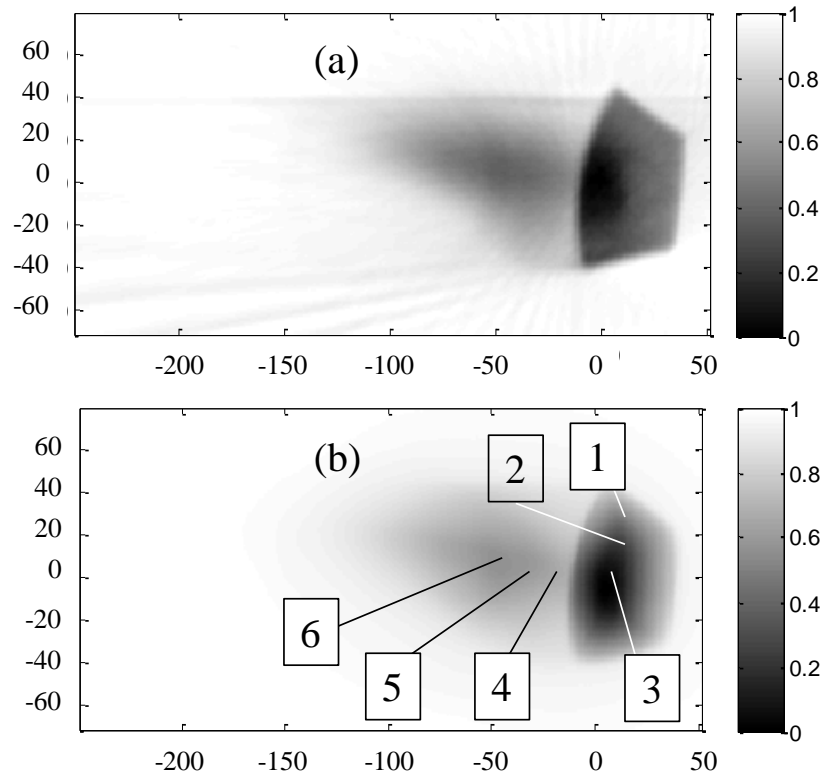


Figure 64. The 2-D panchromatic images of the flame with spreader from (a) the integration of the CTI hyperspectral data cube and (b) the filtered backprojection. In each figure, the scale is in pixels with ≈ 0.75 mm/pixel. The (0,0) coordinate is approximately the optic axis for the collection.

Extracted Spectra

A portion of the spectra (450 – 650 nm) is provided in Figure 65 for both the CTI (top) and LCTF (bottom) instruments for the points near the torch nozzle as indicated in the integrated panchromatic image shown in Figure 63. The CTI instrument clearly identifies strong band emission from C₂ and CH. The spectral resolution and sampling of the LCTF is insufficient to observe the blue shading of these bands and to resolve the CH emission. The spectra are bright for positions A and B, discernible for C, and not detected at more distant points except for some intensity near the 600 nm peak. The peak at 512 nm is much brighter in the CTI data than in the LCTF when compared to the other spectral lines although both sets have been corrected for the relative response of each system. The C₂ A ³Π_g → X³Π_u Swan bands for the Δv = 2, 1, 0, -2, and -2 sequences are assigned as features I – V, respectively.

Table 10 provides the transition assignments, wavelengths and associated Franck Condon factors, $q_{v'v''}$ [103]. With several bands responsible for each of the observed peaks, it is difficult to make a vibrational temperature measurement based on the line intensities. Indeed, inverting the linear combination of vibrational populations that contribute to each band yields negative concentrations for $v' = x$, for both the CTI and LCTF spectra, indicating incomplete detector spectral response characterization at these shorter wavelengths and sensitivity to the matrix inversion.

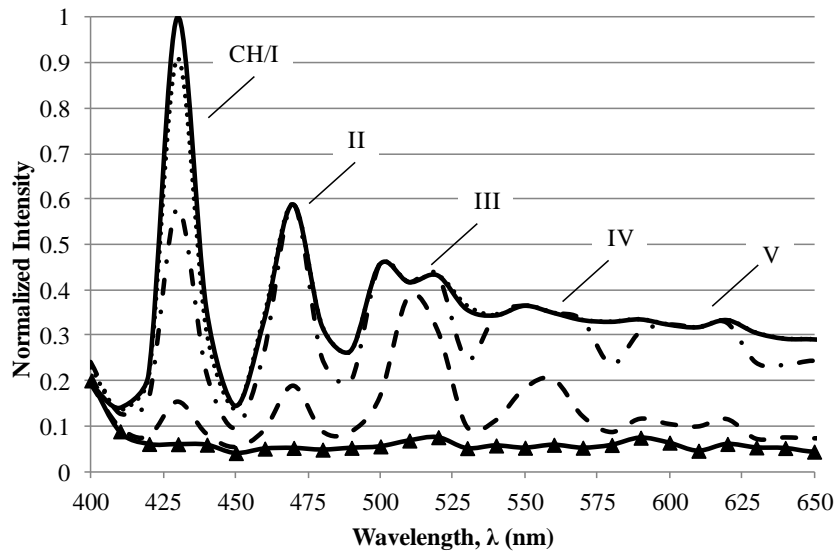
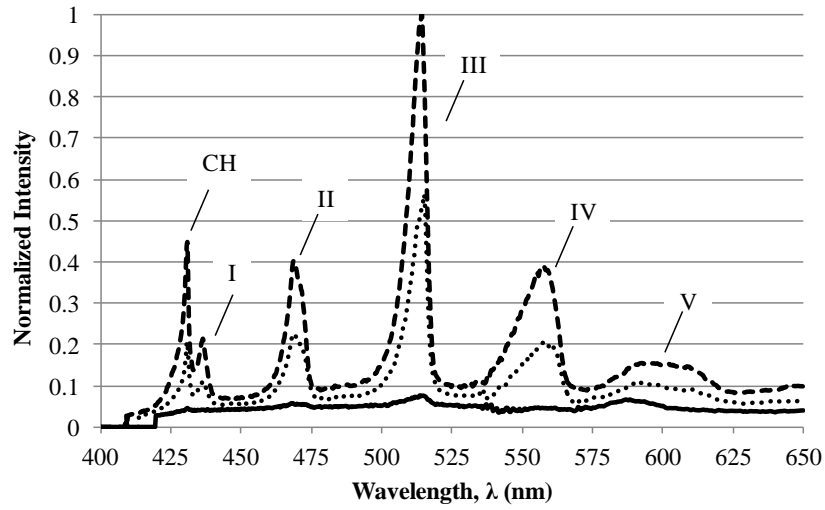


Figure 65. The CTI (above) and LCTF (below) emission spectra at locations in the image as noted in Figure 63. In each case, the intensity decreases as the points, denoted in Figs. 63a and 63b become farther from the torch. The format of the plotted lines are varied for clarity.

Table 10. The C₂ Swan bands as measured by the CTI and LCTF.

C₂ Peak	ν', ν''	$\lambda_{\nu'\nu''}$ (nm)	λ_{CTI} (nm)	λ_{LCTF} (nm)	$q_{\nu'\nu''}$
I	4,2	436.5	436.2	427.9	0.097
	3,1	437.1			0.060
	2,0	438.2			0.024
II	4,3	468.4	468.7	468.0	0.427
	3,2	469.7			0.405
	2,1	471.5			0.356
	1,0	473.7			0.237
III	2,2	509.7	513.6	511.8	0.162
	1,1	512.9			0.363
	0,0	516.5			0.731
IV	3,4	550.1	556.5	557.9	0.265
	2,3	554.0			0.280
	1,2	558.5			0.280
	0,1	563.5			0.211
V	2,4	605.9	608.8	604.8	0.124
	1,3	612.2			0.088
	0,2	619.1			0.042

With the flame spreader in place, a broadband emission is observed in the near infrared. The panchromatic image of Figure 64 identifies several points in the gas plume and on the metal spreader surface. The corresponding CTI spectra are provided in Figure 66. No strong molecular emission bands are observed at shorter wavelengths using the spreader. The temperature of the spreader is estimated from a simple fit of a Planckian distribution multiplied by the CTI spectral response function. This yields a poor result with temperatures in excess of 1800° C, approximately 900° C above the melting temperature of brass (900° – 940° C). This is likely due to intensity artifacts in the reconstructed data cube caused by the large spatial extent of the spreader, modifying the effective instrumental lineshape for this specific target.

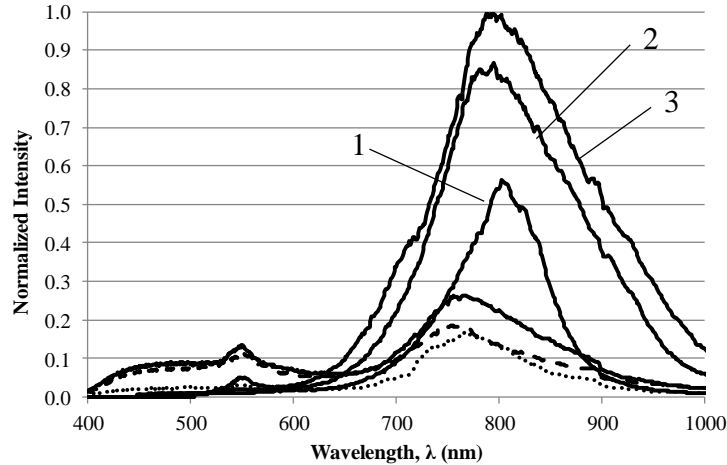


Figure 66. Near infrared spectra of the flame and spreader at several points in the image as denoted in Figure 64b. In the flame, points 4 (unmarked solid line), 5 (dashed line) and 6 (dotted line) show little if any spectral content as the open flame did. Points 1, 2, and 3 in the spreader indicate the emission is brighter in the center of the spreader.

This effect on the lineshape can be estimated since the spatial properties of the spreader are well defined from the 2-D image reconstruction CTI data and observed to be independent of wavelength in the 3-D construction. This knowledge of the scene can be used as input to the CTI system model to calculate an artifact transfer function which contributes to the system spectral response. To demonstrate, an input scene was created from the spatial properties of the 2-D reconstructed image and assigned the spectral intensity of a uniformly emitting blackbody at a temperature of 800° C. This input is run through the system model, and then reconstructed using the same techniques in the experiment. A comparison of the predicted spectra for an 800° C blackbody and that extracted from the reconstructed synthetic scene at the center of the spreader (point 1) is provided in Figure 67. The peak wavelength is shifted by nearly 30 nm from the observation with considerable change in shape. From these two curves, an estimate for the artifact transfer function can be obtained. This function is spatially dependent and

must be calculated for all points in the scene. To derive the estimated temperature for the spreader from the data, the artifact transfer function derived from the model for a temperature T at point (x,y) is convolved out of the data and fit to a blackbody function corrected for system response at that temperature. An iterative approach is taken which finds the temperature at which this method yields a best fit between the deconvolved data and the corrected blackbody function reducing dependence on the initial guess. The result for a particular point is given in Figure 68, with the best fit to data at 750°C .

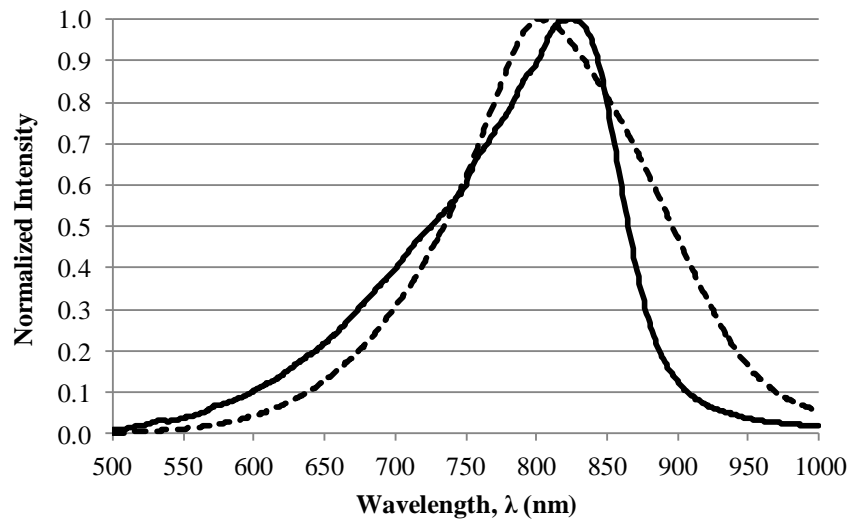


Figure 67. The BB intensity curves for an 800°C BB (solid line) and the reconstructed intensity using a model of the CTI with an 800°C BB in the shape of the spreader as input. Artifacts in the reconstruction cause the spectral intensity to be shifted to the right and misshapen.

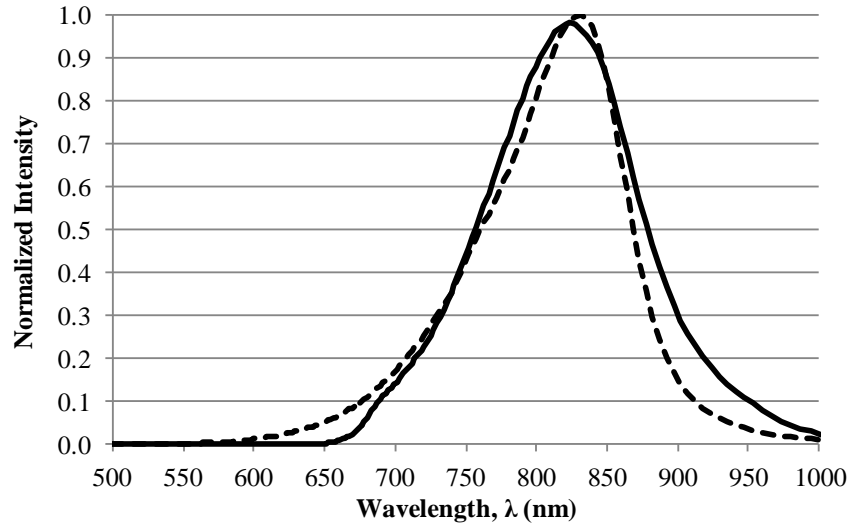


Figure 68. Deriving a correction function from the CTI model using data such as that shown in Fig. 67, the intensity from the 3D CTI reconstruction can be corrected for the artifacts, plotted as a solid line. The best fit BB to this curve is at 750° C, plotted as a dashed line.

With no spectral emission peaks evident in the flame (points 4, 5, and 6 in Figure 64), a similar technique was used to assess the affect of artifact transfer function in the plume reconstruction to estimate temperature in the plume as well as the hot metal. The results of this process are provided in Figure 69. Temperatures across the brass spreader range from about 500° C to 1000° C which is much more reasonable than the previous result. The temperature of the flame is hotter on the lower edge (2000° C) than in the center (1750° C). Documented temperatures for a propane flame are 1900° – 2000° C when burning in air. Further development of radiometric calibrations of the CTI instrument will be required to extract accurate flame temperatures.

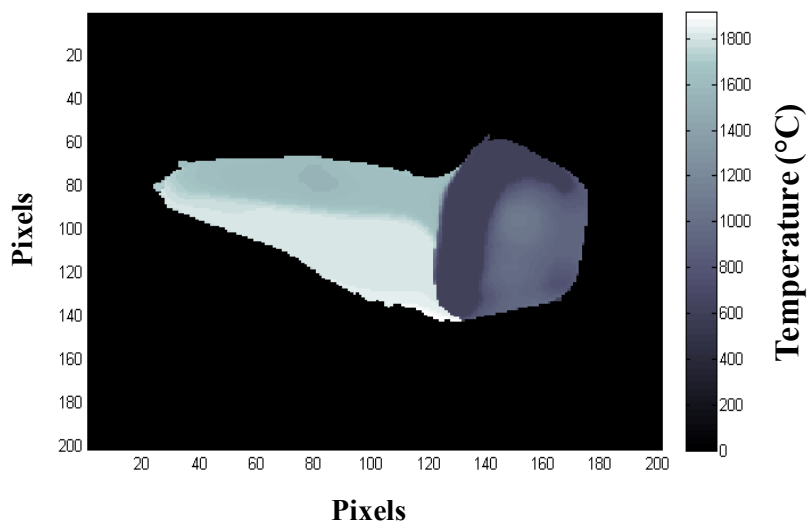


Figure 69. The temperature profile of the torch with the spreader in place. The brass spreader is at 1000° C or below, while the flame is near 1900° C in the hottest areas. The pixel scale is $\approx 1900^\circ\text{C}$.

Hyperspectral Imagery

Turning to the spatial information in the hyperspectral data cubes, the images of the spectral bins corresponding to each of the 6 peaks identified in the CTI spectra of Figure 65 are compared with the LCTF images in Figures 71 – 75. In each case, the LCTF provided a clearer representation of the spatial data in the plume. The CTI captures the bright core with some accuracy and the spatial extent of the plume. However, a large component of the energy in the plume is due mostly to artifacts in the data reconstruction. The intensities for the CH band image relative to the images for the C₂ bands II and IV are brighter in the core of the flame, likely due to reconstruction artifacts. The spatial distributions of intensities in the other spectral bands are more strongly correlated. The spatial quality of the reconstructed CTI images limits the analysis of spectral components of the flame as function of position.

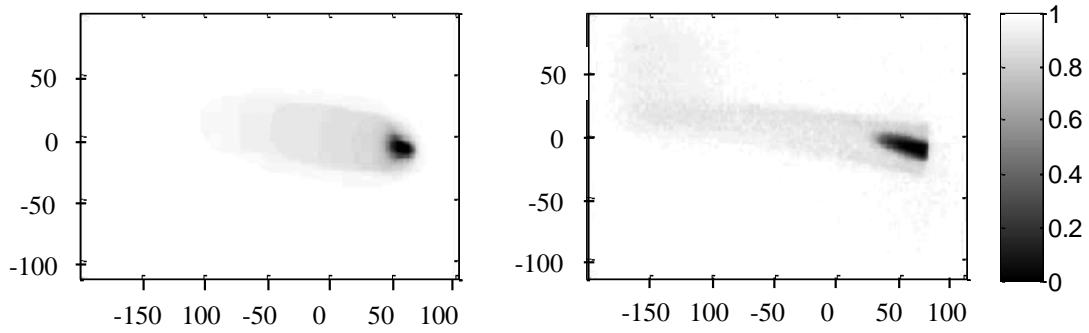


Figure 70. Spectral image of the CH emission peak from the CTI (left) and the LCTF (right).

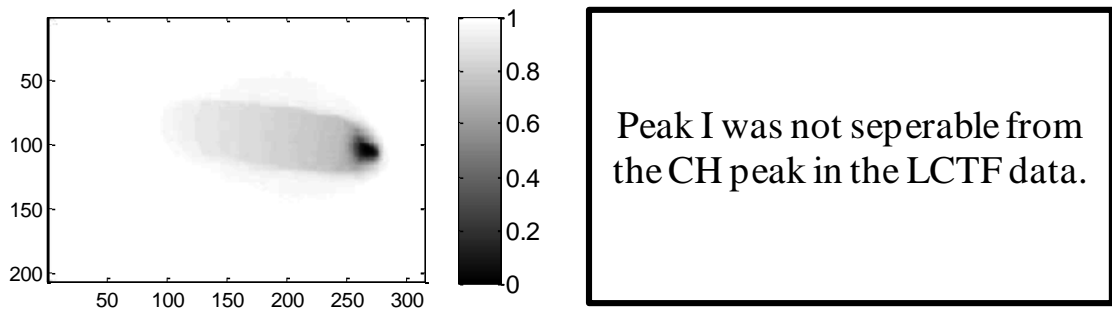


Figure 71. Spectral image of the C₂ band I emission peak from the CTI (left). The LCTF could not separate the C₂ band I peak from the CH peak at 432 nm.

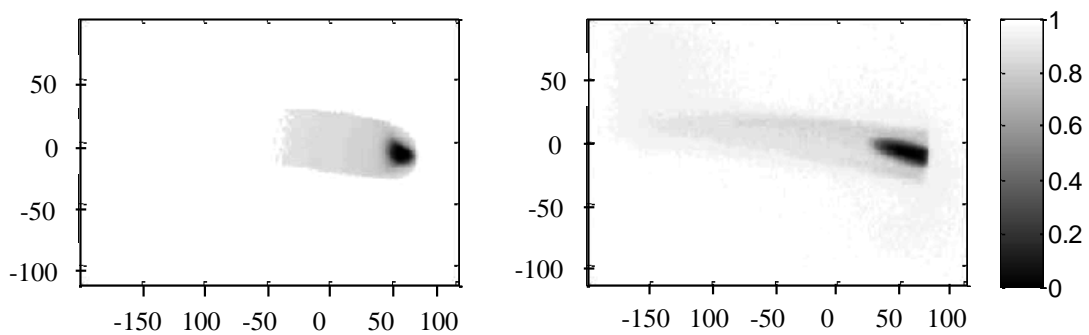


Figure 72. Spectral image of the C₂ band II emission peak from the CTI (left) and the LCTF (right).

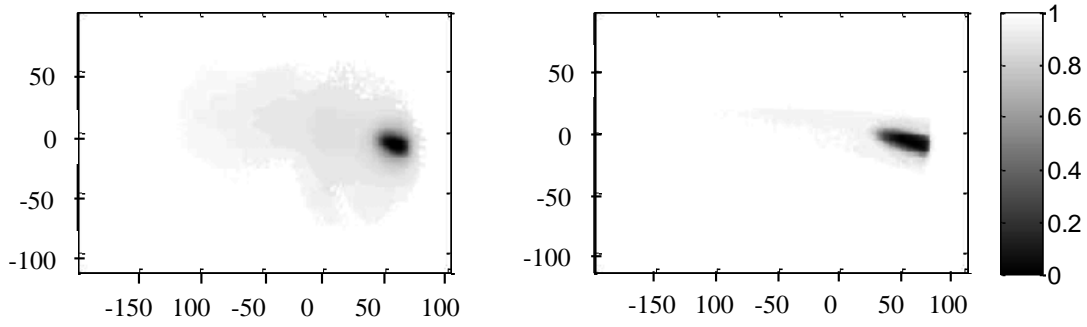


Figure 73. Spectral image of the C_2 band III emission peak from the CTI (left) and the LCTF (right).

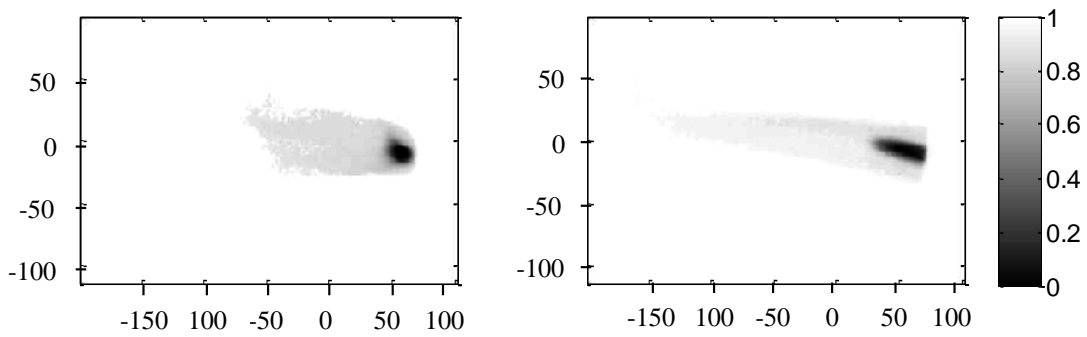


Figure 74. Spectral image of the C_2 band IV emission peak from the CTI (left) and the LCTF (right).

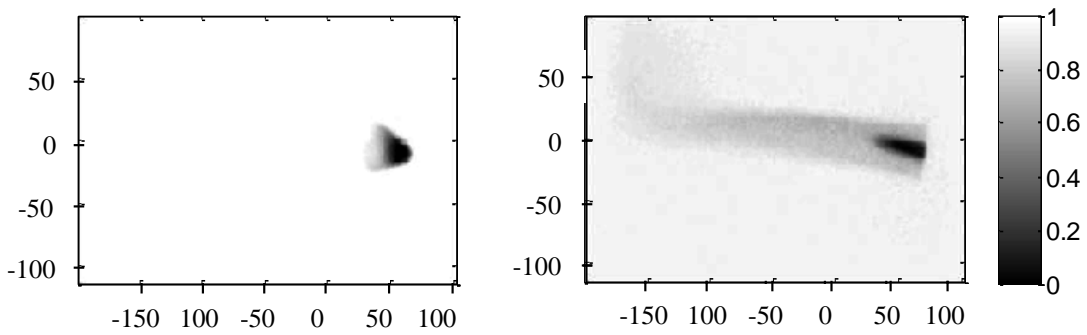


Figure 75. Spectral image of the C_2 band V emission peak from the CTI (left) and the LCTF (right).

Conclusions

The first application of chromotomosynthesis for producing hyperspectral images of a combustion source has been reported. The visible spectra of CH and C₂ are readily identified and distinguished from broadband surface emission.

The CTI 2-D imagery suffers from artifacts due to the very bright and high contrast source at the center of the flame. This is similar to artifacts observed in medical CT data with implants or other material that scatters x-rays. More projections would have reduced the appearance of the artifacts, but likely not recovered the low intensity shape of the flame without more additional optimization of the collection. The CTI instrument did capture the spatial characteristics of the spectral emission features from the CH and C₂ Swann peaks in the core of the flame. However, they appeared to be somewhat degraded from the LCTF data, and the CTI did not observe the weaker spectral features far from the core of the flame.

Neither the LCTF nor CTI images were able to calculate vibrational population distributions or temperatures, due to problems associated with radiometric calibrations. Despite this, qualitative classification of plume regions by temperature or species concentrations is possible. Using the 2-D wideband image and specialized reconstruction techniques based upon effects predicted by a model of the system enables improved reconstruction for a temperature map for the target. Improved methods of artifact removal are necessary to provide better spectral imagery and radiometrically accurate images. The number of CTI projections required depends on both the spatial characteristics of the scene and the spatial intensity gradients.

The data collected by the CTI provided 600 bins of spectral data. In contrast, the LCTF with limited spectral resolution afforded about 100. With the instrumentation in this experiment, the CTI data could be collected in about 2 seconds, whereas the LCTF would take nearly 10 seconds. It would have taken over 30 s to acquire the same 600 bins of spectral data with the LCTF even if the resolution supported it. In addition, the projection data collected by the CTI allows for the analysis of essentially slitless spectral data collected at 36 Hz. CTI offers superior performance for scenarios requiring fast imaging, with modest spectral resolution at the expense of degraded spectral imagery.

VIII. Conclusions

A prototype chromotomosynthetic instrument operating in the visible (400 – 900 nm) portion of the spectrum was built and characterized as the foundation of this research. Though the design, mathematical transforms, modeled performance, and collection examples can be found in the literature, this study has documented the relationships between design and performance as a hyperspectral imager and has quantified the utility of this type of instrument in collections and data exploitation against target types of interest. The research was done in such a way that results may be generalized and performance predicted for different instrument designs and for different spectral regions.

The dependence of spectral resolution in reconstructed hyperspectral data on the prism design was defined and shown to range from 0.6 – 10 nm as wavelength increased over the operating range of the instrument. The $f = 100$ mm focal length instrument maintained a per-pixel field of view of 0.6 mrad as defined by the optics and the detector, but unlike a traditional imaging system needed to be limited to a full field of view of 71.6 mrad in order to capture information from all spectral projections. The CTI data is collected in fundamentally the same way as a prism spectrometer data with a fixed prism. However, unlike normal dispersive spectrometers, CTI cannot dramatically improve spectral resolution by simply increasing the focal length except near the undispersed wavelength. This is because the image of the field of view must be collected and be rotated for all wavelengths about the undeviated wavelength and not extend beyond the collection array. Minor adjustments can be made to the distance between the back lens

and the detector array to minimize optical blur at a desired wavelength and somewhat improve spatial and spectral resolution.

The spectral resolution is dependent on the dispersive properties of the DVP and is the same as that expected from a traditional prism spectrograph using the same collection system. For this study, in the absence of systematic error the system performance is primarily limited by chromatic aberrations for the transmissive optics. The spectral and spatial resolution in the reconstructed data was defined through this general transform used to reconstruct the 3-D hyperspectral data cube and with respect to the instrument's fundamental performance as an imaging system.

Data Collection and Reconstruction

The critical measure of performance of the CTI is in the 3-D hyperspectral space, which is mathematically reconstructed from the data which are 2-D spectral projections over a range of prism rotation angles. The spectral projection geometry of the system does not allow for an analytic reconstruction due to the limited support in the Fourier Space of the data as required by the Fourier slice theorem. Unlike most of the previous work which has focused on direct inversion of the CTI forward transform to reconstruct 3-D hyperspectral imagery, this research has utilized a more general and standard method. The modified backprojection is analogous to medical tomosynthesis methods and more natural with respect to the way the data is collected. This algorithm does not significantly degrade the spatial resolution of the system provided the detector sampling is a small contribution to the overall performance.

In addition to the 3-D hyperspectral imagery, a 2-D wideband image of the target scene can be reconstructed to provide data equivalent to that which would be taken if the prism were not in the optical system. This is possible because each CTI projection is equivalent to a 1-D spatial projection of the 2-D image at each prism rotation angle. This is a critical first step in the data reconstruction process, as the backprojection algorithm can be modified and constrained based on spatial content analysis of the 2-D imagery of each scene. This modification should allow the backprojection to achieve performance equivalent to that of the iterative maximum likely-hood methods for this type of data without the need for algorithm iteration. It is certain that more complex mathematical methods can be subsequently employed based on the desired spectral range or spatial features following analysis of the initial hyperspectral imagery from the backprojection. Quality of data reconstruction was found to be dependent on target spatial and spectral properties; however, the 3-D reconstruction can be optimized from target properties derived from the reconstructed 2-D wideband image and by pre-processing the raw projection data.

The 2-D data reconstruction is valuable and perhaps critical but also drives the number of projections needed for accurate reconstruction. Unlike the 3-D reconstruction where spectral sampling is incomplete, the spatial projection of the 2-D data into 1-D line projections is a complete Radon projection. The number of projections required for the best 2-D spatial reconstruction will approach the theoretical sampling size of $\pi \cdot (N/2)$ necessary for the sampling resolution of a square detector FOV of N^2 pixels. This demonstrates that for quality reconstruction, the detector array must sample at 100-200

times the rotation period of the prism. With this constraint, an array which can frame at 1 kHz should be able to collect hyperspectral imagery at 100s of Hz.

This ability of the CTI to collect more data at a higher rate than the traditional systems is crucial in exploiting fast transient events. This also allows for flexibility in analysis of the data. The projections taken in one full rotation of the prism can be used to reconstruct a 3-D hyperspectral image cube. The data taken over $\frac{1}{2}$ a prism rotation can be used to reconstruct the 2-D wideband image. Finally, the spectrally dispersed projections themselves are collected at the framing rate of the detector and can be exploited as slitless spectroscopy.

Effect of Systematic Error

All results of instrument performance assume the system spectral dispersion and other instrument properties are adequately characterized, and in all previous research this was assumed to be the case. In practice, reconstruction of hyperspectral data cubes requires an exact estimation of the instrument component properties which define the forward transform to realize this theoretical performance. Any instrumental error will alter this forward projection and if unaccounted for will degrade the spatial and spectral quality of the reconstructed hyperspectral imagery. It is necessary to consider degradation of performance in the reconstructed image cube, not in the measured 2-D (projection) space. A general mathematical relationship between major sources of systematic error for diagnosis of performance was developed for application to any general CTI design to model the degradation of performance in the presence of these errors. This error function was developed so that design tolerances can be diagnosed for

four primary sources of instrumental error: (1) error in knowledge of the angular prism dispersion, (2) those due to tilt in the detector array and distance between the detector array and the lens L_3 , (3) error in prism and mount misalignment, and (4) error in estimation of the prism rotation angle θ . The error kernel derived for each of the phenomena apply to any set of data given the general nature of the equations describing and can be convolved with each spectral bin for assessment. A significant outcome of the error analysis is a methodology for calibration of the instrument to compensate for possible errors.

The AFIT instrument was found to be most sensitive to errors at $\lambda < 500$ nm where prism dispersion is a maximum and thus best spectral performance is achieved. System performance was found to be most sensitive to misalignment of the prism mount. Mount misalignment of 0.25° in both axes caused factor of 2 degradation of spectral resolution, shifted the centroid of the point source image by 1 – 1.5 pixels and caused a 30% reduction in spatial resolution. No substantial degradation occurred at $\lambda > 500$ nm. Line shape distortions occur with mount misalignment and may lead to further error in spectral performance not captured by this research. Error in knowledge of prism rotation angle also resulted in loss of spectral resolution to a lesser extent. An error of 0.50° can produce a factor of 2 degradation in spatial resolution for $\lambda < 450$ nm. Shifts in the centroid of the 2-D point spread function were noticeable with detector array tilt, but only significant for $\lambda < 450$ nm and shown to be less than 1 pixel for a 3° tilt.

Error in prism dispersion, prism misalignment, and distance to the detector array resulted only in spectral line shifting, but again limited to shorter wavelengths where dispersion is the greatest. An array distance error of 1 mm caused a greater than 1 nm

spectral shift for $\lambda < 500$ nm. Prism misalignment parallel to the dispersion axis of 0.5° produces a similar shift. Shifts in the wavelength of the reconstructed spectrum on the order of the spectral resolution were observed across the entire spectral range. These shifts were caused by both array distance error of 2 mm and constant prism dispersion error of 0.05° . These errors can be interpreted as loss of spatial and spectral resolution in the spectral bin of true emission if there is no correction for the spectral shift.

Practically speaking, the results of the error analysis study showed that instrument calibration is critical. The CTI can be calibrated by measuring the radius of displacement of a point as a function of wavelength and projection angle thus empirically determining the forward projection. Appendix B describes the method of doing this based on measurements at several discrete wavelengths. In a case where calibration is not possible, the observable effects of instrument error in the projection data can be used to diagnose the source of the error. This is done by realizing that the trace the image a monochromatic point source should make on the array is a perfect circle at some known radius and center. Analyzing deviations from this function and comparing to the shapes predicted by the error kernel using instrument design parameters may provide information regarding the source of systematic error.

Utility Assessment of the CTI

The capstone of this work built upon the system metrology and performance assessment to investigate and document the performance and utility of the CTI. To accomplish this, a set of targets were designed to represent a variety of applicable scenarios. The targets, though diagnostic in nature, represent an increasing level of

spatial and spectral complexity. Performance was assessed by comparing the CTI results to hyperspectral data collected by replacing the DVP with a liquid crystal tunable filter (LCTF). Performance metrics were compared as well as overall ability to characterize spatially and spectrally the given set of targets. This analysis demonstrated how quality of data reconstruction was dependent on target spatial and spectral properties and how reconstruction can be optimized from target properties and by pre-processing the raw projection data. The overall advantage of the CTI was that data could be collected much faster and the visible spectrum could be resolved into any one or all of several hundred bins. However, the CTI was much more susceptible to artifacts which degraded both spectral and spatial performance of the system.

In these target collections, with a continuous framing camera it would have taken 2 seconds to collect the CTI data used to reconstruct the 400 spectral bins, with the time to collect limited by the system rotation rate of the prism. The LCTF would have taken 40 seconds to acquire an equivalent number of bins, with the collection time directly proportional to the number of bins desired.

Point Source Targets

As a first test, data were collected on a collection of randomly spaced point-like targets with varying spectral properties. The targets were purposefully chosen to be spatially simple. Results of analysis of the spatial and spectral properties of the CTI were very comparable to those obtained from the continuously variable filter method in terms of target classes identified using a k-means classification algorithm. There were differences in the specific targets assigned to each class; however, analysis of data indicated that two of the classes were nearly identical and overall the results were

consistent. There was some residual energy in the red wavelengths for the CTI spectra of predominantly blue targets, a first indication of possible artifacts in the data.

The 2-D reconstructed images spatially matched the image of the target scene taken by the instrument with no dispersive element in place and target energies for each target matched to within 5%. Because more frames of data are collected to reconstruct the image, the background bias in the 2-D reconstructed image was nearly a factor of 10 less than that in the 2-D wideband image and noise was reduced by about 35%. This reconstructed 2-D image was used to create an optimized algorithm to retrieve the 1-D spectral information from the point source targets based upon knowledge their spatial locations. The results of this algorithm were nearly identical to that of the full backprojection reconstruction of the 3-D data cube. This method reduced the necessary processing time by nearly a factor of 30 for point source targets.

While reconstruction of 3-D hyperspectral imagery is the rationale for collecting spectral projections with a rotating prism for these point sources, an argument could be made that a simple slitless spectrometer could have been used to achieve the same results. However, two advantages for rotating the prism in collecting point source spectral data with essentially a slitless spectrometer were observed. First, by rotating the prism about the undeviated wavelength and therefore undisplaced location, both location of a source as well as the registration of the spectral data can be calculated. Second, if many sources are present in the scene in close proximity, there is a high probability of spectral overlap or entanglement. By rotating the prism and taking many samples at different angles, “clean” versions of point source spectral can be derived.

Mosaic Array

Following the point source study, a spectrally diverse 5x5 mosaic of spatially extended narrow bandpass filters was evaluated. Though not spatially complicated, the larger non-point images of the filters clearly revealed artifacts in the 3-D reconstruction which prove to be a major drawback of the instrument. Energy from bright elements was observed in bins where the energy should not have been present which translated to spectral artifacts when examining spectral intensity of other elements. Even with these isolated artifacts, the CTI did provide the similar overall quality of data as that collected by the LCTF.

The 2-D image reconstructed from 180 projections at 1° intervals was a very close match to the wideband image collected without the prism in place with respect to target metrics, and compared better to the spectrally integrated LCTF image in terms of the Colsher discrepancy value and percent difference. However, the 2-D reconstructed image did contain more spatially correlated noise as a result of residual spatial artifacts even with the 180 projections. There was a 10-20% degradation in image quality with 36 projections used, and a barely acceptable image was formed using only 18 projections.

In the hyperspectral data, the peak centers for each element calculated from the CTI data were within +/-2 nm of the filter specifications for most elements. In cases of poor agreement with these values, the CTI did match the calculated LCTF values in all but 2 instances. The spectral resolution derived from the lineshape function for each element demonstrated the expected better performance of the CTI by 50% at lower wavelengths, and converged to a $\Delta\lambda$ of about 35 nm at $\lambda = 750$ nm. Unlike in the LCTF data, the spectral lineshape was shown to be a function of the spatial location within the target

image. The lineshape did not become wider which would indicate loss of spectral resolution, but did become decidedly non-Gaussian. The largest discrepancies between the LCTF and CTI data were shown to be in cases with dimmer targets that had lower SNR where artifacts are a larger percent of the energy.

Overall, the results were consistent with 18, 36 or 180 projections used in the 3-D reconstruction as nearly identical Colsher values were calculated for most elements. In 2-3 of the dimmest elements, there was as much as a 20% difference in the spectral imagery. In these cases, better agreement was achieved with more projections as the magnitude of the artifacts from brighter elements was reduced. Modifications to the backprojection algorithm to make it similar to an iterative algorithm based on the 2-D reconstructed image did reduce the overall affect of artifacts for this target due to the discrete locations of the filters in the array. However, for an array with a spatially continuous distribution of energy, this technique will not improve results.

Flame and Extended Blackbody Source

The first well-documented application of the CTI for exploiting hyperspectral images of a combustion source was done as a part of this research. The visible spectra of CH and C₂ molecular emission peaks were readily identified and distinguished from broadband surface emissions in the hyperspectral imagery. Compared to the mosaic, the CTI 2-D imagery suffered from artifacts due to the very bright and high spatial frequency source at the center of the flame. The projections were taken at 5° intervals; optimal for the 3-D reconstruction. For these more continuous targets it became evident that the 2-D reconstruction requirements are more severe with respect to sampling criteria.

While the CTI instrument did capture the spatial characteristics of the flame in the spectral bins corresponding to the emission features from the CH and C₂ Swan peaks, they were degraded from the LCTF data, and the CTI did not observe the weaker spectral features far from the core of the flame. For a target with continuous spatial and spectral features and slowly varying intensities, the spatial information will be severely degraded by the presence of artifacts from neighboring spectral bins.

The second target used in this experiment consisted of a hot blackbody in the form of a flame spreader placed on the end of the torch. Because of the smaller variations in intensity across the image, a better 2-D spatial representation was reconstructed. Using the assumption of a blackbody source, a temperature map was calculated for the spreader from the hyperspectral data. This resulted in reported temperatures which were impossibly high (near 2000° C). It was determined that these results were due to spatial artifacts in the data causing shifts of the derived spectra at each point in the imagery. The integrated spatial intensity of the target from the 2-D spatial reconstruction was used as input to the forward model of the instrument to approximate a temperature dependent correction at each point. An iterative algorithm then found the best correction by minimizing errors in fits of modeled predictions to the data at each point. Temperatures calculated from these adjusted spectra ranged from 800° – 1000° C across the brass spreader, which are much more reasonable. This specialized reconstruction technique based upon effects predicted by the model of the system is not generalized, but shows again that the 2-D image is a critical component of 3-D reconstruction. These results built upon the analysis of the mosaic, where it was shown that a more spatially continuous source with both bright and dim features is difficult for the CTI to exploit.

Summary

The CTI design is rather simple and offers a level of flexibility in data collection and processing which does make it an attractive option for collecting coarse hyperspectral imagery when compared to instruments dedicated to this task. In its basic function, it is a slitless spectrometer and thus performs best when there are many small separated targets where spectral information can become entangle for any one or small numbers of projections. Further development of the CTI instrument is required for objects with more diverse spatial frequencies. In particular, the sensitivity of reconstructed images to systematic errors for scenes with increased spatial and spectral mixing must be developed. Many factors affect the achievable spatial and spectral resolution attainable from an operational CTI system. More specifically, the contrast values that define the ability to detect and resolve spatial features at a given wavelength require further study.

The CTI offers superior performance for scenarios requiring fast imaging, though it is done with modest spectral resolution and at the expense of degraded spectral imagery. Even with perfect reconstruction, spatial and spectral resolution in reconstructed spectral bins is reduced by the presence of artifacts which are analogous to contamination from out of band energy. Artifacts become more difficult to remove as targets and scenes become more spatially and spectrally uniform. This dependence is also demonstrated by the cone of missing data in the Fourier projection space defined by the Radon transform. With the missing data, a direct inverse of transform does not exist and there is not enough information to exactly reconstruct the hyperspectral object. However, these artifacts can be better mitigated in the individual projections in conjunction with using the 2-D spatial wideband scene to derive known characteristics of the desired target as shown with the

targets in this study. The amount of data collected enables higher order algorithms to be used. A model of the system also allows for predictive behavior of spatial and spectral artifacts so that corrective measures can be implemented.

While fast, the complications introduced with the data artifacts as scenes become more spectrally and spatially continuous may limit the use in situations where intensive data analysis cannot be done, or multi-utility is not necessary. Sharp spatial and spectral features are discernible and can be fairly easily exploited at a high frame rate with the right instrumentation. Also with the rotating prism, wideband imagery can be recovered even with the dispersive element in place. By collecting all spectral and spatial data in each projection, a large set of data is available to implement a wide variety of image processing and other algorithms to achieve a level of satisfactory performance. Thus, there is utility for CTI in situations where a wide variety of spatial and spectral targets must be exploited over a wide field of view and with a sampling rate of 10 – 1000 Hz.

Recommendations and Future Work

Though beyond the scope of this research, an obvious outcome and an area where clearly more analysis is required is in processing of the projection data to reconstruct the 3-D hyperspectral imagery. In this study, a general methodology was the focus with some specific modifications based upon the specific target used. The mathematical methodology for constraining the SAA or other iterative algorithm by the spatial image 2-D panchromatic image should be formalized and optimized. Based on automated target recognition in the 2-D data, the filtering process for the SAA based on the requirement for overlapping or intersecting energy can be more selectively employed. Also, by

looking at change detection in the 2-D data, the targets of interest could be identified and masked, such that only this energy of interest is considered, reducing artifacts from unwanted background. It is also recommended that a more thorough analysis of existing tomosynthesis algorithms be completed, to determine which are most applicable even with the limited spectral projection angle.

Even without optimization to provide better 3-D hyperspectral data, the generic process of reconstruction documented here could certainly be optimized to execute in a much faster manner. The MATLAB code used was written such that a diagnosis of performance could be made for any given step. Many of the processes could be done in parallel, and much of the spatial shifting could be done in frequency space reducing mathematical operations. If this methodology were to be used “operationally” for a field instrument, better user interfaces would need to be created to take advantage of target reconstruction in spatial and spectral areas of interest. Also, preprocessing of the projection data to remove noise and other unwanted features based on expected behavior of the target energy in the 2-D space can improve reconstruction accuracy in the 3-D space. In a time resolved collection scenario, it is recommended that the 2-D panchromatic images be created to analyze the evolution and characteristics of the scene of interest. The spatial location of the target can be determined as well as the frames in which it appears. This could be used as background suppression for unwanted energy in the data to reduce magnitude of artifacts.

In this research, results are quantified for performance of the CTI in terms of spectral, spatial and temporal resolution. A study on the applied exploitation of diagnostic targets is also presented. The goal is that these results will lead designers to

determine mission applicability against real-world targets of interest. At AFIT, corresponding work is being done to determine what extracted features from spatial, spectral and temporal measurements of ground truth events are necessary for classification. A review of this work was presented in Section II. However, this work was done given the data specifically for characterization of events with several instruments available to acquire the highest quality collects. Given that that high-order physics models have been developed and validated using this data, an analysis of minimum system requirements for spatial, spectral and temporal parameters to achieve classification of targets in CTI is needed. The degree of both absolute and relative radiometric accuracy should be considered given the potential issue with radiometric accuracy in CTI in the presence of artifacts. This information would determine true minimum spectral and spatial requirements for high-speed CTI.

Once a set of mission requirements are determined, a CTI instrument should be designed from the component level. A trade between spectral resolution and spectral range needs to be considered, as well as spectral dispersion of the prism across the range of use. To reduce the artifacts in the data and reduce the volume of the missing cone in the Fourier Space, the projection angle of the prism needs to be increased to $10^\circ - 20^\circ$. A more linear dispersion across the spectral range is desired to more efficiently exploit the spectral data across the full detector system response, though true linearity is not possible with the two glass design. The prism in combination with a bandpass filter or a calibrated 3-color CCD can be used to reduce artifacts from spectral regions that are not of interest.

Appendix A. Component Selection and Development

The basic design of the chromotomosynthetic instrument used in this study was presented in Section II. Here, a more detailed description of the components used is provided as well as how and why they were selected. Though a specific mission was not required, primary requirements for the laboratory system were for a large enough field of view to capture a 10 cm diameter circular area in the target plane and limit the input angles to the direct vision prism (the field angle). To begin, the CTI schematic is shown again in Figure 76. Schematic design of the CTI instrument. L_1 and L_2 are essentially an afocal telescope to collimate incoming light. The rotating DVP disperses light as a function of wavelength, and L_3 acts as a focusing lens to produce an image on the detector array.

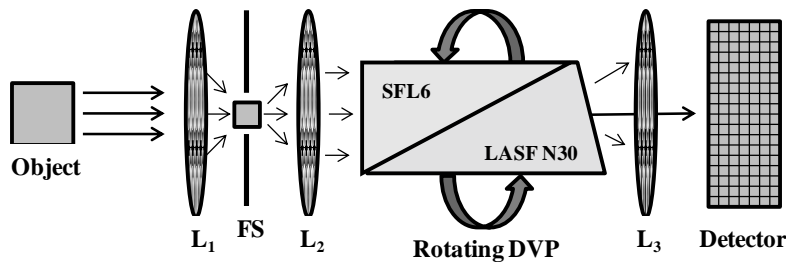


Figure 76. Schematic design of the CTI instrument. L_1 and L_2 are essentially an afocal telescope to collimate incoming light. The rotating DVP disperses light as a function of wavelength, and L_3 acts as a focusing lens to produce an image on the detector array.

With cost and schedule driving design, the AFIT CTI was built with an existing DVP design purchased off-the-shelf from a commercial vendor with the only requirement on performance being that it has an undeviated wavelength near the center of the visible

spectrum. The prism is fabricated from two types of glass bonded together as shown in Figure 77.

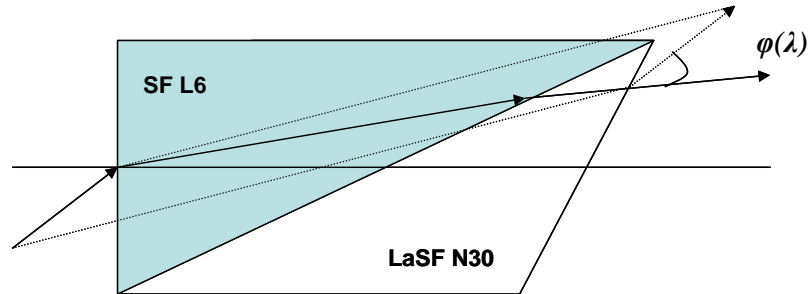


Figure 77. The AFIT DVP. The full assembly is 21 mm in diameter and 38.51 mm in length at the center. Definition of $\varphi(\lambda)$ is also shown in the diagram as well as the material (Schott Glass nomenclature).

The dispersion $\varphi(\lambda)$ as modeled using the material properties of the DVP is shown in Figure 78 for an input ray normal to the face of the prism. The undeviated wavelength, λ_c , is defined by $\varphi(\lambda) = 0^\circ$, which occurs at about 548 nm.

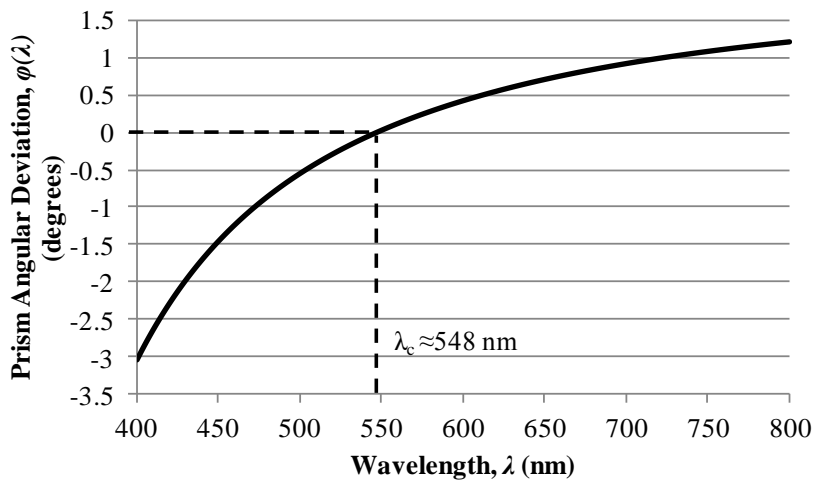


Figure 78. The angular dispersion of the direct vision prim. The undeviated wavelength, λ_c , is at approximately 548 nm. Note the decrease in dispersion at longer wavelengths.

In Figure 78, one can immediately see that the dispersion at shorter wavelengths much higher compared to that at longer wavelengths, where the spectral dispersion starts to level off. The modeled dispersion of the prism has been validated against the vendors provided specifications, as well as by simple measurements at AFIT using the prism. The prism is mounted and inserted into a Newport PM360A-0065 high-precision rotation stage which can spin at a uniform rate of 200 °/sec.

The Detector Array

As with the DVP, the detector array selected was based on available equipment and not specifically designed for this research. A Princeton Instruments PI-MAX Intensified CCD camera is used which has a 1024x1024 pixel array, with a pixel pitch of 13 μm giving a total detection area of about 1.33 x 1.33 cm^2 [90]. The spectral response of the camera defines the spectral range of the CTI covering about 400 – 800 nm. The camera is powered and controlled by an ST-133 controller.

Choosing Optical Elements

With the prism and detector identified the choice of the optical lens elements L_1 , L_2 , and L_3 remains and with some options. We begin with L_3 as the focal length of this lens, f_3 , ultimately determines the spectral displacement of the system on the detector and determines the spectral resolution. Longer focal lengths will increase the size of detector required to collect the shorter wavelength energy where dispersion is greatest. To illustrate this, Figure 79 shows the total displacement $r(\lambda)$ in pixels on the detector array for three choices for f_3 ; 50 mm, 100 mm and 150 mm.

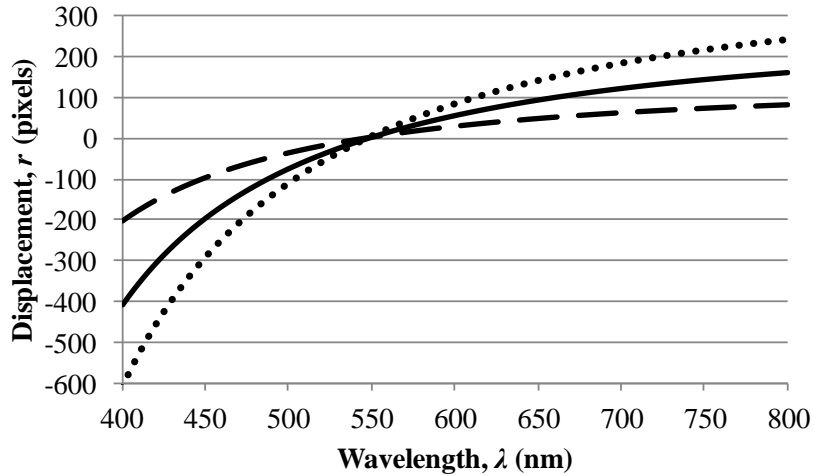


Figure 79. The displacement, r , at the detector in pixels for L_3 focal lengths of $f_3=50$ mm (dashed line), $f_3=100$ mm (solid line), and $f_3=150$ mm (dotted line).

With 1024 pixels minimum in any linear direction in the camera's CCD, a point source whose image would be at the center of the array can be displaced by a maximum 512 pixels (recall the prism is rotating, and therefore dispersive axis is rotating) and still be collected. A further constraint here is that this is an *imaging* system, and thus the need to collect the entire FOV as the prism rotates, not just a single point. In any case, the $f_3 = 150$ mm lens is not an option since we want to operate at wavelengths below 450 nm.

The spectral resolution of the CTI is directly dependent on the separation of images observed at the focal plane for a given difference in spectral wavelength, or $\Delta r/\Delta\lambda$. The plot in Figure 80 of $\Delta r/\Delta\lambda$ for the three lenses in consideration indicates the spectral resolution falls off considerably for the $f_3 = 50$ mm lens with very poor performance at wavelengths longer than 600 nm. The $f_3 = 100$ mm will be selected as it leaves reasonable margin in pixels for the FOV to fill and provides adequate spectral

performance. If higher resolution is desired and a smaller FOV and/or narrower spectral range is acceptable, a longer focal length can be used.

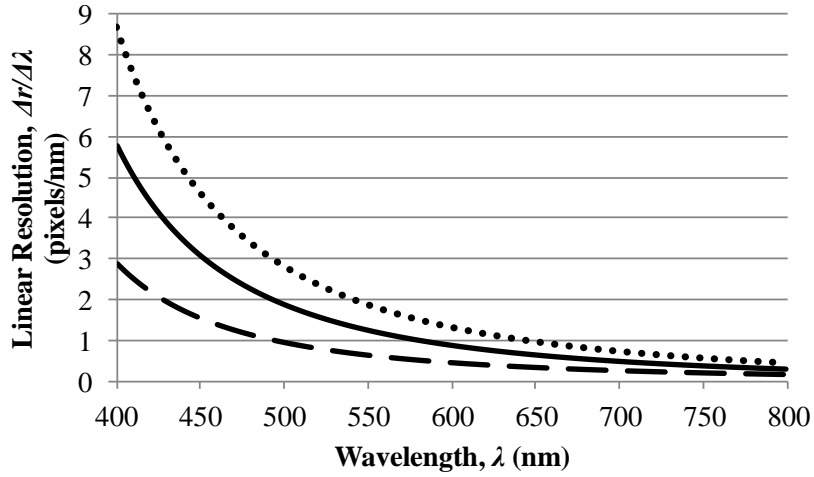


Figure 80. The plot of linear resolution, $\Delta r/\Delta\lambda$, at the detector array for L_3 focal lengths of $f_3=50$ mm (dashed line), $f_3=100$ mm (solid line), and $f_3=150$ mm (dotted line).

The forward optics can be designed to give the system magnification necessary to put the required object plane FOV into the area available on the detector array. In this experiment, the object area is a distance of $o = 1397$ mm from the position of the front lens of the instrument with a 10 cm FOV diameter. The data for the $f_3 = 100$ mm lens displacement in Figure 79 limits the radius of the image of the FOV to 108 pixels (1.4mm) on the detector array. The resulting magnification of the system, M_{sys} , must then be less than or equal to 0.028, with the largest possible value to maximize spatial resolution. The relationship between the system magnification and the focal lengths of L_1 , L_2 , and L_3 is given by:

$$M_{sys} = \frac{f_1 \cdot f_3}{(o - f_1) \cdot f_2} \quad (49)$$

Given $f_3 = 100$ mm, the constraint on M_{sys} , and assuming $o \gg f_l$, we have that:

$$\frac{f_1}{f_2} \leq 0.39. \quad (50)$$

A second design requirement is derived from the fact that these two lenses also define the input field angle to the prism, or the speed of the system. This is an important consideration, as $\varphi(\lambda)$ is a function of the incident angle to the prism, so will change with field angle which will make data reconstruction inaccurate, or at least much more complicated. To minimize the effect, an optically slow system is desired. To quantify this requirement, consider Figure 81, where the change in linear displacement $r(\lambda)$ from its value for an incident angle of 0° (ray on the optic axis) as a function of λ is plotted. The corresponding error in calculated wavelength is determined by dividing the data by the $\Delta r/\Delta \lambda$ and is also plotted in Figure 81.

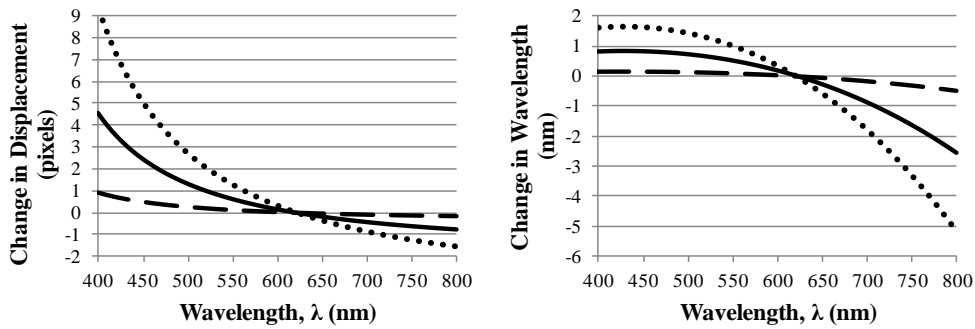


Figure 81. The change in the value of $r(\lambda)$ as a function of the field angle is given in the plot on the left for field angles of 0.1° (dashed line), 0.5° (solid line) and 1.0° (dotted line). The plot in the left shows the resulting error in wavelength that corresponds to the error in pixel displacement.

Notice that for a 1° field angle incident to the prism, the value for $r(\lambda)$ at 400 nm is nearly 10 pixels different than for the center of the FOV where the field angle is 0° . This would produce a registration error of approximately 2 nm for the chosen f_3 lens, and

blurring in the reconstructed image would occur as there is now a systematic error in the knowledge of $r(\lambda)$. Equation (51) gives the relationship between the field angle, θ_I , and the focal lengths of lenses:

$$\tan(\theta_I) = \frac{(\frac{1}{2} \cdot FOV) \cdot f_1}{(o - f_1) \cdot f_2}. \quad (51)$$

To keep the error in wavelength calculation at 400 nm at 1 nm or less, θ_I will have to be less than 0.65° . Using Equation (51) and again assuming $o \gg f_1$,

$$\frac{f_1}{f_2} \leq 0.32 \quad (52)$$

which also satisfies the restriction derived from M_{sys} in Equation (49). In the interest of telescope design, one may want to choose the shortest possible configuration to reduce space. The shortest available achromatic lenses at AFIT are 2" diameter 50.8 mm and 76.2 mm. These would then require a 158.75 mm and 238.13 mm focal length for L_2 , respectively, with 150 mm, 200 mm, and 250 mm 2" diameter achromatic lenses available. A 50.8/150 combination has $M_{sys} = 0.025$ which puts the FOV near the upper limit and edge of the detector array, and results in $\theta_I = 0.69^\circ$. The 76.2/250 combination gives an M_{sys} of 0.023, with $\theta_I = 0.65^\circ$. This combination will be chosen as the θ_I is acceptable and gives some margin at the edge of the detector array. This arrangement of a fast/slow optical lens does limit throughput of the system as compared to using lenses of comparable focal lengths, however the field angles would be increased to 1° - 2° .

The requirements for the AFIT CTI are obtained by considering the available hardware, desired field of view, and spectral resolution. Though we chose components piecewise by maximizing the spectral resolution given an FOV, the overall trade space

between FOV, spectral resolution, and spatial resolution can be summarized by looking at the relationships between the three. The FOV and spatial resolution will define the maximum focal length, f_{max} , allowable by the third lens, given that $\phi(\lambda)$ and the detector pitch and number of pixels are fixed. This is given by Equation (53), where p is the detector pixel pitch, n_p is the minimum number of pixels in the array in the any direction, FOV is the field of view at the object, GSD is the ground spatial distance (minimum spatial resolution not considering the point response function) for each pixel, and λ_{max} is the wavelength at which maximum prism dispersion occurs (400 nm in our case):

$$f_{max} = \frac{p \cdot (n_p - FOV/GSD)}{2 \cdot \tan(\phi(\lambda_{max}))}. \quad (53)$$

The $\Delta r/\Delta\lambda$ of the system, on which spectral resolution is dependent, is in turn a function of f_{max} :

$$\Delta r/\Delta\lambda = \left| \frac{f_{max} \cdot [\tan(\phi(\lambda_1)) - \tan(\phi(\lambda_2))]}{\lambda_1 - \lambda_2} \right| \quad (54)$$

where $\Delta\lambda = \lambda_1 - \lambda_2$. Though the CTI used in this experiment was built based solely on the availability of critical components, this research is extendible to other similar designs using these equations which define general relationships. These will also aid in designing a system which can meet basic mission requirements.

Appendix B. Calibration of the Chromotomosynthetic Imaging System

For all experiments, the AFTI CTI is calibrated using a standard method to determine the spectral displacement at the detection array as a function of wavelength and prism rotation angle θ . To accomplish this, a representative point aperture is positioned in the center of the instrument's field of view and separately illuminated by 8 known sources. For each source, data was taken at 8 equally spaced θ over $0^\circ - 360^\circ$ to investigate dependence of $r(\lambda)$ on θ . For the n^{th} spectral source and m^{th} projection angle, $r_{n,m}(\lambda_n, \theta^m)$ was calculated by measuring the center position of the image of the dispersed point source and subtracting it from the location of the undispersed image (determined prior to inserting the prism into the optics). A mean value for $r_n(\lambda)$ was found by averaging over all θ . In practice, the variance in $r_n(\lambda)$ would be used to estimate the spectral accuracy. An empirical value d_{min} was estimated by finding the value for d which minimizes the error between the left and right sides of Equation (9c) using the modeled $\varphi(\lambda)$ and the measured $r_n(\lambda)$. Next, a constant offset C was applied to minimize any residual bias. The final equation defining the relationship between displacement at the image plane and wavelength is given by:

$$r(\lambda) = d_{min} \cdot \tan(\varphi(\lambda)) + C. \quad (55)$$

For example, in Section VI, the estimated value for d_{min} was 7706.6 pixels, or 100.19 mm which is very close to the nominal focal length of L_3 (100 mm), and C was found to be -1.19 mm. The wavelengths and sources used, as well as the calculated $r_n(\lambda)$ compared to results from using Equation (55), are given in Table 11.

Table 11. Sources used and results of CTI system calibration.

λ	Source	$r(\lambda)$, data	$r(\lambda)$, model	Δr (pixels)	$\Delta\lambda$ (nm)
404.70	Hg	-381.21	-383.19	-1.98	-0.37
408.00	Hg	-364.76	-365.61	-0.84	-0.16
435.80	Hg	-243.76	-244.41	-0.65	-0.18
473.00	Laser	-134.00	-133.37	0.63	0.26
532.00	Laser	-23.19	-22.25	0.94	0.65
577.50	Hg	31.87	33.49	1.62	1.57
594.00	Laser	48.52	49.62	1.10	1.20
633.00	Laser	82.36	81.50	-0.86	-1.19

For each n points, the overall RMSE in $r_m(\lambda, \theta^n)$ was less than 1.25 pixels for each of the 8 sources, thus a dependence on θ was not considered in the calibration. As mentioned, this will result in an error in spectral registration. If a better fit is desired, a second order correction would be necessary. The individual residuals in $r(\lambda)$ varied from by as much as two pixels at $\lambda = 404.7$ nm, but because spectral dispersion is highest for shorter wavelengths the error in spectral registration is lowest here as indicated by the $\Delta\lambda$ column in Table 11.

One final calibration considered was in correcting for any error in the rotation angles θ . In the experiment each are assumed to be integral values at 1° increments from 0° - 360° . The error in measured θ from the data is within 0.04° of this assumption at all angles, which is negligible so no correction was made.

Bibliography

1. Klingenberg, G. and J. M. Heimerl. "Gun Muzzle Blast and Flash," *Progress in Astronautics and Aeronautics*, 139: 3-14 (1992).
2. Bagby, W. F. *Spectral and Temporal Characterization of High-Temperature Events*. MS thesis, AFIT/GAP/ENP/01M-01, Graduate School of Engineering and Management, Air Force Institute of Technology (AU), Wright-Patterson AFB OH, March 2001.
3. Orson, J. A., W. F. Bagby, and G. P. Perram. "Infrared Signatures from Bomb Detonations," *Infrared Physics & Technology*, 44: 101-107 (2003).
4. Steward, B. J. "Muzzle Flash Test: NIR Quick-look," Report, Air Force Institute of Technology (AU), Wright-Patterson AFB OH, December 2005.
5. Warren, T. *Characterization of Detonation Phenomena Observed in High-speed, Visible Imagery*. MS thesis, AFIT/GAP/ENP/06-20. Graduate School of Engineering and Management, Air Force Institute of Technology (AU), Wright-Patterson AFB OH, March 2006.
6. Gross, K. C., J. Wayman, and G. P. Perram. "Phenomenological Fireball Model for Remote Identification of High Explosives," *Proceedings of SPIE*, 6566: 656613 (April 2007).
7. Gross, K. C. *Phenomenological Model for Infrared Emissions from High-Explosive Detonation Fireballs*. Ph. D. dissertation, AFIT/DS/ENP/07-03. School of Engineering and Management, Air Force Institute of Technology (AU), Wright-Patterson AFB OH, September 2007.
8. Gordon, J. M., K. C. Gross, and G. P. Perram. "Empirical Model for the Temporally Resolved Temperatures of Post-detonation Fireballs for Aluminized High Explosives," *Proceedings of SPIE*, 8018: 80181M (March 2011).
9. Steward, B. J., K. C. Gross, and G. P. Perram. "Optical Characterization of Large Caliber Muzzle Blast Waves," *Propellants, Explosives, Pyrotechnics*, 36: 564-575 (2011).
10. Crow, D. R. and C. F. Coker. "High-Fidelity Modeling of Infrared Emissions from Missile and Aircraft Exhaust Plumes," *Proceedings of SPIE*, 2741: 242-250 (April, 1996).
11. Simmons, F. S. *Rocket Exhaust Plume Phenomenology*, El Segundo, CA: The Aerospace Press, 2000.

12. Spidell, M. T., J. M. Gordon, J. Pitz, K. C. Gross, and G. P. Perram. "High Speed Radiometric Measurements of IED Detonation Fireballs," *Proceedings of SPIE*, 7668: 76680C-76680C-10 (April 2010).
13. Orson, J. A. *Collection of Detonation Signatures and Characterization of Spectral Features*. MS thesis, AFIT/GSO/ENP/00M-01. Graduate School of Engineering and Management, Air Force Institute of Technology (AU), Wright-Patterson AFB OH, March 2000.
14. Gross, K. C., J. M. Gordon, and G. P. Perram. "Temporally-resolved, Infrared Spectra from the Detonation of Advanced Munitions," *Proceedings of SPIE*, 7330: 733006 (April 2009).
15. Steward, B. J., G. P. Perram, and K. C. Gross. "Visible and Near-Infrared Spectra of the Secondary Combustion of a 152 mm Howitzer," *Applied Spectroscopy*, 65(12): 1363-1371 (2011).
16. Dills, A. N. *Classification of Battlespace Detonations from Temporally Resolved Multi-Band Imagery and Mid-Infrared Spectra*. Ph. D. dissertation, AFIT/DS/ENP/05-03. School of Engineering and Management, Air Force Institute of Technology (AU), Wright-Patterson AFB OH, March 2005.
17. Gross, K. C. and G. P. Perram. "The Phenomenology of High Explosive Fireballs from Fielded Spectroscopic and Imaging Sensors for Event Classification," *International Journal of High Speed Electronics and Systems*, 18 (1): 19-29 (2008).
18. Steward, B. J. *Characterization and Discrimination of Large Caliber Gun Blast and Flash Signatures*. Ph. D. dissertation, AFIT/DS/ENP/11-D01, School of Engineering and Management, Air Force Institute of Technology (AU), Wright-Patterson AFB OH, October 2011.
19. Wolfe, W. *Introduction to Imaging Spectrometers*, Bellingham, WA: SPIE Optical Engineering Press (1997).
20. Kerekes, J. P. and J. R. Schott. *Hyperspectral Imaging Systems, in Hyperspectral Data Exploitation: Theory and Applications*. Hoboken, NJ: John Wiley & Sons, Inc., Ch. 2, (2006).
21. Eismann, M. T. *Hyperspectral Remote Sensing*, SPIE Press (2012).
22. Moreau, L., C. Roy, C. Vallières, L. Levesque, and M. Soucy. "A New Fast Infrared Imaging Spectroradiometer," *Proceedings of SPIE*, 7300: 73000U (April 2009).
23. Gross, K. C., K. C. Bradley, and G. P. Perram. "Remote Identification and Quantification of Industrial Smokestack Effluents via Imaging Fourier-Transform Spectroscopy," *Environ. Sci. Technol.*, 44(24): 9390-9397 (November 2010).

24. Bradley, K. C., K. C. Gross, and G. P. Perram. "Imaging Fourier Transform Spectrometry of Chemical Plumes," *Proceedings of SPIE*, 7304: 73040J (May 2009).
25. Gross, K. C., A. M. Young, C. Borel, B. J. Steward, and G. P. Perram. "Simulating Systematic Scene-Change Artifacts in Fourier Transform Spectroscopy," *Proceedings of SPIE*, 7695: 76951Y (April 2010).
26. Niklason, L. T., B. T. Christian, L. E. Niklason, D. B. Kopans, D. E. Castleberry, B.H. Opsahl-Ong, C. E. Landberg, P. J. Slanetz, A. A. Giardino, R. Moore, D. Albagli, M. C. DeJule, P. F. Fitzgerald, D. F. Fobare, B. W. Giambattista, R. F. Kwasnick, J. Liu, S. J. Lubowski, G. E. Possin, J. F. Richotte, C. Y. Wei, and R. F. Wirth. "Digital Tomosynthesis in Breast Imaging," *Radiology* 205: 399-406 (1997).
27. Stevens, G. M., R. L. Birdwell, C. F. Beaulieu, D. M. Ikeda, and N. J. Pelc. "Circular Tomosynthesis: Potential in Imaging of Breast and Upper Cervical Spine –Preliminary Phantom and In Vitro Study," *Radiology*, 228: 569-575 (2003).
28. Nett, B. E., J. Zambelli, C. Riddell, B. Belanger and G. Chen. "Circular Tomosynthesis Implemented with a Clinical Interventional Flat-Panel Based C-Arm: Initial Performance Study," *Proceedings of SPIE*, 6510: 65101N – 65113N (February 2007).
29. des Plantes, Z. "Eine neue method zur differenzierung in der roentgenographie," *Acta. Radiol.*, 13: 182-192 (1932).
30. Grant, D. G. "Tomosynthesis: a three-dimensional radiographic imaging technique," *IEEE Transactions in Bio-Medical Engineering*. 1: 20-28 (1972).
31. Levin, G.G. and G. N. Vishnyakov. "On the possibilities of chromotomography of high speed processes," *Optics Communications*, 56(4): 231-234, (1985).
32. Okamoto, T., A. Takahashi, and I. Yamaguchi. "Simultaneous Acquisition of Spectral and Spatial Intensity Distribution," *Society for Applied Spectroscopy*, 47(8): 1198-1202 (1993).
33. Mooney, J. M. "Angularly Multiplexed Spectral Imager," *Proceedings of SPIE*, 2480: 65-77 (April 1995).
34. Mooney, J. M. and W. S. Ewing. "Characterization of a Hyperspectral Imager," IRIS Proceedings on CD-ROM (1998).
35. Descour, M. and E. Dereniak. "Computed-Tomography Imaging Spectrometer: Experimental Calibration and Reconstruction Results," *Applied Optics*, 34(22): 4817 – 4826 (1995).

36. Descour, M. R., C. E. Volin, E. L. Dereniak, and K. J. Thome. "Demonstration of a Computed Tomography Imaging Spectrometer Using a Computer-Generated Hologram Dispenser," *Applied Optics*, 36(16): 3694-3698 (1997).
37. Descour, M. R., C. E. Volin, E. L. Dereniak, and K. J. Thome. "Demonstration of a High-Speed Non-Scanning Imaging Spectrometer," *Optics Letters*, 22(16), 1271-1273 (1997).
38. Ford, B. K. and M. R. Descour. "Large-Image-Format Computed Tomography Imaging Spectrometer for Fluorescence Microscopy," *Optics Express*, 9(9): 444-453 (October 2001).
39. Hagen, H., E. L. Dereniak and D. T. Sass. "Maximizing the Resolution of a CTIS Instrument," *Proceedings of SPIE*, 6302: 63020L-1 - 63020L-11 (September 2006).
40. Hagen, N. and E. L. Dereniak. "Analysis of Computed Tomographic Imaging Spectrometers. I. Spatial and Spectral Resolution," *Applied Optics*, 47(28): F85-F95 (October 2008).
41. O'Dell, D. *Development and Demonstration of a Field-Deployable Fast Chromotomographic Imager*. MS thesis, AFIT/GEO/ENP/10-M01. School of Engineering and Management, Air Force Institute of Technology (AU), Wright-Patterson AFB OH, March 2010.
42. Ewing, B., J. Mooney, B. Kreh, T. Reeves, and P. Pellegrini. "Spectrometer Performance Comparison for the Characterization of Transient Events," *MSS Specialty Group on IR Counter Measures*, March 2001.
43. Murguia, J. E., T. D. Reeves, J. M. Mooney, W. S. Ewing, F. D. Sheperd, and A. Brodzik. "A Compact Visible/Near Infrared Hyperspectral Imager," *Proceedings of SPIE*, 4208: 457-468 (April 2000).
44. Shepherd, F., J. M. Mooney, T. E. Reeves, and P. Dumont. "Adaptive MWIR Spectral Imaging sensor," *Proceedings of SPIE*, 7055: 705506 (August 2008).
45. Mooney, J. M., A. K. Brodzik and M. An. "Principal Component Analysis in Limited-Angle Chromotomography," *Proceedings of SPIE*, 3118: 170-178 (July 1997).
46. Brodzik, A. K. and J. M. Mooney. "Convex Projections Algorithm for Restoration of Limited-Angle Chromotomographic Images," *Journal of the Optical Society of America*, 16(2): 246-258 (1999).
47. An, M., A. K. Brodzik, J. M. Mooney, and R. Tolimieri. "Data Restoration in Chromotomographic Hyperspectral Imaging," *Proceedings of SPIE*, 4123: 150-161 (2000).

48. Nelson, R. J. "Imager to Spectrometer: Extracting Spectral Data from the Two-Dimensional Array," *Proceedings of SPIE*, 5563: 88 (August 2004).
49. Deming, R., S. Higbee, D. Dwyer, M. Welsler, L. Perlovsky, and P. Pellegrini. "Robust Detection and Spectrum Estimation of Multiple Sources from Rotating-Prism Spectrometer Images," *Proceedings of SPIE*, 6365: 636502 (September 2006).
50. Deming, R. W. "Chromotomography for a Rotating-Prism Instrument Using Backprojection, Then Filtering," *Optics Letters*, 31(15): 2281-2283 (2006).
51. Dearing, A. J. *Simulating a Chromotomographic Sensor for Hyperspectral Imaging in the Infrared*. MS thesis, AFIT/GE/ENG/04-05. School of Engineering and Management, Air Force Institute of Technology (AU), Wright-Patterson AFB OH, March 2004.
52. Gustke, K. C. *Reconstruction Algorithm Characterization and Performance Monitoring in Limited-Angle Chromotomography*. MS thesis, AFIT/GE/ENG/04-12. School of Engineering and Management, Air Force Institute of Technology (AU), Wright-Patterson AFB OH, March 2004.
53. Gould, M. and S. Cain. "Development of a Fast Chromotomographic Spectrometer," *Optical Engineering Letters*, 44(11): 110503-1 – 110503-3 (2005).
54. Gould, M. G. *Reconstruction of Chromotomographic Imaging System Infrared Hyperspectral Scenes*. MS thesis, AFIT/GE/ENG/05-04. School of Engineering and Management, Air Force Institute of Technology (AU), Wright-Patterson AFB OH, March 2005.
55. LeMaster, D. A. *Design and Model Verification of an Infrared Chromotomographic Imaging System*. MS thesis, AFIT/GAP/EMP/04-06. School of Engineering and Management, Air Force Institute of Technology (AU), Wright-Patterson AFB OH, December 2004.
56. O'Dell, D. C., R. L. Bostick, M. R. Hawks, E. D. Swenson, J. T. Black, R. G. Cobb, and G. P. Perram. "Chromotomographic Imager Field Demonstration Results," *Proceedings of SPIE*, 7668-3: 766804 (April 2010).
57. Bostick, R. L. and G. P. Perram. "Spatial and Spectral Performance of a Chromotomosynthetic Hyperspectral Imaging System," *Rev. Sci. Instrum.*, 83: 033110 (2012).
58. Sheirich, P. *An Engineering Trade Space Analysis for a Space-Based Hyperspectral Chromotomographic Scanner*. MS thesis, AFIT/GA/ENY/09-M08. School of Engineering and Management, Air Force Institute of Technology (AU), Wright-Patterson AFB OH, March 2009.

59. Book, T. A. *Design Analysis of a Chromotomographic Hyperspectral Imaging Experiment*. MS thesis, AFIT/GA/ENY/10-M01. School of Engineering and Management, Air Force Institute of Technology (AU), Wright-Patterson AFB OH, March 2010.
60. Neiderhauser, J. D. *Design and Characterization of a Space Based Chromotomographic Hyperspectral Imaging Experiment*. MS thesis, AFIT/GA/ENY/11-J02. School of Engineering and Management, Air Force Institute of Technology (AU), Wright-Patterson AFB OH, June 2011.
61. Hecht, E. *Optics*, San Francisco: Addison Wesley, p. 424 (2002).
62. Bocage, E. M. "Technique and Mechanism of a Moving X-ray Film." Paris, France French patent No. 536464, 1921.
63. Massiot, J. "History of Tomography," *MedicaMundi*, 19 (3): 106-115 (1974).
64. Hsieh, J. *Computed Tomography: Principles, Design, Artifacts, and Recent Advances*, Bellingham, WA: John Wiley & Sons, Inc., 2009.
65. Ruttimann, U. E., R. A. Groenhuis, and R. L. Webber. "Restoration of Digital Multiplane Tomosynthesis by a Constrained Iteration Method," *IEEE Trans. Med. Imaging*, 3(3): 141-148 (1984).
66. Brooks, R. A. and G. Di Chiro. "Principles of Computer Assisted Tomography (CAT) in Radiographic and Radioisotopic Imaging," *Phys. Med. Biol.*, 21(5): 689-732 (1976).
67. Kak, A. C. and M. Slaney. *Principles of Computerized Tomographic Imaging*. New York: IEEE Press, 1988.
68. Gordon, R., R. Bender, and G. T. Herman. "Algebraic reconstruction Techniques (ART) for three-Dimensional Electron Microscopy and X-ray Photography," *Journal of Theoretical Biology*, 29: 471-481 (1970).
69. Van de Sompel, D. and M. Brady. "A Systematic Performance Analysis of the Simultaneous Algebraic Reconstruction Technique (SART) for Limited Angle Tomography," *Conf Proc IEEE Eng Med Biol Soc*, 2008: 2729 – 2732 (August 2008).
70. Jiang, K. and G. Wang. "Convergence of the Simultaneous Algebraic Reconstruction Technique (SART)," *IEEE Transactions of Image Processing*, 12(8): 957-961 (August 2003).
71. Hanson, K. M. and G. W. Wecksung. "Bayesian Approach to Limited-Angle Reconstruction in Computed Tomography," *J. Opt. Soc. Am.*, 73(11): 1501-1509 (1983).

72. Dusaussoy, N. J. "Some New Multiplicative Algorithms for Image Reconstruction from Projections," *Linear Algebra and its Applications*, 130: 111-132 (1990).
73. Pan, X., E. Y. Sidky, and M. Vannier. "Why do Commercial CT Scanners Still Employ Traditional, Filtered Back Projection for Image Reconstruction?" *Inverse Probl.*, 25(12): 1-50 (2009).
74. Ruttiman, U. E., R. A. J. Groenhuis, and R. L. Webber. "Computer Tomosynthesis: A Versatile Three-Dimensional Imaging Technique," *Proceedings of the Annual Symposium on Computer Applications in Medical Care*, 783-786 (October 1983).
75. Wu, T., R. H. Moore, E. A. Rafferty, and D. B. Kopans. "A Comparison of Reconstruction Algorithms for Breast Tomosynthesis," *Medical Physics*, 31: 2636-2647 (2004).
76. Stevens, G., R. Fahrig and N. Pelc. "Filtered Backprojection for Modifying the Impulse Response of Circular Tomosynthesis," *Medical Physics*, 28 (3): 372-380 (2001).
77. Matsuo, H., A. Iwata, I. Horiba, and N. Suzumura. "Three-Dimensional Image Reconstruction by Digital Tomo-Synthesis Using Inverse Filtering", *Transactions on Medical Imaging*, 12 (2): 307-313 (1993).
78. Chen, P. and K. E. Barner. "Three-Dimensional Multi-Resolution Statistical Reconstruction for Tomosynthesis," *IEEE International Symposium on Biomedical Engineering: Nano to Macro*, 1: 559-562 (April 2004).
79. Dobbins, J. T. and D. J. Godfrey. "Digital X-Ray Tomosynthesis: Current State of the Art and Clinical Potential", *Phys. Med. Biol.*, 48: R65-R106 (2003).
80. Warp, R. J., D. G. Godfrey and J. T. Dobbins III. "Applications of Matrix Inverse Tomosynthesis," *Proceedings of SPIE*, 3977: 376-383 (February 2000).
81. Godfrey, D. J., R. J. Warp, and J. T. Dobbins III. "Optimization of Matrix Inverse Tomosynthesis," *Proceedings of SPIE*, 4320: 696-704 (February 2001).
82. Godfrey, D. J., A. Rader, and J. T. Dobbins III. "Practical Strategies for the Clinical Implementation of Matrix Inversion Tomosynthesis (MITS)," *Proceedings of SPIE*, 5030: 379-389 (February 2003).
83. Chen, Y., J. Y. Lo, J. A. Baker, and J. T. Dobbins III. "Gaussian Frequency Blending Algorithm with Matrix Inversion Tomosynthesis (MITS) and Filtered Back Projection (FBP) for Better Digital Breast Tomosynthesis Reconstruction," *Proceedings of SPIE*, 6142: 122 – 130 (February 2006).

84. Dills, A. N., G. A. Zimmer, and G. P. Perram. "Preliminary Test Report from AFIT Sensors for Brilliant Flash Tests (July 2002)." Technical Report AFIT/EN-TR-03-02, Air Force Institute of Technology, Wright-Patterson AFB, OH, 2002.
85. Dills, A. N. and G. P. Perram. "Brilliant Flash II Preliminary Test Report from AFIT Sensors." Technical Report, Air Force Institute of Technology, Wright-Patterson AFB, OH, 2003 (unpublished).
86. Gordon, J. M., K. C. Gross, and G. P. Perram. "Temporally-Resolved, Infrared Spectra from the Detonation of Advanced Munitions," *Proceedings of SPIE*, 7330: 733006 (April 2009).
87. Fruchter, A. S. and R. N. Hook. "Drizzle: A Method for the Linear Reconstruction of Undersampled Images," *Publ. of the Astron. Soc. Pac.*, 114: 144-152 (2002).
88. *Pen-Ray Line Sources*. Product Catalog. Leatherhead, Surrey, UK: L.O.T.-Oriol.
89. National Institute of Standards and Technology. "*NIST Atomic Spectra Database Lines Form*." http://physics.nist.gov/PhysRefData/ASD/lines_form.html. March 2008.
90. *PI-MAX / PI-MAX2 System User Manual*. Trenton, NJ: Princeton Instruments (2004).
91. Wagadarikar, A. A., N. P. Pitsianis, X. Sun, and D. J. Brady. "Video Rate Spectral Imaging Using a Coded Aperture Snapshot Spectral Imager," *Optics Express*, 17(8): 6369 - 6388 (2009).
92. Elvidge, C. D., D. M. Keith, B. T. Tuttle, and K. E. Baugh. "Spectral Identification of Lighting type and Character," *Sensors*, 10(4): 3961-3988 (2010).
93. Giglio, L. and C. O. Justice. "Effect of Wavelength Selection on Characterization of Fire Size and Temperature," *Int. J. Remote Sens.*, 24(17): 3515-3520 (2003).
94. Casadioa, S., O. Arinob, and D. Serpea. "Gas Flaring Monitoring from Space Using the ATSR Instrument Series," *Remote Sens. Environ.*, 116: 239-249 (2012).
95. Bostick, R. L. and G. P. Perram. "Instrumental Error in Chromotomosynthetic Hyperspectral Imaging," *Applied Optics*, 51(21): 5186-5200 (2012).
96. *VARISPEC Liquid Crystal Tunable Filters*. Instrument Specifications Sheet. Cambridge, MA: Cambridge Research and Instrumentation, Inc. <http://www.cri-inc.com/> (2010).
97. Seber, G. A. F. *Multivariate Observations*. New York: Wiley, 1984.

98. Spath, H. (translated by J. Goldschmidt). *Cluster Dissection and Analysis: Theory, FORTRAN Programs, Examples*. New York: Halsted Press, 1985.
99. Bostick, R. L. and G. P. Perram, "Classification of Visible Point Sources Using Hyperspectral Chromotomosynthetic Imagery," *J. Appl. Remote Sens.*, 6(1): 063584 (October 2012).
100. Colsher, J. G. "Iterative Three-Dimensional Image Reconstruction from Tomographic Projections", *Comput. Grap. Image Processing*, 6: 513-537 (1977).
101. De Man, B. "Metal Streak Artifacts in X-ray Computed Tomography: A Simulation Study," *Nuclear Science Symposium*, 3: 1860-1865 (November 1998).
102. Noël, P. B., J. Xu, K. R. Hoffman, J. J. Corso, S. Schafer, and A. M. Walczak. "High Contrast Artifact Reduction in Cone Beam Computed Tomography by Using Geometric Techniques," *Proceedings of SPIE*, 7258: 72583A (February 2009).
103. Nicholls, R. W. "The Interpretation of Intensity Distributions in the CN Violet, C₂ Swan, OH Violet and O₂ Schumann-Runge Band Systems by use of their r-Centroids and Franck-Condon Factors," *Proc. Phys. Soc., Section A.*, 69(10): 741 – 753 (1959).
104. Mentall, J. E. and R. W. Nicholls. "Absolute Band Strengths for the C₂ Swan System," *Proc. Phys. Soc.*, 86 (4): 873 – 876 (1965).

Vita

Randall L. Bostick was born and raised in Springfield Ohio, where he graduated from Greenon High School in 1989. He then began studying at Wright State University in Dayton, OH, where he earned an undergraduate degree in Secondary Math Education with a Minor in Physics in 1994. He continued at WSU and in 1997 graduated with a Masters degree in Physics. That same year, he began work supporting the National Air and Space Intelligence Center (NASIC) as a contractor at Ball Aerospace. In 2002, he accepted a Dayton Area Graduate Studies Institute scholarship to begin coursework in pursuit of a Doctorate Degree in Physics in the field of Electro-Optics. In 2003, he accepted a job as an Air Force Civilian at NASIC and was chosen for the long-term full-time training program to complete the necessary class work and requirements to be accepted as a PhD candidate. Since then, he has been conducting research and finishing the degree while working full time at NASIC as the R&D subject matter expert for space based DoD and Intelligence sensors. Upon graduation, he will continue to serve as the R&D lead for these systems at NASIC.

REPORT DOCUMENTATION PAGE

*Form Approved
OMB No. 0704-0188*

The public reporting burden for this collection of information is estimated to average 1 hour per response, including the time for reviewing instructions, searching existing data sources, gathering and maintaining the data needed, and completing and reviewing the collection of information. Send comments regarding this burden estimate or any other aspect of this collection of information, including suggestions for reducing the burden, to Department of Defense, Washington Headquarters Services, Directorate for Information Operations and Reports (0704-0188), 1215 Jefferson Davis Highway, Suite 1204, Arlington, VA 22202-4302. Respondents should be aware that notwithstanding any other provision of law, no person shall be subject to any penalty for failing to comply with a collection of information if it does not display a currently valid OMB control number.

PLEASE DO NOT RETURN YOUR FORM TO THE ABOVE ADDRESS.

1. REPORT DATE (DD-MM-YYYY) 01-03-2013		2. REPORT TYPE Doctoral Dissertation		3. DATES COVERED (From - To) June 2005 - September 2012	
4. TITLE AND SUBTITLE DEVELOPMENT AND CHARACTERIZATION OF A CHROMOTOMOSYNTHETIC HYPERSPECTRAL IMAGING SYSTEM				5a. CONTRACT NUMBER	
				5b. GRANT NUMBER	
				5c. PROGRAM ELEMENT NUMBER	
6. AUTHOR(S) Bostick, Randall L., Civilian, GG-14				5d. PROJECT NUMBER N/A	
				5e. TASK NUMBER	
				5f. WORK UNIT NUMBER	
7. PERFORMING ORGANIZATION NAME(S) AND ADDRESS(ES) Air Force Institute of Technology Graduate School of Engineering and Management (AFIT/ENP) 2950 Hobson Way, Building 640 WPAFB OH 45433-8865				8. PERFORMING ORGANIZATION REPORT NUMBER AFIT-ENP-DS-13-M-02	
9. SPONSORING/MONITORING AGENCY NAME(S) AND ADDRESS(ES) National Air and Space Intelligence Center Mr. Michael Sherry, NASIC/GSP 4180 Watson Way WPAFB OH 45433-8865 (937) 656-0186, michael.sherry@us.af.mil				10. SPONSOR/MONITOR'S ACRONYM(S)	
				11. SPONSOR/MONITOR'S REPORT NUMBER(S)	
12. DISTRIBUTION/AVAILABILITY STATEMENT Distribution Statement A. Approved for Public Release; Distribution is Unlimited					
13. SUPPLEMENTARY NOTES					
14. ABSTRACT A chromotomosynthetic imaging (CTI) methodology based upon mathematical reconstruction of a set of 2-D spectral projections to collect high-speed (>100 Hz) 3-D hyperspectral data cube has been proposed. The CTI system can simultaneously provide usable 3-D spatial and spectral information, provide high-frame rate slitless 1-D spectra, and generate 2-D imagery equivalent to that collected with no prism in the optical system. The wavelength region where prism dispersion is highest (<500 nm) is most sensitive to loss of spectral resolution in the presence of systematic error, while wavelengths >600 nm suffer mostly from a shift of the spectral peaks. The quality of the spectral resolution in the reconstructed hyperspectral imagery was degraded by as much as a factor of two in the blue spectral region with less than 1° total angular error in mount alignment in the two axes of freedom. Even with no systematic error, spatial artifacts from the reconstruction limit the ability to provide adequate spectral imagery without specialized image reconstruction techniques as targets become more spatially and spectrally uniform.					
15. SUBJECT TERMS hyperspectral imaging, chromotomography, chromotomosynthesis, high speed imagery, battlespace characterization, target discrimination					
16. SECURITY CLASSIFICATION OF:			17. LIMITATION OF ABSTRACT SAR	18. NUMBER OF PAGES 232	19a. NAME OF RESPONSIBLE PERSON Glen P. Perram, PhD, USAF
a. REPORT U	b. ABSTRACT U	c. THIS PAGE U			19b. TELEPHONE NUMBER (Include area code) (937) 255-3636 x4504 (glen.perram@afit.edu)

Reset